

Modelling and Experimental Characterization of Nanoindentation Responses of Various Biocomposite Materials



Pengfei Duan

School of Engineering

Newcastle University

A thesis submitted for the degree of

Doctor of Philosophy

February 2018

Abstract

In the past decades, composite materials (which are usually classified into fibre-reinforced composites and particle-reinforced composites, depending on the geometry of the reinforcements) have been widely applied in tissue engineering as implant scaffolds. A lot of work has been done on the bulk mechanical properties of these composites. However, there is lack of nanomechanical characterization of such composites, which is crucial for understanding the cell-material interactions at small scale, and further optimizing the design of scaffold materials to promote the formation of new viable tissue.

Nanoindentation has been used for nanomechanical characterization of a wide range of composite materials, but there is lack of comprehensive modelling of these composites. Therefore, this thesis begins with the modelling of the nanomechanics of inclusion-reinforced composite materials. In this part, finite element analysis (FEA) is adopted to study the spatial-dependent mechanical response of fibre/matrix and particle/matrix composites. The effects of various factors (such as inclusion geometry, indenter geometry, inclusion orientation and relative indentation location) on the nanomechanical response are studied. Various indentation-based empirical or semi-analytical models have been examined and novel analytical models are proposed to describe the nanomechanical behaviour of these inclusion-reinforced composites.

Towards the end of this thesis, the nanoindentation characterization of typical biocomposite materials is presented, namely extracellular matrix. For these complex composites, the existing analytical models may not be directly applied. However, with the aid of a statistical model and FEA, it has been demonstrated that mechanical properties of each individual component can be determined.

Acknowledgements

I would like to express my deeply thanks to all the people I came across during this four years. Among these, I would like to especially express my deep gratitude to the following people and organisation:

- My supervisors, Dr Jinju Chen and Prof Steve Bull, for sharing their invaluable and vast knowledge. Without their enlightening guidance and encouragement, I could not have finished this thesis. Their conscientiousness and carefulness inspire me not only in this project but also in my future study.
- Newcastle University for providing the Teaching Scholarship.
- All the colleagues and staff in School of Chemical Engineering and Advanced materials and School of Mechanical and System Engineering for their friendliness and support. Dr Jose Portoles, Dr Zhongxu Hu, Dr Oana Bretcanu, Prof Peter Cumpson and Prof Yanping Cao for their technical support. Dr David Swailes, Dr Francis Franklin, Dr Piergiorgio Gentile and Mr Robert Davidson for their kindness and friendship. Special thanks to Dr Mohammed Al-Washahi, Dr Ana Ferreira-Duarte and Mr Murhamdilah Morni who helped me a lot, especially in the beginning.
- Dr Ria Toupaniari and Dr Simon Partridge for providing the mineralized matrix samples. Dr Saikat Jana for providing the inclusion/matrix samples.
- All my friends for their encouragement, support and friendship.
- My girlfriend Boru for her understanding, encouragement and support. My family for their spiritual and financial support without any expectation of return.

List of Publications

1. **Duan, P.**, Kandemir, N., Wang, J. and Chen, J. (2017) 'Rheological Characterization of Alginate Based Hydrogels for Tissue Engineering', *MRS Advances*, 2(24), pp. 1309-1314.
2. **Duan, P.** and Chen, J. (2015) 'Nanomechanical and microstructure analysis of extracellular matrix layer of immortalized cell line Y201 from human mesenchymal stem cells', *Surface and Coatings Technology*, 284, pp. 417-421.
3. **Duan, P.**, Bull, S. and Chen, J. (2015) 'Modeling the nanomechanical responses of biopolymer composites during the nanoindentation', *Thin Solid Films*, 596, pp. 277-281.
4. Kandemir, N., Xia, Y., **Duan, P.**, Yang, W. and Chen, J. (2018) 'Rheological Characterization of Agarose and Poloxamer 407 (P407) Based Hydrogels', *MRS Advances*, pp.1-6.
5. Cao, Y., Su, B., Chinnaraj, S., Jana, S., Bowen, L., Charlton, S., **Duan, P.**, Jakubovics, N.S. and Chen, J. (2018) 'Nanostructured titanium surfaces exhibit recalcitrance towards *Staphylococcus epidermidis* biofilm formation', *Scientific Reports*, 8(1), p. 1071.
6. Cao, Y., **Duan, P.** and Chen, J. (2016) 'Modelling the nanomechanical response of a micro particle-matrix system for nanoindentation tests', *Nanotechnology*, 27(19), p. 195703.
7. Wang, W.B., Fu, Y.Q., Chen, J.J., Xuan, W.P., Chen, J.K., Wang, X.Z., Mayrhofer, P., **Duan, P.F.**, Bittner, A. and Schmid, U. (2016) 'AlScN thin film based surface acoustic wave devices with enhanced microfluidic performance', *Journal of Micromechanics and Microengineering*, 26(7), p.075006

8. Chen, J. and **Duan, P.** (2014) 'Nanomechanical responses of biopolymer composites determined by nanoindentation with a conical tip', *European Cells and Materials*, Vol. 28. Suppl. 4, p.65, ISSN 1473-2262, <http://www.ecmjournal.org>

Table of Contents

Abstract	i
Acknowledgements	ii
List of Publications.....	iii
List of Figures	x
List of Tables.....	xxi
Nomenclature	xxiii
Chapter 1. Introduction	1
1.1 Introduction	2
1.2 Aim and objectives.....	3
1.3 Thesis outline.....	3
Chapter 2. Nanoindentation Techniques	7
2.1 Introduction to nanoindentation.....	8
2.2 Force-displacement curves.....	9
2.2.1 General parameters in a $P\text{-}\delta$ curve	9
2.2.2 Extraction of elastic modulus and hardness from the $P\text{-}\delta$ curves... <td>12</td>	12
2.2.2.1 Unloading curve method	12
2.2.2.2 Loading curve method	16
2.2.2.3 Energy-based method.....	20
2.2.2.4 Slope-based method.....	24
2.2.3 Extraction of time-dependent properties from the $P\text{-}\delta$ curves	25
2.2.3.1 Dynamic nanoindentation test.....	25
2.2.3.2 Quasi-static nanoindentation test.....	27
2.2.4 Extraction of other mechanical properties from the $P\text{-}\delta$ curves.....	32

2.3	Indenter geometry and selection.....	33
2.4	Factors affecting the nanoindentation results	37
2.4.1	Load frame compliance.....	38
2.4.2	Tip geometry	39
2.4.3	Surface roughness.....	41
2.4.4	Initial penetration depth.....	42
2.4.5	Thermal drift and creep.....	43
2.4.6	Piling-up and sinking-in.....	45
2.4.7	Indentation size effect.....	46
2.5	Application of nanoindentation in biomaterials.....	47
2.5.1	Mineralized tissues	47
2.5.2	Soft tissues	50
2.5.3	Acellular biomaterials (Inclusion-reinforced composites)	51
2.6	Summary	54

Chapter 3. Nanomechanical Modelling of Viscoelastic Fibre in Viscoelastic Matrix	55	
3.1	Introduction	56
3.2	Finite element method	59
3.3	Results and discussion	64
3.3.1	Model validation.....	64
3.3.2	The Young's modulus determined by FEA.....	67
3.3.3	Comparison of the various empirical models	72
3.3.4	Alternative models	78
3.3.5	A new linear-based model	92
3.4	Summary	94

Chapter 4. Nanomechanical Modelling of Elastic-Plastic Particles in Elastic-Plastic Matrix	95
4.1 Introduction	96
4.2 Analytical method	97
4.3 Methodology	98
4.3.1 Finite element modelling setting up.....	98
4.3.2 Model calibration.....	103
4.3.3 Elastic-plastic material model.....	103
4.3.4 Curve fitting.....	106
4.4 Results and discussion	106
4.4.1 Model validation	106
4.4.2 Typical load-displacement curves	110
4.4.3 Model elastic-plastic response of the composites during nanoindentation	117
4.5 Summary	134
Chapter 5. Nanomechanical Modelling of Elastic Fibre with Different Orientations in Elastic Matrix.....	135
5.1 Introduction	136
5.2 Methodology	137
5.2.1 Analytical method.....	137
5.2.2 Finite element method	138
5.2.3 Model calibration and curve fitting.....	143
5.3 Results and discussion	144
5.3.1 The apparent Young's modulus determined by FEA.....	144
5.3.2 Extraction of the elastic modulus of the inclusion and the matrix	152
5.3.3 Effect of indenter geometry	156
5.4 Summary	162

Chapter 6. Nanomechanical Case Study on Mineralized Matrix: Experimental Characterization and Finite Element Modelling	163
6.1 Introduction	164
6.2 Materials and experimental methods	165
6.2.1 Sample preparation	165
6.2.2 Thickness measurement.....	166
6.2.3 Surface analysis	167
6.2.3.1 Optical microscope	168
6.2.3.2 Profilometer	168
6.2.3.3 Scanning electron microscope and energy-dispersive X-ray spectroscopy	169
6.2.3.4 Atomic-force microscope	171
6.2.4 Nanoindentation.....	174
6.2.4.1 Hysitron Triboindenter.....	174
6.2.4.2 Different test modes.....	176
6.2.5 Statistical analysis	179
6.2.6 Finite element modelling	180
6.3 Results and discussion	182
6.3.1 Surface analysis	182
6.3.2 Nanoindentation results	191
6.3.2.1 The apparent elastic modulus and hardness	191
6.3.2.2 Data analysis by the Gaussian mixture model	200
6.3.3 Finite element simulations	210
6.4 Summary	212
Chapter 7. Conclusions and Further Work.....	215
7.1 Conclusions	216
7.2 Further follow up	217

Appendix A. Experimental Tests of a Viscoelastic Fibre in a Viscoelastic Matrix	219
A.1 Introduction	219
A.2 Description of the samples and the instrument	219
A.3 Experiment results	221
A.4 Finite element modelling results	223
Appendix B. Nanomechanical Modelling of a Porous Structure	227
B.1 Modelling of a porous structure.....	227
B.2 Finite element modelling results	227
References.....	229

List of Figures

Figure 1.1 A flow chart of the structure of this thesis	5
Figure 2.1 Schematic of a typical force and displacement curve of an elastic-plastic material indented by a pyramidal indenter.	11
Figure 2.2 Schematic of a cross section of an indentation with the assumption that piling-up and sinking-in are negligible. Various dimensions that used in the analysis are indicated (Oliver and Pharr, 1992).	13
Figure 2.3 Schematic of the radial displacement of the deformed surface after load removal (Hay <i>et al.</i> , 1999).	16
Figure 2.4 Schematic of a non-perfect indenter with a rounded tip (Sun <i>et al.</i> , 1999).....	20
Figure 2.5 Dynamic mechanical model of a nanoindentation instrument. m is the mass of the indenter and shaft, C_f is the load frame compliance, S is the contact stiffness, λ_S is a damping coefficient of the contact, k_s is the stiffness of the mounting spring, and λ is a damping coefficient related to the instrument (Fischer-Cripps, 2011e).....	27
Figure 2.6 Mechanical models of a viscoelastic material. (a) A two-element Maxwell model. (b) A three-element Voigt model. (c) Combined Maxwell-Voigt model. η is the coefficient of viscosity, E_1 and E_2 are elastic modulus related to the relaxation modulus (Fischer-Cripps, 2011e).....	28
Figure 2.7 Schematic of cracks introduced by (a) Vickers indenter and (b) Berkovich indenter. Crack length c is the distance between the centre of the impression and the crack tip, and crack length l is the distance between the corner of the impression and the crack tip (Fischer-Cripps, 2007).....	32
Figure 2.8 A representative uniaxial stress-strain response for an ideal elastic-plastic material. x is the strain hardening index, Y is the yield stress, and the proportionality constant $K = Y(E/Y)^x$. For $x = 0$, the material is elastic perfectly-plastic.	33

Figure 2.9 Schematic of indenting a tissue sample with various indenters, (a) a spherical tip with a large diameter, (b) a spherical tip with a small diameter, (c) a sharp indenter, and (d) a cylindrical flat punch with a large diameter (Ebenstein and Pruitt, 2006).....	37
Figure 2.10 Schematic of the comparison of contact area between an ideal conical tip and a non-ideal conical tip (Fischer-Cripps, 2011b).	40
Figure 2.11 Illustration of the contact of a conical indenter with a fractal surface (Bobji and Biswas, 1999).....	41
Figure 2.12 Schematic of the existence of initial penetration depth (Fischer-Cripps, 2011b).....	43
Figure 2.13 Schematic of the nose phenomenon on the P- δ curve indented from a viscoelastic material (Ebenstein and Pruitt, 2006).....	44
Figure 2.14 Illustration of sinking-in and piling-up during nanoindentation (Fischer-Cripps, 2011b).....	45
Figure 2.15 Schematic of mechanical transition between dentin and enamel. The plot showed the corresponding mechanical properties determined from indentations. It showed that both hardness and elastic modulus rapidly decreased from enamel region to dentin region (Marshall <i>et al.</i> , 2001a)....	49
Figure 2.16 Hierarchical structure of the FE model of lobster cuticle: (I) N-acetyl-glucosamine molecules, (II) α -chitin chains, (III) representative volume element (RVE) of a chitin fibre, (IVa) RVE of chitin fibres arranged in twisted plywood without canals, (IVb) RVE of mineral-protein matrix, (V) transversely isotropic cuticle without canals, (VI) cuticle with a hexagonal array of canals, and (VII) composite cuticle (Nikolov <i>et al.</i> , 2010).	50
Figure 2.17 Schematic of nanocomposites reinforced by (a) aligned fibres, (b) randomly oriented fibres, (c) aligned platelets, and (d) particles (Liu and Brinson, 2008).....	52

Figure 2.18 Computational model of (a) a cylindrical indenter indenting into a composite with uniform distribution of fibres, (b) a cylindrical indenter indenting into a composite with random distribution of fibres, and (c) a cylindrical indenter with irregular profile indenting into a composite with random distribution of elliptical fibres (Cao and Chen, 2012)	53
Figure 2.19 Schematic of the grid indentation for a composite material. Small displacement enables the mechanical characterization of each individual constituent, while large displacement leads to the properties of the homogenized medium (Constantinides <i>et al.</i> , 2006).....	53
Figure 3.1 Schematic of the indentation of a two-phase biopolymer composite.....	60
Figure 3.2 Finite element mesh for the inclusion/matrix system, (a) the overview of the inclusion/matrix system, (b) enlarged details of inclusion elements underneath the tip.	61
Figure 3.3 Ramping-holding procedure.....	61
Figure 3.4 Absolute deviation ($ F_0 - F_i /F_0$) between the force from the models with different mesh density, indented by the indenters with (a) $\theta = 70.3^\circ$, $r = 0.1 \mu m$, (b) $\theta = 60^\circ$, $r = 0.1 \mu m$, and (c) $\theta = 70.3^\circ$, $r = 0.01 \mu m$	65
Figure 3.5 Absolute deviation ($ F_{Hertz} - F_{Simulated} /F_{Hertz}$) between the theoretical data and the simulated data indented by a spherical indenter..	67
Figure 3.6 Force-displacement curves of the 10 MPa inclusion surrounding by matrix with increasing elastic modulus from 2 to 50 MPa, indented by the indenters with (a) $\theta = 70.3^\circ$, $r = 0.1 \mu m$, (b) $\theta = 60^\circ$, $r = 0.1 \mu m$, and (c) $\theta = 70.3^\circ$, $r = 0.01 \mu m$	68
Figure 3.7 The Young's modulus of the inclusion/matrix system, $E(\text{composite})$, measured by the indenters with (a) $\theta = 70.3^\circ$, $r = 0.1 \mu m$, (b) $\theta = 60^\circ$, $r = 0.1 \mu m$, and (c) $\theta = 70.3^\circ$, $r = 0.01 \mu m$	70

Figure 3.8 Fit the E (*composite*) by (a) Equation 3.1, (b) Equation 3.4, (c) Equation 3.5, and (d) Equation 3.6, when the half-included angle of the indenter equals 70.3° , and the tip radius of the indenter equals $0.1 \mu\text{m}$72

Figure 3.9 Fit the E (*composite*) by Clifford model, (a) $\theta = 70.3^\circ$, $r = 0.1 \mu\text{m}$, $E_M < E_I$, (b) $\theta = 70.3^\circ$, $r = 0.1 \mu\text{m}$, $E_M > E_I$, (c) $\theta = 60^\circ$, $r = 0.1 \mu\text{m}$, $E_M < E_I$, (d) $\theta = 60^\circ$, $r = 0.1 \mu\text{m}$, $E_M > E_I$, (e) $\theta = 70.3^\circ$, $r = 0.01 \mu\text{m}$, $E_M < E_I$, and (f) $\theta = 70.3^\circ$, $r = 0.01 \mu\text{m}$, $E_M > E_I$74

Figure 3.10 Plot the E (*composite*) using modified Equation 3.16, (a) $\theta = 70.3^\circ$, $r = 0.1 \mu\text{m}$, $E_M < E_I$, (b) $\theta = 70.3^\circ$, $r = 0.1 \mu\text{m}$, $E_M > E_I$, (c) $\theta = 60^\circ$, $r = 0.1 \mu\text{m}$, $E_M < E_I$, (d) $\theta = 60^\circ$, $r = 0.1 \mu\text{m}$, $E_M > E_I$, (e) $\theta = 70.3^\circ$, $r = 0.01 \mu\text{m}$, $E_M < E_I$, and (f) $\theta = 70.3^\circ$, $r = 0.01 \mu\text{m}$, $E_M > E_I$80

Figure 3.11 Plot the E (*composite*) using modified Equation 3.17, (a) $\theta = 70.3^\circ$, $r = 0.1 \mu\text{m}$, $E_M < E_I$, (b) $\theta = 70.3^\circ$, $r = 0.1 \mu\text{m}$, $E_M > E_I$, (c) $\theta = 60^\circ$, $r = 0.1 \mu\text{m}$, $E_M < E_I$, (d) $\theta = 60^\circ$, $r = 0.1 \mu\text{m}$, $E_M > E_I$, (e) $\theta = 70.3^\circ$, $r = 0.01 \mu\text{m}$, $E_M < E_I$, and (f) $\theta = 70.3^\circ$, $r = 0.01 \mu\text{m}$, $E_M > E_I$83

Figure 3.12 Plot the E (*composite*) using modified Equation 3.18 and Equation 3.20, (a) $\theta = 70.3^\circ$, $r = 0.1 \mu\text{m}$, $E_M < E_I$, (b) $\theta = 70.3^\circ$, $r = 0.1 \mu\text{m}$, $E_M > E_I$, (c) $\theta = 60^\circ$, $r = 0.1 \mu\text{m}$, $E_M < E_I$, (d) $\theta = 60^\circ$, $r = 0.1 \mu\text{m}$, $E_M > E_I$, (e) $\theta = 70.3^\circ$, $r = 0.01 \mu\text{m}$, $E_M < E_I$, and (f) $\theta = 70.3^\circ$, $r = 0.01 \mu\text{m}$, $E_M > E_I$86

Figure 3.13 Plot the E (*composite*) using modified Equation 3.19, (a) $\theta = 70.3^\circ$, $r = 0.1 \mu\text{m}$, $E_M < E_I$, (b) $\theta = 70.3^\circ$, $r = 0.1 \mu\text{m}$, $E_M > E_I$, (c) $\theta = 60^\circ$, $r = 0.1 \mu\text{m}$, $E_M < E_I$, (d) $\theta = 60^\circ$, $r = 0.1 \mu\text{m}$, $E_M > E_I$, (e) $\theta = 70.3^\circ$, $r = 0.01 \mu\text{m}$, $E_M < E_I$, and (f) $\theta = 70.3^\circ$, $r = 0.01 \mu\text{m}$, $E_M > E_I$89

Figure 4.1 Schematic of the indentation of (a) the spherical particle embedded in the matrix and (b) the cylindrical particle embedded in the matrix.....99

Figure 4.2 Overview of the finite element mesh and the enlarged details of elements underneath the tip for (a) the spherical particle embedded in the matrix and (b) the cylindrical particle embedded in the matrix.....101

Figure 4.3 Schematic of the loading-unloading indentation protocol which has a maximum displacement of 0.1 μm	102
Figure 4.4 Rheological model of an elastic-plastic material by arranging the spring and the friction element in series. The spring represents the elastic behaviour and the friction element represents the plastic behaviour.	105
Figure 4.5 Uniaxial elastic-plastic stress-strain curve. x is the strain hardening index, and the proportionality constant $K = Y(E/Y)^x$. For $x = 0$, the material is elastic perfectly-plastic (Yu, 2006).	105
Figure 4.6 Absolute deviation ($ F_0 - F_i /F_0$) between the force from the models with different mesh density for (a) semi-spherical particle (0.5 μm) embedded in the matrix, (b) cylindrical particle (0.437 μm) embedded in the matrix and (c) cylindrical particle (0.5 μm) embedded in the matrix.	108
Figure 4.7 Absolute deviation ($ F_{Hertz} - F_{Simulated} /F_{Hertz}$) between the theoretical data and the simulated data for each particle/matrix system when indented by a spherical indenter.	110
Figure 4.8 The load-displacement curves for the indentation test upon a semi-spherical particle within the matrix, (a) HA particle embedded in polymer 1, (b) HA particle embedded in polymer 2, (c) HA particle embedded in polymer 3, (d) polymer 1 embedded in the HA matrix, (e) polymer 2 embedded in the HA matrix and (f) polymer 3 embedded in the HA matrix.	111
Figure 4.9 Composite elastic modulus (E_c) against RID for (a) three different HA particles embedded in polymer 1 and (b) three different particles of polymer 1 embedded in the HA matrix.....	115
Figure 4.10 Composite hardness (H_c) against RID for (a) three different HA particles embedded in polymer 1 and (b) three different particles of polymer 1 embedded in the HA matrix.....	116

Figure 4.11 Plots of $\frac{E_C^* - E_P^*}{E_M^* - E_P^*}$ against z using Equation 4.1 for, (a) semi-spherical HA particles (0.5 μm) in polymers, (b) semi-spherical polymers (0.5 μm) in HA matrix, (c) cylindrical HA particles (0.437 μm) in polymers, (d) cylindrical polymers (0.437 μm) in HA matrix, (e) cylindrical HA particles (0.5 μm) in polymers and (f) cylindrical polymers (0.5 μm) in HA matrix. 118

Figure 4.12 Plots of $\frac{H_C - H_P}{H_M - H_P}$ against z using Equation 4.3 for, (a) semi-spherical HA particles (0.5 μm) in polymers, (b) semi-spherical polymers (0.5 μm) in HA matrix, (c) cylindrical HA particles (0.437 μm) in polymers, (d) cylindrical polymers (0.437 μm) in HA matrix, (e) cylindrical HA particles (0.5 μm) in polymers and (f) cylindrical polymers (0.5 μm) in HA matrix. 121

Figure 4.13 Plots of $\frac{E_C^* - E_P^*}{E_M^* - E_C^*}$ against z using Equation 4.13 for, (a) semi-spherical HA particles (0.5 μm) in polymers, (b) semi-spherical polymers (0.5 μm) in HA matrix, (c) cylindrical HA particles (0.437 μm) in polymers, (d) cylindrical polymers (0.437 μm) in HA matrix, (e) cylindrical HA particles (0.5 μm) in polymers and (f) cylindrical polymers (0.5 μm) in HA matrix. 126

Figure 4.14 Plots of $\frac{H_C - H_P}{H_M - H_C}$ against z using Equation 4.14 for, (a) semi-spherical HA particles (0.5 μm) in polymers, (b) semi-spherical polymers (0.5 μm) in HA matrix, (c) cylindrical HA particles (0.437 μm) in polymers, (d) cylindrical polymers (0.437 μm) in HA matrix, (e) cylindrical HA particles (0.5 μm) in polymers and (f) cylindrical polymers (0.5 μm) in HA matrix. 129

Figure 5.1 Schematic of the indentation of reinforced fibre with different orientations in matrix. (a) A vertical fibre embedded in the matrix and (b) a horizontal fibre embedded in the matrix, with the indenter just above the centre of the inclusion. 139

Figure 5.2 Finite element mesh for (a) the vertical fibre model and (b) the horizontal fibre model in the case of $d/r = 2$, indented by the conical indenter. 141

Figure 5.3 Finite element mesh for the vertical fibre model in the case of $d/r = 2$, indented by the Berkovich indenter with two different orientations. That is, (a) the pyramid flat faces toward the fibre and (b) the pyramid edge faces toward the fibre.	142
Figure 5.4 Loading-unloading procedure.	143
Figure 5.5 The $F-\delta$ curves for the indentation test on (a) vertical fibre model and (b) horizontal fibre model, with the conical indenter.	145
Figure 5.6 The composite elastic modulus for (a) the vertical fibre model and (b) the horizontal fibre model, with different distances between the conical indenter and the inclusion.	146
Figure 5.7 Von Mises stress contours for the vertical fibre model with a displacement of 0.5 μm , when (a) $d/r = 0$, (b) $d/r = 1$, (c) $d/r = 2$, (d) $d/r = 3$ and (e) $d/r = 5$. For standardization, all the figures share the same stress scale.	147
Figure 5.8 Von Mises stress contours for the horizontal fibre model from two orthogonal cross-sections with a displacement of 0.5 μm , when (a) $d/r = 0$, (b) $d/r = 0.5$, (c) $d/r = 2$, (d) $d/r = 3$, (e) $d/r = 4$ and (f) $d/r = 5$. For standardization, all the figures share the same stress scale.	150
Figure 5.9 Comparison of the von Mises stress contours for the vertical fibre model with $d/r = 2$, indented by (a) the Berkovich indenter with the pyramid flat facing toward the fibre, (b) the Berkovich indenter with the pyramid edge facing toward the fibre and (c) the conical indenter. For standardization, the maximum stress limit was set to 1.2 MPa and the minimum stress limit was set to 0 MPa in all the figures.	157
Figure 5.10 The apparent elastic modulus for the vertical fibre model in the case of $d/r = 2$, indented by different indenters and orientations.	160

Figure 5.11 The quantification of 0.2 MPa contour line of von Mises stress contours shown in Figure 5.9. That is, the contour lines of the vertical fibre model with $d/r = 2$, when indented by (a) the Berkovich indenter with the pyramid flat facing toward the fibre, (b) the Berkovich indenter with the pyramid edge facing toward the fibre and (c) the conical indenter. The origin of each coordinate system represents the indentation point.	160
Figure 6.1 Schematic of the crater within the sample produced by a ball crater tester. In practice, the outer circle will be irregular for a coating layer with non-uniform thickness.	167
Figure 6.2 Representative surface profile of a mineralized matrix sample.....	168
Figure 6.3 Illustration of the main components of a typical SEM (Mintz, 2015).	169
Figure 6.4 Schematic diagram of various signals emitted from the interaction volume when the electron beam hits the sample surface (Claudionico, 2015).	170
Figure 6.5 Schematic of an AFM using beam deflection detection (Nobelium, 2015).	172
Figure 6.6 Relation between interatomic force and tip-to-sample distance, when the van der Waals force is dominated (Howland and Benatar, 1996; Maver <i>et al.</i> , 2013).	172
Figure 6.7 Schematic of AFM image artefacts due to (a) the bluntness of the tip, (b) a faster scanning speed, and (c) a steep sample topography.....	173
Figure 6.8 Pictures of Hysitron Triboindenter, (a) granite base, X-Y positioning stage, top-down optical microscope, TriboScanner and transducer, (b) schematic of the three-plate capacitive transducer, and (c) vibration isolation platform and acoustic enclosure (Wang <i>et al.</i> , 2009).	175

Figure 6.9 Schematic of various load functions, (a) a typical loading-unloading function, (b) a loading-unloading function with holding period at maximum load, (c) multi-cycling load function for constant repetition mode with holding period in each cycle, (d) multi-cycling load function for ramping mode, (e) multi-cycling load function for constant repetition mode, and (f) multi-cycling load function for ramping mode with holding period in each cycle (Nowicki <i>et al.</i> , 2003; Chen and Bull, 2008; Bull <i>et al.</i> , 2012)	176
Figure 6.10 Schematic of the multi-cycling loading function	179
Figure 6.11 Schematic of (a) the model with distribution of different indented locations, (b) vertical distance of each indentation points away from the interface, and (c) the meshes for the model.	181
Figure 6.12 Typical SEM images of cells cultured at different conditions (A: day 7, BM; B: day 14, BM; C: day 21, BM; D: day 7, OM; E: day 14, OM), an enlargement of the marked area in figure C is shown in Figure 6.13.	184
Figure 6.13 Minerals observed on samples cultured in BM for 21 days.....	186
Figure 6.14 EDS spectrum for the minerals observed on the sample cultured in BM for 21 days.....	186
Figure 6.15 Representative intensity profile of calcium and phosphorus for the minerals detected in the line scan mode and the corresponding percentage of calcium and phosphorus.	187
Figure 6.16 Representative AFM images of samples cultured at different conditions (A: day 7, BM; B: day 14, BM; C: day 21, BM; D: day 7, OM; E: day 14, OM).	188
Figure 6.17 Representative polarized light images of samples harvested from (a, b) day 14, BM, (c, d) day 14, OM. Among them, image (a, c) are samples viewed with parallel polars, and image (b, d) are the same field viewed with crossed polars.....	190
Figure 6.18 Representative force-displacement curve from multi-cycling tests for sample cultured in BM for 21 days.	191

Figure 6.19 Young's modulus (\pm SD) of samples cultured in (a) BM and (b) OM ($P<0.001$), as a function of average contact depth for nanoindentation tests in the peak load range 1~9 mN.....	194
Figure 6.20 Hardness (\pm SD) of samples cultured in (a) BM and (b) OM ($P<0.001$), as a function of average contact depth for nanoindentation tests in the peak load range 1~9 mN.....	195
Figure 6.21 Histograms of elastic modulus for reported engineered bone produced by C3H10T1/2 MSC line grown in vivo for 28 days (Pelled <i>et al.</i> , 2007a).....	197
Figure 6.22 Histograms of elastic modulus for mineralized matrix samples cultured from (a) day 7, (b) day 14 and (c) day 21, tested at two different peak loads (1000 μ N and 7000 μ N).....	198
Figure 6.23 Representative distributions of Young's modulus for the matrix harvested from (a) day 14, BM, (b) day 14, OM, tested at a peak load of 1000 μ N.....	202
Figure 6.24 Young's modulus of two different components in the matrix cultured in different media for (a) 7 days, (b) 14 days and (c) 21 days, determined by the Gaussian mixture model for nanoindentation tests in the peak load range 1~9 mN.....	203
Figure 6.25 Hardness of two different components in the matrix cultured in different media for (a) 7 days, (b) 14 days and (c) 21 days, determined by the Gaussian mixture model for nanoindentation tests in the peak load range 1~9 mN.....	204
Figure 6.26 The (a) Young's modulus and (b) hardness of each component in the matrix cultured in different media as a function of culture period.....	206
Figure 6.27 Elastic anisotropy ratio for samples cultured in (a) BM and (b) OM, and hardness anisotropic ratio for samples cultured in (c) BM and (d) OM, as a function of average contact depth for nanoindentation tests in the peak load range 1~9 mN.	208

Figure 6.28 The elastic modulus of the numerical model indented at different locations (as illustrated in Figure 6.11) around the interface between (a) two orthogonal fibres, and (b) mature and immature bone nodules.....	211
Figure A.1 Schematic of a fibre/matrix cube, with an 8mm diameter through-hole in the centre.	220
Figure A.2 Microscope image for the conical tip, which has the tip radius of 43 μm	221
Figure A.3 Fit the experiment results with (a) Equation 3.16 and (b) Equation 3.20.	222
Figure A.4 Overview of the finite element mesh for the inclusion/matrix composite, and the enlarged details of elements underneath the tip.....	224
Figure A.5 Fit the FEM results with (a) Equation 3.16 and (b) Equation 3.20.	225
Figure B.1 Finite element meshes for the porous model. The diameter of the hole was set as 3.78 μm , symmetric boundary conditions were applied to the sides to simulate a periodically porous structure, and the distance between the centre of the hole and indented surface varied between 4 μm and 6 μm	228
Figure B.2 The elastic modulus of the porous model with hole arranged to a lower, middle or upper position.....	228

List of Tables

Table 2.1 Parameters for various types of indenters (Oliver and Pharr, 1992; Oliver and Pharr, 2004; Fischer-Cripps, 2011c).	36
Table 3.1 Geometries of the indenters used in the FE model.	59
Table 3.2 Fitting parameters for the Clifford model.	77
Table 3.3 Comparison of fitting parameter b for various equations.....	79
Table 3.4 Fitting parameters for Equation 3.16.	92
Table 3.5 Fitting parameters for Equation 3.20.	93
Table 4.1 Summary of geometries and dimensions of the particles.	99
Table 4.2 Input parameters for materials properties in the FE model.	103
Table 4.3 Best fitting parameters of Clifford model (Equation 4.1 and Equation 4.3) for semi-spherical particle model ($r=0.5 \mu\text{m}$ with volume of $0.131 \mu\text{m}^3$) in this study.....	124
Table 4.4 Best fitting parameters of Clifford model (Equation 4.1 and Equation 4.3) for cylindrical particle model ($r=t=0.437 \mu\text{m}$ with volume of $0.131 \mu\text{m}^3$) in this study.....	124
Table 4.5 Best fitting parameters of Clifford model (Equation 4.1 and Equation 4.3) for cylindrical particle model ($r=t=0.5 \mu\text{m}$ with volume of $0.196 \mu\text{m}^3$) in this study.	125
Table 4.6 Best fitting parameters of modified Clifford model (Equation 4.13 and Equation 4.14) for semi-spherical particle model ($r=0.5 \mu\text{m}$ with volume of $0.131 \mu\text{m}^3$) in this study.	132
Table 4.7 Best fitting parameters of modified Clifford model (Equation 4.13 and Equation 4.14) for cylindrical particle model ($r=t=0.437 \mu\text{m}$ with volume of $0.131 \mu\text{m}^3$) in this study.	132

Table 4.8 Best fitting parameters of modified Clifford model (Equation 4.13 and Equation 4.14) for cylindrical particle model ($r=t=0.5 \mu\text{m}$ with volume of $0.196 \mu\text{m}^3$) in this study.....	133
Table 5.1 Fitting parameters of the linear equation (Equation 5.5) for the vertical fibre model.....	154
Table 5.2 Fitting parameters of the polynomial equation (Equation 5.6) for the vertical fibre model	154
Table 5.3 Fitting parameters of the linear equation (Equation 5.5) for the horizontal fibre model	155
Table 5.4 Fitting parameters of the polynomial equation (Equation 5.6) for the horizontal fibre model.....	155
Table 6.1 Surface roughness of the samples for different culture periods in BM and OM.....	183
Table 6.2 Elastic modulus, hardness and contact depth of samples cultured in BM detected by multi-cycling tests with different maximum force in each cycle.	192
Table 6.3 Elastic modulus, hardness and contact depth of samples cultured in OM detected by multi-cycling tests with different maximum force in each cycle.	193
Table A.1 Elastic modulus and Poisson's ratio of acrylic and stainless steel indenters.....	220
Table A.2 Elastic modulus of the tested materials extracted by the stainless steel spherical indenter.	223
Table A.3 Fitting parameters for Equation 3.16 and Equation 3.20 when fitted with the experiment results.	223
Table A.4 Fitting parameters for Equation 3.16 and Equation 3.20 when fitted with the FEM results.	226

Nomenclature

Latin Symbols

A	Area, fitting parameter for analytical model
a	Contact radius
A_c	Projected contact area
B_i	Fitting parameter for the analytical model
b	Fitting parameter for the analytical model
C	Coefficient for normalized relaxation modulus expression, total compliance, fitting parameter for the analytical model
C_i	Coefficient for area function expression
c	Crack length
C_f	Load frame compliance
C_s	Compliance of the indented material
D	Diameter of outer circle
d	Distance between the inclusion and the indenter, diameter of inner circle
E	Young's modulus
E^*	Combined or reduced elastic modulus, complex modulus
E'	Storage modulus
E''	Loss modulus
E_0	Instantaneous modulus
E_1	Elastic modulus of spring 1
E_2	Elastic modulus of spring 2
E_∞	Equilibrium modulus
$E_{t=0}$	Instantaneous modulus
E_r	Reduced elastic modulus
$E(t)$	Relaxation modulus
$\bar{E}(t)$	Normalized relaxation modulus
$F(x)$	Predicted data from fitting equation

$f(x)$	Probability distribution function
g_i	Material related constant
g_∞	Normalized equilibrium modulus
H	Hardness
\dot{h}_h	Creep rate at the end of holding period
H_0	Bulk hardness
H_m	Measured indentation hardness
H_v	Vickers hardness
K	Coefficient for stress-strain response in uniaxial plastic regime, constant for determining initial penetration depth
k	Geometric constant
K_{ep}	Loading curve fitting parameter for elastic-plastic behaviour
K_e	Loading curve fitting parameter for elastic behaviour
K_p	Loading curve fitting parameter for plastic behaviour
k_s	Stiffness of the mounting spring
l	Crack length
m	Power law exponent, mass of indenter and shaft, number of terms in Prony series, number of the components in the probability distribution function
n	Geometric constant, power law exponent, fitting parameter for the Clifford model
P	Load, fitting parameter for the Clifford model
\dot{P}	Initial unloading rate
P_0	Amplitude of dynamic load
P_{max}	Maximum load
Q	Fitting parameter for the Clifford model
R	Radius of indenter, radius of sphere
R^2	Minimum coefficient of determination
$\%R$	Percentage of elastic recovery
r	Tip radius, radius of particle, radius of inclusion
RCF	Ramp correction factor

<i>resnorm</i>	Fitting parameter that represents the goodness of the fitting
<i>S</i>	Contact stiffness
<i>t</i>	Time, coating thickness, thickness of particle
<i>t_R</i>	Rise time of loading period
<i>V_p</i>	Volume of the residual impression
<i>w</i>	Radius of inclusion, volume fraction in probability distribution function
<i>W_e</i>	Elastic work of indentation
<i>W_p</i>	Plastic work of indentation
<i>W_t</i>	Total work of indentation
<i>x</i>	Work hardening exponent
<i>Y</i>	Yield stress
<i>y</i>	Observed data from simulation
<i>ȳ</i>	Mean of the observed data
<i>z</i>	Relative contact radius

Greek Symbols

α	Effective cone angle, roughness parameter
β	Geometry correction factor
γ	Geometry correction factor, strain
δ	Displacement, phase difference
δ_c	Contact depth
δ_{max}	Maximum depth
δ_{res}	Residual depth
δ_s	Elastic depth
ε	Tip-dependent intercept factor, strain
$\dot{\varepsilon}$	Strain increment
η	Viscosity coefficient
θ	Half included indenter angle
κ	Tip-dependent constant
λ	Damping coefficient related to the instrument

λ_s	Damping coefficient of the contact
ν	Poisson's ratio
ξ	Correction factor
σ	Stress
σ_s	Material constant related to surface roughness
σ_Y	Yield stress
τ	Material time constant
ψ	Empirical constant
ω	Frequency of dynamic load
ϕ	Empirical constant, phase difference

Acronyms

AFM	Atomic force microscope
BM	Basal medium
BSE	Back-scattered electrons
CSM	Continuous stiffness method
EDS	Energy-dispersive X-ray spectroscopy
EDTA	Ethylenediaminetetraacetic acid
FEA	Finite element analysis
FEM	Finite element modelling
HA	Hydroxyapatite
hMSCs	Human mesenchymal stem cells
hTERT	Human telomerase reverse transcriptase
ISE	Indentation size effect
Nylon 6	Polyamide 6
OM	Osteogenic medium
PDLLA	Poly-DL-lactic acid
PDMS	Polydimethylsiloxane
PE	Polyethylene
PGA	Polyglycolic acid
PLA	Polylactic acid
PLLA	Poly-L-lactic acid

PP	Polypropylene
RID	Relative indentation depth
RVE	Representative volume element
SD	Standard deviation
SE	Secondary electrons
SEM	Scanning electron microscope

Chapter 1

Introduction

Chapter 1. Introduction

1.1 Introduction

Composite materials are multiphase materials made from two or more components. After combining individual components together, the system performance of composite materials has been reported to be significantly better than that of the original materials (Hull and Clyne, 1996; Matthews and Rawlings, 1999; Barbero, 2010). In our daily life, composite materials are practical and can be widely implemented in various fields, such as space craft, aircraft, marine, automobile, construction, electrical, medicine and sports, due to their highly advanced properties compared to conventional bulk materials (Lou and Schapery, 1971; Bakis *et al.*, 2002; Kalia *et al.*, 2009; Akil *et al.*, 2011; Ozbakkaloglu *et al.*, 2016). In the past decades, due to the bioactivity, biodegradability and biocompatibility of some nanocomposites, the application of composite materials has been extended to tissue engineering as well (Yang *et al.*, 2011; Hasan *et al.*, 2013; Dadbin and Naimian, 2014; Jiang *et al.*, 2014; Kubozono *et al.*, 2014; Pradid *et al.*, 2014; Tayton *et al.*, 2014; Zong *et al.*, 2014).

Tissue engineering is a method of using a combination of cells, biomaterials and suitable biochemical and physicochemical factors to improve or replace biological tissues, which involves the application of a scaffold for the formation of new viable tissue for a medical purpose (Venugopal and Ramakrishna, 2005; Rezwan *et al.*, 2006). From the mechanical point of view, implanted scaffolds must be strong enough to avoid fracture and the new tissue should show similar mechanical properties to the surrounding biological tissues (Hutmacher, 2000). Thus, the mechanical characterization of both the scaffold and newly formed tissue is crucial, not only for their practical use, but also for understanding the cell-material interactions, and further optimizing the design of scaffold materials (Cao and Chen, 2012; Chen, 2014).

As the main method in this thesis, nanoindentation has been proven to be completely able to assess the nanomechanical properties of thin coatings (Li and Bhushan, 1998; Lim *et al.*, 1999; Chen and Bull, 2008; Chen *et al.*, 2009), synthetic (Chakraborty and Bhowmik, 2014; Eggedi *et al.*, 2014; Luo *et al.*, 2014)

and natural tissues (Chen *et al.*, 2010a; Oyen, 2013; Chen *et al.*, 2014; Cyganik *et al.*, 2014; De Silva *et al.*, 2014; Jaramillo-Isaza *et al.*, 2014; Sun *et al.*, 2014), which are also composite materials in nature. Thus, the motivation of this thesis is that by using nanoindentation techniques the spatial-dependent mechanical properties of synthesized composite materials and newly formed tissues can be understood, so that how mechanical response will be affected by various practical indentation protocols, indenter geometry, chemical composition of each constituent, and microstructure must also be understood.

1.2 Aim and objectives

This study aims to employ a nanomechanical approach to understand the mechanical response of typical biocomposites (fibre-reinforced composites, particle-reinforced composites and complex mineralized matrix). The specific objectives that this thesis intends to address are as follows:

- To understand the spatial-dependent mechanical properties of fibre-reinforced composite materials by empirical analytical models, and propose novel analytical models if necessary.
- To analyse the effects of particle size and shape on the nanomechanical response of particle-reinforced composite materials.
- To investigate the effects of fibre orientation and indentation location on the nanomechanical response of fibre-reinforced composite materials.
- To study the nanomechanics, microstructure and chemical composition of complex mineralized matrix (newly formed tissues synthesized by immortalized cell line Y201), and then further establish the correlations between them.

1.3 Thesis outline

This thesis contains seven chapters (as illustrated in Figure 1.1), which are organised as follows:

- Chapter 2 will introduce what are nanoindentation techniques, why nanoindentation techniques are powerful tools, how to obtain various mechanical properties by nanoindentation techniques, what will affect the nanoindentation results and their application in biomaterials. Then, depending on the complexity of the specimens, all the studies of biocomposite materials will be presented from Chapter 3 to Chapter 6.
- In Chapter 3, the viscoelastic response of fibre-reinforced composites during the nanoindentation are investigated by finite element simulations. Various empirical equations are compared and new models are proposed to describe the viscoelastic behaviour of fibre/matrix composites.
- In Chapter 4, the elastic-plastic response of particle embedded composites during nanoindentation are studied by finite element simulations. Particles with various sizes and shapes are examined to evaluate the effects of particle geometry. New analytical models are introduced to describe the elastic-plastic behaviour of these particle/matrix systems.
- In Chapter 5, the effects of fibre orientation and indentation location on the elastic response of fibre-reinforced composites during nanoindentation are presented.
- In Chapter 6, a nanomechanical case study on extracellular matrix composites synthesized by immortalized cell line Y201 is presented. Besides, the study of topography and chemical characterization of these samples are also included.
- In Chapter 7, the results for various inclusion/matrix composite materials are discussed and summarized, and the further work which will follow this thesis is identified.

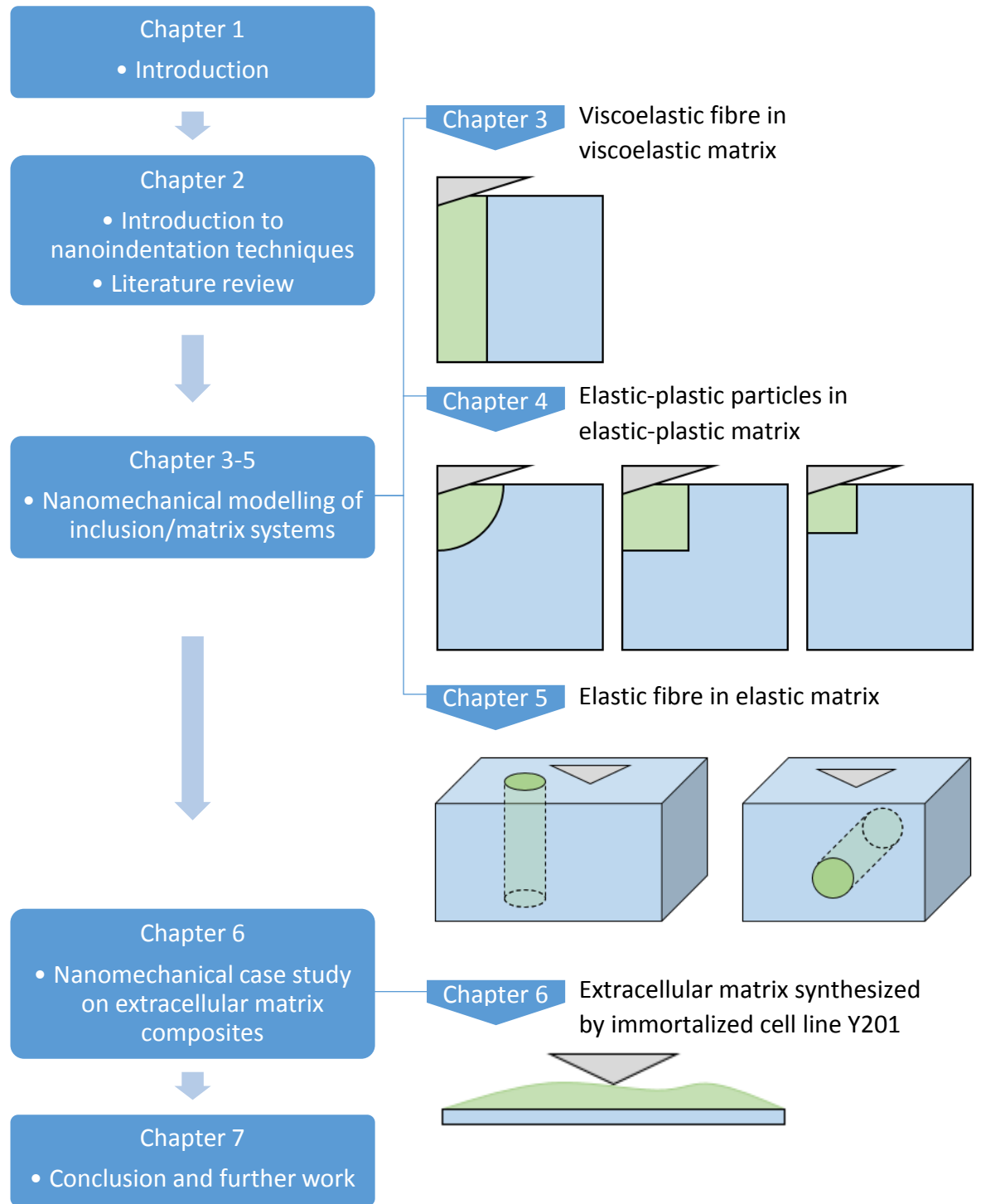


Figure 1.1 A flow chart of the structure of this thesis.

Chapter 2

Nanoindentation Techniques

Chapter 2. Nanoindentation Techniques

2.1 Introduction to nanoindentation

The origins of the indentation technique can be traced back to the Mohs hardness in 1824 (Tabor, 1954), in which a qualitative hardness scale of various minerals was given by the ability of harder mineral to leave a scratch in a softer one. Thereafter, various quantitative hardness tests were established by indenting a material whose mechanical properties were unknown with another material whose geometry and mechanical properties were known. Among which, nanoindentation techniques were developed in the early seventies of last century (Bulychev *et al.*, 1975; Newey *et al.*, 1982; Pethica *et al.*, 1983; Georges and Meille, 1984; Wierenga and Franken, 1984; Doerner and Nix, 1986), to meet the growing requirements of knowing the mechanical properties of thin films, coatings and samples with small volumes.

Nanoindentation is a technique with the same principle as macroindentation and microindentation (*i.e.* conventional indentation tests), while measuring the properties of materials at the length scale of nanometres. This difference also gives the nanoindentation tests a distinctive feature, that is, an indirect measurement of contact area between the sample and the indenter. In conventional indentation tests, the projected area of residual impression left on the sample surface after indenter removal is usually measured by light microscopy. The hardness is then determined by the peak load divided by the projection of the residual area (or surface area in the case of Vickers hardness). Whereas in nanoindentation tests, the size of residual impression can be less than 1 micrometre which is difficult to be accurately measured by the conventional optical methods (Doerner and Nix, 1986). For this reason, an alternative method is to analyse the continuously recorded force-displacement curve and correlate it to the hardness and elastic modulus for a given indenter geometry. The contact area can then be indirectly determined from the contact depth with the known geometry of the indenter (Doerner and Nix, 1986; Oliver and Pharr, 1992; Hainsworth and Page, 1994; Oliver and Pharr, 2004). In other words, this leads to different definitions between the hardness measured from conventional indentation tests and the hardness measured from nanoindentation tests. In the

former case, hardness is defined as the ratio of maximum force over the residual area, in which case the elastic recovery of the contact area will not be considered. While in the latter case, hardness is determined by maximum force over contact area under load, having corrected for the elastic deflection of the sample surface.

It is not only the hardness (H) that nanoindentation can provide. By carefully selecting the indenter, designing the loading protocol and choosing the appropriate analysis model, various properties can be extracted from the recorded force-displacement curves, such as elastic modulus (E), fracture toughness, viscoelastic properties, film adhesion and strain-hardening exponent (Ebenstein and Pruitt, 2006; Yang *et al.*, 2006; Chen and Bull, 2010). Nowadays, nanoindentation techniques have not only been widely used for the study of coatings (Oliver and Pharr, 1992; Bull, 2001; Berasategui and Page, 2003; G-Berasategui *et al.*, 2004), but also gained the popularity in the study of biomaterials (Hasler *et al.*, 1998; Haque, 2003; Kinney *et al.*, 2003; Aryaei and Jayasuriya, 2013; Chen, 2014), nanocomposites (Gao and Mäder, 2002; Lee *et al.*, 2007) and specimens in high temperature environments (Beake and Smith, 2002; Schuh *et al.*, 2005).

2.2 Force-displacement curves

2.2.1 General parameters in a P - δ curve

During the nanoindentation test, the applied force (P) and displacement (δ) of the indenter are continuously recorded as force-displacement curves. This force-displacement curve has been considered as the mechanical “fingerprint” of a material (Page and Hainsworth, 1993), in which a number of basic parameters can be quantified and used to assess the mechanical properties of the specimen. Figure 2.1 shows a typical P - δ curve from the nanoindentation test. According to Page and Hainsworth, the basic parameters that can be quantified are listed below (Page and Hainsworth, 1993):

- P_{max} , the maximum applied load.

- S , the contact stiffness. This quantity, sometimes referred to as the dP/dh , is evaluated from the slope of the upper part of the unloading curve (Doerner and Nix, 1986; Oliver and Pharr, 1992).
- δ_{max} , the maximum displacement of the indenter beneath the sample free surface at the maximum load.
- δ_c , the contact depth, which is the depth between the contact circle and the apex of the indenter. The mathematical expression of this parameter will be described in Section 2.2.2.1. The radius of the contact circle is defined as the contact radius, a_c . The area of the contact circle is defined as the contact area, A_c , which is also the projected area of the indenter at depth δ_c .
- δ_{res} , the depth of residual impression after removal of the indenter.
- W_p , the plastic work of indentation. It indicates the energy loss (e.g. as heat) due to plastic deformation, and equals the area enclosed by the P - δ curve.
- W_e , the elastic work of indentation. It is the energy recovered elastically during the unloading, and it equals the area underneath the unloading curve.
- W_t , the total work done during the indentation. It equals the sum of W_p and W_e , and is given by the area underneath the loading curve.
- $\%R$, the percentage of displacement recovered during the unloading to the maximum displacement, i.e. $\%R = \frac{\delta_{max} - \delta_{res}}{\delta_{max}}$. It characterizes the elastic portion of the maximum displacement.

The P - δ curves can be generally divided into several regions depending on the behaviour of the test material with respect to the displacement (or applied load):

- **Segment AB**, this is the full elastic region that no residual impression left in the surface after removal of load. For a sharp indenter, the occurrence

of this elastic region results from the tip blunting, which will be described in Section 2.4.2.

- **Segment BC**, this is the region that behaviour transits from elastic behaviour to elastic-plastic behaviour.
- **Segment CD**, this is a plastic-dominated region where a fully developed plastic zone obtained.
- **Segment DE**, this is the initial part of the unloading curve. It is assumed that, within this region, the contact area keeps constant with the decreasing displacement.
- **Segment EF**, this is the region in which elastic recovery occurs and the shape of impression changes with the decreasing displacement.

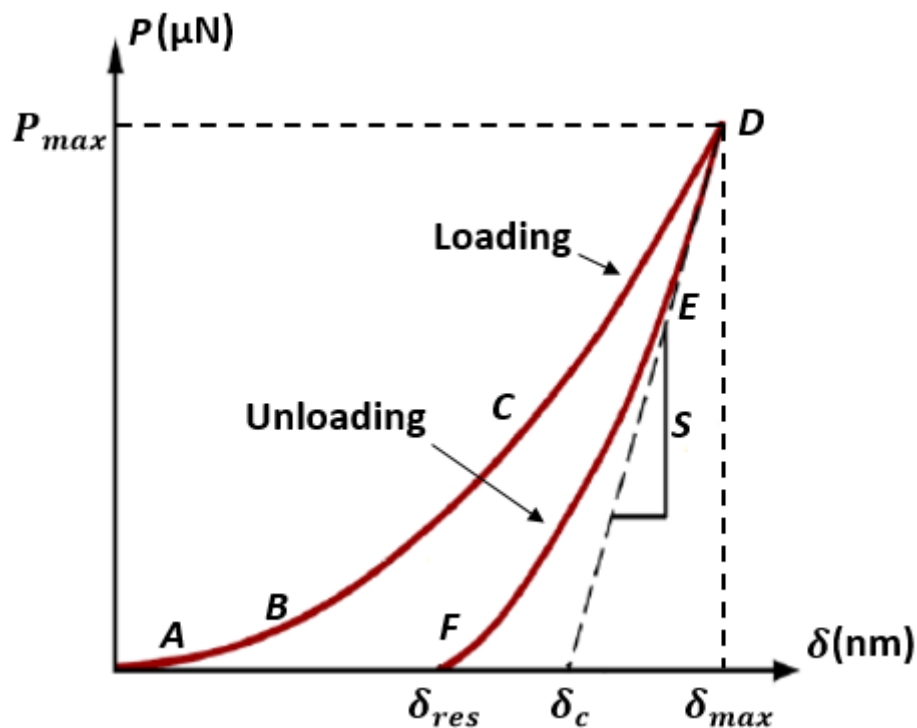


Figure 2.1 Schematic of a typical force and displacement curve of an elastic-plastic material indented by a pyramidal indenter.

Based on the information shown in Figure 2.1, various analytical methods have been developed to obtain the basic mechanical properties such as the hardness and elastic modulus, which will be described in Section 2.2.2. In practice, several other features may occur in the P - δ curves depending on the

nature of the material or the structure of the material. Features such as creep, cracks, adhesion, piling-up and sinking-in will also be discussed in the following section.

2.2.2 Extraction of elastic modulus and hardness from the $P\text{-}\delta$ curves

Various methods have been developed to extract E and H from the $P\text{-}\delta$ curves. These methods include but are not limited to: unloading curve method, loading curve method, energy-based method, slope-based method, and dynamic method. Among them, Oliver and Pharr method (Oliver and Pharr, 1992) is the most popular one, and it has been used to investigate the materials with a wide range of elastic modulus and hardness.

2.2.2.1 Unloading curve method

Modelling the material response of a loading curve is much more complex, as it may consist of both plastic and elastic behaviours. Therefore, the unloading curve is normally used to obtain elastic modulus and hardness by assuming there is only elastic behaviour involved in the unloading. Based on the analysis for the elastic unloading curve with a flat punch indenter (Sneddon, 1965), Doerner and Nix proposed a linear relationship in the first one third of the unloading curve for nanoindentation by a flat punch indenter (Doerner and Nix, 1986). Soon, Oliver and Pharr extended this method to the cases of various indenters by proposing a power law relationship in the initial part of the unloading curve. The validity of Sneddon analysis for various indenters was verified by them as well (Oliver and Pharr, 1992). In the Sneddon analysis, the elastic modulus is given by (Sneddon, 1965),

$$S = \frac{dP}{dh} = \frac{2}{\sqrt{\pi}} E_r \sqrt{A_c} \quad (2.1)$$

where E_r is the reduced modulus that combines the modulus of the indenter and the test specimen, which can be described as,

$$\frac{1}{E_r} = \frac{1 - v_s^2}{E_s} + \frac{1 - v_i^2}{E_i} \quad (2.2)$$

where E_s and ν_s are the Young's modulus and the Poisson's ratio for the specimen, respectively. E_i and ν_i are the Young's modulus and the Poisson's ratio for the indenter, respectively. For a commercially used diamond tip, the Young's modulus is 1141 GPa and the Poisson's ratio is 0.07.

In order to obtain the contact stiffness from the P - δ curve, Oliver and Pharr proposed a power law relationship for the initial part of the unloading curve, which is expressed as,

$$P = B(\delta - \delta_{res})^m \quad (2.3)$$

where B , m and δ_{res} are the fitting constants determined by the least squares fitting procedure. By differentiating Equation 2.3 with respect to the depth, the unloading slope at the peak depth can be mathematically expressed as,

$$S = \frac{dP}{d\delta} \Big|_{\delta=\delta_{max}} = mB(\delta_{max} - \delta_{res})^{m-1} \quad (2.4)$$

According to the Oliver and Pharr method, the contact area is calculated from the contact depth rather than the optical measurement. In order to unveil the relationship between different dimensions, a cross section through an indentation was provided by Oliver and Pharr, as shown in Figure 2.2.

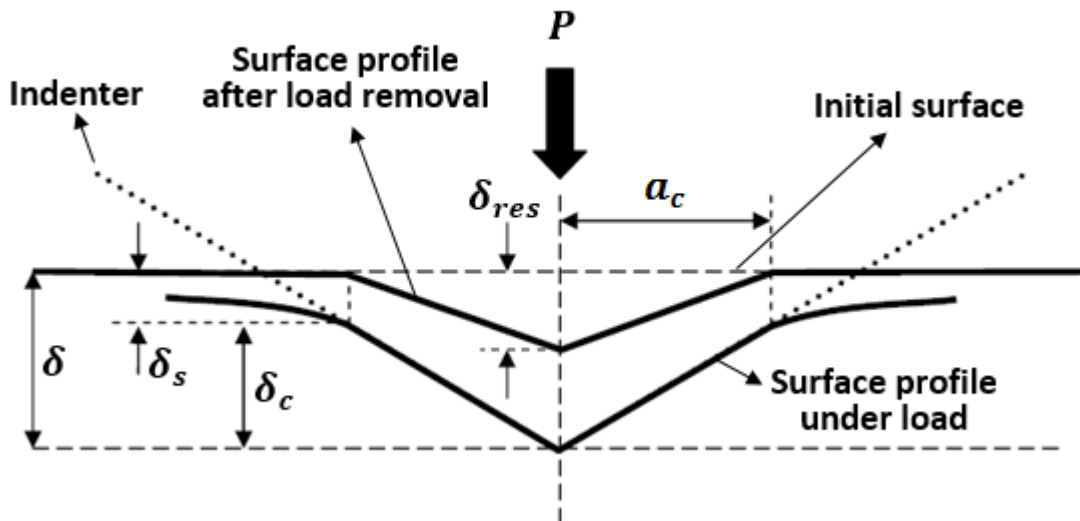


Figure 2.2 Schematic of a cross section of an indentation with the assumption that piling-up and sinking-in are negligible. Various dimensions that used in the analysis are indicated (Oliver and Pharr, 1992).

At any time during the loading, total depth, δ , can be written as,

$$\delta = \delta_c + \delta_s \quad (2.5)$$

where δ_c is the contact depth between the contact circle and the apex of the indenter. δ_s is the elastic deflection of the surface which equals the depth between the contact circle and the sample free surface. In the Sneddon analysis, it is given by,

$$\delta_s = \varepsilon \frac{P_{max}}{S} \quad (2.6)$$

where ε is a geometric constant. For a flat punch indenter, $\varepsilon = 1$. For a spherical (paraboloid of revolution) indenter, $\varepsilon = 0.75$. For a Berkovich (pyramidal) indenter and conical indenter, ε should be theoretically equal to $\frac{2}{\pi}(\pi - 2)$, but Oliver and Pharr have indicated that $\varepsilon = 0.75$ will better represent experimental results (Oliver and Pharr, 1992).

Whereupon, by substituting Equation 2.6 into Equation 2.5, the contact depth can be expressed as,

$$\delta_c = \delta_{max} - \varepsilon \frac{P_{max}}{S} \quad (2.7)$$

Once contact depth is calculated, the contact area can be presented as a function of contact depth with the known geometry of the indenter (Pethica *et al.*, 1983). For a perfect Berkovich indenter,

$$A(\delta_c) = C_0 \delta_c^2 = 24.5 \delta_c^2 \quad (2.8)$$

In practice, more terms are added to Equation 2.8 to account for the inaccuracies of the area brought by a non-perfect indenter,

$$A(\delta_c) = C_0 \delta_c^2 + C_1 \delta_c + C_2 \delta_c^{1/2} + C_3 \delta_c^{1/4} + \dots + C_8 \delta_c^{1/128} \quad (2.9)$$

where C_0 is the geometric constant which represents the projected area to depth ratio of an ideal indenter, and $C_0 = 24.5$ for a Berkovich indenter. C_1 to C_8 are the fitting parameters obtained by calibration tests on a reference material with known

mechanical properties. Actually, elastically isotropic materials, such as fused quartz and aluminium, are widely used as the reference materials due to their elastic moduli are independent of displacement (Oliver and Pharr, 1992). Besides, the surface quality of the reference material should be carefully controlled, as this may affect the independency of its elastic modulus (Zheng *et al.*, 2007).

The hardness of test sample is given by,

$$H = \frac{P}{A(\delta_c)} \quad (2.10)$$

It is very important to note that one of the simplified assumptions for the Sneddon equation (in the case of a flat punch indenter) is that the sides of the shape after fully unloaded are straight. Since most commercial indenters are not flat-ended punches, a correction for the contact stiffness in the Sneddon equation is required to account for the corresponding inward deformation of the surface (as shown in Figure 2.3) after removal of the indenter. With the extensive use of the finite element modelling (FEM) method, Hay *et al.* indicated the discrepancy relates to both the geometry of the indenter and the test sample, and introduced a correction factor γ . For a pyramidal or conical indenter with $\theta > 60^\circ$, γ is given by (Hay *et al.*, 1999; Hay and Wolff, 2001; Malzbender, 2002),

$$\gamma = \pi \frac{\frac{\pi}{4} + 0.1548 \cot \theta \frac{1 - 2\nu}{4(1 - \nu)}}{\left[\frac{\pi}{2} - 0.8312 \cot \theta \frac{1 - 2\nu}{4(1 - \nu)} \right]^2} \quad (2.11)$$

For a pyramidal or conical indenter with $\theta \leq 60^\circ$, this factor is described as,

$$\gamma = 1 + \frac{2(1 - 2\nu)}{4(1 - \nu) \tan \theta} \quad (2.12)$$

For a spherical indenter this factor is given by,

$$\gamma = 1 + \frac{2(1 - 2\nu)a_c}{3\pi(1 - \nu)R} \quad (2.13)$$

where θ is the half included angle of the indenter, ν is the Poisson's ratio of the test material, a_c is the contact radius and R is the radius of the spherical indenter.

For a pyramidal indenter, θ should be its effective cone angle, namely, $\theta=70.3^\circ$ for a Berkovich indenter.

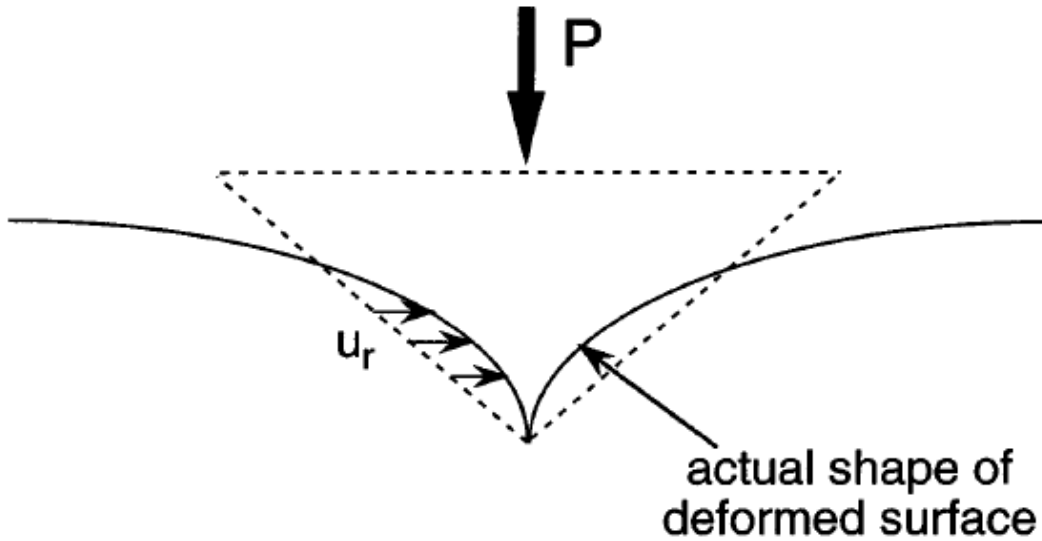


Figure 2.3 Schematic of the radial displacement of the deformed surface after load removal (Hay *et al.*, 1999).

For the symmetry of the indenter, King introduced an extra correction factor β to account for the deviation of data from the non-axially symmetric indenter (King, 1987). Though many researchers reported different values of β , a value of 1.034 has actually been widely adopted. Taking these corrections into consideration, the reduced modulus of specimen can be obtained by rewriting Equation 2.1,

$$E_r = \frac{1}{\beta\gamma} \frac{\sqrt{\pi}}{2} \frac{S}{\sqrt{A_c}} \quad (2.14)$$

In this section, the situations of creep, sinking-in and pulling-up are not considered. Actually, they will influence the extraction of elastic modulus and hardness from the $P-\delta$ curve, and will be discussed in Section 2.4.

2.2.2.2 Loading curve method

As an alternative method, the loading curve method does not require contact area to be determined, which is an advantage over other methods. The method is based on the loading curve analysis for a Vickers indenter by Loubet *et al.*

(Loubet *et al.*, 1986), starting from the P - δ relationship previously developed by Sneddon (Sneddon, 1965). During loading, for the case of a non-adhesive conical indenter with half included angle of θ in contact with the surface of a smooth elastic body, the P - δ relationship can be expressed as (Sneddon, 1965),

$$P = \frac{2E \tan \theta}{(1 - \nu^2)\pi} \delta^2 \quad (2.15)$$

Based on the analysis of experimental loading curves, a general relation between force and displacement for an elastic-plastic loading is found and given by (Loubet *et al.*, 1986),

$$P = K_{ep} \delta^n \quad (2.16)$$

where K_{ep} is a constant depending on the nature of contact, namely: elastic, elastic-plastic, or purely plastic. n is a geometric constant depending on the geometric of the indenter. For Berkovich (pyramidal) and conical indenters, $n=2$. By assuming the total displacement can be disassociated into a plastic part and an elastic part, Equation 2.16 can be rewritten as,

$$P_p = K_p \delta_p^2 \quad (2.17)$$

$$P_e = K_e \delta_e^2 \quad (2.18)$$

where K_p and K_e are the proportionality factors of plastic behaviour and elastic behaviour, respectively. δ_p and δ_e are the plastic contributed displacement and the elastic contributed displacement, respectively. Finally, by assuming that Equation 2.17 and Equation 2.18 are used for two springs in series and $\delta = \delta_p + \delta_e$, therefore,

$$(K_{ep})^{-\frac{1}{2}} = (K_p)^{-\frac{1}{2}} + (K_e)^{-\frac{1}{2}} \quad (2.19)$$

By carefully selecting the plastic and elastic proportionality factors, Loubet *et al.* expressed Equation 2.16 in terms of the Vickers hardness (H_v) as (Loubet *et al.*, 1986),

$$K_{ep} = \left[0.92 \left(\frac{1 - \nu^2}{E} \right) \sqrt{H_v} + \frac{0.194}{\sqrt{H_v}} \right]^{-2} \quad (2.20)$$

In 1996, a further development on loading curve analysis was given by Hainsworth *et al.* (Hainsworth *et al.*, 1996). In their method, δ_p and δ_e were related to δ_c and δ_s in Equation 2.5, respectively. For Berkovich (pyramidal) and conical indenters, by rearranging Equation 2.8 and Equation 2.10, the plastic depth is given by,

$$\delta_p = \frac{1}{\sqrt{C_0}} \sqrt{\frac{P}{H}} = \phi \sqrt{\frac{P}{H}} \quad (2.21)$$

where C_0 is the geometric constant shown in Equation 2.8. ϕ is an empirical constant proposed by Hainsworth *et al.*, which is mathematically equal to $1/\sqrt{C_0}$. Substituting Equation 2.1 into Equation 2.6, and assuming that the indenter is much stiffer than the specimen, the elastic depth is given by,

$$\delta_e = \frac{\varepsilon \sqrt{\pi} (1 - \nu^2)}{2} \frac{P}{E} \sqrt{\frac{H}{P}} = \psi \frac{P}{E} \sqrt{\frac{H}{P}} \quad (2.22)$$

where ν is the Poisson's ratio of test specimen and ε is the geometric constant shown in Equation 2.6. ψ is another empirical constant proposed by Hainsworth *et al.*, which is mathematically equal to $\varepsilon \sqrt{\pi} (1 - \nu^2)/2$. Therefore, the total depth can be expressed as,

$$\delta = \delta_p + \delta_e = \phi \sqrt{\frac{P}{H}} + \psi \frac{P}{E} \sqrt{\frac{H}{P}} \quad (2.23)$$

Substituting Equation 2.23 into Equation 2.16 (in the case of $n=2$) gives,

$$K_{ep} = \left(\phi \frac{1}{\sqrt{H}} + \psi \frac{\sqrt{H}}{E} \right)^{-2} \quad (2.24)$$

$$P = \left(\phi \frac{1}{\sqrt{H}} + \psi \frac{\sqrt{H}}{E} \right)^{-2} \delta^2 \quad (2.25)$$

By best-fitting the experimental data, Hainsworth *et al.* expressed Equation 2.25 in terms of a used Berkovich indenter as,

$$P = \left(\frac{0.194}{\sqrt{H}} + 0.930 \frac{\sqrt{H}}{E} \right)^{-2} \delta^2 \quad (2.26)$$

which is identical to the expression of a Vickers indenter (Equation 2.20). This is not surprising due to the fact that Berkovich indenter has the same projected area to depth ratio as a Vickers indenter, which theoretically makes these two indenters have the same values of ϕ and ψ .

Based on Equation 2.25, Malzbender *et al.* took the indenter deformation into consideration and rewrote the equation with the reduced modulus instead of the Young's modulus. In the case of a perfect Berkovich (pyramidal) or conical indenter, the P - δ relationship is then given by (Malzbender and den Toonder, 2000),

$$P = \left(\frac{1}{\sqrt{C_0} \sqrt{H}} + \varepsilon \frac{\sqrt{\pi H}}{2E_r} \right)^{-2} \delta^2 \quad (2.27)$$

For a non-perfect indenter, an alternative relationship is given by,

$$P = \left(\frac{1}{\sqrt{C_0} \sqrt{H}} + \varepsilon \frac{\sqrt{\pi H}}{2E_r} \right)^{-2} (\delta + \xi)^2 \quad (2.28)$$

where ξ accounts for the tip rounding for a non-perfect indenter, as shown in Figure 2.4.

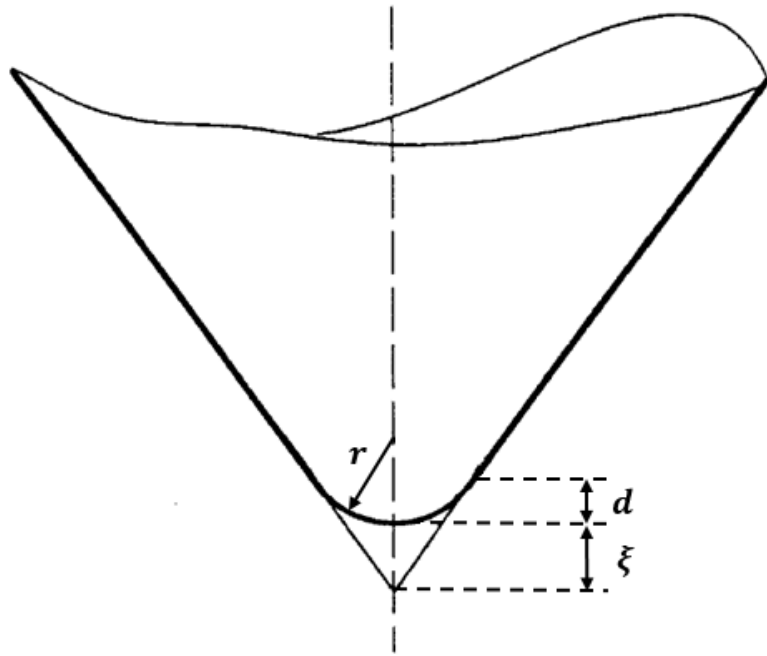


Figure 2.4 Schematic of a non-perfect indenter with a rounded tip (Sun *et al.*, 1999).

In general, this loading curve analysis provides a useful method to determine hardness or elastic modulus if one of them is already known without precise contact area to be determined. The disadvantage of this method is that a fully plastic response should be obtained, otherwise the load is not proportional to the square of the displacement. Also, any discontinuities (such as pop-ins) of the loading curve may also introduce the deviation to the results.

2.2.2.3 Energy-based method

The hardness of a material can also be related to the energy involved during indentation, and is expressed as the work required to produce a unit volume of indentation,

$$H = \frac{W_p}{V_p} = \frac{W_t - W_e}{V_p} \quad (2.29)$$

where W_t and W_e are the total work and elastic work during the indentation, respectively. V_p is the volume of the indentation, which is equal to the volume of the residual impression. In order to calculate the involved work of indentation, in

the case of a Berkovich indenter, Equation 2.16 is rewritten as (Fischer-Cripps, 2011a),

$$P_{loading} = K_{ep}\delta^2 \quad (2.30)$$

$$P_{unloading} = K_e(\delta - \delta_{res})^m \quad (2.31)$$

At the maximum load, the boundary condition is given by,

$$P = K_{ep}\delta_{max}^2 = K_e(\delta_{max} - \delta_{res})^m \quad (2.32)$$

where K_{ep} and K_e are the constants depending on the nature of contact, namely: elastic, elastic-plastic, or purely plastic. m is the power law index proposed in Equation 2.3, and m should be smaller than two due to the fact that the sides of the residual impression are curved during the unloading. In practice, these parameters can be extracted by a least squares fitting procedure. Then, the involved work of the indentation is calculated by integrating the force with respect to the displacement,

$$W_t = \int_0^{\delta_{max}} K_{ep}\delta^2 = \frac{K_{ep}\delta_{max}^3}{3} \quad (2.33)$$

$$W_e = \int_0^{\delta_{max}} K_e\delta^m = \frac{K_e(\delta_{max} - \delta_{res})^{m+1}}{m + 1} \quad (2.34)$$

By dividing Equation 2.34 by Equation 2.33 and expressing the ratio K_e/K_{ep} in terms of Equation 2.32, a linear relationship between the ratio of elastic work to the total work and the ratio of residual depth to maximum can be obtained,

$$\frac{W_e}{W_t} = \frac{3}{m + 1} \left(1 - \frac{\delta_{res}}{\delta_{max}}\right) \quad (2.35)$$

By assuming the radius of the contact circle is the same at maximum load and full unload, the volume of the indentation is given by,

$$V_p = \frac{\pi}{3}a_c^2\delta_{res} \quad (2.36)$$

In this mathematical method, the evaluation of contact area (or contact radius) is required, which will be influenced by the unnoticed sinking-in or piling-up. Alternatively, Tuck *et al.* proposed a method without calculation of the contact area (Tuck *et al.*, 2001). By rewriting Equation 2.10 and Equation 2.16 at the maximum load, a linear relationship between the contact depth and the maximum depth can be obtained,

$$P_{max} = HC_0 \delta_c^2 \quad (2.37)$$

$$P_{max} = K_{ep} \delta_{max}^2 \quad (2.38)$$

where K_{ep} can be extracted by the least squares fitting procedure, and the contact depth is proportional to the maximum depth. Then, Tuck *et al.* proposed that $A_c = k\delta_m^2$, where k is a geometric constant, and the total work of indentation is given by,

$$P_{max} = Hk\delta_{max}^2 \quad (2.39)$$

$$W_t = \int_0^{\delta_{max}} P d\delta = \frac{kH\delta_{max}^3}{3} \quad (2.40)$$

Substituting Equation 2.39 into Equation 2.40, the hardness is given by,

$$H = \frac{3W_t}{k\delta_{max}^3} = \frac{P_{max}^3}{9kW_t^2} \quad (2.41)$$

It can be observed that, in these equations, the calculation of the contact area is not required. Thus, this method avoids the problems associated with the contact area. It was reported that the hardness obtained by this method agrees well with the values obtained by Oliver and Pharr method at big loads (Tuck *et al.*, 2001; Bull, 2002). However, it was also reported that there are big errors for the hardness extraction from highly elastic materials by this method, which can be up to 70% when the H/E ratio is higher than 0.025.

In 2002, based on FEM for a conical indenter, Cheng *et al.* observed the linear relationship described in Equation 2.35 and then proposed a linear relationship between the ratio of elastic work to the total work and the ratio of

hardness to reduced modulus for pyramidal indenters with $60^\circ < \theta < 80^\circ$ (Cheng *et al.*, 2002),

$$\frac{W_e}{W_t} = \kappa^{-1} \frac{H}{E_r} \quad (2.42)$$

where κ is a constant depending on the indenter half included angle, and is approximately equal to 5.3 when $\theta=70.3^\circ$. Substituting Equation 2.1 and Equation 2.10 into Equation 2.42, the hardness and the reduced modulus are expressed as,

$$H = \kappa^2 \frac{\pi}{4} S^2 \left(\frac{W_e}{W_t} \right)^2 \frac{1}{P_{max}} \quad (2.43)$$

$$E_r = \kappa \frac{\pi}{4} S^2 \frac{W_e}{W_t} \frac{1}{P_{max}} \quad (2.44)$$

For spherical indenters, Ni *et al.* observed similar relation between W_e/W_t and H/E_r , which is expressed as (Ni *et al.*, 2004),

$$\frac{W_e}{W_t} = 1.6869 \left(\frac{R}{\delta_{max}} \right)^{0.62} \frac{H}{E_r} \quad (2.45)$$

Although the linear equations between the ratio of W_e/W_t and H/E_r were commonly accepted, it has been found that non-linear relationship will be more accurate to describe this ratio (Malzbender, 2002; Chen and Bull, 2009c). The expressions are given by,

$$\frac{W_e}{W_t} = \left(\frac{\varepsilon}{2} + \frac{\gamma}{\pi \tan \theta} \frac{E_r}{H} \right)^{-1} \quad (2.46)$$

$$\frac{W_e}{W_t} = \frac{1.5(1.24 + 0.2x)\pi}{(0.24 + 0.2x)\gamma} \frac{H}{E_r} \tan \theta \left(\frac{1}{1 + \frac{\pi\varepsilon}{2\beta} \frac{H}{E_r} \tan \theta} \right) \quad (2.47)$$

where x is the work hardening exponent, which will be further described in Section 2.2.4.

2.2.2.4 Slope-based method

By rearranging Equation 2.10 and Equation 2.14, Joslin and Oliver demonstrated that the parameter given by the load divided by the square of the unloading contact stiffness (S_u) was independent of the displacement or the contact area, which is given by (Joslin and Oliver, 1990),

$$\frac{P}{S_u^2} = \frac{\pi H}{4\beta^2 E_r^2} \quad (2.48)$$

This equation shows the advantage that it is more sensitive to changes in elastic modulus of the specimen than the changes of the hardness, and the contact area is not involved.

Based on the relation between the force and the square of the displacement presented in Equation 2.27, the expression of the loading contact stiffness (S_l) is given by differentiating the equation with respect to the displacement (Malzbender and den Toonder, 2000; Oliver, 2001),

$$S_l = 2 \left(\frac{1}{\sqrt{C_0} \sqrt{H}} + \frac{\varepsilon \sqrt{\pi H}}{\beta} \frac{1}{2E_r} \right)^{-2} \delta \quad (2.49)$$

Then, the ratio between loading slope and unloading slope is given by (Oliver, 2001),

$$\frac{S_u}{S_l} = \frac{E_r}{H \sqrt{\pi C_0}} + \frac{\varepsilon}{2} \quad (2.50)$$

Substituting Equation 2.10 and Equation 2.14 into Equation 2.50, the expressions for the hardness and elastic modulus can be described as,

$$E_r = \sqrt{\frac{\pi}{C_0}} \frac{1}{2P_{max}\beta} \left(\frac{S_u^2 S_l}{2S_u - \varepsilon S_l} \right) \quad (2.51)$$

$$H = \frac{1}{C_0 P_{max}} \left(\frac{2S_u - \varepsilon S_l}{S_u S_l} \right)^{-2} \quad (2.52)$$

As this method is based on the assumption that the load is proportional to the square of the displacement. This method is supposed to show the same limitation as the loading curve method, namely, a fully plastic response should be obtained. Creep would also affect the loading slope and unloading slope. In an extreme case, a negative unloading slope will be obtained.

2.2.3 Extraction of time-dependent properties from the P- δ curves

Solid-like materials store energy when undergoing deformation and quickly return to their original state following removal of stress. Viscous materials dissipate energy when undergoing deformation and present a time-dependent deformed state after the removal of stress. A material that undergoes elastic deformation, but exhibits time-dependent behaviour is called viscoelastic. Nanoindentation also offers the quantitative measurement of such viscoelastic properties. In one way, a small sinusoidal force is integrated to the main load. The resulting oscillatory displacement signal is used to provide the elastic and viscous properties of the specimen in the frequency domain. In the other way, the force or displacement is held at a specified value for a certain period. The resulting creep or relaxation data, associated with an appropriate mechanical model, is used to characterize the elastic and viscous properties of the specimen in the time domain.

2.2.3.1 Dynamic nanoindentation test

In 1988, Pethica and Oliver introduced a continuous stiffness method (CSM), which enables the measurement of the contact stiffness continuously, by superimposing a small sinusoidal oscillatory force to the main load (Pethica and Oliver, 1988). This small alternating current force is modulated with a frequency ω and amplitude P_0 , and is given by (Lucas *et al.*, 1998),

$$P = P_0 e^{i\omega t} \quad (2.53)$$

The resulting oscillatory displacement will have the same oscillatory frequency, but with a phase difference Φ ($0 < \Phi < 90^\circ$),

$$\delta = \delta_0 e^{i(\omega t + \Phi)} \quad (2.54)$$

Therefore, the velocity and acceleration of the mass is given by taking the first and second differentiations with respect to time,

$$\frac{d\delta}{dt} = i\omega\delta \quad (2.55)$$

$$\frac{d^2\delta}{dt^2} = -\omega^2\delta \quad (2.56)$$

Here, for the model shown in Figure 2.5, the force is expressed as,

$$P = \left[\left(\frac{1}{S} + C_f \right)^{-1} + k_s - m\omega^2 + i\omega(\lambda + \lambda_s) \right] \delta \quad (2.57)$$

The magnitude of the stiffness of the contact can be calculated from the amplitude of the displacement to force ratio,

$$\left| \frac{P_0}{\delta_0} \right| = \sqrt{\left[\left(\frac{1}{S} + C_f \right)^{-1} + k_s - m\omega^2 \right]^2 + \omega^2(\lambda + \lambda_s)^2} \quad (2.58)$$

Or from the phase difference Φ between the load and displacement,

$$\tan \Phi = \frac{\omega(\lambda + \lambda_s)}{\left(\frac{1}{S} + C_f \right)^{-1} + k_s - m\omega^2} \quad (2.59)$$

Within these unknown parameters, the calibration of C_f will be discussed in Section 2.4.1. k_s , m and λ can be obtained by oscillating the indenter in air. Therefore, the storage modulus (E'), loss modulus (E''), complex modulus (E^*) and the phase difference (δ) between the stress (σ) and strain (γ) in the test material are given by,

$$E' = \frac{\sigma_0 \cos \delta}{\gamma_0} = \frac{S\sqrt{\pi}}{2\sqrt{A_c}} \quad (2.60)$$

$$E'' = \frac{\sigma_0 \sin \delta}{\gamma_0} = \frac{\omega\lambda_s\sqrt{\pi}}{2\sqrt{A_c}} \quad (2.61)$$

$$E^* = E' + iE'' \quad (2.62)$$

$$\tan \delta = \frac{E''}{E'} \quad (2.63)$$

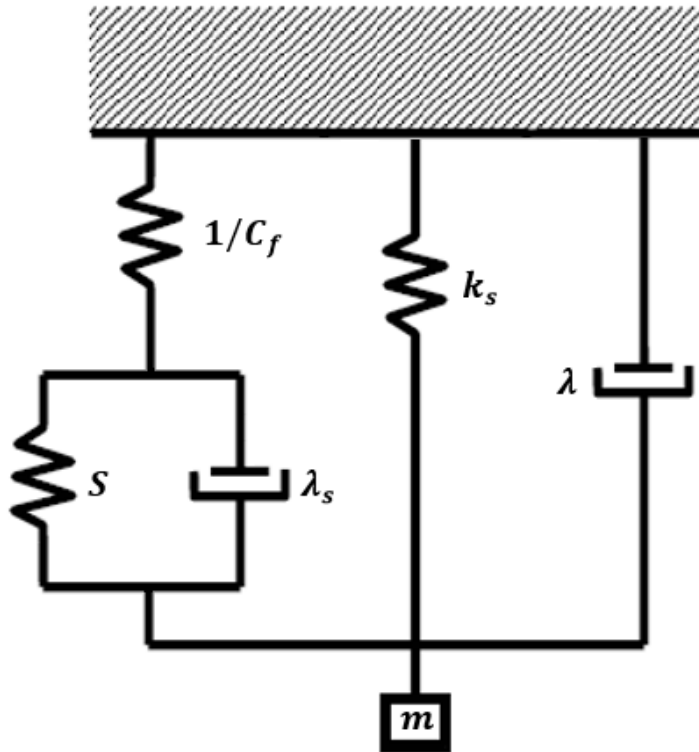


Figure 2.5 Dynamic mechanical model of a nanoindentation instrument. m is the mass of the indenter and shaft, C_f is the load frame compliance, S is the contact stiffness, λ_s is a damping coefficient of the contact, k_s is the stiffness of the mounting spring, and λ is a damping coefficient related to the instrument (Fischer-Cripps, 2011e).

2.2.3.2 Quasi-static nanoindentation test

In Quasi-static nanoindentation test, a holding period is usually used to decouple the viscous behaviour and elastic-plastic behaviour (Zhang *et al.*, 2005). For a force or displacement controlled test, load or displacement is held at a fixed value and changes in displacement (creep) or load (stress relaxation) is recorded as a function of time. An empirical approach based on spring-dashpot combinations is usually adopted to analyse the viscoelastic properties of materials with the feature of focusing on the phenomena rather than the physical mechanisms involved in the deformation. Viscoelastic behaviour of materials in the time domain is conventionally simulated in terms of mechanical models such

as the Maxwell model, the Voigt model and the combined Maxwell-Voigt model as shown in Figure 2.6.

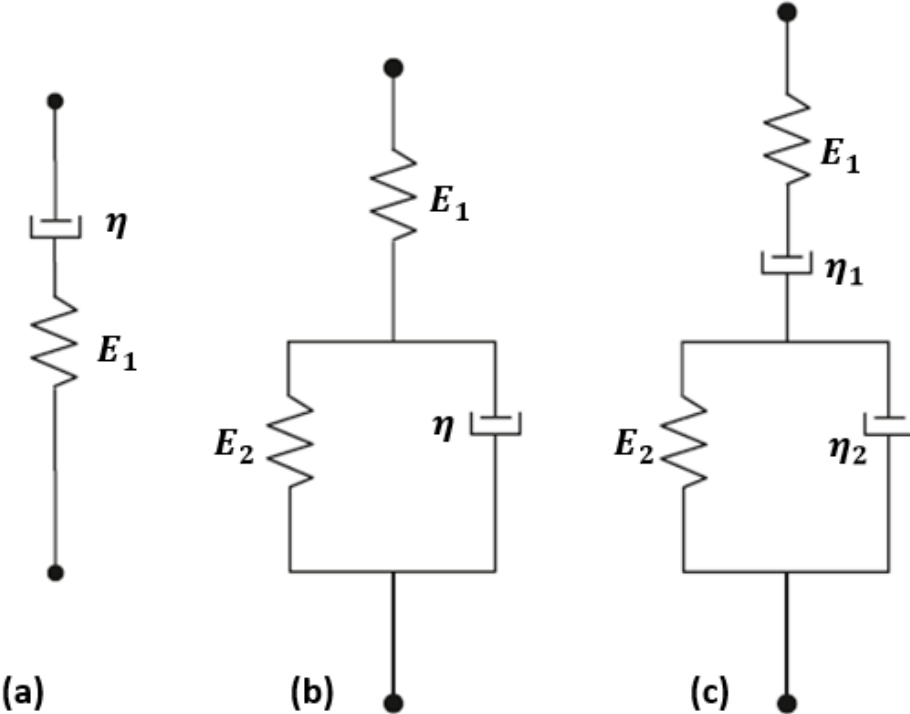


Figure 2.6 Mechanical models of a viscoelastic material. (a) A two-element Maxwell model. (b) A three-element Voigt model. (c) Combined Maxwell-Voigt model. η is the coefficient of viscosity, E_1 and E_2 are elastic modulus related to the relaxation modulus (Fischer-Cripps, 2011e).

For the case of a Maxwell model, the relaxation modulus $E(t)$ during the holding period can be described as,

$$\frac{1}{E(t)} = \frac{1}{E_1} + \frac{1}{\eta} t \quad (2.64)$$

For the case of a Voigt model, $E(t)$ is given by,

$$\frac{1}{E(t)} = \frac{1}{E_1} + \frac{1}{E_2} \left(1 - e^{-t\frac{E_2}{\eta}}\right) \quad (2.65)$$

For the case of a combined Maxwell-Voigt model, $E(t)$ is given by,

$$\frac{1}{E(t)} = \frac{1}{E_1} + \frac{1}{E_2} \left(1 - e^{-t\frac{E_2}{\eta_2}}\right) + \frac{1}{\eta_1} t \quad (2.66)$$

In practice, these fundamental models are combined with additional elements to describe different time-dependent behaviours. For example, for the case of a Prony series model which is widely used in practice, $E(t)$ is given by (Cao *et al.*, 2010; Chen and Lu, 2012),

$$E(t) = E_0 \left[1 - \sum_{i=1}^m g_i \left(1 - e^{-\frac{t}{\tau_i}} \right) \right] = E_\infty + E_0 \sum_{i=1}^m g_i e^{-\frac{t}{\tau_i}} \quad (2.67)$$

where $E_0 = E(t = 0)$ is the instantaneous modulus, E_∞ is the equilibrium modulus once the material is totally relaxed, g_i is the material related constant, τ_i is the material time constant, and m is the number of terms in the series.

Whereupon, for the case of a constant load P_0 with a pyramidal indenter or spherical indenter, the depth creep of penetration is expressed as,

$$\delta^2(t) = \frac{\pi(1 - \nu^2)}{2 \tan \theta} \frac{P_0}{E(t)} \quad \text{pyramidal or conical indenter} \quad (2.68)$$

$$\delta^{3/2}(t) = \frac{3(1 - \nu^2)}{4\sqrt{R}} \frac{P_0}{E(t)} \quad \text{spherical indenter} \quad (2.69)$$

Or in the case of a constant displacement δ_0 with a pyramidal indenter or spherical indenter, the relaxation load is given by,

$$P(t) = \frac{2 \tan \theta \delta_0^2}{\pi(1 - \nu^2)} E(t) \quad \text{pyramidal or conical indenter} \quad (2.70)$$

$$P(t) = \frac{4\sqrt{R}\delta_0^{3/2}}{3(1 - \nu^2)} E(t) \quad \text{spherical indenter} \quad (2.71)$$

By applying the Buckingham Pi theorem in dimensional analysis, Cao *et al.* proposed that the normalized relaxation modulus $\bar{E}(t)$ (the ratio of relaxation modulus to instantaneous modulus) is independent of the geometry of the indenter and sample surface, but depends only on the load history (Cao *et al.*, 2009; Cao *et al.*, 2010). The relationship between the normalized relaxation modulus and the load history is given by,

$$\bar{E}(t) = \frac{E(t)}{E_0} = \frac{P(t)}{P_0} = C \frac{P(t)}{\delta_0} \quad (2.72)$$

where P_0 and δ_0 are the applied load and resultant displacement at the starting point of relaxation, respectively. C is the ratio between δ_0 and P_0 . The significance of this work is that it is independent of displacement and geometry of the indenter, and it can be used to porous materials as well.

After fitting creep or relaxation curves to the selected model, the time-dependent properties can be extracted in terms of relaxation modulus. While it is very important to note that Equations 2.64-2.72 assume a Heaviside unit step increase in load or displacement. In practice, a step increase in load or displacement is not experimentally feasible, and a finite time period is required for the load or displacement increases from zero to the set value. If the loading time is comparable to the material time constant, the resulting instantaneous modulus can be very much less than the nominal value of the material.

In consequence, the accuracy of results fitted from these equations is highly dependent on the loading rate and the time-dependent nature of the material. To account for the influence from the loading period, many sophisticated models have been developed. In 2005, Oyen analysed the difference between creep functions of the ramp loading and step loading in the case of indenting a spherical indenter into viscoelastic polymers, and proposed a dimensionless ramp correction factor (Oyen, 2005),

$$RCF_i = \frac{\tau_i}{t_R} \left(e^{\frac{t_R}{\tau_i}} - 1 \right) \quad (2.73)$$

where t_R is the rise time of loading period. It indicates that, once the loading time is in an order less than the material time constant, the effect from the loading time can be ignored and the numerical errors from fitting the creep or relaxation data by Equations 2.68-2.72 will be negligible. In contrast, once the loading time is comparable to the material time constant, the effect from the loading time should be considered and Equations 2.68-2.72 should be modified by the ramp correction factor. In the case of indenting a spherical indenter into a viscoelastic material, when a Prony series model is adopted, the modified relaxation force

during the holding period (*i.e.* $t \geq t_R$) is derived by substituting Equation 2.67 and Equation 2.73 into Equation 2.71 (Chen and Lu, 2012),

$$P(t) = \frac{4\sqrt{R}\delta^{3/2}(t)}{3(1-\nu^2)} \left[E_\infty + E_0 \sum_{i=1}^m g_i e^{-\frac{t}{\tau_i}} \left[\frac{\tau_i}{t_R} \left(e^{\frac{t_R}{\tau_i}} - 1 \right) \right] \right] \quad (2.74)$$

The force during the finite ramping period (*i.e.* $0 < t \leq t_R$) is given by,

$$P(t) = \frac{4\sqrt{R}\delta^{3/2}(t)}{3(1-\nu^2)} \left[E_\infty + E_0 \sum_{i=1}^m g_i \frac{\tau_i}{t} \left(1 - e^{-\frac{t}{\tau_i}} \right) \right] \quad (2.75)$$

In the similar way, for a pyramidal indenter, the modified relaxation force during the holding period is expressed as,

$$P(t) = \frac{2 \tan \theta \delta^2(t)}{\pi(1-\nu^2)} \left[E_\infty + E_0 \sum_{i=1}^m g_i e^{-\frac{t}{\tau_i}} \left[\frac{\tau_i}{t_R} \left(e^{\frac{t_R}{\tau_i}} - 1 \right) \right] \right] \quad (2.76)$$

The force during the finite ramping period is given by,

$$P(t) = \frac{2 \tan \theta \delta^2(t)}{\pi(1-\nu^2)} \left[E_\infty + E_0 \sum_{i=1}^m g_i \frac{\tau_i}{t} \left(1 - e^{-\frac{t}{\tau_i}} \right) \right] \quad (2.77)$$

In general, E_0 and E_∞ represent the viscoelastic properties in the time domain, E' and E'' represent the viscoelastic properties in the frequency domain. They are given by different nanoindentation tests, and can be related by a Fourier transform. In the case of presenting the relaxation function in the time domain as a Prony series model, the relationship between these parameters is expressed as (Cao *et al.*, 2009),

$$E'(\omega) = E_\infty + E_0 \sum_{i=1}^m g_i \frac{\omega^2 \tau_i^2}{1 + \omega^2 \tau_i^2} \quad (2.78)$$

$$E''(\omega) = E_0 \sum_{i=1}^m g_i \frac{\omega \tau_i}{1 + \omega^2 \tau_i^2} \quad (2.79)$$

2.2.4 Extraction of other mechanical properties from the P - δ curves

It is not only hardness and elastic modulus that are of interest in material science. Nanoindentation techniques can also be used to measure fracture toughness, strain hardening exponent, residual stress and surface adhesion.

For brittle materials, vast majority of fracture toughness measurements are performed with a sharp pyramid indenter. As shown in Figure 2.7, the radial crack often begins at the corners of the impression with increasing applied load. The fracture may lead to a pop-in event in the P - δ curve. Fracture toughness can then be calculated from measuring the length of the crack, or based on the pop-in event in the curve (Page and Hainsworth, 1993; Malzbender and de With, 2000; Malzbender *et al.*, 2000; Den Toonder *et al.*, 2002; Malzbender and de With, 2002; Field *et al.*, 2003; Chen and Bull, 2006a; Chen and Bull, 2007; Fischer-Cripps, 2007; Chen and Bull, 2009a; Chen, 2012).

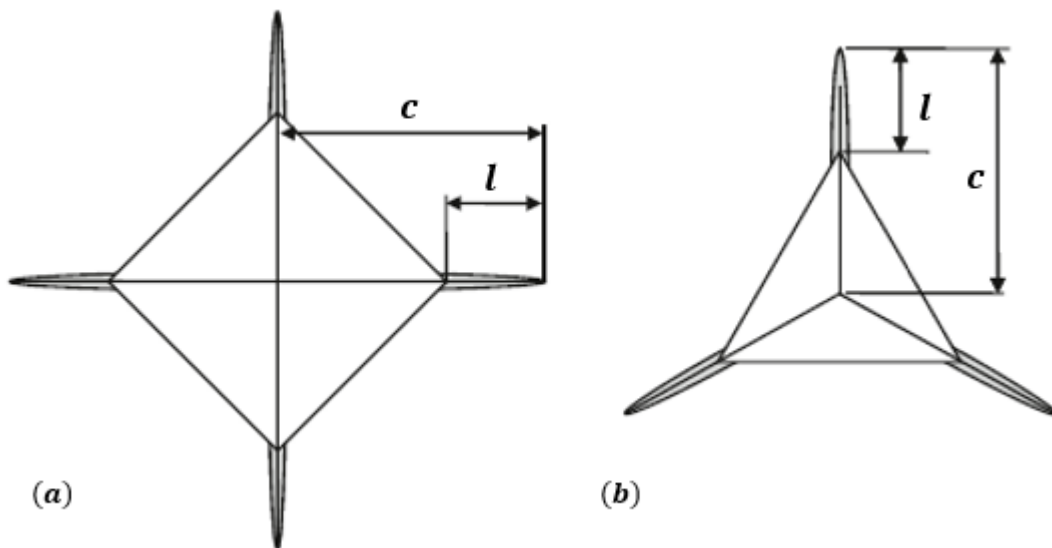


Figure 2.7 Schematic of cracks introduced by (a) Vickers indenter and (b) Berkovich indenter. Crack length c is the distance between the centre of the impression and the crack tip, and crack length l is the distance between the corner of the impression and the crack tip (Fischer-Cripps, 2007).

For many materials, such as annealed metals, the plasticity of the material depends on the strain. When $\varepsilon \geq Y/E$, due to strain hardening, the material appears to be harder with increasing strain. A representative uniaxial stress-strain curve for a work-hardening material is shown in Figure 2.8. The strain

hardening exponent x is usually calculated from the uniaxial stress strain curve given by a traditional tensile test. Indeed, it can also be extracted from the P - δ curve generated by the nanoindentation test (Shinohara *et al.*, 1994; Ahn and Kwon, 2001; Pelletier, 2006).

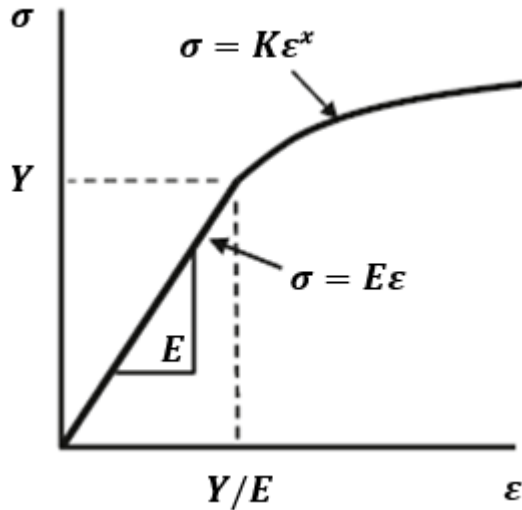


Figure 2.8 A representative uniaxial stress-strain response for an ideal elastic-plastic material. x is the strain hardening index, Y is the yield stress, and the proportionality constant $K = Y(E/Y)^x$. For $x = 0$, the material is elastic perfectly-plastic.

In addition, the possible residual stress and surface adhesion can also affect the determination of hardness and Young's modulus extracted from the P - δ curves. By employing appropriate advanced methods, these residual stress and surface adhesion can be quantified (Johnson *et al.*, 1971; Underwood, 1973; Roberts *et al.*, 1999; Talijat and Pharr, 1999).

2.3 Indenter geometry and selection

The tip end of the indenter is typically made from very stiff material, such as diamond or sapphire, thereby it is much stiffer than most of the tested materials. From the view of the indenter shape, there are various types of indenters can be chosen for a specific task, such as flat, pyramidal, spherical or conical shape. The parameters of the commonly used indenters are summarized in Table 2.1, and these indenters include:

- Cylindrical flat punch indenter

This type of indenter has the advantage of a constant contact geometry. The contact area is independent of the depth and is less likely to be influenced by creep or thermal drift. Therefore, it is relatively straightforward to interpret the data. The drawback is high stress concentration around edge (Chen, 2014). It is usually used in the study of soft solids or viscoelastic materials (Cheng *et al.*, 2000).

- Spherical indenter

For a spherical indenter, the indentation strain (which represents the ratio of contact radius to effective indenter radius) is initially small and produces only elastic deformation. With the increase of strain, such an indenter provides a smooth transition from elastic to plastic deformation. Thus, it is usually used in the study of elastic to plastic transition, or in the case that only elastic deformation is desired (Bell *et al.*, 1992; Field and Swain, 1995). This type of indenter is difficult to be manufactured from hard materials with high quality and typically made as a spheroc-conical shape.

- Conical indenter

A conical indenter has a much smaller contact area compared with flat punch indenter and spherical indenter. Due to its axial symmetry, it is convenient to treat the nanoindentation data from a pyramidal indenter as the data taken with an equivalent conical indenter with an effective cone angle α (Fischer-Cripps, 2011c). On the other hand, its axial symmetry avoids the stress concentration at the sharp edges which are involved in a pyramidal indenter. However, very few nanoindentation tests have been performed with conical indenter, as it is challenging to manufacture a sharp diamond conical tip at small scale (Chen, 2014).

For an ideal sharp conical indenter (or equivalent conical indenter) a condition of fully plastic deformation from the moment that indenter contacts with the specimen is expected. However, during the manufacture or the use of indenter in practice, tip blunting is inevitable that would lead

to an elastic response during the initial contact (Chen and Bull, 2006c; Chen and Bull, 2009b; Fischer-Cripps, 2011d).

- Berkovich indenter

The Berkovich indenter is the most frequently used indenter in nanoindentation. It is a three-sided pyramid with the advantage that three planes are more readily machined to meet at a single point thus ensuring a more precise indentation process, compared to a Vickers indenter (Bhushan and Li, 2003). It has a half included angle of 65.27° and a total included angle (edge to plane) of 142.3° . The tip radius for a brand new Berkovich indenter is usual around 50-100nm, and typically rises to about 200nm with use. Therefore, the primary applications of Berkovich indenter are bulk materials, thin films greater than 100nm, scratch testing and in-situ imaging.

- Vickers indenter

The Vickers indenter is a square pyramid and similar to Berkovich indenter due to the same area to depth ratio. However, it is less commonly used in the nano range than the Berkovich indenter, because it is difficult to machine the four planes to a single point at such small scale and the resulting line of conjunction at the tip is inevitable (Tsui *et al.*, 1996; Bhushan and Li, 2003).

- Cube corner indenter

The Cube corner indenter is similar to the Berkovich indenter except it has a half included angle of 35.26° and a total included angle of 90° . Because of the sharpness of the tip, this type of indenter produces much higher stress and strain on the contact area, and a much more confined plastic deformation zone. Therefore, this type of indenter is commonly used in the study of the fracture toughness, where small cracks will be intentionally produced in brittle materials, or in the case of thin coatings where the effect from the substrate can be minimized (Pharr, 1998; Fischer-Cripps, 2011c).

- Knoop indenter

Similar to the Vickers indenter, the Knoop indenter is a four-sided pyramid with unequal length edges. This results a rhombic residual impression, with the long diagonal approximately seven times the short diagonal. This type of indenter is particularly helpful in the study of hard materials, as the relatively large size of the impression is readily measured by light microscopy compared to the impression made by pyramidal or spherical indenters (Knoop *et al.*, 1939). For highly elastic materials, this indenter also shows the ability to investigate the elastic properties of the specimen, based on the observation that the elastic recovery mainly occurs along the short diagonal, and the recovery along the long diagonal is negligible (Marshall *et al.*, 1982; Riester *et al.*, 2001).

Indenter Type	Projected Contact Area, A_c	Half Included Angle, θ	Effective Cone Angle, α	Intercept Factor, ε	Geometry Correction Factor, β
Cylindrical Flat Punch	πR^2	-	-	1	1
Sphere	$\pi(2R\delta_c - \delta_c^2)$	-	-	0.75	1
Cone	$\pi\delta_c^2 \tan^2 \alpha$	α	α	$\frac{2(\pi - 2)}{\pi}$	1
Berkovich	$3\sqrt{3}\delta_c^2 \tan^2 \theta$	65.27°	70.3°	0.75	1.034
Vickers	$4\delta_c^2 \tan^2 \theta$	68°	70.3°	0.75	1.012
Cube Corner	$3\sqrt{3}\delta_c^2 \tan^2 \theta$	35.26°	42.28°	0.75	1.034
Knoop	$2\delta_c^2 \tan \theta_1 \tan \theta_2$	$\theta_1 = 86.25^\circ$ $\theta_2 = 65^\circ$	77.64°	0.75	1.012

Table 2.1 Parameters for various types of indenters (Oliver and Pharr, 1992; Oliver and Pharr, 2004; Fischer-Cripps, 2011c).

In addition to the selection of the indenter geometry, the size of the tip may also be significant for composite materials. Taking the tissue sample as an example, as shown in Figure 2.9 (which does not take the influence of tissue surface adhesion on the contact area into account), if the purpose is to measure the generalized properties, a spherical or flat punch indenter with a relatively larger diameter should be chosen so that the contact area will be much greater than the size of each individual component. In contrast, if localized properties or mechanical mapping are desired, a sharper tip should be chosen to maximize the spatial resolution.

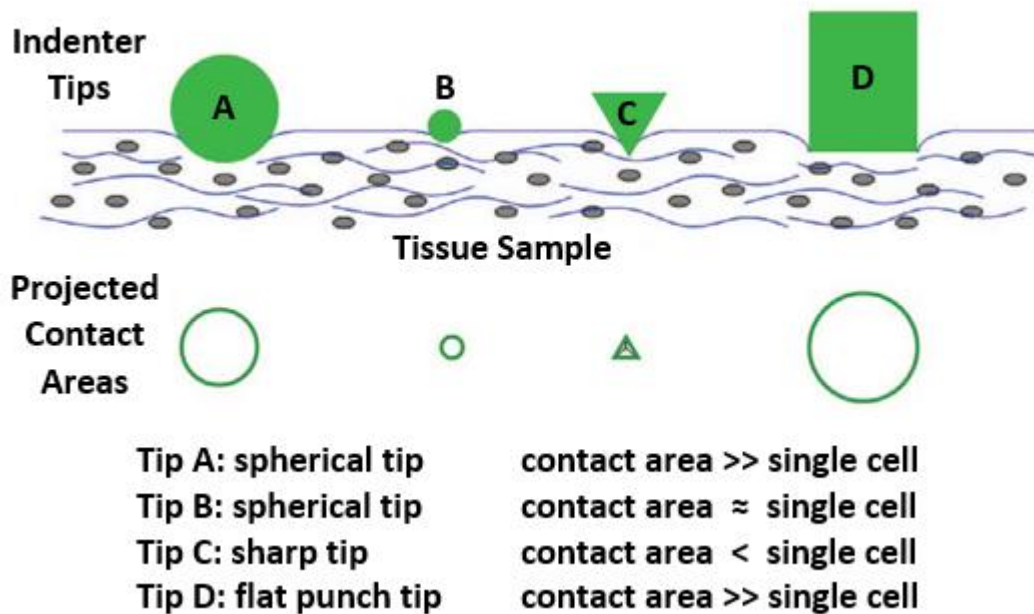


Figure 2.9 Schematic of indenting a tissue sample with various indenters, (a) a spherical tip with a large diameter, (b) a spherical tip with a small diameter, (c) a sharp indenter, and (d) a cylindrical flat punch with a large diameter (Ebenstein and Pruitt, 2006).

2.4 Factors affecting the nanoindentation results

In the nanoindentation test, the size of the residual impression is in submicron region and the contact area is usually calculated from the recorded force and displacement data. In practice, various factors will bring errors during this process. These errors are usually associated with instrument-related issues, non-ideal geometry of the indenter, environmental changes during the indentation test, and material-related issues.

2.4.1 Load frame compliance

Both the displacement and applied force will be recorded during the nanoindentation test. However, this recorded displacement data is the sum of the depth of penetration within the specimen and the deflection of the load frame arising from the reaction force. Oliver and Pharr considered the load frame compliance and sample compliance as two springs in series, therefore the total compliance is given by (Oliver and Pharr, 1992),

$$C = C_f + C_s \quad (2.80)$$

where C is the total compliance, and it equals dh/dP . C_f is the load frame compliance. C_s is the compliance of the indented material, and it equals the inverse of the stiffness, S , which is given by Equation 2.1. Then, Equation 2.80 can be rewritten as,

$$\frac{dh}{dP} = C_f + \frac{\sqrt{\pi}}{2\beta E_r \sqrt{A_c}} \quad (2.81)$$

It shows that, by making various indents on a reference material with known elastic modulus, the plot of dh/dP versus $A_c^{-1/2}$ should be linear and the intercept would give the load frame compliance directly. The disadvantage of this method is that the data obtained at large forces is preferred, as it results a more obvious observation of load frame compliance effects and a less influence from tip defects (such as tip blunting). On the other hand, since this method depends upon an accurate indenter area function, an iterative process is required to reach a convergent value. However, it was reported that, in the case of a very high load frame compliance or a quite blunt indenter, this iterative process is time-consuming or even fails to obtain a convergent value (Oliver and Pharr, 2004).

Alternately, to avoid the contact area involved in the expression, Equation 2.48 is substituted into Equation 2.80, then yields,

$$\frac{dh}{dP} = C_f + \frac{\sqrt{\pi H}}{2\beta E_r \sqrt{P}} \quad (2.82)$$

Afterwards, the value of load frame compliance can be obtained by fitting a linear relationship between dh/dP and $P^{-1/2}$. Once the load frame compliance is calculated, the deflection of the load frame can be subtracted from the recorded total displacement δ , and the depth of penetration within the specimen δ' is then given by,

$$\delta' = \delta - C_f P \quad (2.83)$$

2.4.2 Tip geometry

In the nanoindentation test, the contact area is determined indirectly from the contact depth with the known geometry of the indenter. However, the contact areas given in Table 2.1 are mathematically derived from perfect indenter shapes, which is impossible to achieve in practice, especially for sharp indenters. The inaccurate contact area arising from non-ideal geometry of the indenter will in turn result in the errors in extracted mechanical properties. Normally, as shown in Figure 2.10, the non-ideal indenter often has a larger contact area than the ideal indenter at the same depth. To account for non-ideal geometry of the indenter, a tip area function calibration should be carefully performed by indenting the indenter into the reference material (usually fused silica) for a range of maximum indentation depths. With the known elastic modulus of the reference material, the contact area of the indenter can be expressed as a function of contact depth.

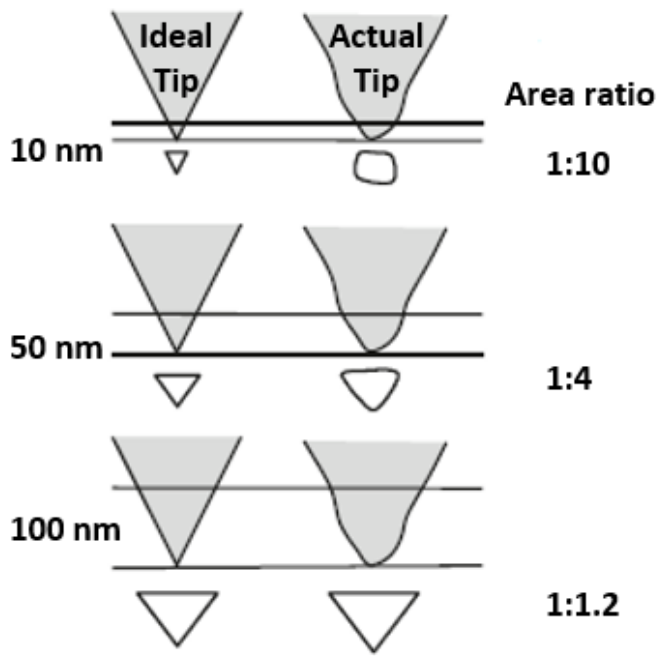


Figure 2.10 Schematic of the comparison of contact area between an ideal conical tip and a non-ideal conical tip (Fischer-Cripps, 2011b).

From the point of view of tip rounding, the tip area function of a sharp indenter is modified by a correction factor ξ (shown in Figure 2.4) and the actual contact area in the case of a Berkovich indenter is given by,

$$A = A(\delta_c + \xi) = 24.5(\delta_c + \xi)^2 \quad (2.84)$$

In this case, the indentation is initially dominated by the spherical region, and the equivalent cone angle decreases gradually from 90° to the nominal value with the increase of the displacement. However, tip cannot always maintain such a spherical shape in practice. Equation 2.9 is the most widely adopted expression due to its ability to fit data over a wide range of contact depths, and it is repeated here for convenience,

$$A(\delta_c) = C_0\delta_c^2 + C_1\delta_c + C_2\delta_c^{1/2} + C_3\delta_c^{1/4} + \dots + C_8\delta_c^{1/128} \quad (2.85)$$

It should be noted that tip bluntness will affect the development of the plastic deformation zone, and a large displacement will be required to achieve the reliable hardness and elastic modulus (Chen and Bull, 2009b; Fischer-Cripps, 2011b). On the other hand, sharp indenter naturally gets blunt with use and the tip area function will consequently change. Hence, the tip area function is required

to be updated at intervals, according to the number of indents and types of indented material (Chen and Bull, 2009b).

2.4.3 Surface roughness

Since the contact area is calculated indirectly, the existence of surface roughness may contribute to the errors in the measurement of contact area between the sample and the indenter. For the contact of a conical indenter with a nominally flat surface shown in Figure 2.11, surface roughness leads to a smaller actual contact area than the calculated contact area, and thus results in the underestimation of hardness and elastic modulus.

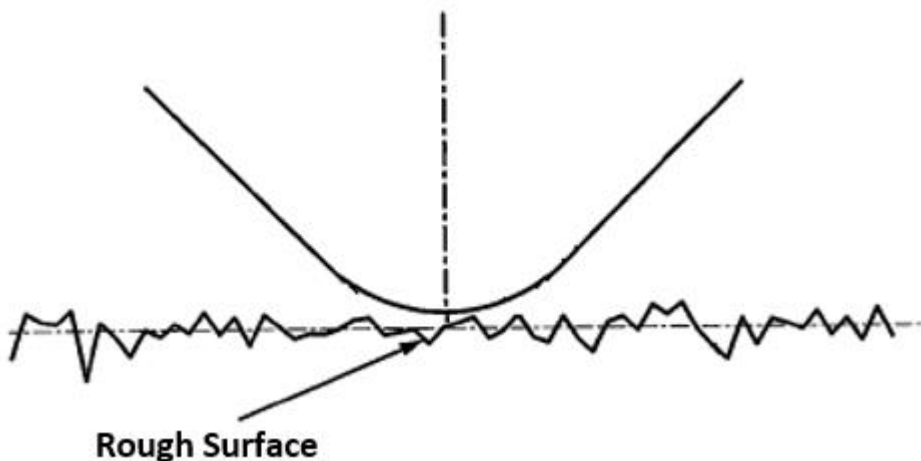


Figure 2.11 Illustration of the contact of a conical indenter with a fractal surface (Bobji and Biswas, 1999).

To account for the effect of surface roughness, Johnson introduced a roughness parameter α and proposed that effect of surface roughness is significant when $\alpha > 0.05$ (Johnson, 1987). This parameter α is given by,

$$\alpha = \frac{\sigma_s R}{a_0^2} \quad (2.86)$$

where σ_s is a material constant related to surface roughness, R is the radius of the indenter and a_0 is the contact radius obtained under the same applied load for the flat surface.

In 1996, Bobji *et al.* proposed a relationship between bulk hardness and measured indentation hardness (Bobji *et al.*, 1996). For a large spherical indenter, it is given by,

$$H_m = H_0 \left(1 + \frac{\delta_e}{\delta} \right) \quad (2.87)$$

For a conical or pyramidal indenter, it is given by,

$$H_m = H_0 \left(1 + \frac{\delta_e}{\delta} \right)^2 \quad (2.88)$$

where δ_e is a material constant related to indenter geometry and surface roughness, H_m is the measured indentation hardness and H_0 is the bulk hardness.

Although there are more complicated expressions existed to account for a more accurate effect of surface roughens on mechanical properties estimation (Johnson, 1987; Bobji and Biswas, 1999; Jiang *et al.*, 2008), they all demonstrated that the effect of roughness is significant when the displacement is comparable to the surface roughness, but negligible when the displacement is much greater than the surface roughness. Therefore, to minimize the effect of roughness, it is useful to indent the sample at a large penetration. Alternatively, sample can be carefully polished to reduce the roughness. However, the polishing procedure may affect the surface properties, especially for some metals.

2.4.4 Initial penetration depth

During a nanoindentation test, the displacement data is ideally recorded from the free surface of the sample. While in practice, the tip must first make contact with the indented surface with an initial penetration depth (δ_i) before the displacement data being recorded. Thus this initial penetration depth is made as small as possible to minimize the errors due to this depth. Although this unrecorded initial penetration depth is minimal, as shown in Figure 2.12, it may still result in errors in all subsequent displacement measurements and errors in the corresponding estimation of hardness and elastic modulus.

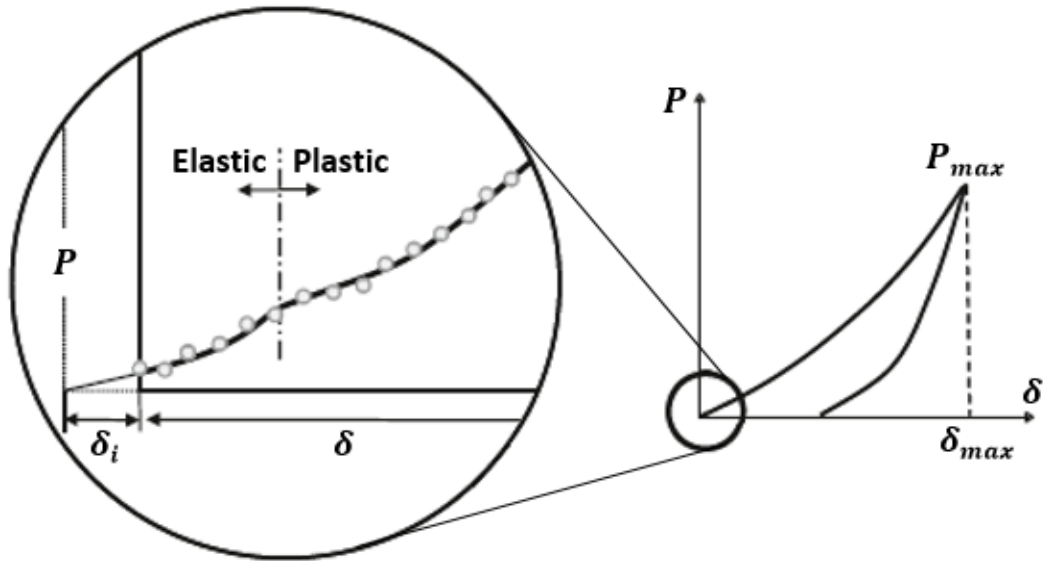


Figure 2.12 Schematic of the existence of initial penetration depth (Fischer-Cripps, 2011b).

Therefore, all subsequent displacement measurements should be modified by adding the initial penetration depth. Based on Equation 2.16, δ_i can be expressed as,

$$P = K(\delta + \delta_i)^n \quad (2.89)$$

where K , n and δ_i are the unknowns that can be extracted by fitting the equation to the initial loading data. Hence, the actual displacement δ' is expressed as,

$$\delta' = \delta + \delta_i \quad (2.90)$$

2.4.5 Thermal drift and creep

During a nanoindentation test, the change in displacement or force during the holding period may result from two types of drift behaviours. The most common one is the thermal drift, which is due to thermal expansion or contraction of the indented material and the instrument. This change in the dimensions of the indented material and the instrument will hence result in errors in the displacement data. To account for the thermal drift effect, a holding period at low value of force is usually set to quantify the rate of change of depth with time, after which all displacement data can be modified accordingly.

Another behaviour is the creep due to the viscosity of materials, such as polymers and biomaterials. An unnoticed creep behaviour may result in an underestimated contact stiffness or even a negative contact stiffness. In the latter case a ‘nose’ phenomenon can be clearly observed on the P - δ curve, as shown in Figure 2.13, which is the case that displacement initially increases with the decreasing force during the initial portion of the unloading. In 2002, Feng and Ngan proposed a modification of the apparent unloading stiffness by setting a holding period as maximum load, and the contact stiffness is given by (Feng and Ngan, 2002),

$$\frac{1}{S} = \frac{1}{S_u} + \frac{\dot{h}_h}{|\dot{P}|} \quad (2.91)$$

where S_u is the apparent unloading stiffness obtained from the P - δ curve, \dot{P} is the initial unloading rate and \dot{h}_h is the creep rate at the end of the holding period.

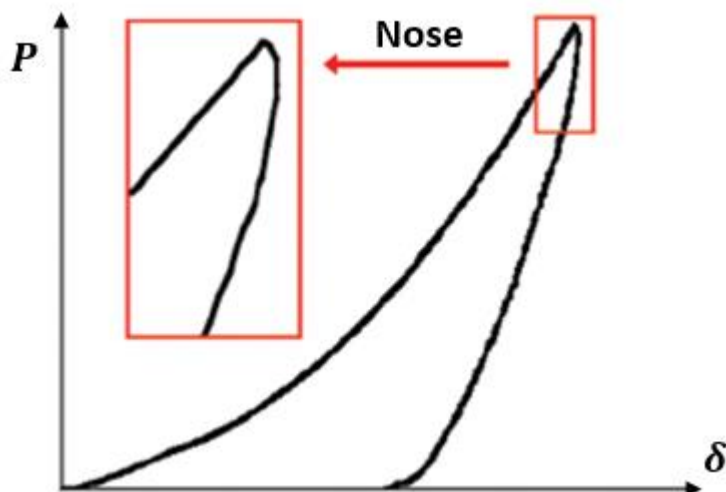


Figure 2.13 Schematic of the nose phenomenon on the P - δ curve indented from a viscoelastic material (Ebenstein and Pruitt, 2006).

In practice, thermal drift and creep behaviours are virtually indistinguishable. A holding period at relatively low load is normally used for thermal drift correction where the creep within indented material is less likely to affect it much. In contrast, to minimize the effect from creep, a holding period at the maximum load is usually used to allow the creep rate to dissipate and reach equilibrium. Viscoelastic properties can also be estimated from this period, which have been described in Section 2.2.3.2.

2.4.6 Piling-up and sinking-in

Piling-up describes the phenomenon that the material around the edges of the impression is pushed upwards, forming a larger contact circle. Inversely, sinking-in is the phenomenon that the sample surface is pushed downwards to form a smaller contact circle. The effect from both of them on the contact area is significant, as shown in Figure 2.14, and the errors on contact area obtained by Oliver and Pharr method can be up to 60% (Bolshakov and Pharr, 1998). The piling-up will lead to an underestimated contact area, which consequently leads to the overestimation of the hardness and the elastic modulus. In contrast, sinking-in will give an overestimated contact area, which results in the underestimation of the hardness and the elastic modulus. To account for the effect of piling-up and sinking-in, the topography of residual impression should be measured by atomic force microscope (AFM) or scanning electron microscope (SEM) (Soare *et al.*, 2004). However, due to the small size of the residual impression, this method is time consuming and may lack of accuracy.

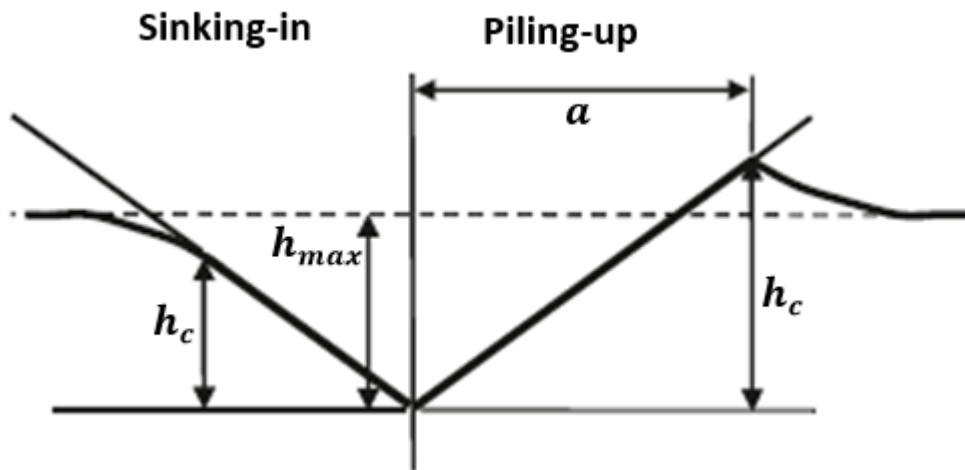


Figure 2.14 Illustration of sinking-in and piling-up during nanoindentation (Fischer-Cripps, 2011b).

The occurrence of piling-up and sinking-in usually relates to the E/Y ratio and the strain-hardening of the tested material. Piling-up is expected to occur in a non-strain-hardening material with a high E/Y ratio (such as strain-hardened metal). Sinking-in is more likely to occur in a strain-hardening material (such as well-annealed metal) or a non-strain-hardening material with a low E/Y ratio (such as ceramic). For a non-strain-hardening material with a high E/Y ratio, a

well-developed plastic deformation zone presents a hemispherical shape meeting the sample surface outside the contact circle, in which case most of the plastic deformation occurs in the area around the tip. For a strain-hardening material, during the nanoindentation test, the material within the plastic deformation zone becomes harder with increasing displacement. Therefore, the material outside the plastic deformation zone tends to be elastically deformed. Since the material within the plastic deformation zone actually acts as an effective indenter and indents downwards, sinking-in occurs. For a non-strain-hardening material with a low E/Y ratio, the plastic deformation is typically confined and the elastic deformation is spread to a larger area to accommodate the indented volume. Thus, sinking-in is to be expected in this case.

2.4.7 Indentation size effect

Indentation size effect (ISE) is the phenomenon that the hardness of a material changes with the decreasing displacement, which is expected to be independent of scale, at very small indentation depth. This phenomenon exists in the nanoindentation of nearly all materials at sufficiently small displacement. In 2003, Bull summarized the various mechanisms of ISE and classified them as the extrinsic causes and the intrinsic causes (Bull, 2003).

Extrinsic causes are the effects related to the sample surface conditions or the tip area function calibration. They can be removed or minimized with careful sample preparation and careful tip area function calibration. These extrinsic causes include:

- The presence of very thin oxide layers arising from environmental exposure. Due to the different mechanical properties of the thin oxide layer, the observed ISE indeed reflects the sample behaviour.
- Errors arising from sample preparation. For some metals, ISE is observed due to work hardening and residual stresses induced by polishing procedure. For ceramics, ISE arises due to cracks at shallow depth and residual stresses induced by polishing procedure.
- The presence of interfacial friction between the tip and indented material (Li *et al.*, 1993).

- Errors arising from inaccurate tip area function, particularly at very small displacement.

ISE may also be caused by intrinsic effects. For the hardness response of most ceramics and metals, the main mechanistic explanation is usually ascribed to geometrically necessary dislocations or discontinuous plastic deformation, depending on the way the plastic zone formation is understood (Bull *et al.*, 1989; Nix and Gao, 1998; Zhang, 2010). Another explanation is related to statistical factors, that is, with the decrease of penetration depth, the indenter has less chance of encountering defects (such as dislocations) within the material and hence plastic deformation is more difficult to achieve (Leipner *et al.*, 2001).

2.5 Application of nanoindentation in biomaterials

Many biomaterials, such as mineralized tissues, soft tissues and many biomimetic materials, are composite materials in nature. Determining the mechanical properties of these composites as well as each individual constituent in many cases is of great importance, not only for their practical application in tissue engineering, but also for understanding the correlations between the properties and microstructures of the tissues, and providing guidelines for optimising material fabrication to achieve desirable properties. In this regard, nanoindentation has been widely used in the field of biomaterials from both experimental and modelling perspectives. Compared to the nanoindentation of conventional materials (e.g. glass and some metal), biomaterials may show significant viscous behaviour during nanoindentation. Therefore, the applicability of statistical and analytical models that established upon conventional materials should be examined, before they are used in the nanoindentation of biomaterials.

2.5.1 Mineralized tissues

Bone tissues have been extensively investigated by nanoindentation and some of these studies have been reviewed by Ebenstein and Pruitt (Ebenstein and Pruitt, 2006) and Lewis and Nyman (Lewis and Nyman, 2008). In these studies, nanoindentation testing was adopted to reveal the difference of mechanical properties between lamellar and interlamellar bones (Rho *et al.*, 2002; Donnelly *et al.*, 2006), individual lamellar layers of osteons (Rho *et al.*, 1999),

trabecular and cortical bones (Turner *et al.*, 1999; Zysset *et al.*, 1999; Hoffler *et al.*, 2000), and healthy and diseased bones (Jämsä *et al.*, 2002; Akhter *et al.*, 2004). In addition, nanoindentation can also be used to reveal the effect of hydration state and sample preparation on bone specimens (Lewis and Nyman, 2008). As an example, Hoffler *et al.* (Hoffler *et al.*, 2005) carried out nanoindentation tests on human cortical bone specimens to investigate the effect of sample preparation and indentation conditions. In their work, cortical bone specimens were separated to different groups depending on the hydration state. All the samples were carefully polished and cleansed prior to the nanoindentation tests. Different loading rates and displacements were adopted. The results showed that the dehydration increased both the hardness and the elastic modulus of bone, the influence of embedded material on the measurements was negligible, and the mechanical properties of bone varied with different loading rates and displacements.

Also, the anisotropic properties of natural and engineered bones have been studied by nanoindentation in conjunction with the finite element analysis (FEA). Chen *et al.* (Chen *et al.*, 2010a) carried out the mechanical characterization on mineralized tissue produced *in vitro* by osteoblasts on titanium alloy coupons. Both quasi-static and dynamic nanoindentation tests were performed to measure the hardness, elastic modulus and time-dependent properties, with a carefully selected displacement to avoid the influence from both the surface roughness and the substrate. It was proposed that this engineered bone has its mechanical properties comparable to woven bone in the rat, and the hardness and elastic modulus has a multi-mode statistical distribution which may due to the microstructure, composition or anisotropy of this engineered bone. Similar results were also observed by Pelled *et al.* (Pelled *et al.*, 2007b), in which the comparison was made between the mechanical properties of stem cell-based engineered bone and animal femoral bone. In the work performed by Carnelli *et al.* (Carnelli *et al.*, 2011), anisotropic bone samples were prepared by cutting bovine cortical bone along axial and transverse directions. Light microscopy was adopted to accurately locate the experimental tests. The measured hardness and elastic modulus were subsequently used as inputs for the FEM simulations of the indentation experiments. The simulated results validated the bone anisotropy,

and proved that FEA is a useful tool to enable us to get a deeper understanding of the mechanical properties of mineralized tissues.

In teeth, nanoindentation testing has been primarily used to obtain the nanomechanical mapping around the dentin-enamel interface to investigate the transition between the less mineralized dentin and the more mineralized enamel (Fong *et al.*, 1999; Urabe *et al.*, 2000; Marshall *et al.*, 2001a), with an example shown in Figure 2.15. In conjunction with the chemical mapping, the changes of hardness, elastic modulus and mineral content around the dentin-enamel interface were extensively studied by nanoindentation (Tesch *et al.*, 2001; Cuy *et al.*, 2002). In addition, nanoindentation testing integrated with other methods was also adopted to reveal the mechanical, chemical and structural difference between the enamel prisms and sheaths (Ge *et al.*, 2005), peritubular and intertubular dentin (Kinney *et al.*, 1996a; Kinney *et al.*, 1996b), cementum and dentin (Ho *et al.*, 2004; Ho *et al.*, 2005), and healthy dentin and carious dentin (Marshall *et al.*, 2001b; Angker *et al.*, 2005).

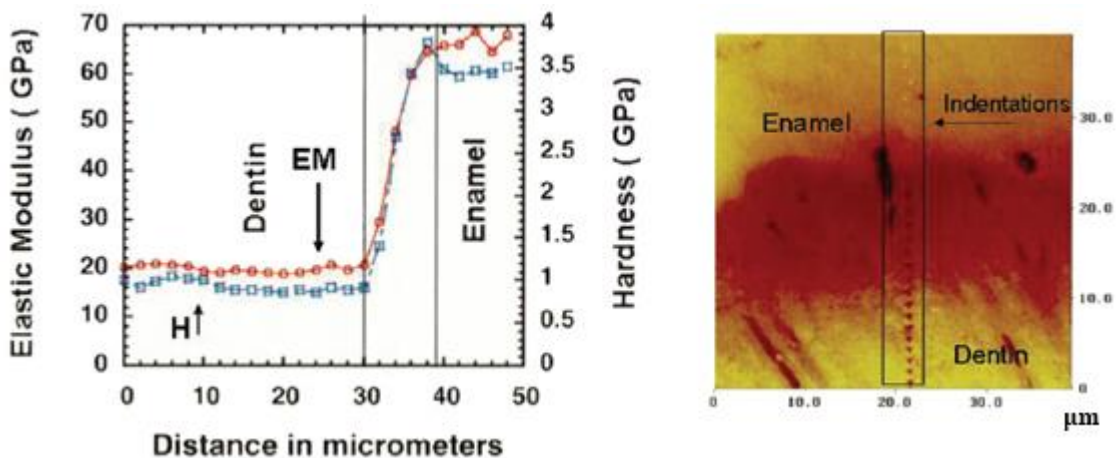


Figure 2.15 Schematic of mechanical transition between dentin and enamel. The plot showed the corresponding mechanical properties determined from indentations. It showed that both hardness and elastic modulus rapidly decreased from enamel region to dentin region (Marshall *et al.*, 2001a).

Another interesting case study of mineralized tissues is the modelling of arthropod exoskeleton carried out by Nikolov *et al.* (Nikolov *et al.*, 2010). Arthropod exoskeleton, such as the lobster cuticle, usually has a hierarchical biological structure with chitin protein fibres. In this study, the lobster exoskeleton was modelled in a multiscale FE model to study the correlation between the

hierarchical structure and the anisotropic properties of the chitin fibre. Figure 2.16 shows the key microstructures of lobster cuticle at various length scales. These simulation results showed that the cholesteric plywood superstructure allowed the reinforcement of the cuticle by chitin-protein fibres, provided the transverse isotropic properties to resist the macroscopic force, prevented microcrack propagation, and enabled energy dissipation during impact loading.

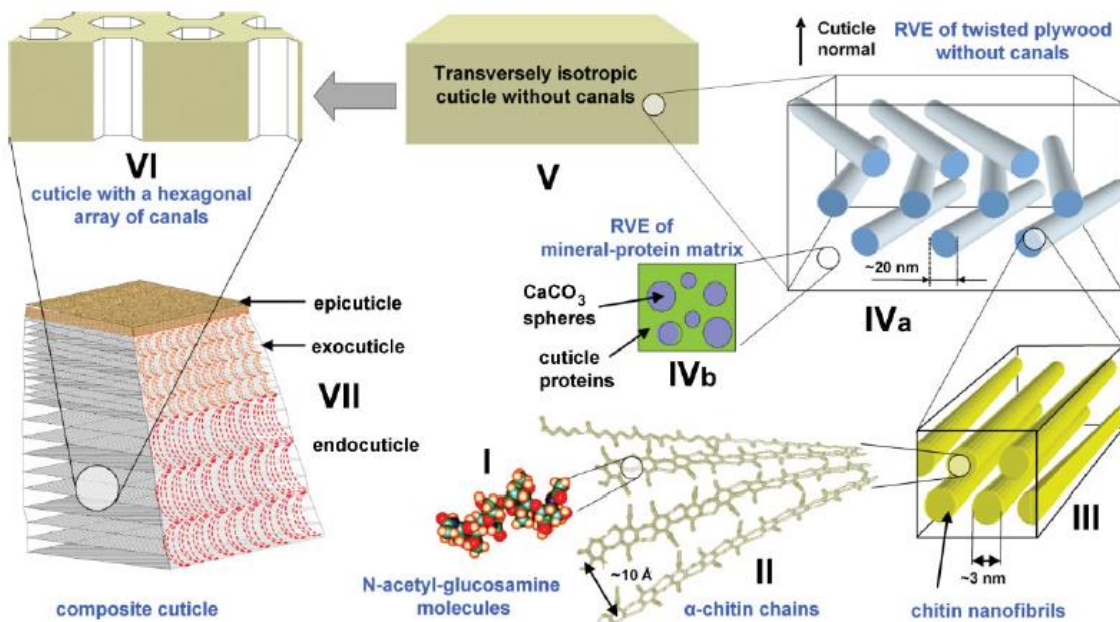


Figure 2.16 Hierarchical structure of the FE model of lobster cuticle: (I) N -acetyl-glucosamine molecules, (II) α -chitin chains, (III) representative volume element (RVE) of a chitin fibre, (IVa) RVE of chitin fibres arranged in twisted plywood without canals, (IVb) RVE of mineral-protein matrix, (V) transversely isotropic cuticle without canals, (VI) cuticle with a hexagonal array of canals, and (VII) composite cuticle (Nikolov *et al.*, 2010).

2.5.2 Soft tissues

For soft tissues, nanoindentation has also proven itself to be a valuable tool for the measurement of mechanical properties of cartilage (Ebenstein *et al.*, 2004; Simha *et al.*, 2004), demineralized dentin (Balooch *et al.*, 1998), the stratum corneum layer of skin (Yuan and Verma, 2006), diseased artery tissue (Ebenstein and Pruitt, 2004) and healthy arteries (Lundkvist *et al.*, 1996). As an example, Lundkvist *et al.* (Lundkvist *et al.*, 1996) carried out AFM-based indentation tests on healthy human artery to investigate the viscoelastic properties. The samples were prepared by cutting the vessel longitudinally into squares and placing in saline solution. Indents were performed in liquid with a spherical indenter. The

creep response of the artery was extracted from a holding period. The viscoelastic properties were then estimated by fitting a Maxwell model to the creep curve.

2.5.3 Acellular biomaterials (*Inclusion-reinforced composites*)

Nanoindentation associated with other methods has also been used in the mechanical characterization of various acellular biomaterials, such as nacre (Katti *et al.*, 2001; Bruet *et al.*, 2005), sponge spicule (Sarikaya *et al.*, 2001), polychaete jaws (Waite *et al.*, 2004), and spider silk fibres (Ebenstein and Wahl, 2006). Based on the understanding of mechanical properties, microstructure and chemical composition of natural biomaterials, there is increasing interest in the design of new biomimetic composite materials with enhanced properties.

In the past decades, biomimetic composites have been widely used in the cosmetic industry, tissue engineering and drug delivery (Ramakrishna *et al.*, 2004; Thomas *et al.*, 2007; De Jong and Borm, 2008). One of the key requirements for these composite materials is that they need to have properties comparable to the mechanical properties of the corresponding natural tissues, or achieve either specific properties. Therefore, it is important to determine the mechanical properties of these composite materials which will guide the optimisation of material processing to achieve the designed properties.

In this regard, nanoindentation associated with FEA has been widely used to determine the mechanical properties of composites, such as fibre-reinforced composites and particle-reinforced composites (Uskokovic *et al.*, 2007; Hu *et al.*, 2010; Yan *et al.*, 2011; Cao and Chen, 2012; Low *et al.*, 2015). In the work conducted by Uskokovic *et al.* (Uskokovic *et al.*, 2007), the localized mechanical properties of ceramic filler-reinforced biocomposite was investigated by nanoindentation with a line scan mode. This mode allowed the surface mechanical properties mapping, and the extraction of mechanical properties of each component. Hu *et al.* (Hu *et al.*, 2010) have classified nanocomposites into four categories depending on the geometry and arrangement of the filler, namely: aligned fibres, randomly oriented fibres, aligned platelets and particles (as illustrated in Figure 2.17). Various theoretical micromechanical models for predicting the upper and lower bounds of elastic modulus of the composites were

summarized. Various FE models used to represent the composites were listed. The advantages of composites in nanoscale and the corresponding mechanisms of mechanical property reinforcement were discussed. In the work conducted by Yan *et al.* and Low *et al.* (Yan *et al.*, 2011; Low *et al.*, 2015), FEA was used to investigate the spatial-dependent hardness and elastic modulus of a semi-spherical particle in a semi-infinite matrix. In the work reported by Cao and Chen (Cao and Chen, 2012), the viscoelastic properties of a fibre-reinforced composite from both the theoretical and FEM analysis were investigated. In this simulation, as illustrated in Figure 2.18, various distributions and shapes of the fibres, as well as various shapes of indenter, were studied. In addition to the prediction of composite properties, nanoindentation associated with statistical analysis was used to determine the mechanical properties of each individual component by carefully setting the grid indentation mode and the maximum displacement (Constantinides *et al.*, 2006; Randall *et al.*, 2009), as demonstrated in Figure 2.19.

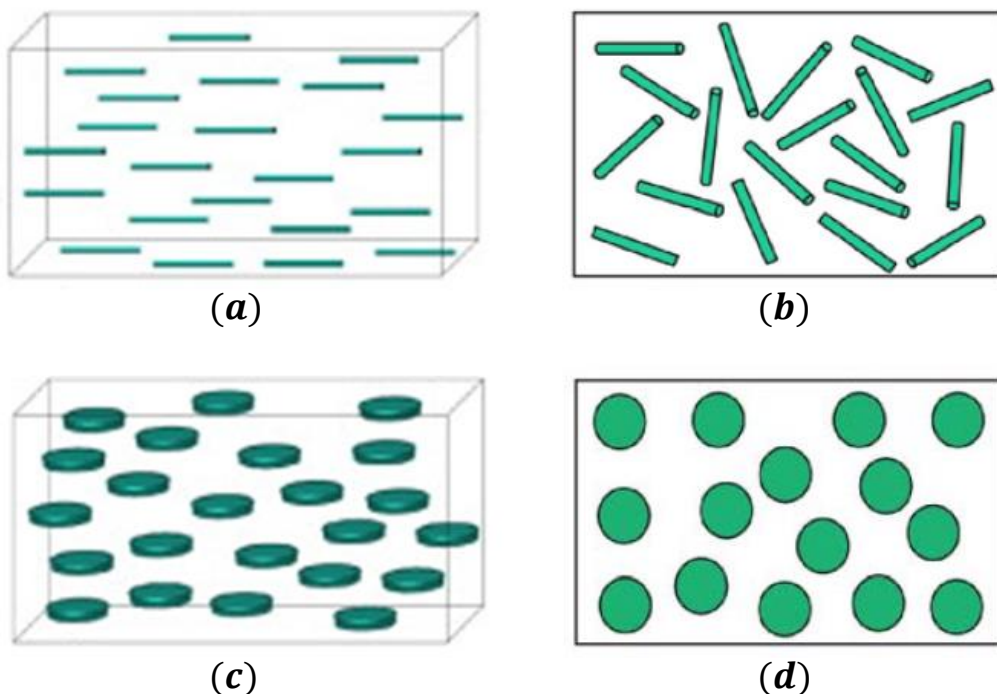


Figure 2.17 Schematic of nanocomposites reinforced by (a) aligned fibres, (b) randomly oriented fibres, (c) aligned platelets, and (d) particles (Liu and Brinson, 2008).

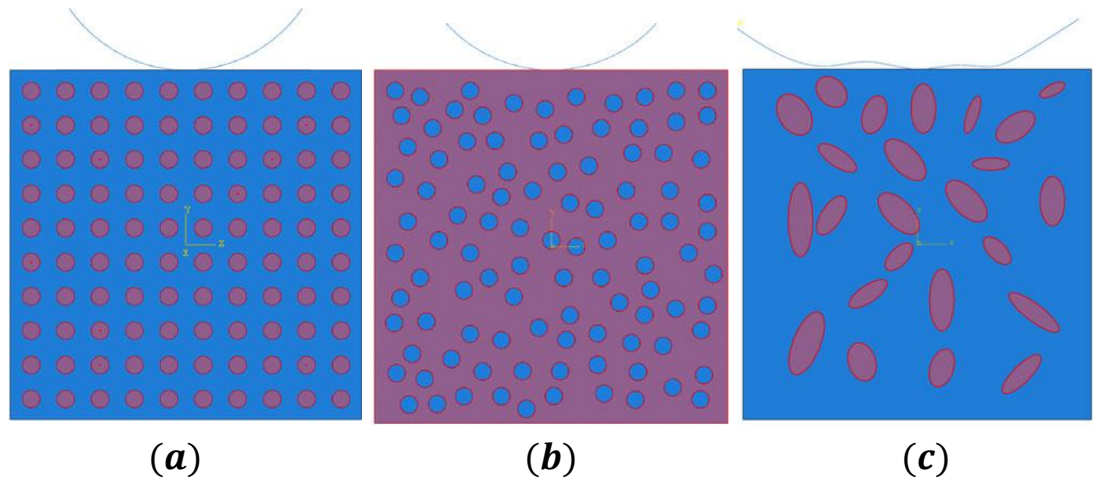


Figure 2.18 Computational model of (a) a cylindrical indenter indenting into a composite with uniform distribution of fibres, (b) a cylindrical indenter indenting into a composite with random distribution of fibres, and (c) a cylindrical indenter with irregular profile indenting into a composite with random distribution of elliptical fibres (Cao and Chen, 2012).

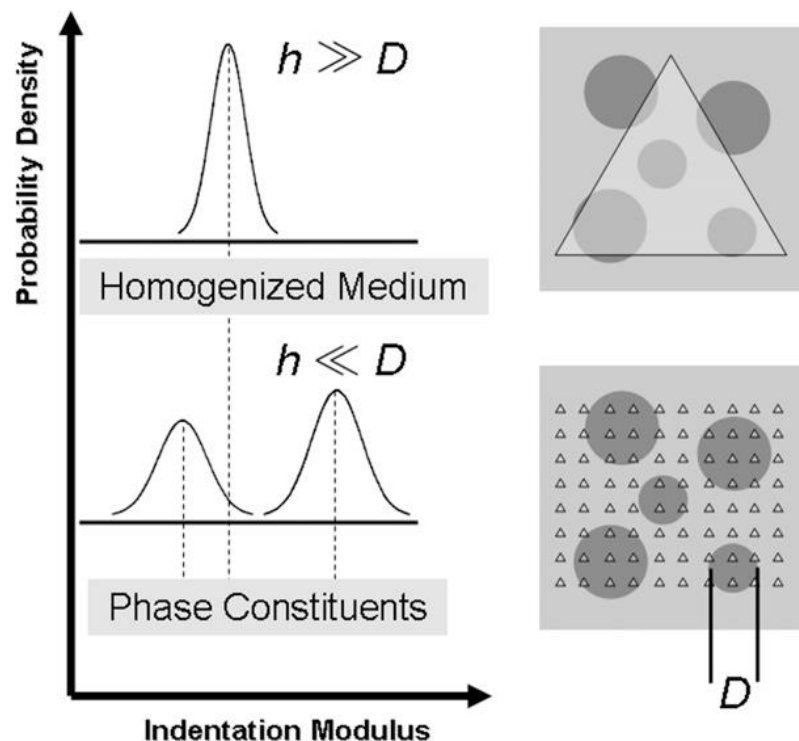


Figure 2.19 Schematic of the grid indentation for a composite material. Small displacement enables the mechanical characterization of each individual constituent, while large displacement leads to the properties of the homogenized medium (Constantinides *et al.*, 2006).

2.6 Summary

In this chapter, a variety of nanoindentation methods were introduced, which were used to estimate mechanical properties of the indented material (hardness, elastic modulus and time-dependent properties). Indenter selection, factors that affect the results, and the application of nanoindentation in biomaterials from both experimental and modelling perspectives were discussed. In the next chapter, based on the computational modelling, a fibre/matrix composite model will be presented to assess its viscoelastic response during nanoindentation.

Chapter 3

Nanomechanical Modelling of Viscoelastic Fibre in Viscoelastic Matrix

Chapter 3. Nanomechanical Modelling of Viscoelastic Fibre in Viscoelastic Matrix

3.1 Introduction

In the past decades, fibre-reinforced polymer composite materials have been widely applied in many fields, such as aerospace, military equipment, automobile, construction and tissue engineering, due to their highly advanced performance over conventional materials (Lou and Schapery, 1971; Bakis *et al.*, 2002; Kalia *et al.*, 2009; Akil *et al.*, 2011; Ozbakkaloglu *et al.*, 2016). For some composite materials, such as glass fibre-reinforced plastic, solid propellant, and some biomimetic materials, they may exhibit significant viscoelastic behaviour (Hashin, 1966; Lou and Schapery, 1971; Calvert, 1992).

Nanoindentation is particularly useful to determine the elastic moduli of individual phases in composite materials such as biopolymer composites for tissue engineering (Herruzo *et al.*, 2014). When performing nanoindentation on these fibre-reinforced composite materials, it is essential to define the influence of the surrounding second phase. Thus, this chapter is focused on the investigation of the viscoelastic response of the unidirectional fibre/matrix composite under nanoindentation test by FEA. FEA of nanoindentation has been widely used to better understand experimental results and guide the design of experimental protocols. This numerical method is based on the assumption that an approximate solution of any indentation problem can be reached by subdividing the tested material, which may have complex structure or properties, into smaller and simpler parts. FEA is a powerful tool to simulate the nanoindentation processes in ideal conditions, which may be limited in an experimental approach. In addition, it can also help extract more information from the experimental results and enable us to get a deeper understanding of the tested material. The disadvantage of the FEA is that the accuracy of the simulations and convergence are dependent on the design of mesh. It is also a continuum solution which is no longer valid at small scale, where individual atomic processes are dominated. The reliability of the model also depends on the careful selection of constitutive models for materials properties.

For complex composite materials, it is challenging to develop analytical models to study their nanomechanical response. Many empirical or semi-analytical models have been proposed to study how the elastic moduli changes with indenter penetration for simple composite materials (such as a coating/substrate composite). For example, based on the linear fit for a coating composite as suggested by ISO standard (ISO14577, 2007), Mencik *et al.* developed some empirical functions to describe the spatial-dependent elastic properties of a coating/substrate composite, which is given by (Menčík *et al.*, 1997; Clifford and Seah, 2006),

$$E^* = E_S^* + B_1(E_C^* - E_S^*)x \quad (3.1)$$

$$x = \frac{a}{t} \quad (3.2)$$

where E^* , E_S^* and E_C^* are the reduced moduli for the coating/substrate composite, substrate and coating, respectively. B_1 is a fitting constant, a is the contact radius between the tip and sample, t is the thickness of the layer, and x is the ratio of a to t . When the indenter is much stiffer than the coating and substrate, E^* is given by (Wenger *et al.*, 2007; Oyen, 2014),

$$E^* = \frac{E}{1 - \nu^2} \quad (3.3)$$

where E and ν are the Young's modulus and the Poisson's ratio for the composite, respectively.

An exponential equation was suggested to describe the spatial-dependent elastic properties of coating/substrate composite by introducing an exponential weight function, as shown below (Menčík *et al.*, 1997; Clifford and Seah, 2006),

$$E^* = E_S^* - (E_S^* - E_C^*)e^{B_2 x} \quad (3.4)$$

in which B_2 is a fitting constant. This equation provides a smooth transition between E_S^* and E_C^* , which is an advantage over Equation 3.1.

In addition, based on the concept of considering the substrate and the coating as two springs in series, reciprocal equations have been proposed to describe

the spatial-dependent elastic properties of a coating/substrate composite (Doerner and Nix, 1986; Menčík *et al.*, 1997; Clifford and Seah, 2006),

$$\frac{1}{E^*} = \frac{1}{E_S^*} + \left(\frac{1}{E_C^*} - \frac{1}{E_S^*} \right) e^{B_3 \cdot x} \quad (3.5)$$

$$\frac{1}{E^*} = \frac{1}{E_C^*} + \left(\frac{1}{E_S^*} - \frac{1}{E_C^*} \right) e^{\frac{B_4}{x}} \quad (3.6)$$

where B_3 and B_4 are the fitting constants similar to the constant in Equation 3.1 and Equation 3.4.

The models above have been widely used to describe the nanomechanical response of a hard coating on a soft substrate. It was found that these models did not work at large penetration. In addition, they did not work well for soft coatings on hard substrates. Therefore, Clifford and Seah proposed the following alternative method based on numerical fitting (Clifford and Seah, 2006),

$$\frac{E^* - E_C^*}{E_S^* - E_C^*} = \frac{Pz^n}{1 + Pz^n + Qz} \quad (3.7)$$

$$z = \frac{a}{t} \left(\frac{E_C^*}{E_S^*} \right)^b \quad (3.8)$$

In the above equation, there are 4 fitting constants, namely: P , Q , n and b . z is the relative contact radius, which takes the effects from the elastic modulus ratio of coating and substrate into consideration. It was found that b equals 0.63 for a soft coating on a hard substrate when indented by a spherical tip (Clifford and Seah, 2006).

Equations 3.1-3.8 were primarily suggested for a coating/substrate composite, thus one of the aims of this work is to examine the applicability of these equations in an inclusion/matrix composite. For Clifford model (Equation 3.7 and Equation 3.8), as demonstrated in the work conducted by Clifford and Seah (Clifford and Seah, 2012), it is applicable to an inclusion/matrix composite after swapping E_C^* to E_I^* (reduced modulus of the inclusion), E_S^* to E_M^* (reduced modulus of the matrix), t to $r_{inclusion}$ (radius of the inclusion). However, it stated

that Clifford model works well when E_I smaller than E_M , with E_I/E_M in the range of 0.1 to 0.33, but is not applicable to the case when E_I/E_M is approaching one (Clifford and Seah, 2012).

In addition, there is lack of understanding as to why this model shows advantages over other models (such as Equation 3.1 and Equations 3.4-3.6). Therefore, in this study, Equation 3.7 will be investigated to reveal the influence of the parameters to its accuracy, and to reduce the numbers of fitting parameters in it.

3.2 Finite element method

In practice, when indenting an inclusion in a matrix, a conical or pyramid tip is often used. Therefore, in this study, to examine if the models above are also applicable to viscoelastic biopolymer inclusion/matrix composite, FEA will be adopted to model the nanomechanical response of various biopolymer composites indented by a conical indenter. As shown in Figure 3.1, a is the contact radius, w is the radius of the inclusion, θ is the half angle of the tip, E_I and E_M are the elastic moduli of inclusion and matrix, respectively. In this study, w equals 1 μm (which is similar to the typical size of reported nanoparticles (Hu *et al.*, 2010)), θ equals 60° and 70.3°, and the typical tip radius r , 0.1 μm and 0.01 μm were selected to represent a blunt probe and a sharp probe. To make it clearer, Table 3.1 summarized the three types of the indenter used in the FE model. In this study, to reveal the tip radius effect, we only vary the tip radius for the indenter with semi-included angle of 70.3° as the similar behaviour should occur for the 60° tip as well.

Indenter	θ	r
Type 1	70.3°	0.1 μm
Type 2	60°	0.1 μm
Type 3	70.3°	0.01 μm

Table 3.1 Geometries of the indenters used in the FE model.

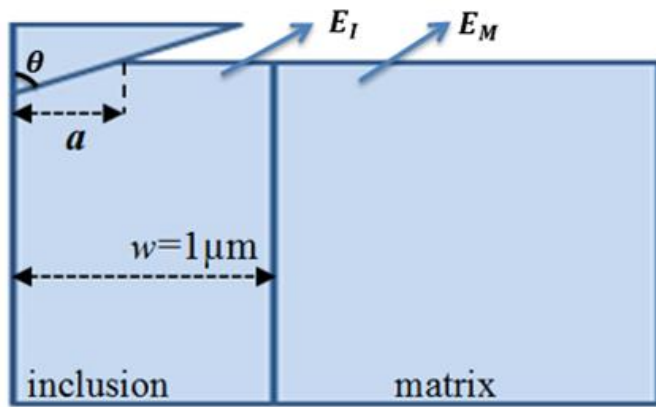


Figure 3.1 Schematic of the indentation of a two-phase biopolymer composite.

Due to the symmetric nature of the indenter and the inclusion/matrix composite, a 2D axisymmetric model was adopted to improve the computational efficiency. The finite element model was created in the ABAQUS 6.10 software. Figure 3.2 shows the details of finite element meshes: (a) an overview of inclusion/matrix system, and (b) enlarged details of inclusion elements underneath the tip. The element type is CAX4R (A 4-node bilinear axisymmetric quadrilateral with reduced integration). A total number of 12822 elements were used to model the inclusion/matrix composite, among which 9748 elements were assigned to the inclusion. Finer elements were arranged beneath the indenter to provide more accurate simulation results. Previous work has demonstrated that the effect of friction on the indentation response was minimal (Chen and Bull, 2009b; Low *et al.*, 2015), thus the contact between the indenter and the sample surface was assumed to be frictionless in this case. As the indenter was much stiffer than the tested sample, the indenter was modelled as a rigid body. The interface between the matrix and the inclusion was assumed to be perfectly bonded. A completely fixed boundary condition was applied to the bottom of the specimen. An axisymmetric boundary condition was applied to the symmetry axis of the indenter and the specimen. Both displacement control and force control can be applied in ABAQUS software. To maximize the efficiency, displacement control with a maximum penetration of 0.2 μm was applied with ramping-holding-unloading segments. As illustrated in Figure 3.3, the indenter reaches the maximum displacement within 1 second, and holds for 10 seconds, then it takes 1 second for the indenter to get back to the original position. The height and the width of the model are sufficiently large compared to the indentation depth so that the simulated response will not be significantly affected by the boundaries.

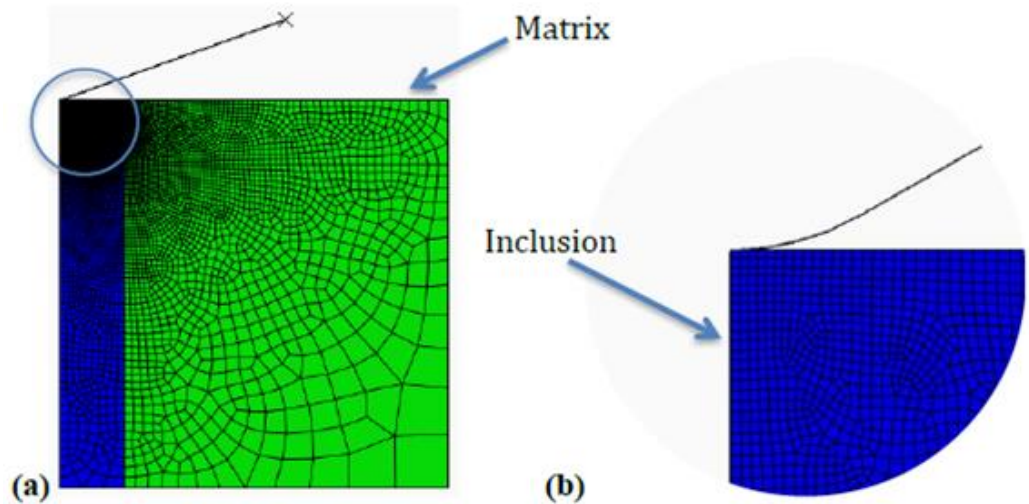


Figure 3.2 Finite element mesh for the inclusion/matrix system, (a) the overview of the inclusion/matrix system, (b) enlarged details of inclusion elements underneath the tip.

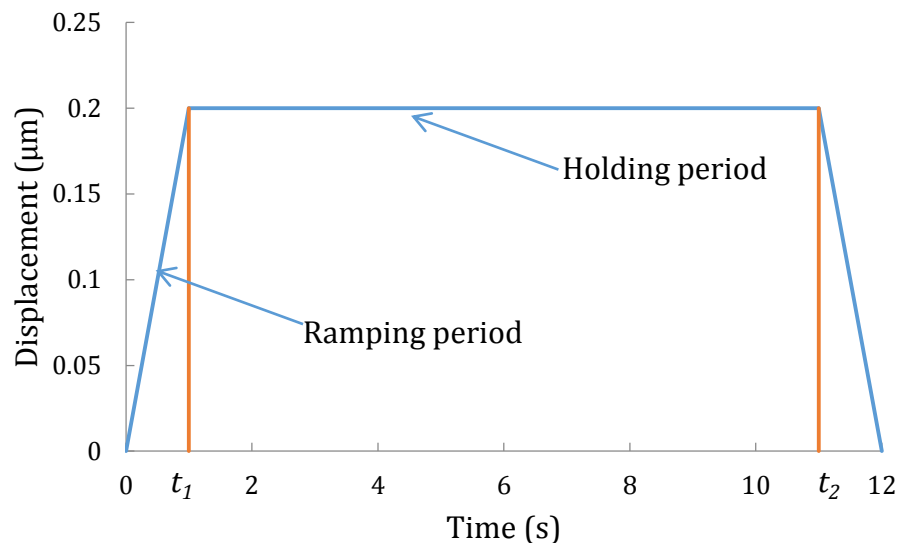


Figure 3.3 Ramping-holding procedure.

The Prony series model (which is the combination of springs and dampers) was used to describe the viscoelastic behaviour of the materials (Cao *et al.*, 2010; Chen and Lu, 2012). In this model, the Young's modulus is given by,

$$E = E_{t=0} g_\infty \quad (3.9)$$

where $E_{t=0}$ is instantaneous elastic modulus. The normalized relaxation modulus $g(t)$ in the Prony series model is given by (Emri and Tschoegl, 1993; Chen and Lu, 2012),

$$g(t) = g_\infty + \sum g_i \exp\left(-\frac{t}{\tau_i}\right) \quad (3.10)$$

$$g_\infty + \sum g_i = 1 \quad (3.11)$$

where g_∞ is the normalized equilibrium modulus, g_i is a material related constant, and τ_i is the time constant. In this study, it is assumed that $i=1$, $g_1 = 0.3$ and $\tau_1 = 1$.

Therefore, the P - δ relationship for a perfectly conical tip during the loading period, $0 \leq t \leq t_1$, as mentioned in the previous chapter (Chapter 2, Section 2.2.3.2), is given by,

$$P(t) = \frac{2\tan\theta}{\pi(1-\nu^2)} \delta^2(t) E_{t=0} \left[g_\infty + g_1 \frac{\tau_1}{t} \left(1 - \exp\left(-\frac{t}{\tau_1}\right) \right) \right] \quad (3.12)$$

where $P(t)$ is the force applied by the indenter and $\delta(t)$ is the displacement. During the stress relaxation period, $t_1 \leq t \leq t_2$, the P - δ relationship is given by,

$$\begin{aligned} P(t) = & \frac{2\tan\theta}{\pi(1-\nu^2)} \delta^2(t) E_{t=0} \left[g_\infty \right. \\ & \left. + g_1 \frac{\tau_1}{t_1} \exp\left(\frac{-t}{\tau_1}\right) \left[\exp\left(\frac{t_1}{\tau_1}\right) - 1 \right] \right] \end{aligned} \quad (3.13)$$

Both hard material embedded in soft matrix and soft material embedded in hard matrix are quite common in biomaterials. For example, mollusc shells (matrix) contain both the organic biopolymer (soft particle) and inorganic aragonite (hard particle) (Li *et al.*, 2004), exoskeleton of crustaceans (matrix) contain both the proteins (soft particle) and mineralized chitin fibrils (hard particle) (Chen *et al.*, 2008), and the bone (matrix) contains both the collagen matrix (soft particle) and hydroxyapatite crystal (hard particle) (Gao, 2006). These biomaterials inspire the innovation of new advanced materials. Hard particles are added for reinforcement. While soft particles are added to improve the fracture resistance, toughness, or for other functional purposes (Yang *et al.*, 2017). Hence, in this work, both cases (*i.e.* hard fibre embedded in soft matrix or soft fibre embedded in hard matrix) should be considered.

In this study, the Poisson's ratios of the inclusion and matrix were fixed at 0.3. According to the elastic modulus of typical biopolymers reported in literature, the equilibrium elastic modulus of inclusion, E_I , was set to 10 MPa (similar to the elastic modulus of 50/50 poly-L-lactic acid (PLLA)/poly-DL-lactic acid (PDLLA) blends (Chen *et al.*, 2003)). While the equilibrium elastic modulus of the matrix, E_M , varied from 2 MPa (similar to the elastic modulus of PDLLA (Chen *et al.*, 2003)) to 50 MPa (similar to the elastic modulus of 50/50 polyglycolic acid (PGA)/gelatin blends (Hajiali *et al.*, 2011)) to define the influence of surrounding second phase, which covers a wide range of typical biopolymers (Chen *et al.*, 2003; Balakrishnan and Banerjee, 2011; Mukherjee and Kao, 2011). Additional simulation was done by assuming $E_M = E_I = 10$ MPa for calibration.

Matlab code was written to perform the curve fitting and extract the fitting parameters in different models. The quality of the fitting was estimated by calculating the minimum '*resnorm*' value, which is given by,

$$resnorm = \sum_i (F(x_i) - y_i)^2 \quad (3.14)$$

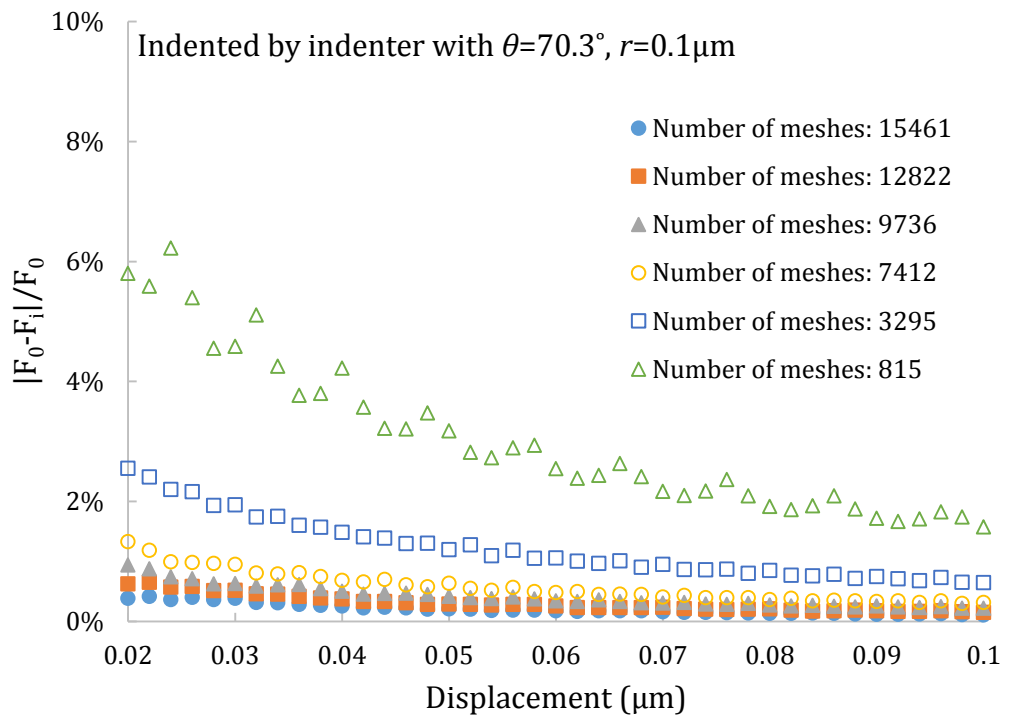
where *resnorm* presents the quality of a fitting. This parameter can be automatically obtained from Matlab software and it varies from zero to infinity. Within this range, a smaller value indicates a better fitting and zero means a perfect fitting. $F(x)$ is the predicted data from fitting equation, and y is the observed data from simulation. During the curve fitting, in order to improve the computational efficiency, the fitting parameter b in Clifford model was predefined and manually adjusted until achieving a minimum *resnorm* value. Besides, the influence of fitting parameters with different decimal places (*i.e.* 1, 2, 3...) on the *resnorm* value were investigated. Then, as a trade-off between efficiency and accuracy, fitting parameters were rounded to 3 decimal places.

3.3 Results and discussion

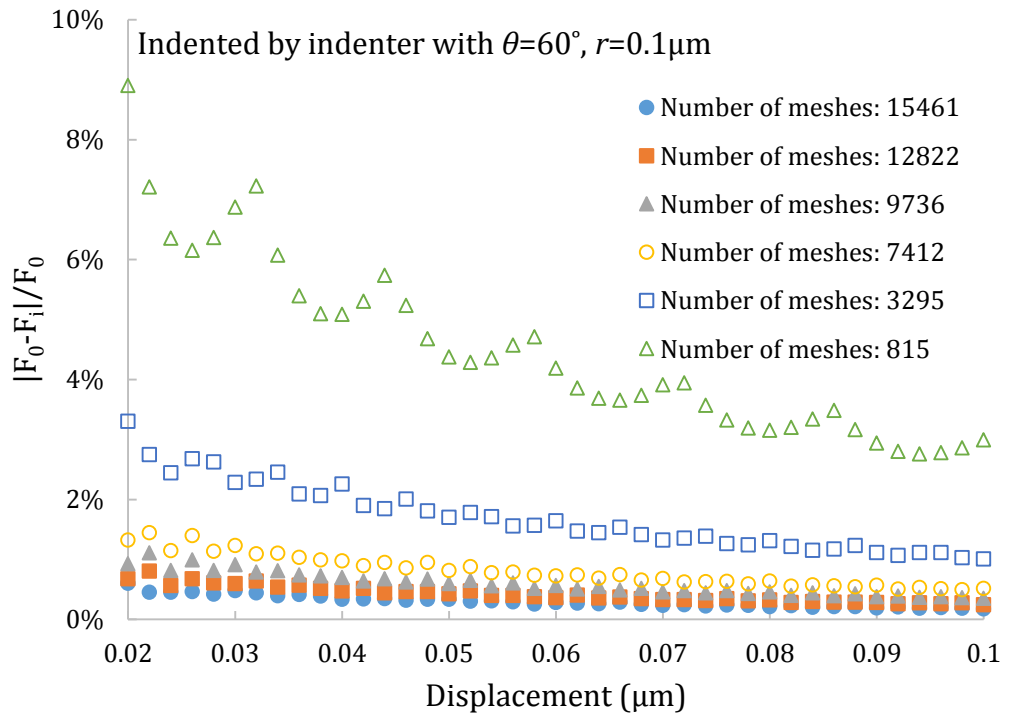
3.3.1 Model validation

Prior to the nanomechanical modelling of the inclusion/matrix systems, the validation of the model should be performed. Since coarse mesh may result in inaccurate simulation results, errors due to the density of mesh should be avoided, and the deviation between the simulated data and the theoretical data should be within an acceptable level.

To investigate the influence of the mesh density, a model with denser or coarser mesh was created by proportionally varying the number of elements in each segment. After setting the number of elements in each segment, the number of elements is then determined by the finite element software. In this work, the maximum number of elements was 29566 and the minimum number was 815. According to the literature, these two values are reasonable to be set as maximum and minimum values. The elastic modulus and the Poisson's ratio of both inclusion and matrix were set as 10 MPa and 0.3, respectively. By performing the nanoindentation modelling with the maximum displacement of 0.2 μm by the conical indenters listed in Table 3.1, the F - δ data from loading period for models with different mesh density were compared. By assuming the data from model with densest mesh (number of elements was 29566) as the reference (F_0), the deviation between F_0 and the data from models with other mesh density (F_i) is plotted in Figure 3.4. A big deviation (higher than 20%) was observed in all cases when the displacement was lower than 0.02 μm , which may due to the fact that the indenter was not touching enough elements at shallow penetration depth. Hence, the data within the displacement range of 0~0.02 μm were discarded. After the indenter touched enough elements, as shown in Figure 3.5, relatively big deviation (higher than 6%) was observed when the number of elements was 815 in all cases. The deviation was lower than 2% when the number of elements was higher than 7412. This indicates that the mesh should be dense enough with the total number of elements higher than 7412 to avoid errors from the mesh density, and the mesh density of the model (a total number of elements was 12822) used in this study is reasonable.

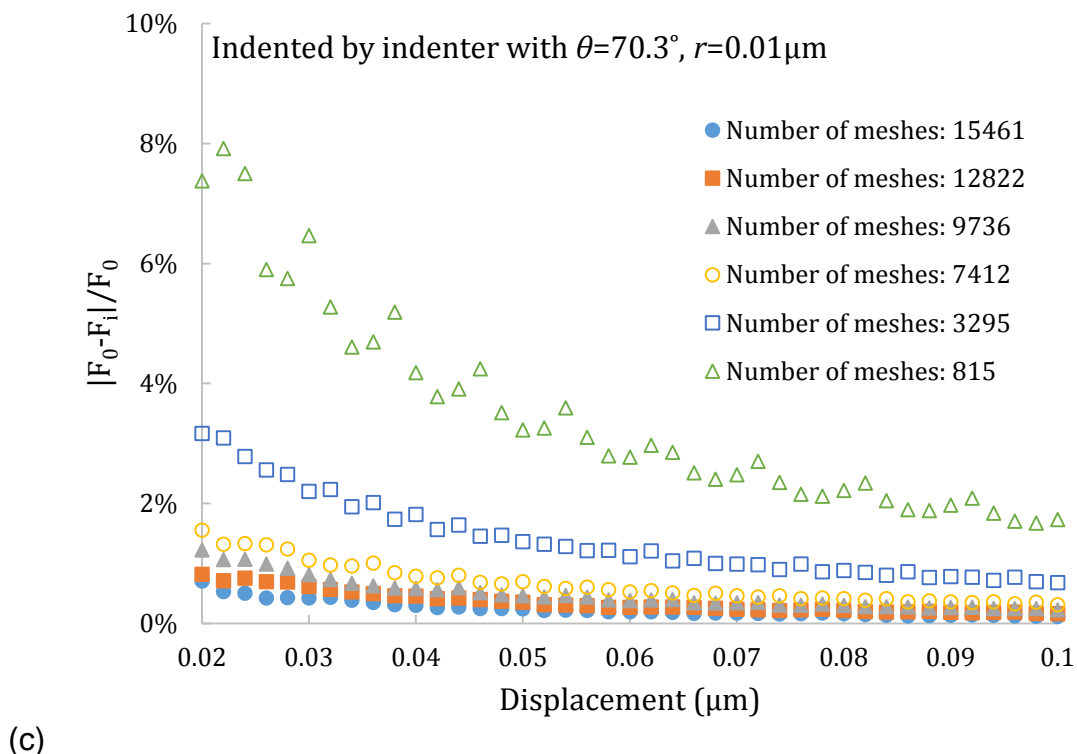


(a)



(b)

Figure 3.4 Absolute deviation ($\frac{|F_0 - F_i|}{F_0}$) between the force from the models with different mesh density, indented by the indenters with (a) $\theta = 70.3^\circ$, $r = 0.1 \mu\text{m}$, (b) $\theta = 60^\circ$, $r = 0.1 \mu\text{m}$, and (c) $\theta = 70.3^\circ$, $r = 0.01 \mu\text{m}$.



(c)

Figure 3.4 (Cont.)

Additional comparison was drawn between the simulated data from FEA and the theoretical data from an empirical equation. Both inclusion and matrix were set as a linear elastic material with an elastic modulus of 10 MPa and a Poisson's ratio of 0.3. By performing the nanoindentation modelling with the maximum displacement of 0.2 μm by a spherical indenter with a radius of 0.5 μm , the $F-\delta$ data from the inclusion/matrix system was compared with the theoretical data calculated from the Hertz equation. As shown in Figure 3.5, the deviation is within the range of 2~6% when the displacement varies from 0.02 μm to 0.2 μm . In general, the Hertz equation is applied to a small strain ($\varepsilon = 0.2a/R$ for a spherical indenter) which is usually lower than 5%. As shown in the graph, the deviation is approximately 2% for a strain of 4.5% (displacement equals 0.02 μm). It will be even lower when the displacement is extrapolated to a smaller displacement. In this case, the deviation is acceptable and less than 2% when the strain is below 5%.

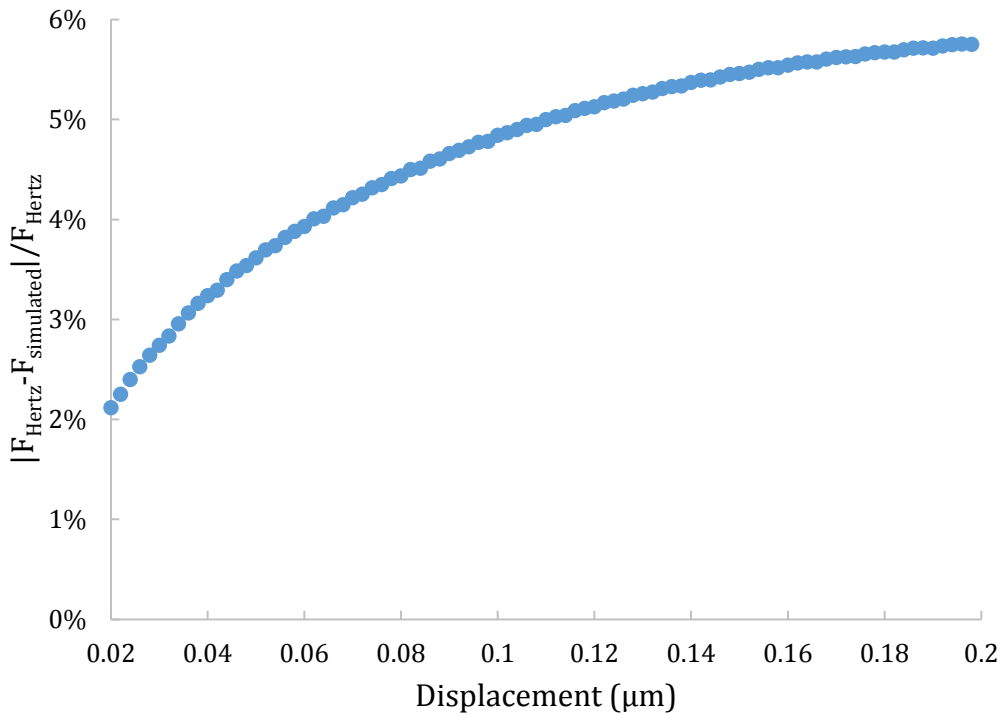
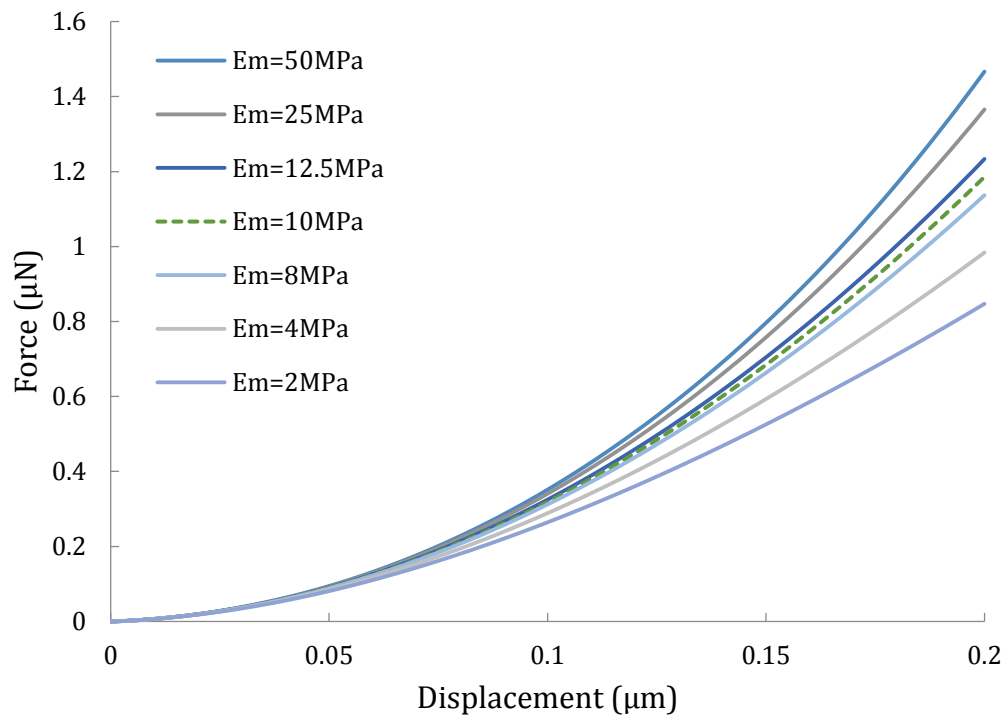


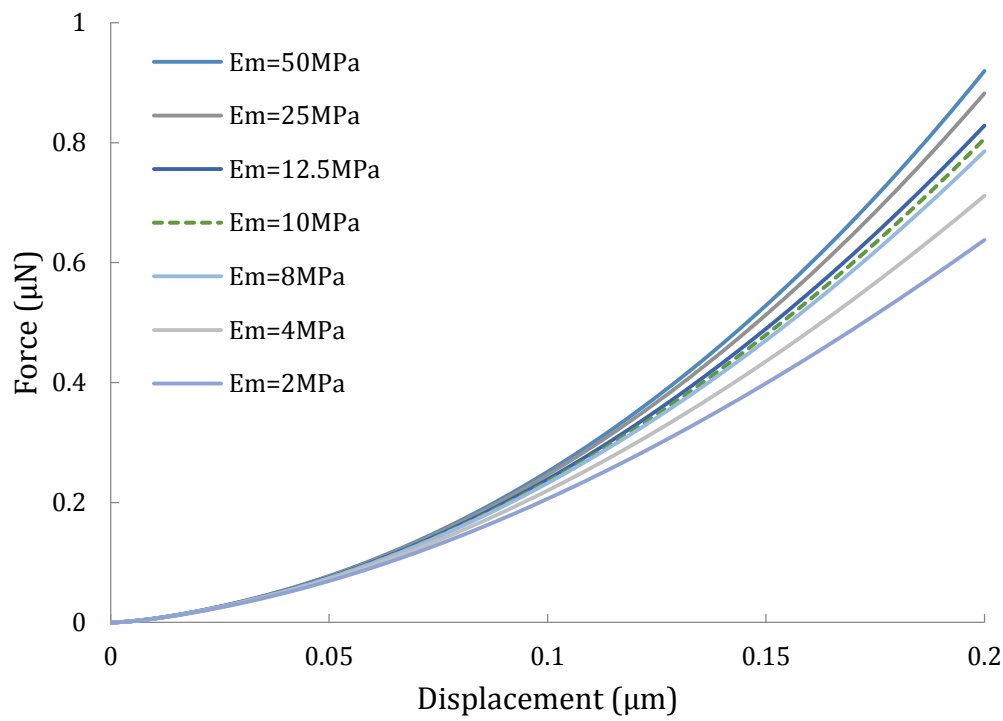
Figure 3.5 Absolute deviation ($\frac{|F_{Hertz} - F_{simulated}|}{F_{Hertz}}$) between the theoretical data and the simulated data indented by a spherical indenter.

3.3.2 *The Young's modulus determined by FEA*

The relations between force and displacement indented by different indenters were simulated by FEA, as depicted in Figure 3.6. During the simulation, forces increase with the increasing displacement and E_M . It shows that the mechanical response is affected by the matrix and the influence becomes more obvious with the increase of the displacement. For the indenters with various half angles, the increase rate of the force decreases with a sharper tip. One possible reason is that, at the same contact depth, the sharper tip generates a smaller contact area which indicates a smaller force (Clifford and Seah, 2006).



(a)



(b)

Figure 3.6 Force-displacement curves of the 10 MPa inclusion surrounding by matrix with increasing elastic modulus from 2 to 50 MPa, indented by the indenters with (a) $\theta = 70.3^\circ$, $r = 0.1 \mu m$, (b) $\theta = 60^\circ$, $r = 0.1 \mu m$, and (c) $\theta = 70.3^\circ$, $r = 0.01 \mu m$.

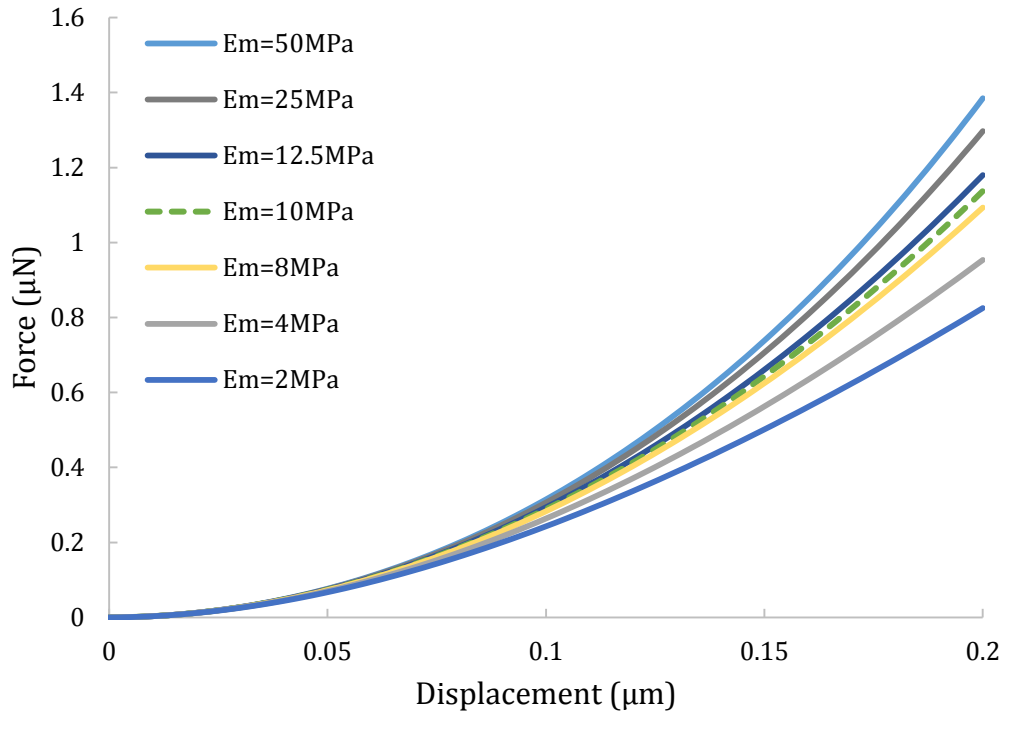


Figure 3.6 (Cont.)

Based on the force-displacement curves generated by FEA, extracting the spatial-dependent elastic response of the composite is possible (Cheng and Cheng, 2004; Chen and Lu, 2012). In this study, the Young's modulus of the composite was obtained by analysing the data in the loading period. By deriving Equation 3.12, the Young's modulus of the composite is expressed as,

$$\frac{P_1(\text{composite})}{P_2(E_M = E_I = 10 \text{ MPa})} = \frac{E_1(\text{composite})}{E_2(E_M = E_I = 10 \text{ MPa})} \quad (3.15)$$

where P_1 is the applied force from simulation when E_M varies from 2 to 50 MPa, P_2 is the applied force from simulation when $E_M = 10 \text{ MPa}$, E_2 equals 10 MPa and it is the Young's modulus by setting $E_M = E_I = 10 \text{ MPa}$ as the control group, and E_1 is the Young's modulus of the inclusion/matrix system which is the only unknown value in this equation. Figure 3.7 shows how the elastic properties of the composite change with the displacement with a maximum penetration of 0.2 μm, for the matrix with varied properties, calculated by Equation 3.15. As expected, When E_M is bigger than E_I , $E(\text{composite})$ is increasing with the increase of the displacement, Young's modulus of the matrix and half angle of the indenter. When E_M is smaller than E_I , $E(\text{composite})$ decreases with the

increase of the displacement, Young's modulus of the matrix and half angle of the indenter.

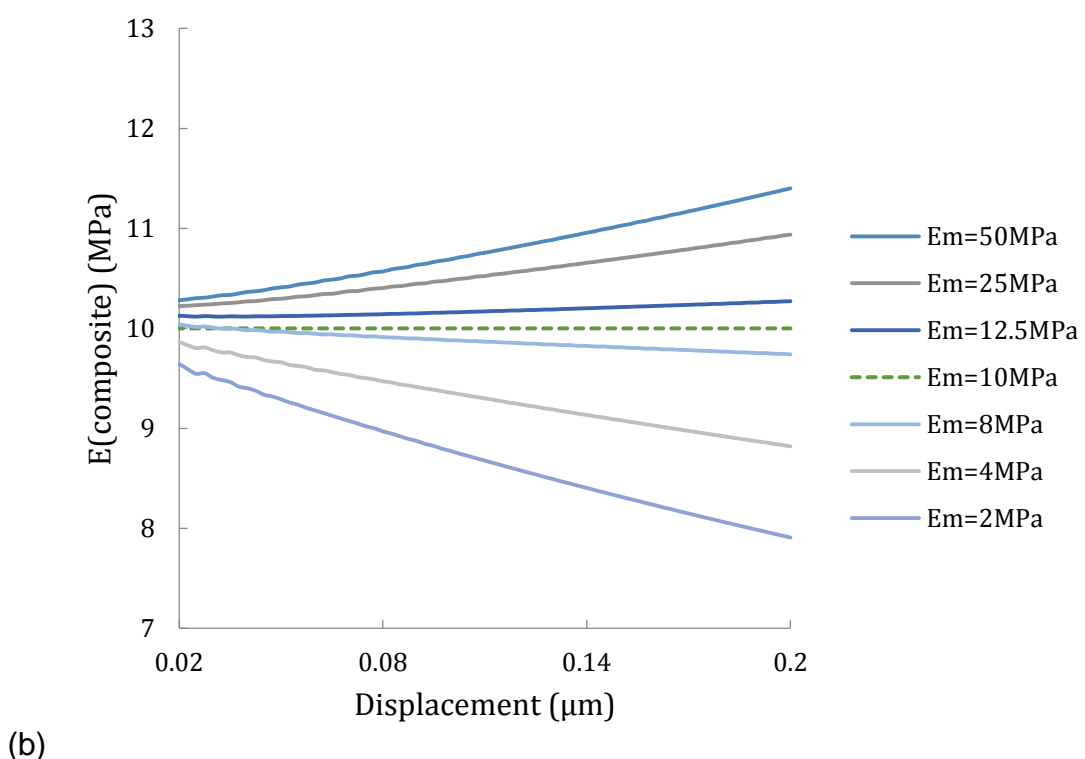
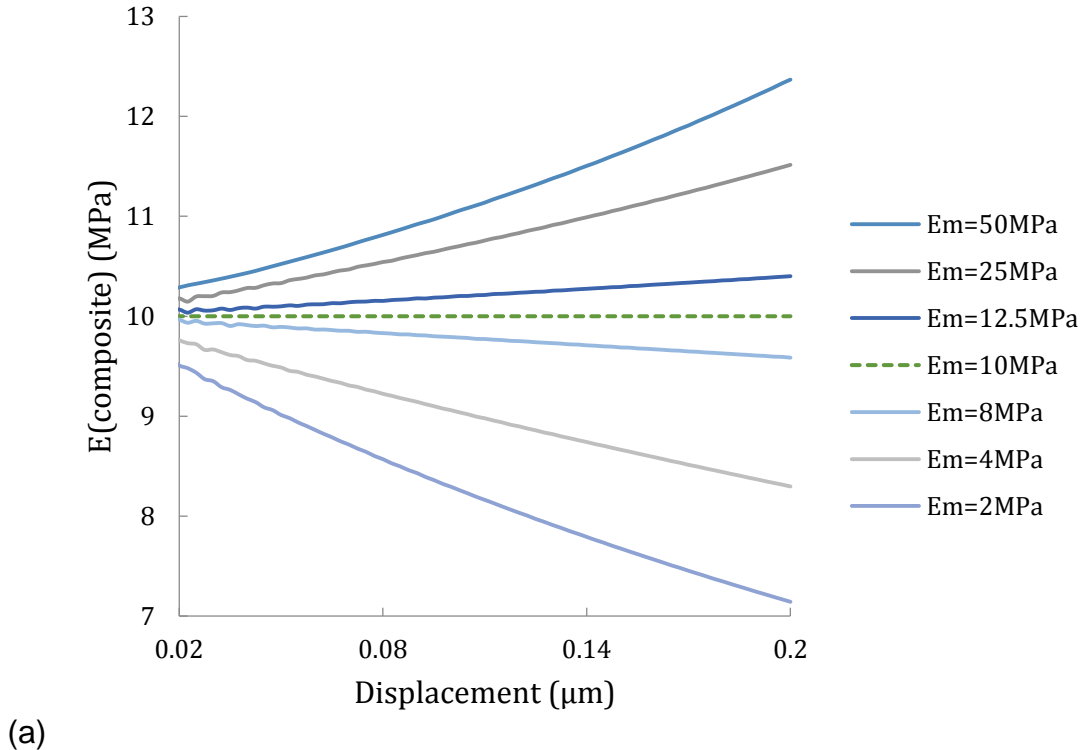


Figure 3.7 The Young's modulus of the inclusion/matrix system, $E(\text{composite})$, measured by the indenters with (a) $\theta = 70.3^\circ$, $r = 0.1 \mu\text{m}$, (b) $\theta = 60^\circ$, $r = 0.1 \mu\text{m}$, and (c) $\theta = 70.3^\circ$, $r = 0.01 \mu\text{m}$.

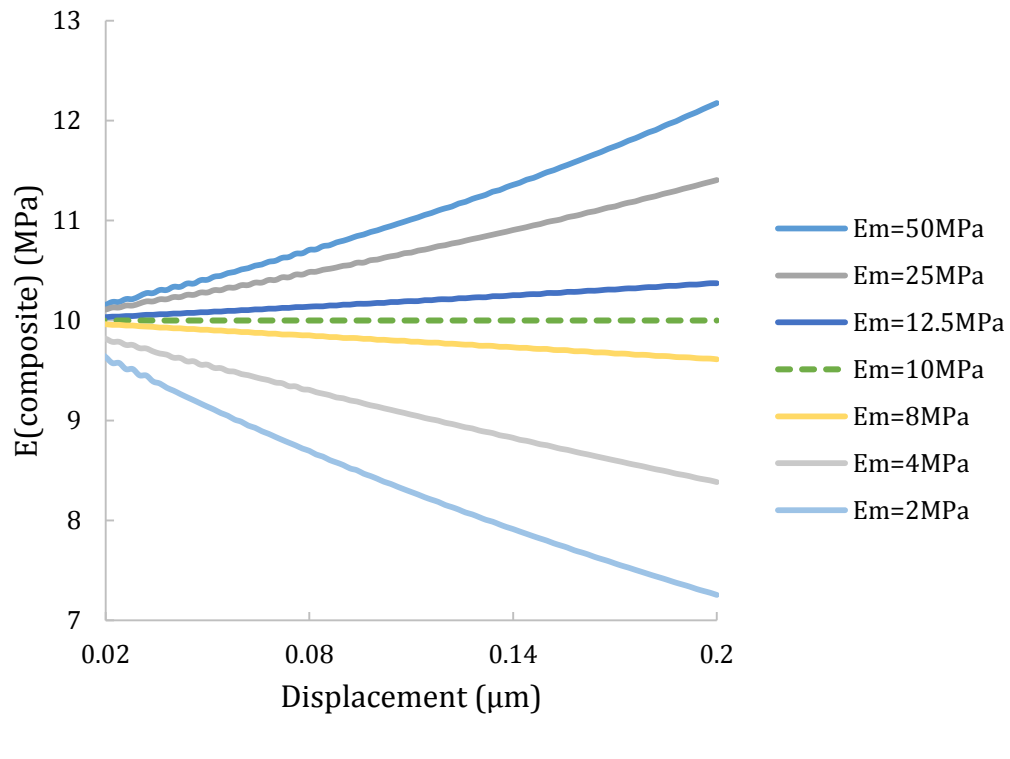
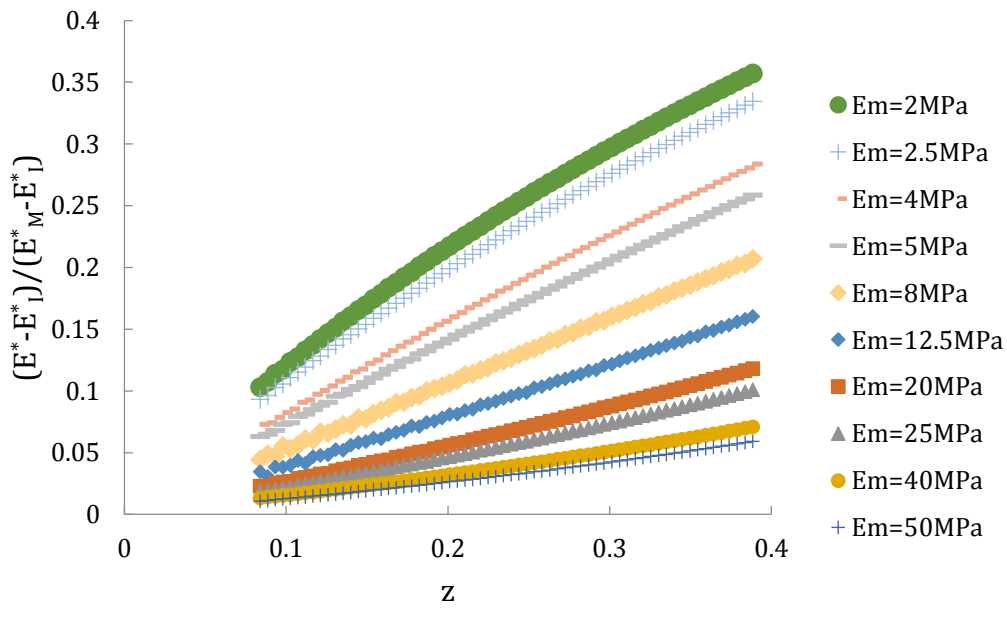


Figure 3.7 (Cont.)

Equation 3.15 has the advantage that the contact area is not included, thus it avoids the influence from the inaccurate determination of the contact area. The calculated composite modulus is a function of the penetration depth, thus it reduces the number of indents. However, it is also very important to note that Equation 3.15 is based on the assumption that the material of the inclusion shares the same time constant as the material of the matrix. In practice, this condition is too strict and limits the application of this equation to materials that present a similar time constant. Alternatively, in order to minimize the influence of the time constant from different materials, the loading rate can be set to be small enough (loading time is at least in an order which is greater than the material time constant). Therefore, the resultant response will be elastic-dominated rather than viscous-dominated.

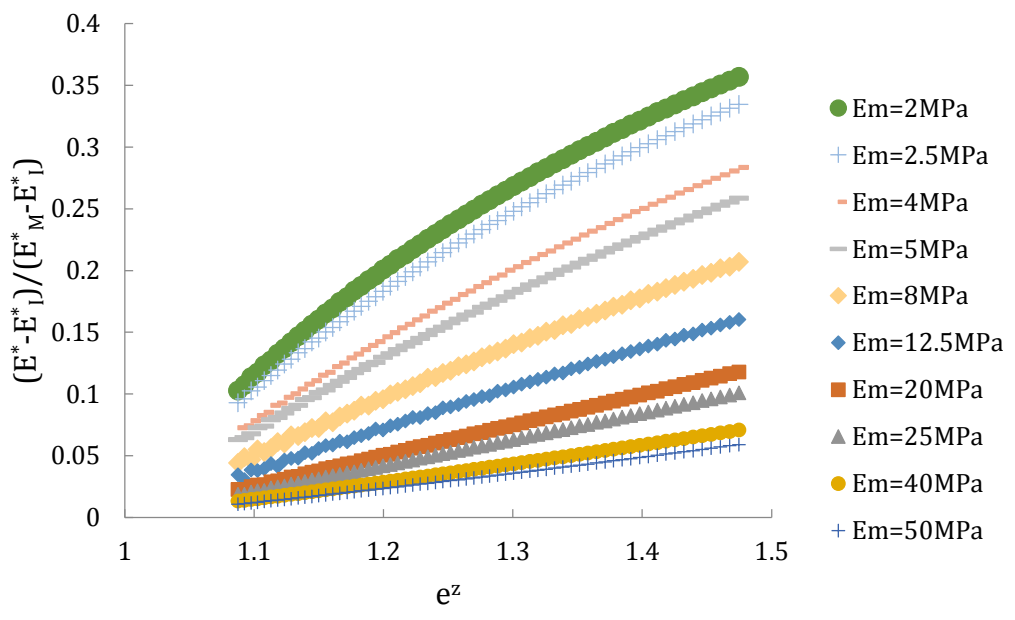
3.3.3 Comparison of the various empirical models

Swapping E_S^* to E_M^* , E_C^* to E_I^* , t to $r_{inclusion}$ in Equation 3.1 and Equations 3.4-3.6 has revealed that Equation 3.1 and Equations 3.4-3.6 are not applicable to describe the nanoindentation response of inclusion/matrix composites as data do not converge to a master curve (as an example, results indented by indenter with θ equals 70.3° and r equals $0.1\text{ }\mu\text{m}$ are shown in Figure 3.8, data indented by other indenters is not shown here). When plotting $\frac{E^* - E_I^*}{E_M^* - E_I^*}$ against z as suggested in the Clifford model (Equation 3.7), the curves converge to a master curve (see Figure 3.9) in nearly all the cases, and only some obvious deviation occurs when the ratio E_I/E_M is approaching one indented with a sharper tip. It demonstrates that Clifford model is also valid for indenting viscoelastic materials by a conical tip. Fitting parameters for the Clifford model are summarised in Table 3.2, and the small *resnorm* value (lower than 0.01) also proved the validity of this model.

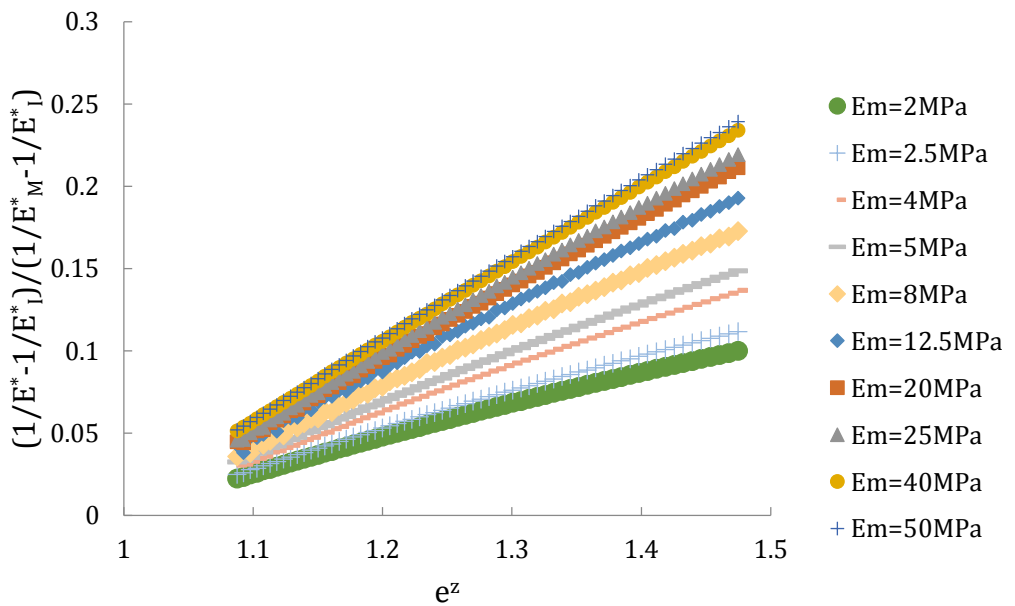


(a)

Figure 3.8 Fit the $E(\text{composite})$ by (a) Equation 3.1, (b) Equation 3.4, (c) Equation 3.5, and (d) Equation 3.6, when the half-included angle of the indenter equals 70.3° , and the tip radius of the indenter equals $0.1\text{ }\mu\text{m}$.

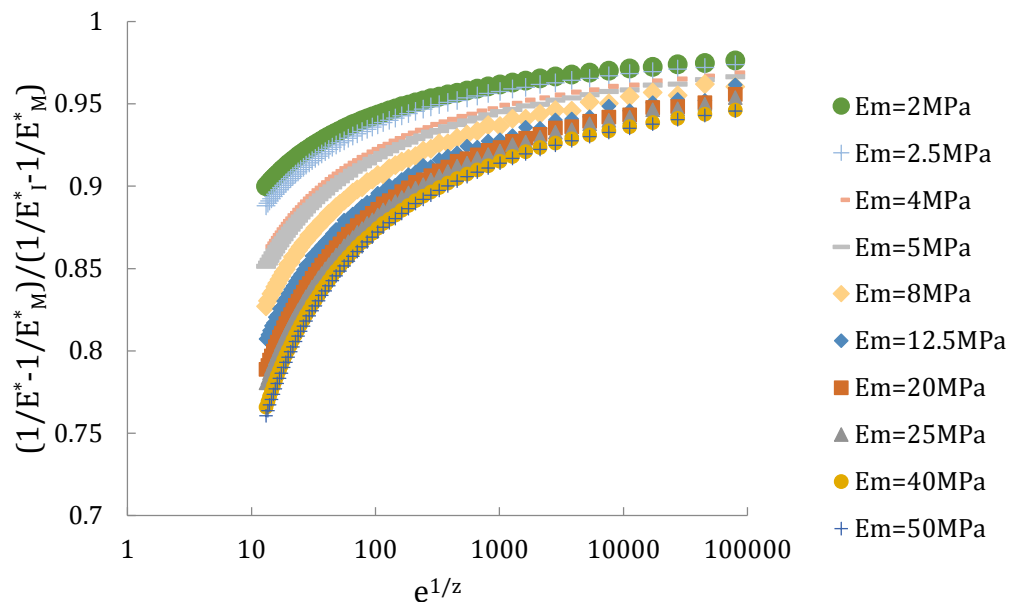


(b)



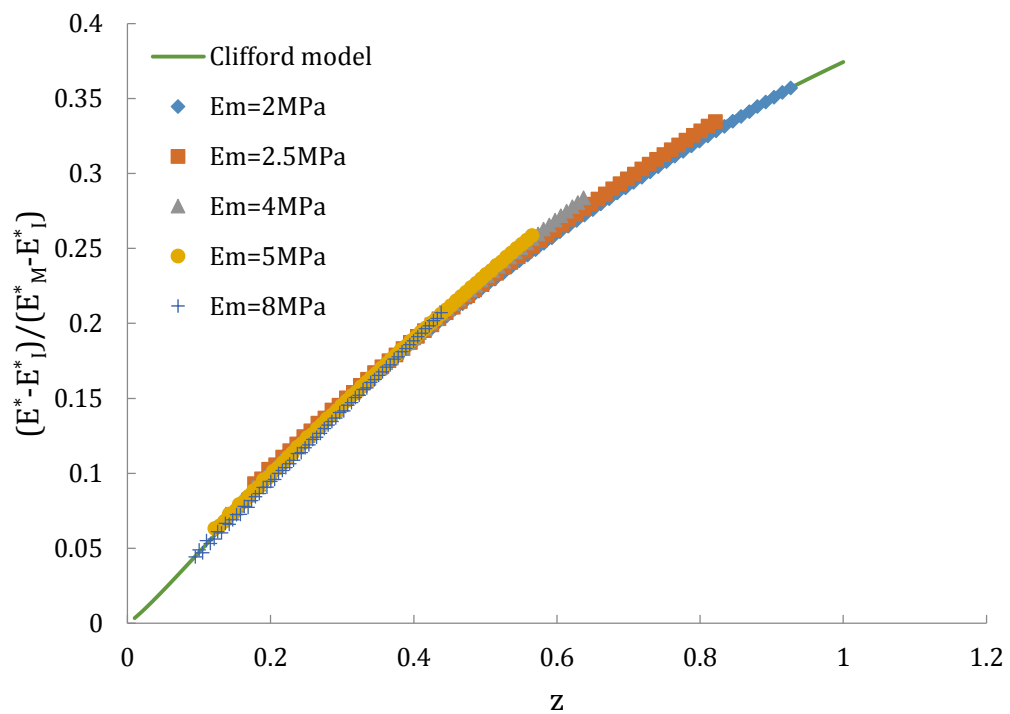
(c)

Figure 3.8 (Cont.)



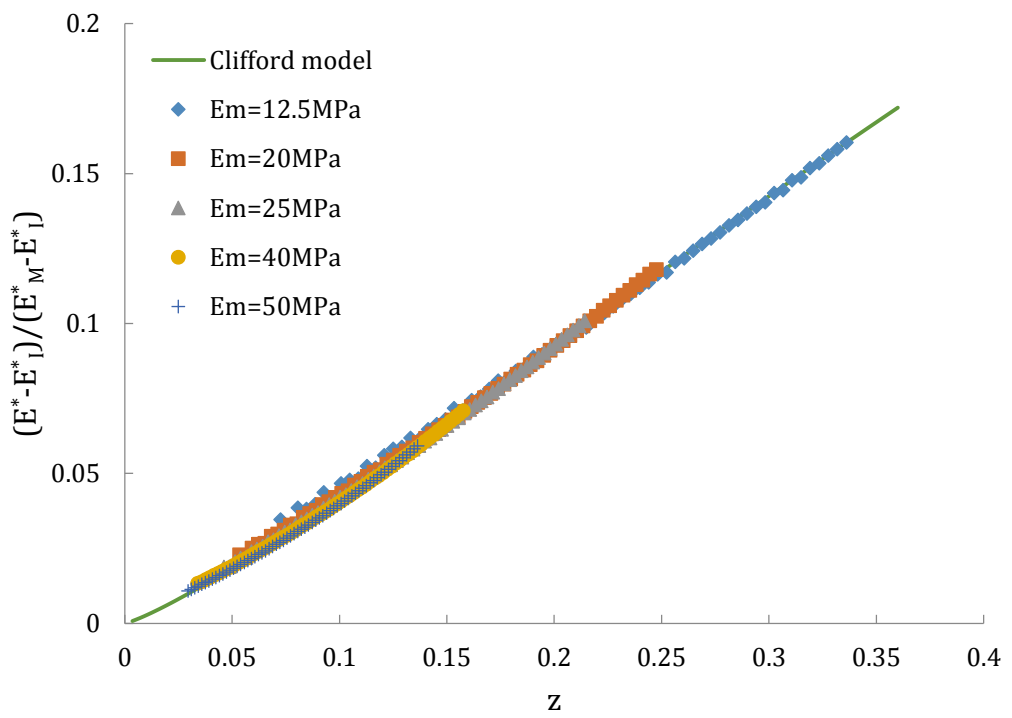
(d)

Figure 3.8 (Cont.)

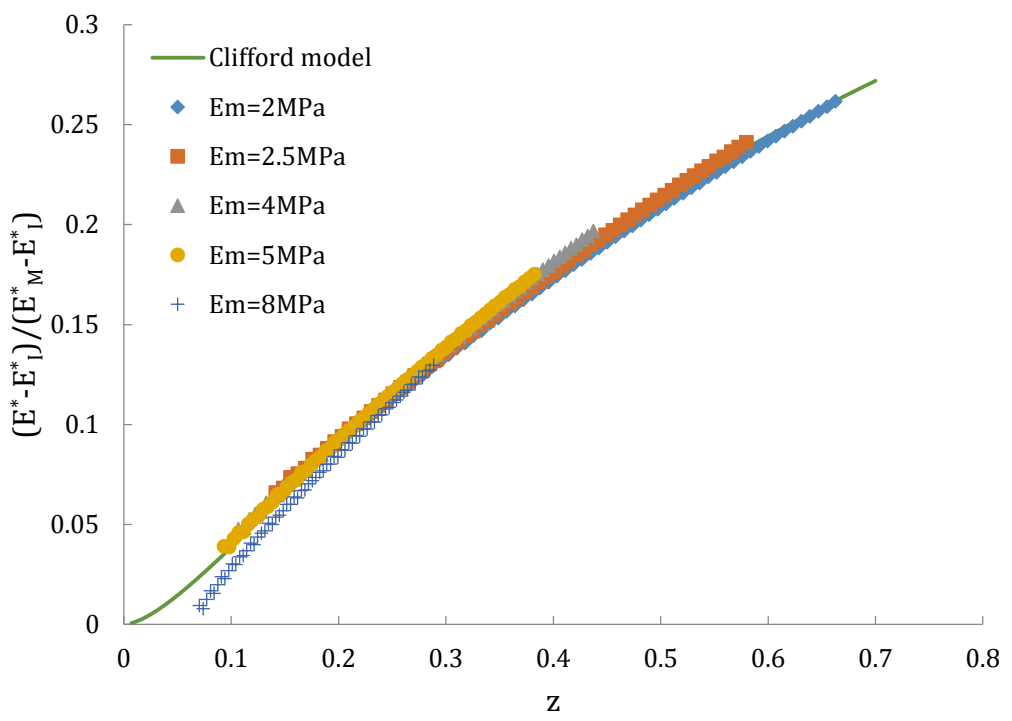


(a)

Figure 3.9 Fit the E (composite) by Clifford model, (a) $\theta = 70.3^\circ$, $r = 0.1 \mu m$, $E_M < E_I$, (b) $\theta = 70.3^\circ$, $r = 0.1 \mu m$, $E_M > E_I$, (c) $\theta = 60^\circ$, $r = 0.1 \mu m$, $E_M < E_I$, (d) $\theta = 60^\circ$, $r = 0.1 \mu m$, $E_M > E_I$, (e) $\theta = 70.3^\circ$, $r = 0.01 \mu m$, $E_M < E_I$, and (f) $\theta = 70.3^\circ$, $r = 0.01 \mu m$, $E_M > E_I$.

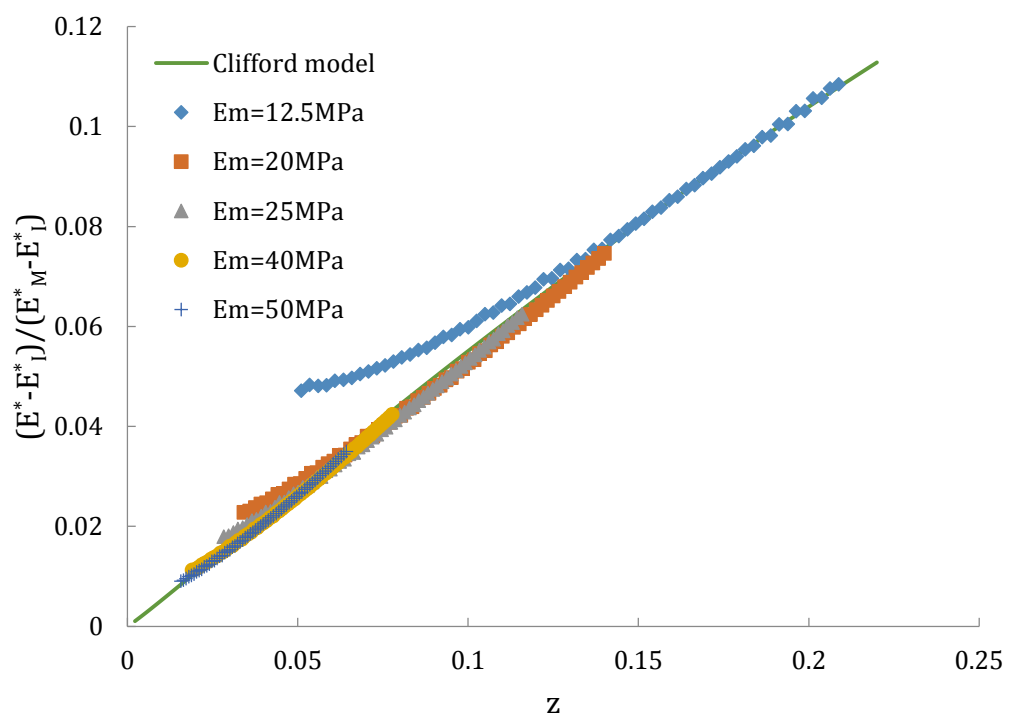


(b)

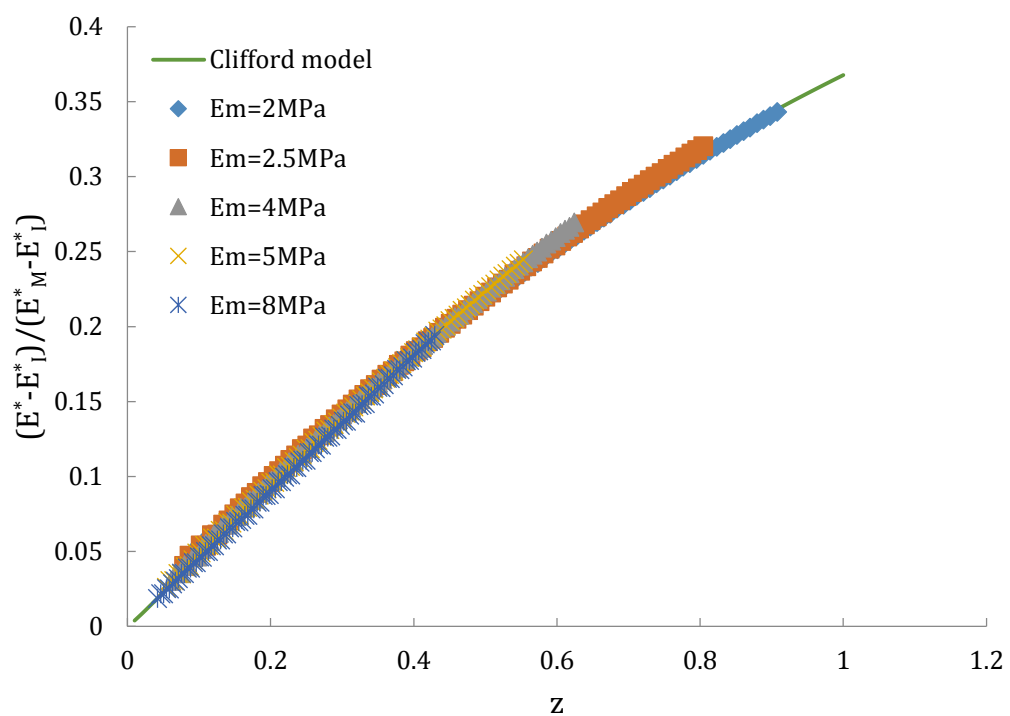


(c)

Figure 3.9 (Cont.)



(d)



(e)

Figure 3.9 (Cont.)

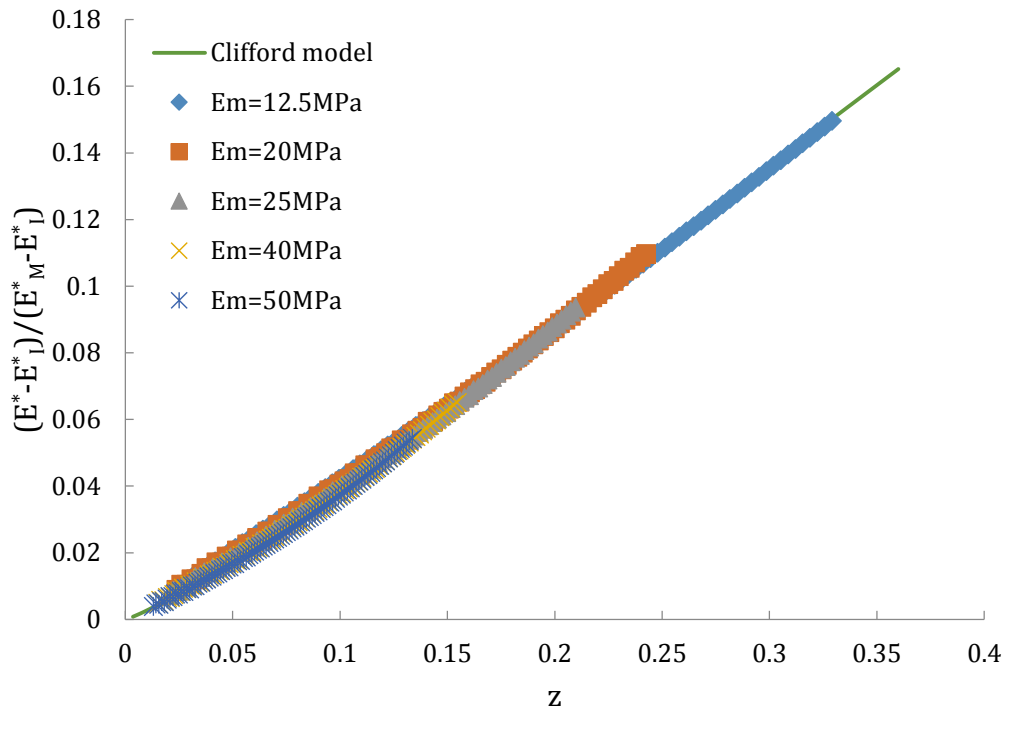


Figure 3.9 (Cont.)

	Indenter	b	P	Q	n	resnorm
Clifford model (Equation 3.7)	$\theta = 70.3^\circ$ $E_M < E_I$	0.54	0.753	0.259	1.169	0.0028
	$r = 0.1 \mu m$ $E_M > E_I$	0.65	0.697	-0.057	1.206	0.0006
	$\theta = 60^\circ$ $E_M < E_I$	0.60	2.677	4.212	1.671	0.0059
	$r = 0.1 \mu m$ $E_M > E_I$	0.85	0.717	0.550	1.066	0.0037
	$\theta = 70.3^\circ$ $E_M < E_I$	0.54	0.629	0.082	1.100	0.0035
	$r = 0.01 \mu m$ $E_M > E_I$	0.65	0.609	-0.215	1.179	0.0009

Table 3.2 Fitting parameters for the Clifford model.

However, it is found that the weighting factor b in Equation 3.8 is not a universal constant as commented by Clifford *et al.*, after they investigated the inclusion/matrix composite indented by a spherical tip. Instead, as suggested in Table 3.2, the parameter b depends on the indenter geometry, and relative stiffness between the inclusion and the matrix, while the parameter b is independent of the tip radius of the indenter.

3.3.4 Alternative models

It is noticed that one of the major differences between Clifford's model and other models lies in the selection of parameter z instead of x . Therefore, in this way, it is proposed to modify Equation 3.1 and Equations 3.4-3.6 by replacing x with z . In such case, the following equations are obtained,

$$\frac{E^* - E_I^*}{E_M^* - E_I^*} = B_5 \cdot z \quad (3.16)$$

$$\frac{E^* - E_I^*}{E_M^* - E_I^*} = e^{B_6 \cdot z} \quad (3.17)$$

$$\frac{1/E^* - 1/E_I^*}{1/E_M^* - 1/E_I^*} = e^{B_7 \cdot z} \quad (3.18)$$

$$\frac{1/E^* - 1/E_M^*}{1/E_I^* - 1/E_M^*} = e^{\frac{B_8}{z}} \quad (3.19)$$

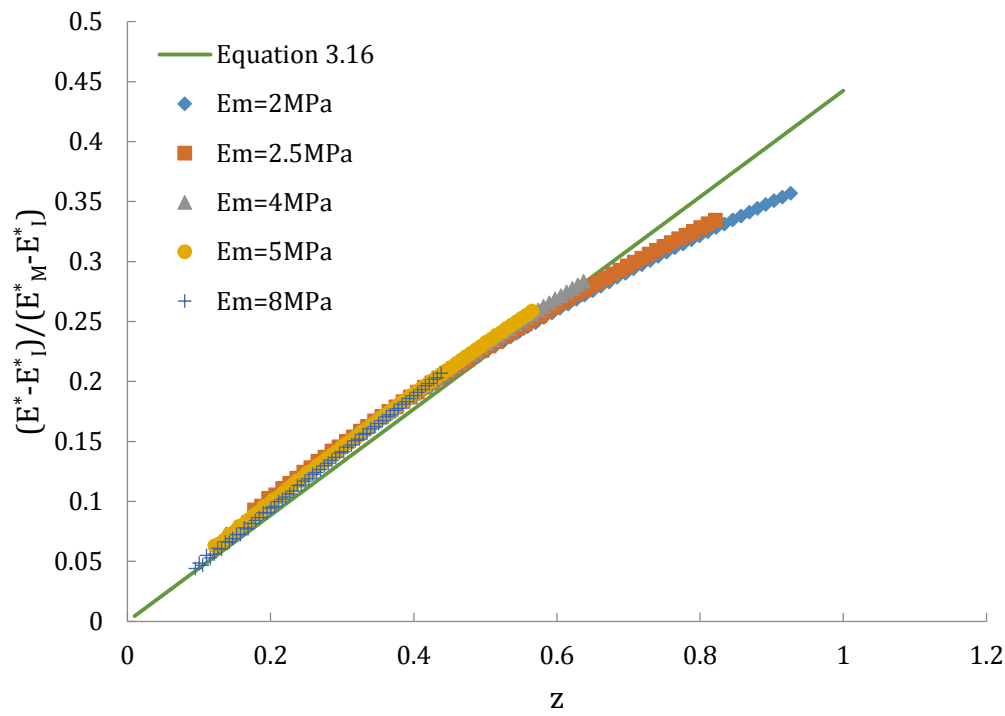
where the B with different subscripts are the fitting constants in each equation.

Figures 3.10-3.13 show the composite elastic modulus fitted with Equations 3.16-3.19. Clearly, the models have been significantly improved as all the data are on the master curve after replacing x with z , although some deviation still exists when the ratio E_I/E_M is approaching one for a sharper tip. Compared to x , z considers the elastic mismatch between the inclusion and the matrix by introducing a power law index b . The comparison of fitting parameter b for Equations 3.16-3.19 is summarized in Table 3.3. For Equation 3.16 and Equation 3.17, when E_M is smaller than E_I , the value of b equals 0.54 and 0.60 for indenters with the half-included angle of 70.3° and 60°, respectively. When the value of E_M is higher than E_I , the value of b equals 0.65 and 0.85 for indenter with the half-included angle of 70.3° and 60°, respectively. For the reciprocal equations (Equation 3.18 and Equation 3.19), when the value of E_M is smaller than E_I , the value of b equals -0.36 and -0.34 for indenters with the half-included angle of 70.3° and 60°, respectively. When the value of E_M is greater than E_I , the value of b equals -0.14 and -0.11 for indenters with the half-included angle of 70.3° and 60°, respectively. In addition, the value of b is identical when indented by

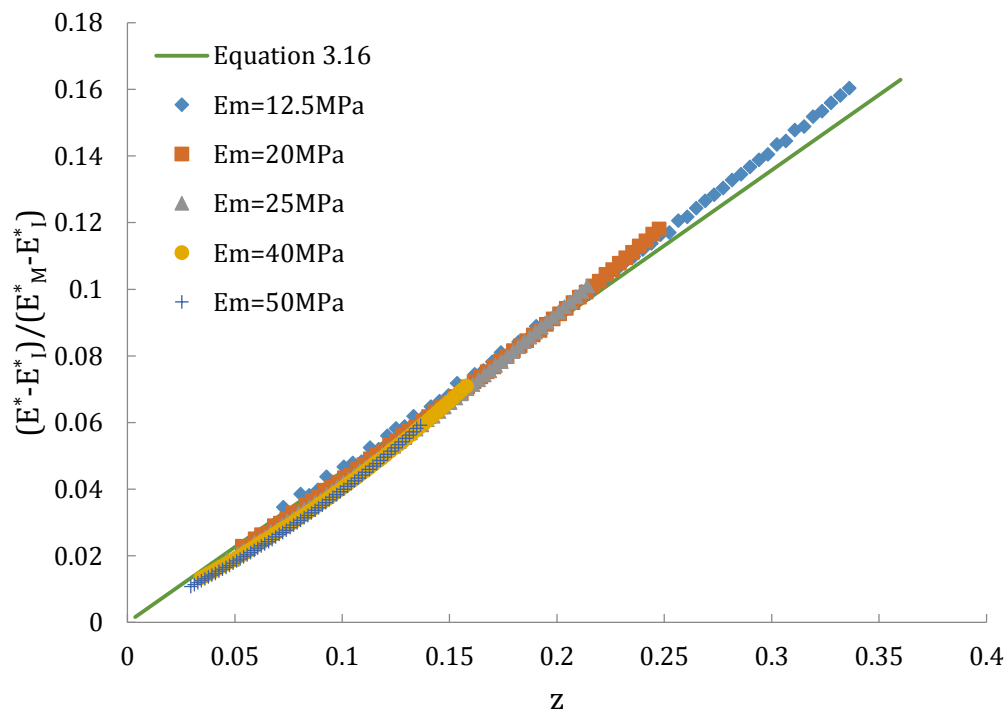
indenters with same half-included angle but different tip radius. It reveals that the value of b is not affected by the tip radius of the indenter, and it may be more dependent on the expression of the left hand side of the equation and the half-included angle of the indenter. On the other hand, Figures 3.11-3.13 reveal that Equations 3.17-3.19 are invalid to fit the data, because for Equation 3.17 and Equation 3.18, these exponential equations violate the initial boundary condition (namely, when z is approaching zero, $E^* - E_I^*$ or $1/E^* - 1/E_I^*$ should be zero). This means when the deformation is infinitely small, the indenter only measures the elastic modulus of the inclusion and the apparent composite modulus should be that of the inclusion. For Equation 3.19 (see Figure 3.13), the expression of the x -axis covers a wide range which makes the data non-sensitive to the equation. It also needs to be pointed out that it is not recommended to add more fitting constants to the above equations to artificially improve the quality of curve fitting. Since it will reduce the fitting efficiency.

Indenter	Clifford model	Equation	Equation	Equation	Equation
	(Equation 3.7)	3.16	3.17	3.18	3.19
$\theta = 70.3^\circ$	$E_M < E_I$	0.54	0.54	0.54	-0.36
$r = 0.1 \mu m$	$E_M > E_I$	0.65	0.65	0.65	-0.14
$\theta = 60^\circ$	$E_M < E_I$	0.60	0.60	0.60	-0.34
$r = 0.1 \mu m$	$E_M > E_I$	0.85	0.85	0.85	-0.11
$\theta = 70.3^\circ$	$E_M < E_I$	0.54	0.54	0.54	-0.36
$r = 0.01 \mu m$	$E_M > E_I$	0.65	0.65	0.65	-0.14

Table 3.3 Comparison of fitting parameter b for various equations.

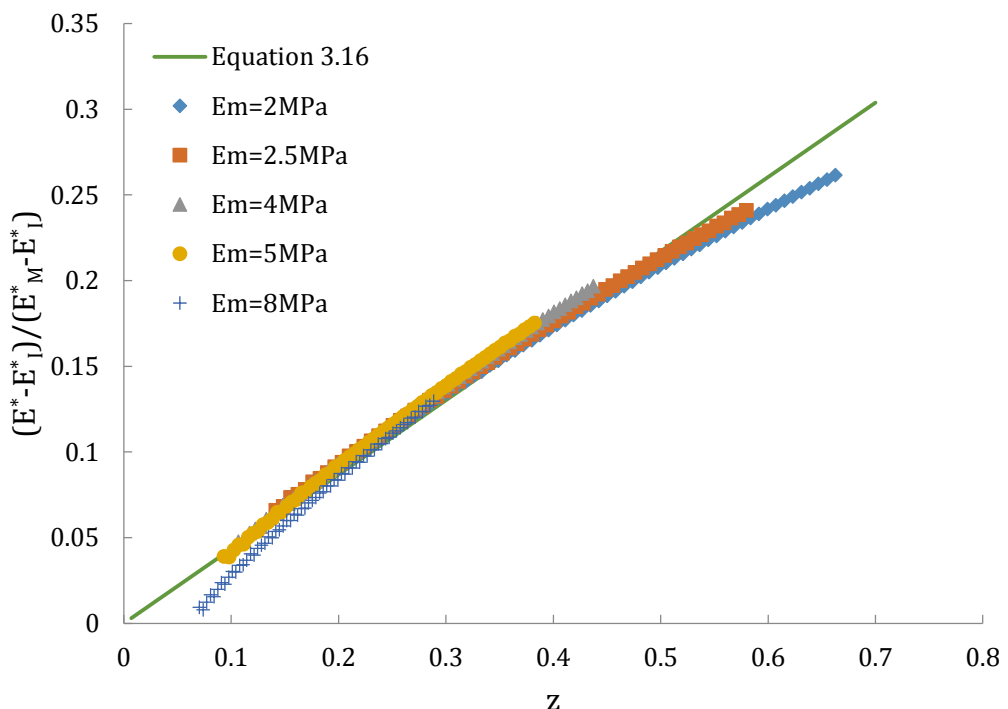


(a)

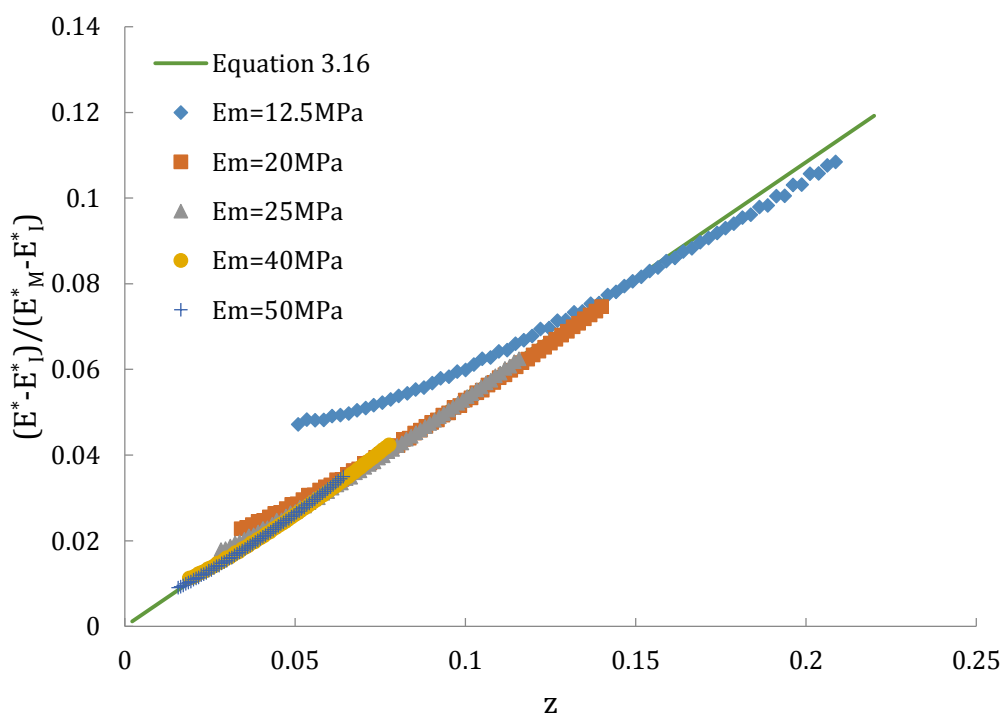


(b)

Figure 3.10 Plot the E (composite) using modified Equation 3.16, (a) $\theta = 70.3^\circ$, $r = 0.1 \mu\text{m}$, $E_M < E_I$, (b) $\theta = 70.3^\circ$, $r = 0.1 \mu\text{m}$, $E_M > E_I$, (c) $\theta = 60^\circ$, $r = 0.1 \mu\text{m}$, $E_M < E_I$, (d) $\theta = 60^\circ$, $r = 0.1 \mu\text{m}$, $E_M > E_I$, (e) $\theta = 70.3^\circ$, $r = 0.01 \mu\text{m}$, $E_M < E_I$, and (f) $\theta = 70.3^\circ$, $r = 0.01 \mu\text{m}$, $E_M > E_I$.

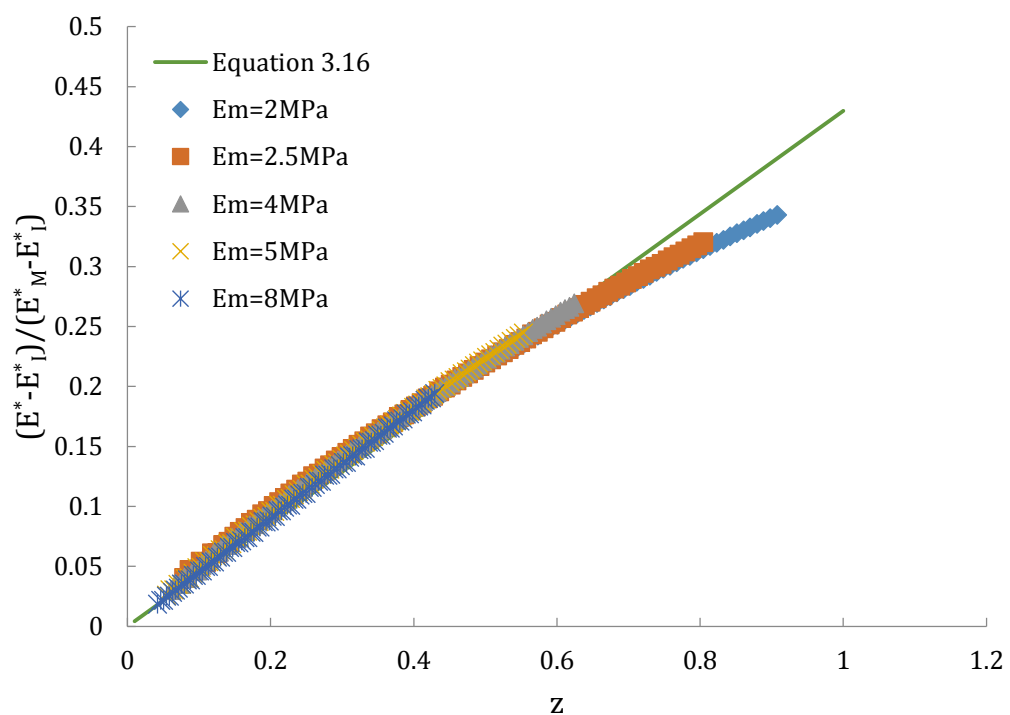


(c)

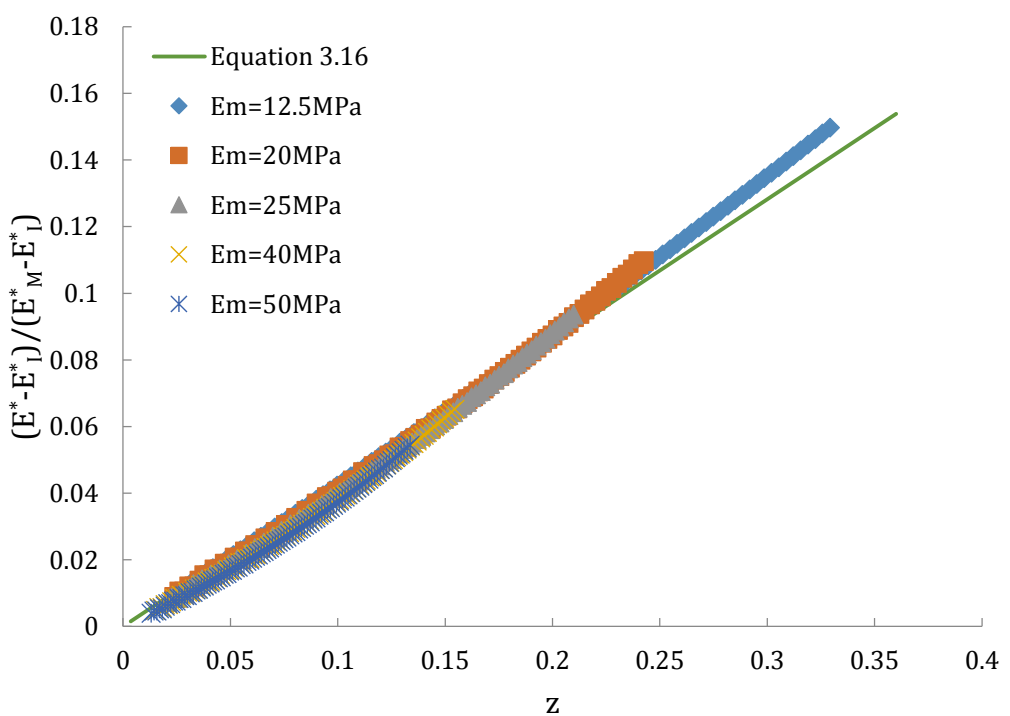


(d)

Figure 3.10 (Cont.)

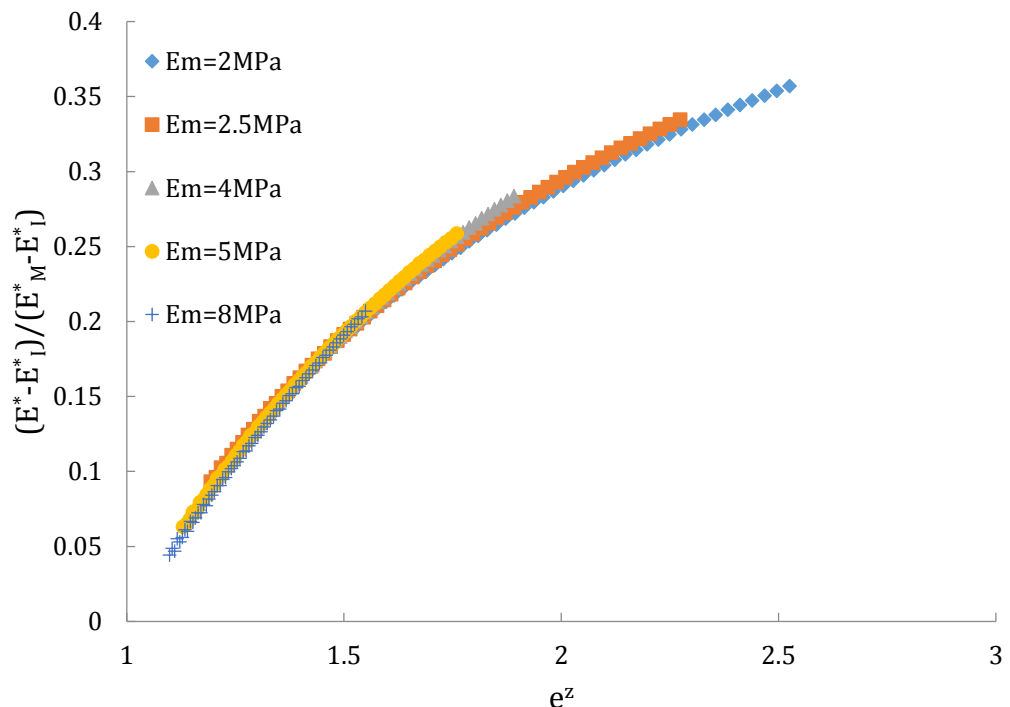


(e)

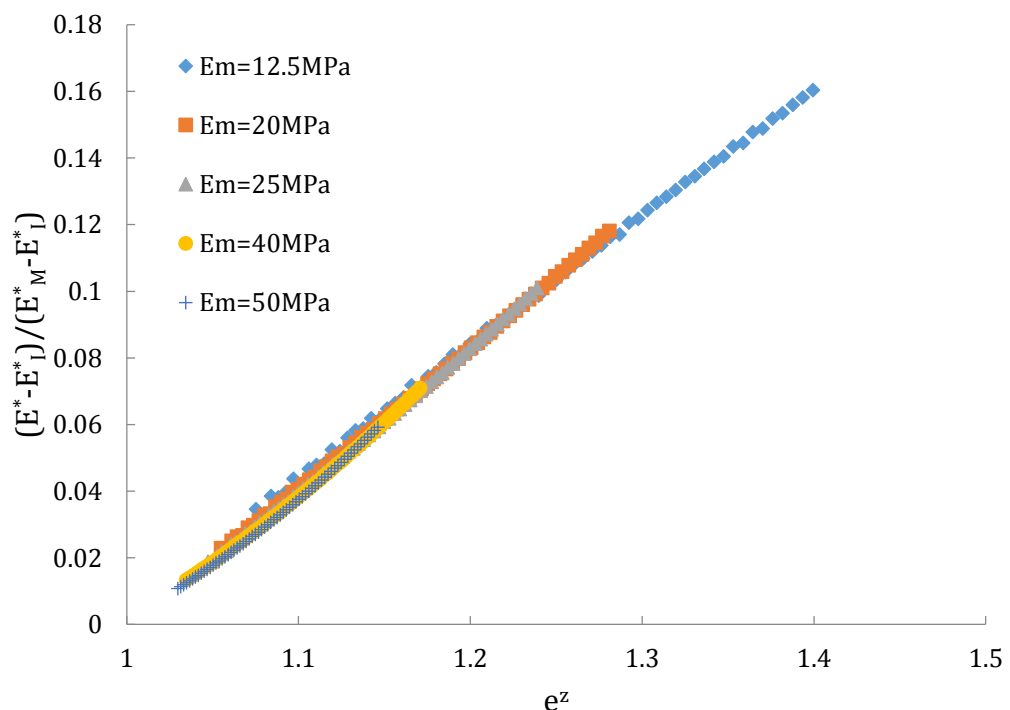


(f)

Figure 3.10 (Cont.)

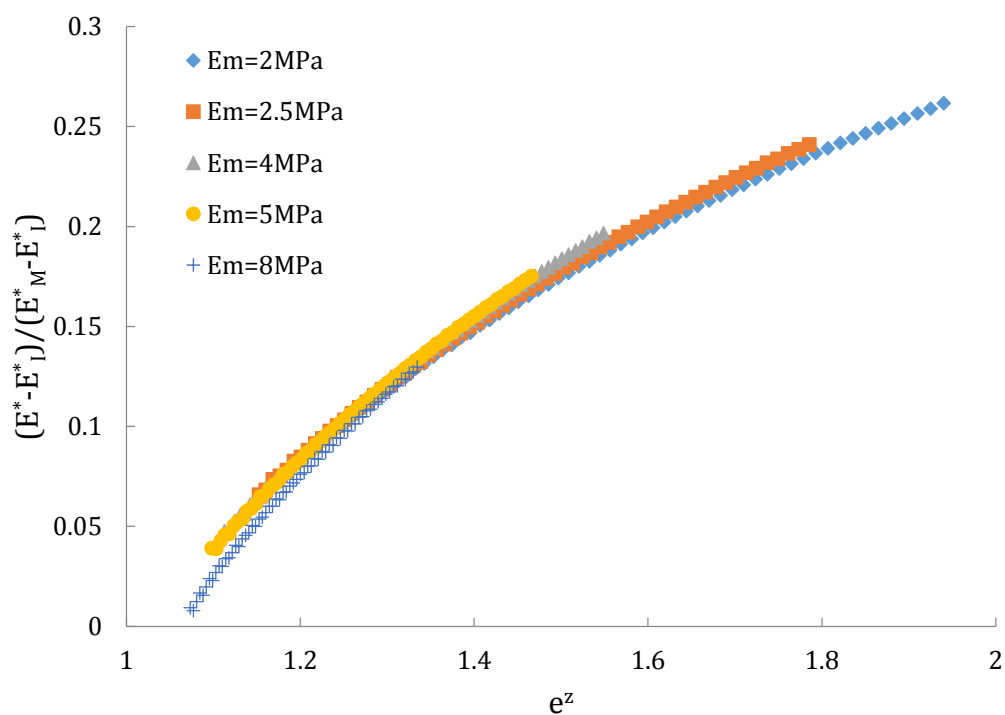


(a)

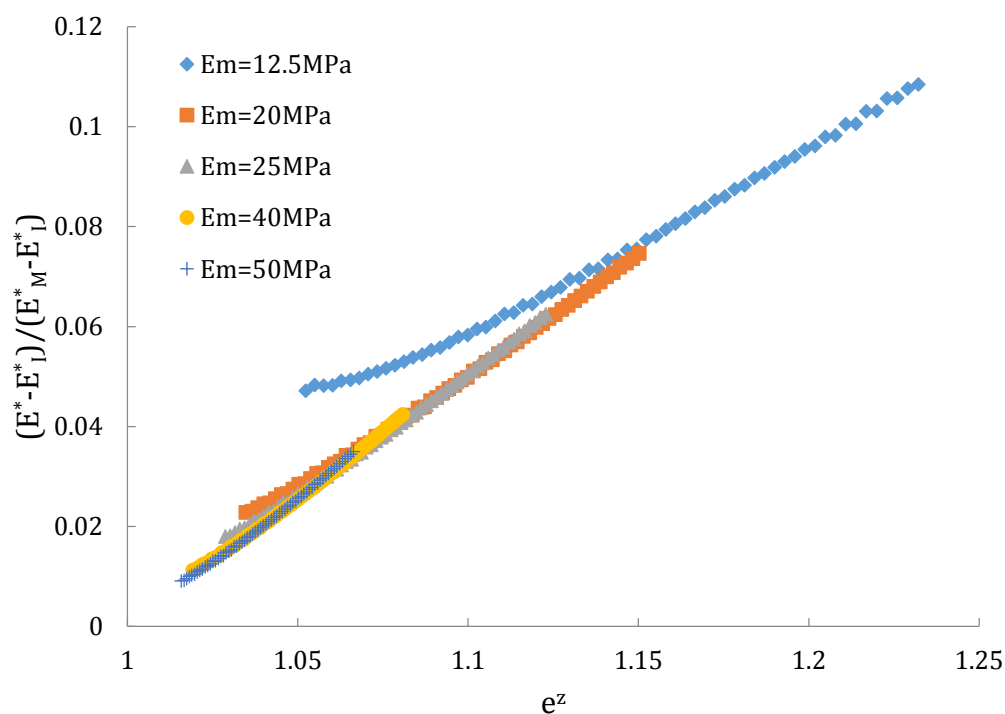


(b)

Figure 3.11 Plot the E (composite) using modified Equation 3.17, (a) $\theta = 70.3^\circ$, $r = 0.1 \mu\text{m}$, $E_M < E_I$, (b) $\theta = 70.3^\circ$, $r = 0.1 \mu\text{m}$, $E_M > E_I$, (c) $\theta = 60^\circ$, $r = 0.1 \mu\text{m}$, $E_M < E_I$, (d) $\theta = 60^\circ$, $r = 0.1 \mu\text{m}$, $E_M > E_I$, (e) $\theta = 70.3^\circ$, $r = 0.01 \mu\text{m}$, $E_M < E_I$, and (f) $\theta = 70.3^\circ$, $r = 0.01 \mu\text{m}$, $E_M > E_I$.

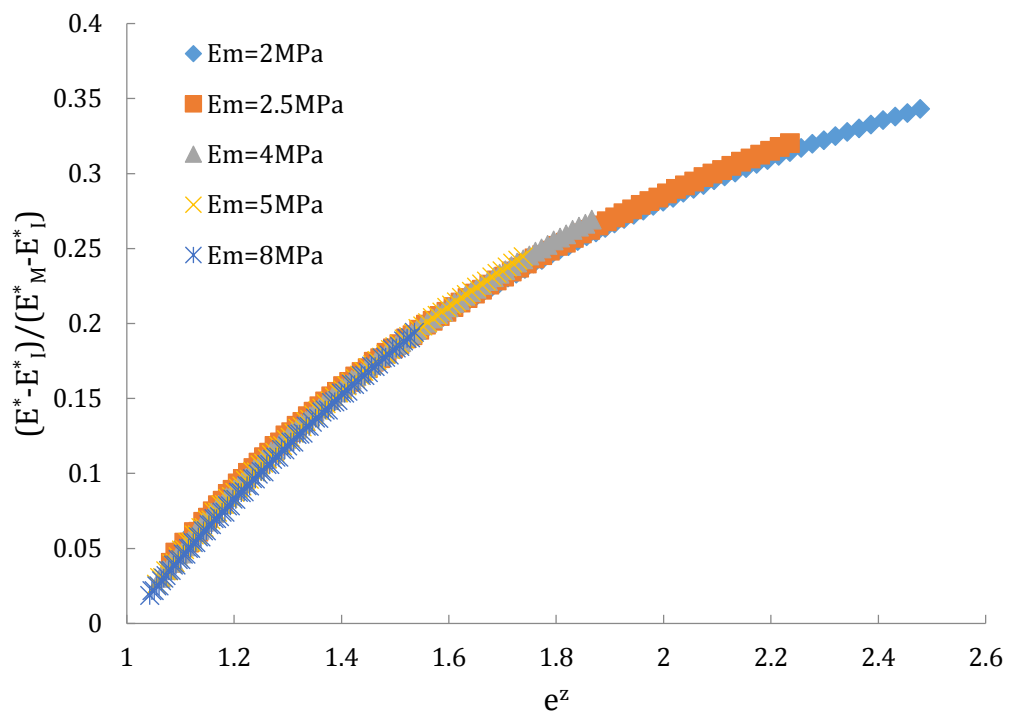


(c)

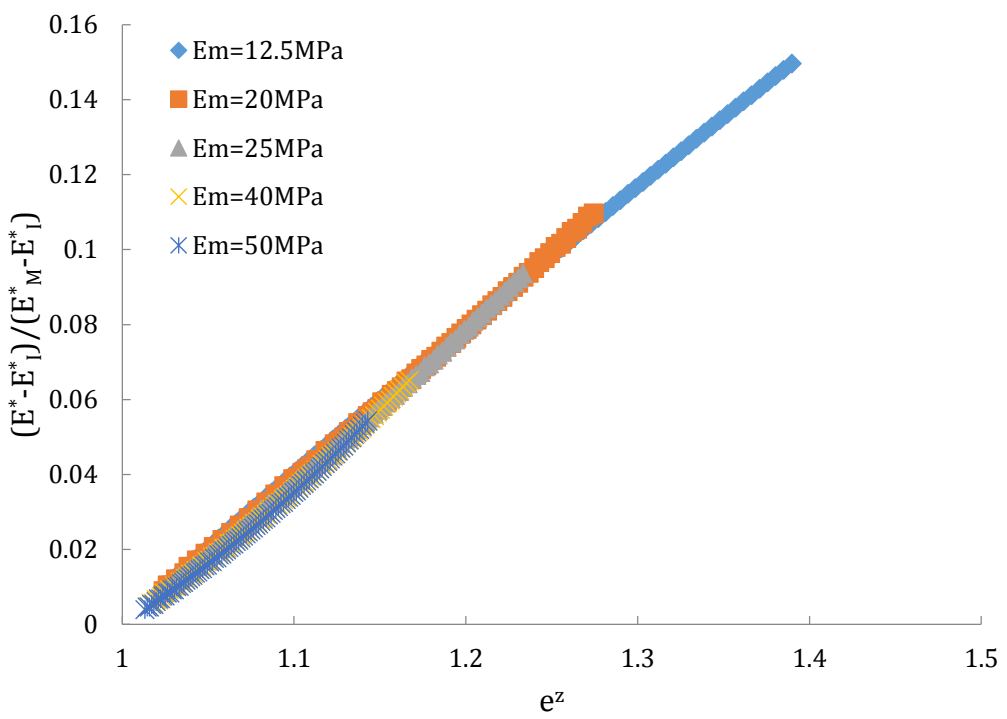


(d)

Figure 3.11 (Cont.)

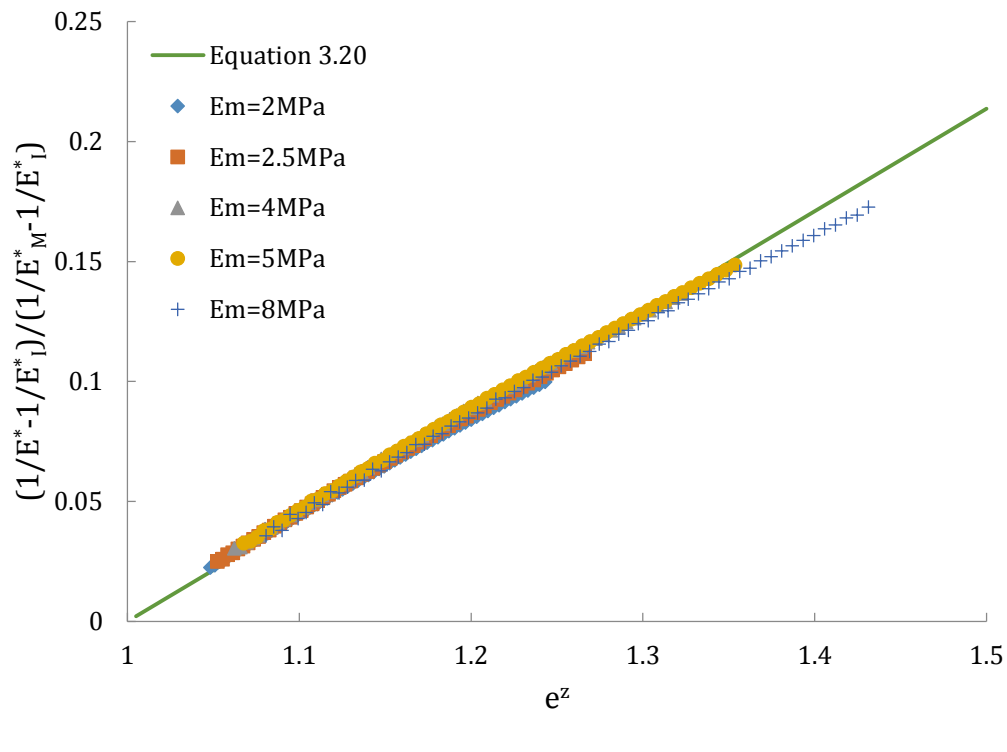


(e)

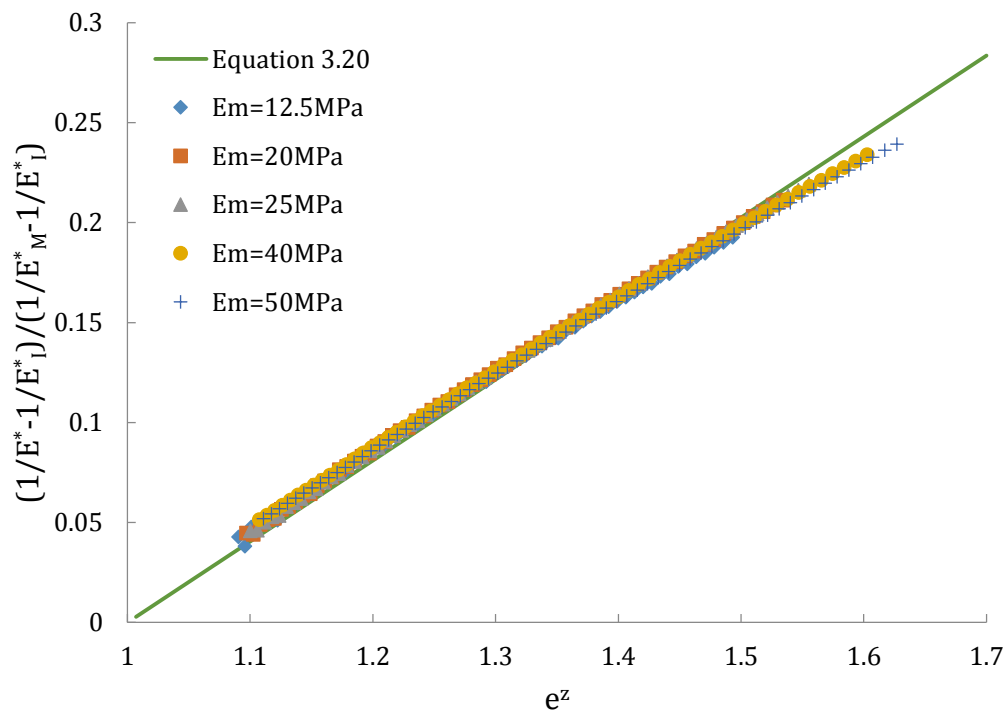


(f)

Figure 3.11 (Cont.)

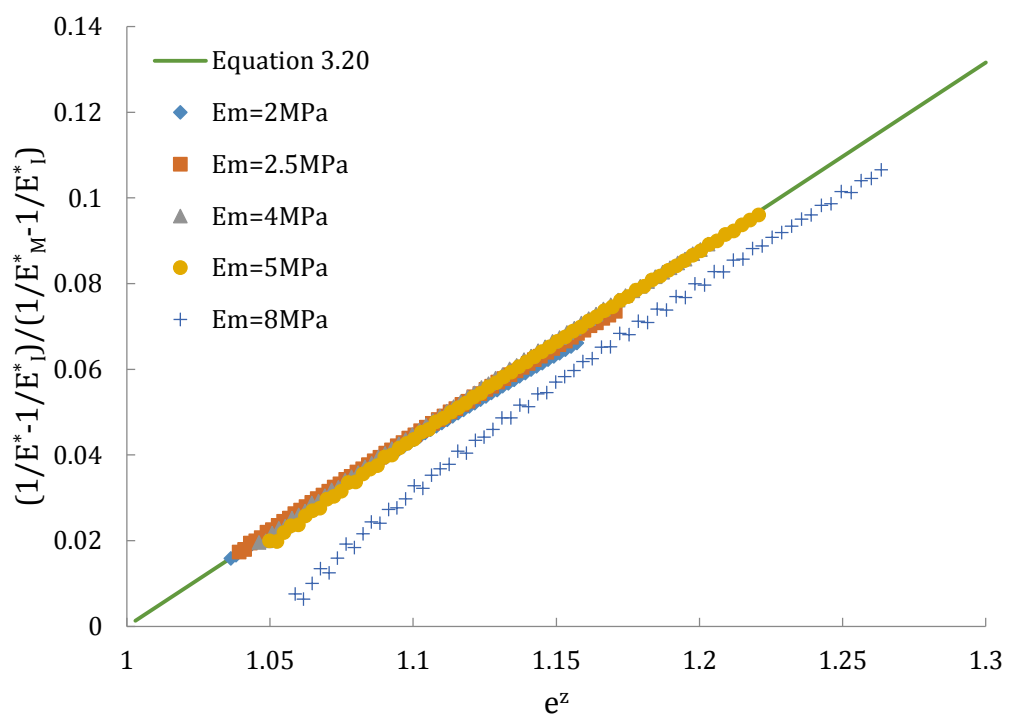


(a)

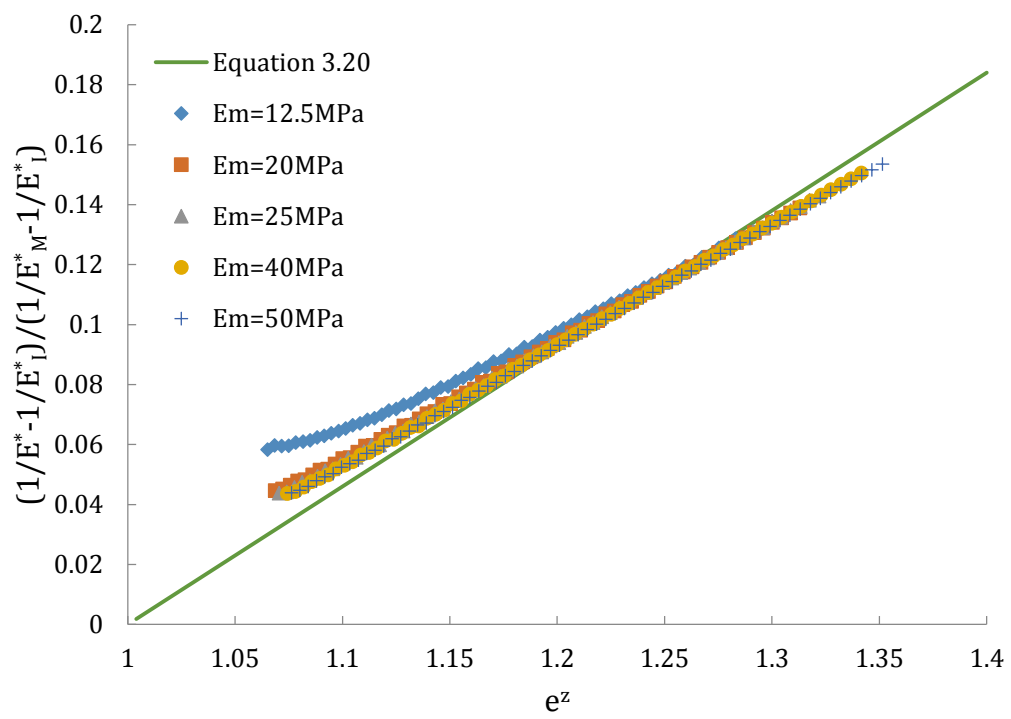


(b)

Figure 3.12 Plot the $E(\text{composite})$ using modified Equation 3.18 and Equation 3.20, (a) $\theta = 70.3^\circ$, $r = 0.1 \mu\text{m}$, $E_M < E_I$, (b) $\theta = 70.3^\circ$, $r = 0.1 \mu\text{m}$, $E_M > E_I$, (c) $\theta = 60^\circ$, $r = 0.1 \mu\text{m}$, $E_M < E_I$, (d) $\theta = 60^\circ$, $r = 0.1 \mu\text{m}$, $E_M > E_I$, (e) $\theta = 70.3^\circ$, $r = 0.01 \mu\text{m}$, $E_M < E_I$, and (f) $\theta = 70.3^\circ$, $r = 0.01 \mu\text{m}$, $E_M > E_I$.

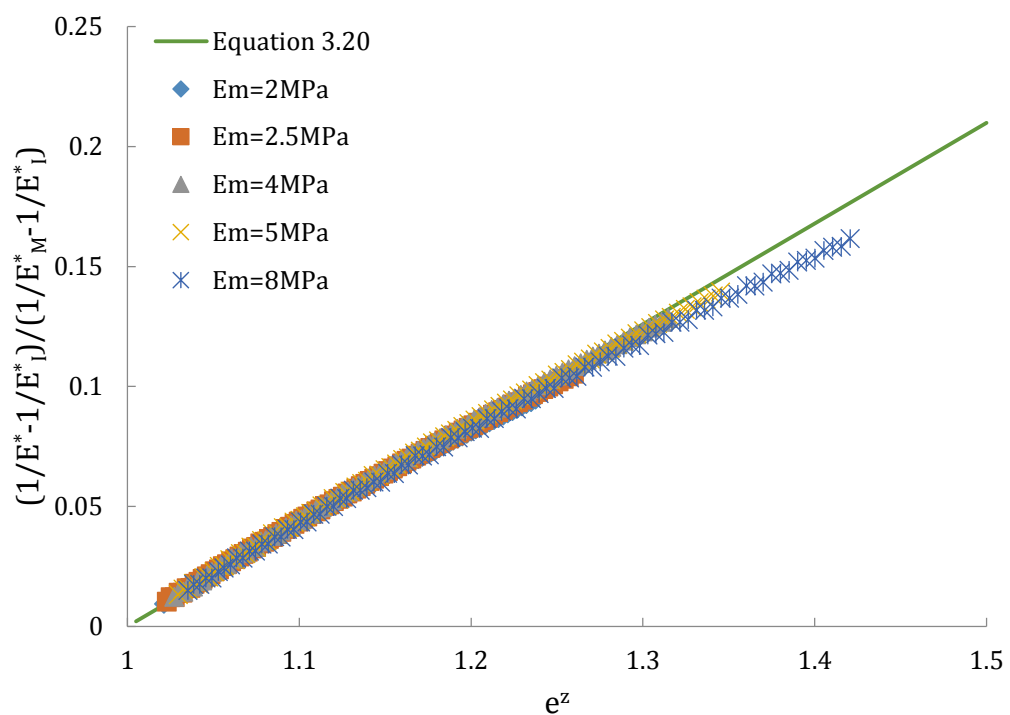


(c)

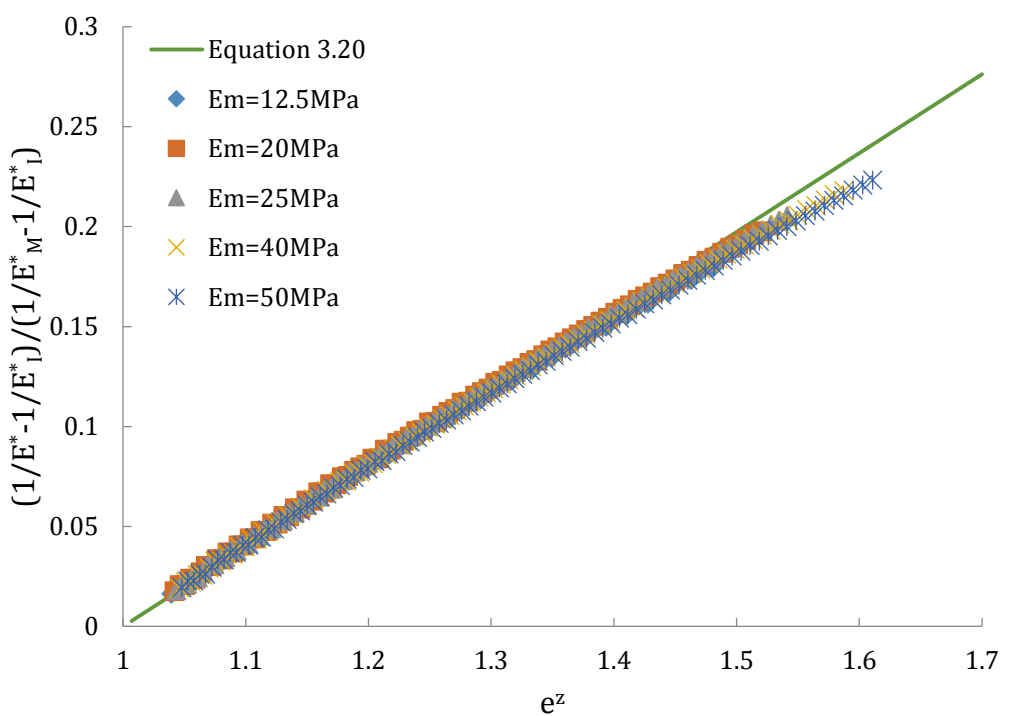


(d)

Figure 3.12 (Cont.)

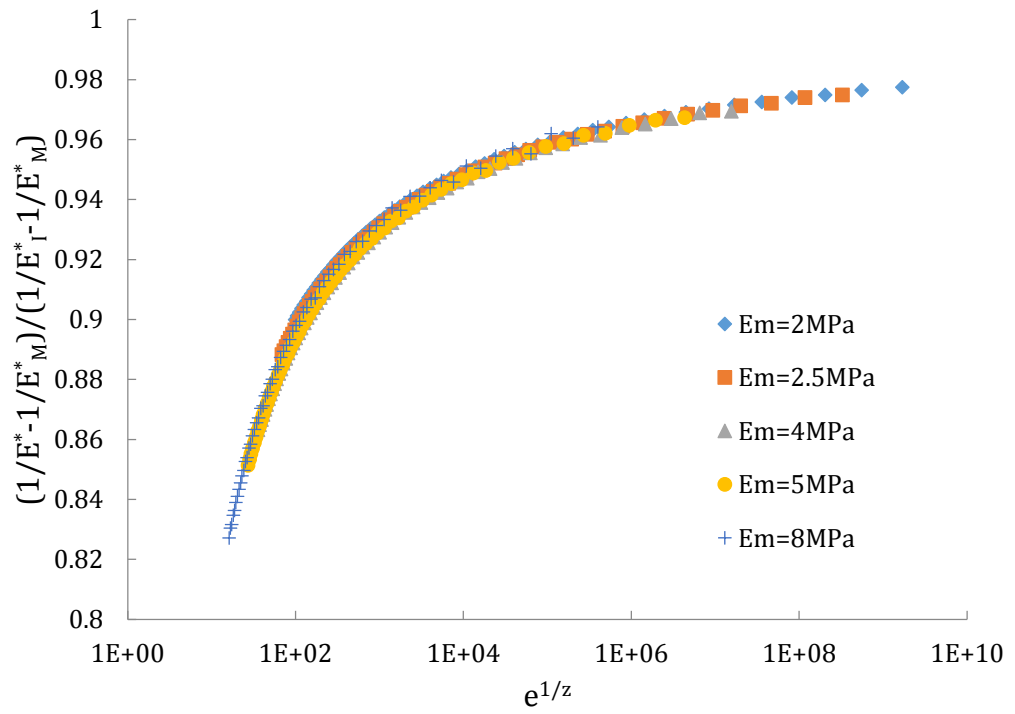


(e)

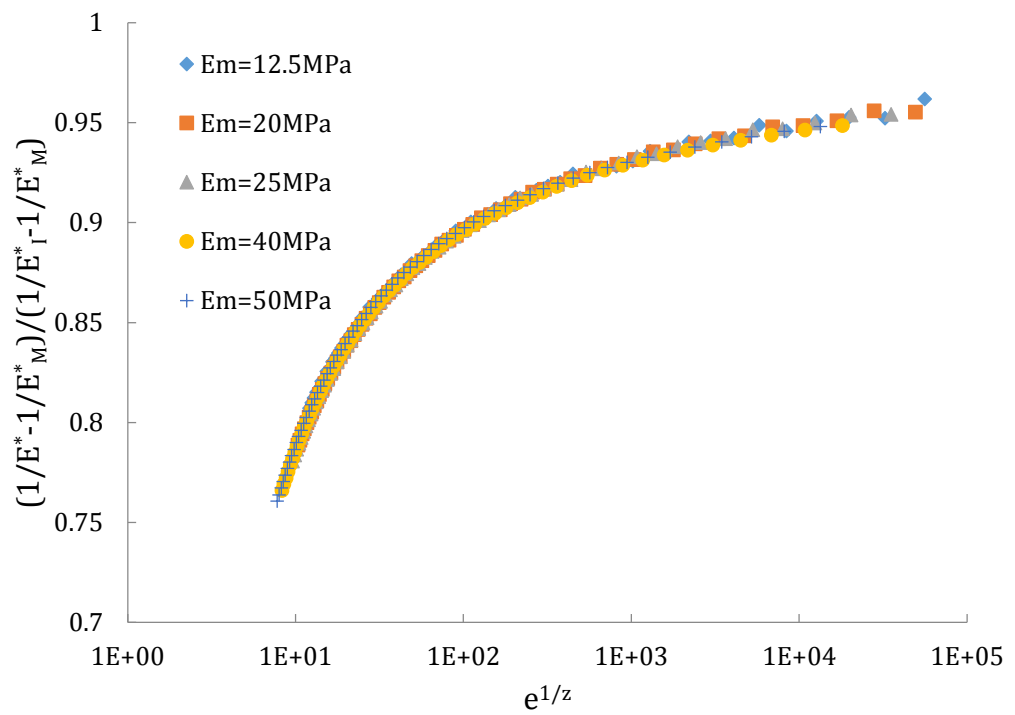


(f)

Figure 3.12 (Cont.)

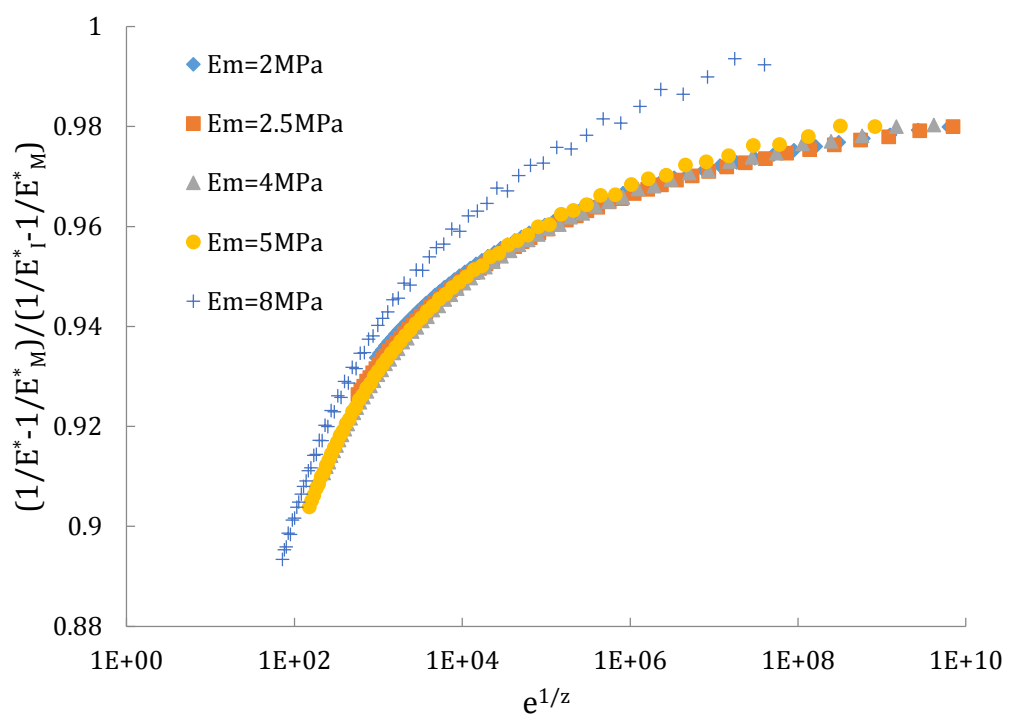


(a)

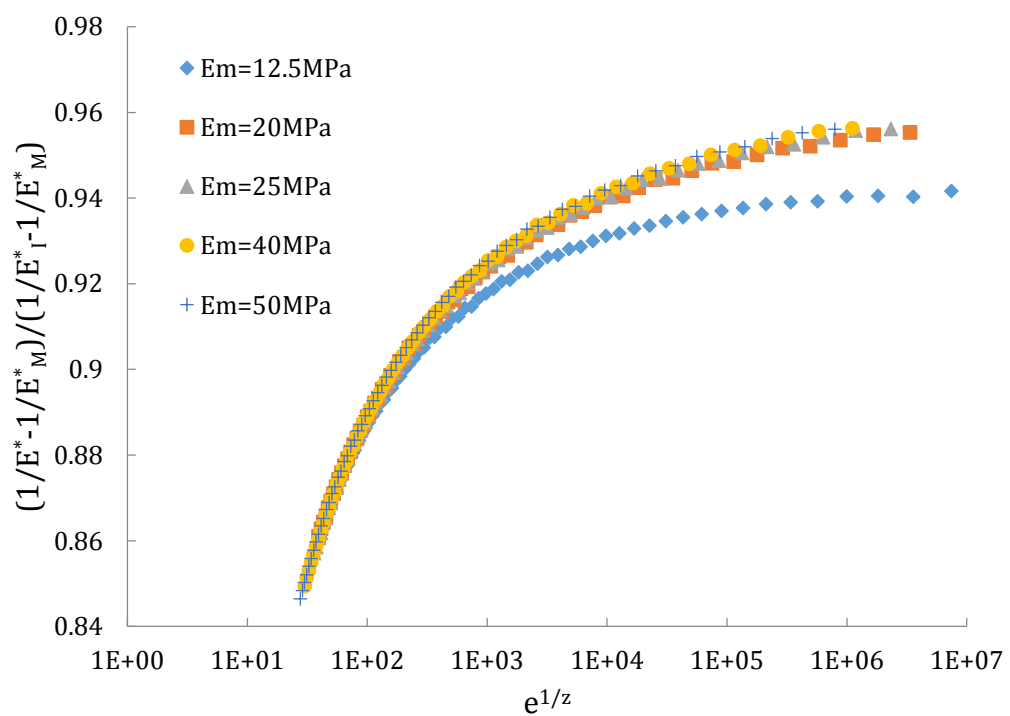


(b)

Figure 3.13 Plot the $E(\text{composite})$ using modified Equation 3.19, (a) $\theta = 70.3^\circ$, $r = 0.1 \mu\text{m}$, $E_M < E_I$, (b) $\theta = 70.3^\circ$, $r = 0.1 \mu\text{m}$, $E_M > E_I$, (c) $\theta = 60^\circ$, $r = 0.1 \mu\text{m}$, $E_M < E_I$, (d) $\theta = 60^\circ$, $r = 0.1 \mu\text{m}$, $E_M > E_I$, (e) $\theta = 70.3^\circ$, $r = 0.01 \mu\text{m}$, $E_M < E_I$, and (f) $\theta = 70.3^\circ$, $r = 0.01 \mu\text{m}$, $E_M > E_I$.

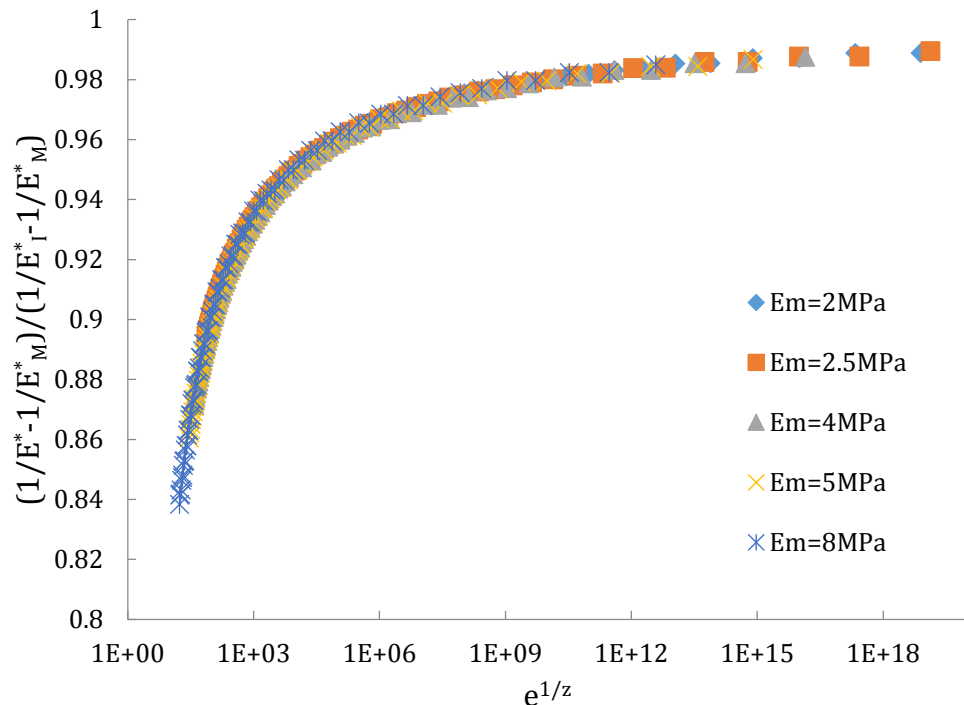


(c)

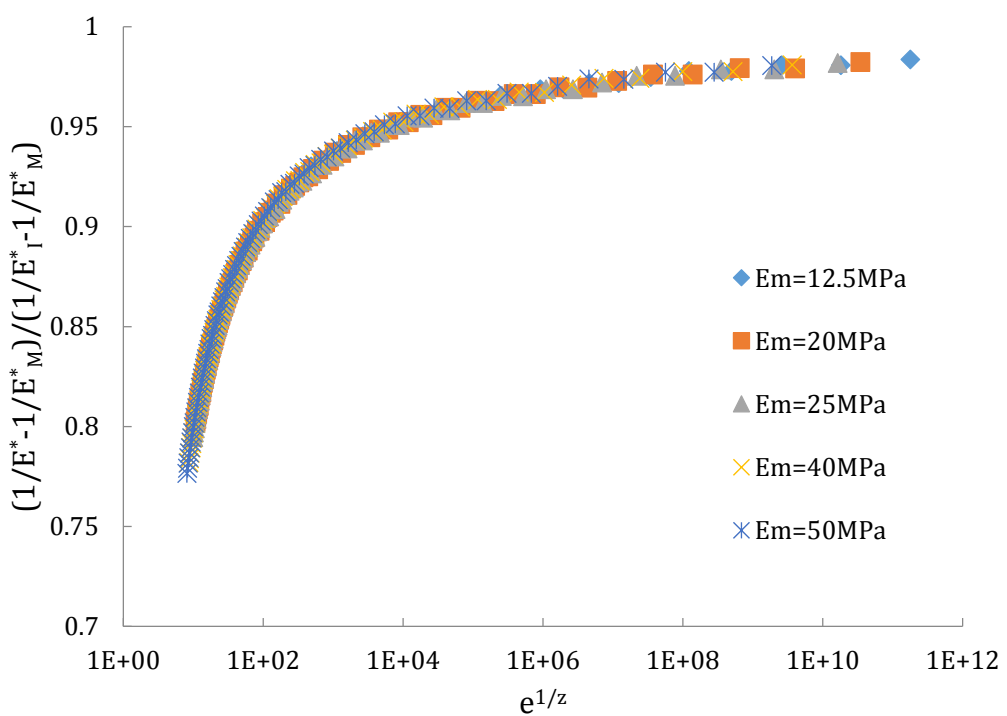


(d)

Figure 3.13 (Cont.)



(e)



(f)

Figure 3.13 (Cont.)

When Equation 3.16 is adopted, similar to the Clifford model, the simulated results converge to a master curve with some deviation for a sharper tip when E_I is approaching E_M (see Figure 3.10). It seems that the linear model shows better performance to describe the trend than other models. From Figure 3.9, Equation

3.16 works as well as the Clifford model. The fitting parameters for Equation 3.16 are provided in Table 3.4. It can be seen that, when the value of E_M is smaller than E_I , the value of B remains almost the same (approximately 0.43~0.44) in all cases. When the value of E_M is greater than E_I , the value of $resnorm$ is relatively closer to zero, the change of the tip radius may negligibly affect the value of B . The value of b is increasing significantly when the half angle θ decreases from 70.3° to 60° . It also seems that the value of b in Equation 3.16 is not sensitive to the tip radius when the tip radius is below 50% of the maximum penetration.

	Indenter		b	B	resnorm
Linear model (Equation 3.16)	$\theta = 70.3^\circ$	$E_M < E_I$	0.54	0.442	0.0660
	$r = 0.1\mu m$	$E_M > E_I$	0.65	0.452	0.0043
	$\theta = 60^\circ$	$E_M < E_I$	0.60	0.434	0.0214
	$r = 0.1\mu m$	$E_M > E_I$	0.85	0.542	0.0041
	$\theta = 70.3^\circ$	$E_M < E_I$	0.54	0.430	0.0618
	$r = 0.01\mu m$	$E_M > E_I$	0.65	0.427	0.0057

Table 3.4 Fitting parameters for Equation 3.16.

3.3.5 A new linear-based model

By observing the trend of the curves in Figure 3.12 and considering the initial boundary condition for z approaching zero, Equation 3.18 is improved to a modified linear-based model, which is given by,

$$\frac{1/E^* - 1/E_I^*}{1/E_M^* - 1/E_I^*} = B_9(e^z - 1) \quad (3.20)$$

where B_9 is the fitting constant. This equation meets the initial boundary condition as when z is approaching zero, $1/E^* - 1/E_I^*$ equals zero. The fitted curves are shown in Figure 3.12, and fitting parameters for this equation are listed in Table 3.5. As the value of $resnorm$ is relatively small (lower than 0.01), it demonstrates

that this new linear-based model can also be adopted for the inclusion/matrix system. The value of the weighting factor b remains the same as that in the previous equations in each condition. The change of the value of B is similar to that in Equation 3.16. Namely, when the value of E_M is lower than E_I , the value of B stays at almost the same value (approximately 0.42~0.44) in all cases. When the value of E_M is higher than E_I , the value of B is increasing obviously from nearly 0.4 to 0.46, when the half-included angle θ decreases from 70.3° to 60°. In the Clifford model, 4 fitting parameters are required (namely, P , Q , n and b), but in the new models presented here (Equation 3.16 and Equation 3.20), only 2 fitting parameters (namely, B and b) are necessary for any indenter geometry and material combination. Compared to the Clifford model, the value of n is approaching one, which makes it similar to that in the linear model.

	Indenter	b	B	$resnorm$
Modified linear-based model (Equation 3.20)	$\theta = 70.3^\circ$	$E_M < E_I$	-0.36	0.427
	$r = 0.1 \mu m$	$E_M > E_I$	-0.14	0.405
	$\theta = 60^\circ$	$E_M < E_I$	-0.34	0.439
	$r = 0.1 \mu m$	$E_M > E_I$	-0.11	0.460
	$\theta = 70.3^\circ$	$E_M < E_I$	-0.36	0.420
	$r = 0.01 \mu m$	$E_M > E_I$	-0.14	0.395

Table 3.5 Fitting parameters for Equation 3.20.

In addition, the verification of these two new models are performed with experimental indentation tests of inclusion/matrix composite which are shown in Appendix A.

3.4 Summary

FE simulations were used to investigate the nanomechanical response of inclusion/matrix polymer composite indented by conical tip with different half-included angle and different tip radius. The ratio of elastic modulus of inclusion over matrix (E_I/E_M) varies from 0.2 to 5, which covers a wide range of polymer composite materials. The FE results have revealed that the measured elastic modulus of the inclusion can be significantly affected by the surrounding matrix well before the indenter touches the matrix. Various indentation-based models have been examined. It is revealed that the Clifford model can be extended to the conical tip, but the constant b will change with the tip geometry. Inspired by the Clifford model, a power law index b was introduced to consider the elastic mismatch between the inclusion and the matrix, which makes the data converge to the same master curve in almost all cases. The fitting results show that a simpler linear model (Equation 3.16) is available for the conical indenter. Moreover, a new linear-based model has been presented here (Equation 3.20), which shows good performance as well. But in these two simpler equations, only two fitting parameters are necessary to describe the nanoindentation response for composites with any material combination, rather than the four fitting parameters in the Clifford model.

In the next chapter, finite element modelling for particle-reinforced composites will be presented to assess their elastic-plastic response during nanoindentation.

Chapter 4

Nanomechanical Modelling of Elastic-Plastic Particles in Elastic-Plastic Matrix

Chapter 4. Nanomechanical Modelling of Elastic-Plastic Particles in Elastic-Plastic Matrix

4.1 Introduction

Nanoindentation has been used to determine the mechanical properties of thin coatings (Li and Bhushan, 1998; Lim *et al.*, 1999; Chen and Bull, 2008; Chen *et al.*, 2009), synthetic (Chakraborty and Bhowmik, 2014; Eggedi *et al.*, 2014; Luo *et al.*, 2014) and biological composite materials (Chen *et al.*, 2010a; Oyen, 2013; Chen *et al.*, 2014; Cyganik *et al.*, 2014; De Silva *et al.*, 2014; Jaramillo-Isaza *et al.*, 2014; Sun *et al.*, 2014). In such cases, it is important to understand how the underlying substrate or surrounding matrix will affect the measured mechanical properties. In coating/substrate systems, for a typical indenter with a semi-included angle between 60–70°, when the maximum indentation depth exceeds 10–30% (depending on coating/substrate combinations) of the coating thickness, a significant effect on the indentation hardness caused by substrate deformation is evident (Chen and Bull, 2006c). For the substrate effect on the indentation modulus, the critical indentation depth is much smaller (Chen and Bull, 2006c; Chen and Bull, 2009b), but it would strongly depend on the material combination.

For the indentation tests on particle/polymer matrix systems, the spatial-dependent mechanical properties have been mainly investigated by numerical simulations (Clifford and Seah, 2012; Yan *et al.*, 2012). The empirical model to describe the spatial-dependent elastic modulus for such particle/polymer matrix system has only been established for linear elastic materials (Clifford and Seah, 2012). Actually, many particle/matrix systems exhibit elastic-plastic behaviour, which has not been well studied. Such particle/matrix systems have wide industrial applications. Recently, these particle/matrix systems have been used for biomedical applications (Yang *et al.*, 2011; Hasan *et al.*, 2013; Dadbin and Naimian, 2014; Jiang *et al.*, 2014; Kubozono *et al.*, 2014; Pradid *et al.*, 2014; Tayton *et al.*, 2014; Zong *et al.*, 2014). For example, hydroxyapatite (HA) particles embedded in biodegradable polymers have been used as scaffold materials for bone tissue engineering (Jiang *et al.*, 2014; Tayton *et al.*, 2014; Zong *et al.*, 2014). Such composites have better bioactivity and improved toughness compared to

HA particles only. Therefore, it is essential to study the spatial-dependent elastic and plastic properties of HA particles embedded in various biopolymers such as polylactic acid (PLA) and polyglycolic acid (PGA).

In this chapter, we will take this particle/matrix system as a representative model system. Both an analytical model and an FE model have been employed to study the nanomechanical response of the particle/matrix systems.

4.2 Analytical method

Various methods have been proposed to study how the elastic deformation of thin coatings will be affected by the substrates (Jönsson and Hogmark, 1984; Doerner and Nix, 1986; Burnett and Rickerby, 1987a; Burnett and Rickerby, 1987b; Bhattacharya and Nix, 1988; Gao *et al.*, 1992; Jung *et al.*, 2004). There are also different empirical models to study how the plastic deformation of the coatings will be affected by the underlying substrates (Westbrook, 1973; Jönsson and Hogmark, 1984; Burnett and Rickerby, 1987a; Burnett and Rickerby, 1987b; Bhattacharya and Nix, 1988). However, it was found that these models were not applicable to particle/matrix systems (Clifford and Seah, 2012). Therefore, Clifford *et al.* (Clifford and Seah, 2012) have proposed the following empirical model to describe the spatial-dependent composite modulus (E_c) for a spherical tip indenting linear elastic particles embedded in the linear elastic matrix, which is given by,

$$\frac{E_c^* - E_P^*}{E_M^* - E_P^*} = \frac{Pz^n}{1 + Pz^n + Qz} \quad (4.1)$$

$$z = \frac{a}{t} \left(\frac{E_P^*}{E_M^*} \right)^b \quad (4.2)$$

where P , Q , n , b are fitting parameters, and the subscripts P , M and C refer to the particle, matrix and composite, respectively. (In this study, b is predefined and manually adjusted to improve the computational efficiency.) The parameters a and t are contact radius during indentation and thickness of particles, respectively. As suggested in the previous work (Chen and Bull, 2006c), the plastic deformation zone may be proportional to the effective elastic influence

zone. Therefore, in this study, we assume that similar principles apply to hardness and we propose the following equations for the spatial-dependent composite hardness (H_C),

$$\frac{H_C - H_P}{H_M - H_P} = \frac{Pz^n}{1 + Pz^n + Qz} \quad (4.3)$$

$$z = \frac{a}{t} \left(\frac{H_P}{H_M} \right)^b \quad (4.4)$$

where the parameters in this equation are similar to what have been defined above. To examine the applicability of these empirical models, FE simulations have been adopted to investigate the spatial-dependent nanoindentation response of these composites, which will be discussed in the following section.

4.3 Methodology

4.3.1 Finite element modelling setting up

When the nano-HA particles were dispersed in the biopolymers, they tend to form a microscale or submicroscale agglomeration which are almost spherical in shape (Sato *et al.*, 2006). For simplification, a semi-spherical HA particle (with a radius of 0.5 μm , which is similar to the typical size of reported nanoparticles (Hu *et al.*, 2010)) embedded in a biopolymer was chosen for the modelling in this work. To evaluate the effects of shape and volume, two different cylindrical particles with radii of 0.437 μm (which gives the same volume as the spherical particle with radius of 0.5 μm) and 0.5 μm were also considered. The vertical dimensions of these cylindrical particles were equal to their radii, which results in volumes of 0.131 μm^3 and 0.196 μm^3 , respectively. To make it clearer, a diagram of these various particle/matrix composites is illustrated in Figure 4.1, with their detailed geometries and dimensions summarized in Table 4.1. It was also assumed that particles were far away from each other so that the indentation stress field will not be affected by the nearby particles. As the volume fraction of the particles is low, we assume isotropic behaviour for the matrix during the nanoindentation tests. A typical conical tip with semi-included angle of 70.3° (equivalent to a Berkovich

indenter) and tip radius of 40 nm was used. Such a tip radius represents a real test.

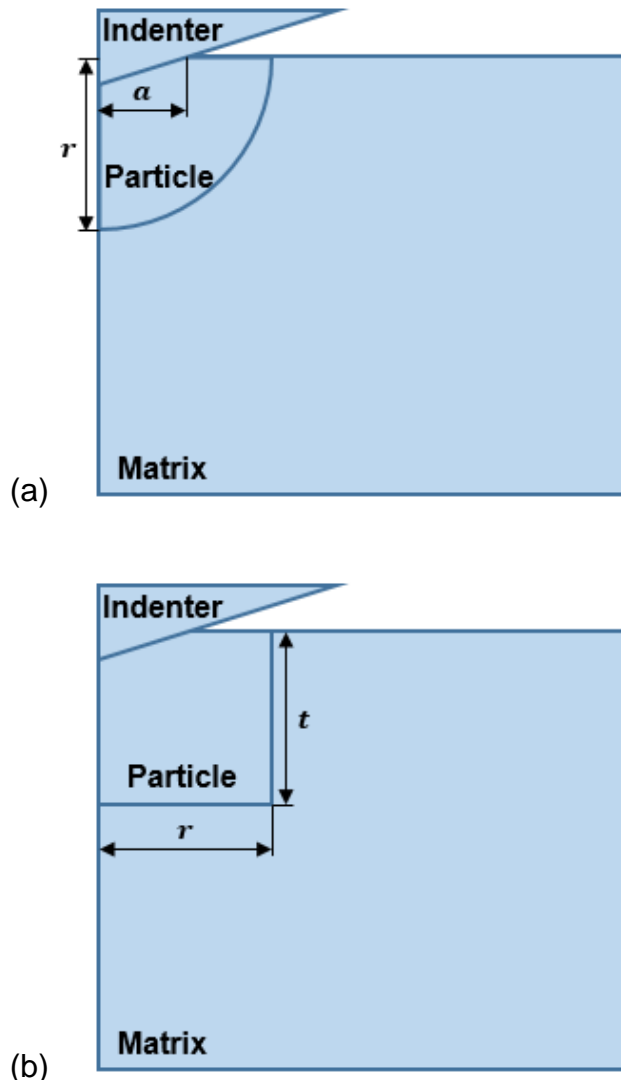


Figure 4.1 Schematic of the indentation of (a) the spherical particle embedded in the matrix and (b) the cylindrical particle embedded in the matrix.

Particles	Radius (r)	Thickness (t)	Volume
Semi-spherical particle	0.5 μm	0.5 μm	0.131 μm^3
Cylindrical particle	0.437 μm	0.437 μm	0.131 μm^3
Cylindrical particle	0.5 μm	0.5 μm	0.196 μm^3

Table 4.1 Summary of geometries and dimensions of the particles.

Due to the symmetric nature of the indenter and the composite specimen, a 2D axisymmetric FE model was developed with the ABAQUS 6.10 software to improve the computation efficiency. Figure 4.2 shows the details of FE mesh for these particle/matrix systems. For each case, a minimum number of 12000 CAX4R four-node elements was used to model the particle and the matrix, with a minimum of 5000 elements assigned to the particle. The density of the FE mesh was designed to increase with proximity to the particle/indenter contact region. The indenter was modelled as a rigid body. The interface between the matrix and the particle was assumed to be perfectly bonded. A completely fixed boundary condition was applied to the bottom of the model. An axisymmetric boundary condition was applied to the symmetry axis of the indenter and the specimen. Previous work has demonstrated that the influence of friction on the indentation response was relatively small (Chen and Bull, 2009b; Low *et al.*, 2015), thus the contact between the indenter and sample surface was assumed to be frictionless. The height and the width of the model are sufficiently large compared to the indentation depth so that the simulated response will not be significantly affected by the boundaries. To maximize the efficiency, the indenter was displacement-controlled and a loading-unloading indentation protocol was applied, with the maximum applied displacement varied from 0.03 μm to 0.1 μm . As shown in Figure 4.3, the indenter reaches the maximum penetration depth within 1 second, and then gets back to the original position after 1 second. In all cases, the elastic modulus and hardness of the composite were determined from the F - δ curves by the Oliver and Pharr method.

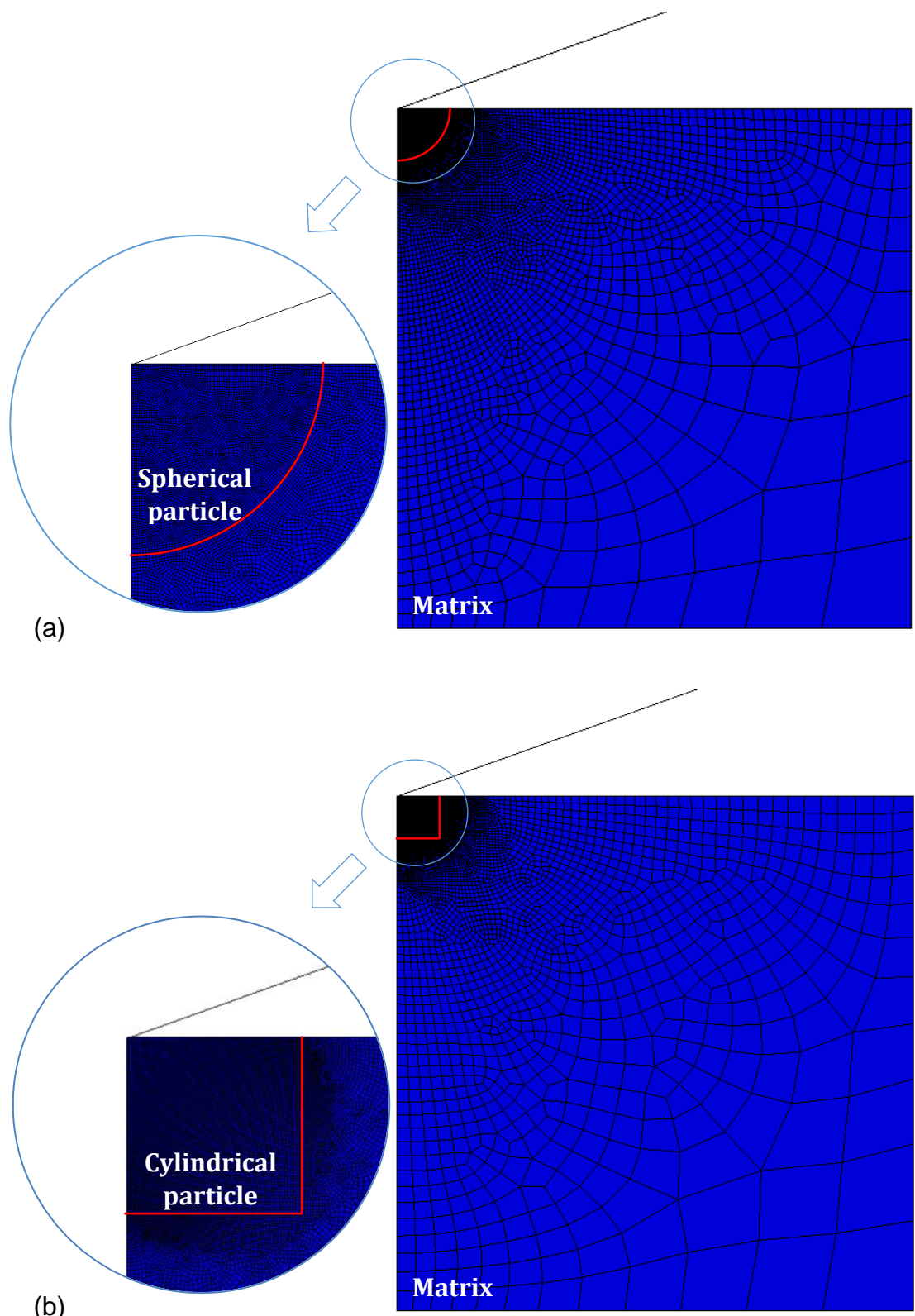


Figure 4.2 Overview of the finite element mesh and the enlarged details of elements underneath the tip for (a) the spherical particle embedded in the matrix and (b) the cylindrical particle embedded in the matrix.

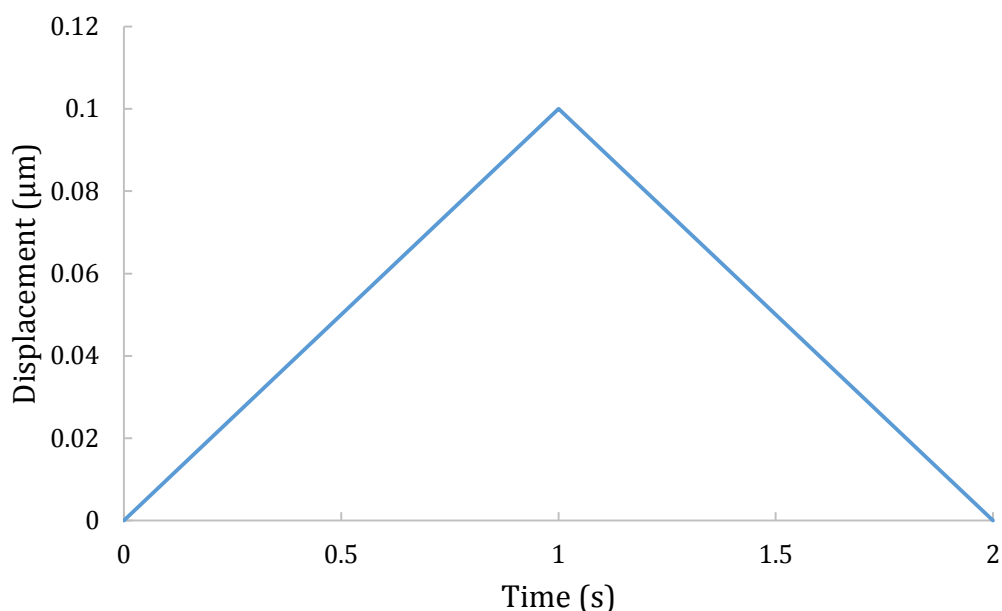


Figure 4.3 Schematic of the loading-unloading indentation protocol which has a maximum displacement of 0.1 μm .

For the mechanical properties, both the particle and the matrix were modelled as elastic-plastic materials. The Poisson's ratios of HA and polymers were fixed at 0.25 and 0.3, respectively. The Young's modulus and hardness of HA was taken from the work conducted by Zamiri and De (Zamiri and De, 2011). For typical non work-hardening materials, the H/Y is in the range of 2.2~2.5 (Chen and Bull, 2006b). Based on this, it is assumed that the yield strength of HA is 2.3 GPa. The elastic moduli of PLA and PGA are reported to be 0.35~3.5 GPa and 6~7 GPa, respectively (Van de Velde and Kiekens, 2002). In the simulation, we chose the representative values of elastic modulus for PLA (1.75 GPa) and PGA (7 GPa), respectively. The selection of these values is arbitrary and will not affect the physics in the modelling. Also, it was assumed that the yield strength of the PLA and PGA are 0.03 GPa and 0.12 GPa, respectively, which are similar to the values reported by Van de Velde and Kiekens (Van de Velde and Kiekens, 2002). In order to expand the range of elastic modulus investigated in this study, rather than modelling a specific material, an additional material with Young's modulus of 35 GPa and yield strength of 0.6 GPa was also considered. In these cases, the E/Y ratios for these biopolymers are identical. To make it clearer, the materials properties used in the FE model are summarised in Table 4.2. In this study, HA particles embedded into three different biopolymer matrices (namely, polymer 1, polymer 2, and polymer 3 in the Table 4.2) were considered. For

comparison, the cases that biopolymer particles embedded in HA matrix were also considered by switching the material properties of particle and matrix. In this case, the elastic modulus ratio between the particle and matrix (E_P/E_M) varies from 0.012 to 83. The yield strength ratio between the particle and the matrix (Y_P/Y_M) varies from 0.013 to 77. Such combinations would cover a wide range of composite materials.

	E (GPa)	Y (GPa)	ν
HA	145	2.3	0.25
Polymer 1	1.75	0.03	0.3
Polymer 2	7	0.12	0.3
Polymer 3	35	0.6	0.3

Table 4.2 Input parameters for materials properties in the FE model.

4.3.2 Model calibration

In this study, the tip radius is 40 nm, which is comparable to the penetration depth. Similar to the experimental tip area function calibration, this study uses numerical simulation as a calibration procedure. The matrix was assigned the same mechanical properties as the nanoparticles. In this case, the elastic modulus and hardness determined by the Oliver and Pharr method were calibrated against the intrinsic elastic modulus and hardness. This generates a new area function for data calibration and also eliminate any numerical instability induced errors.

4.3.3 Elastic-plastic material model

In the case of small penetration depth, based on the rheological model of considering the elastic behaviour and plastic behaviour as a spring and a friction element arranged in series (as shown in Figure 4.4), the total strain increment ($\dot{\varepsilon}$) is decomposed into elastic strain increment ($\dot{\varepsilon}_e$) and plastic strain increment ($\dot{\varepsilon}_p$) (Hibbett *et al.*, 1998; Willam, 2002; Yu, 2006). In the uniaxial stress state, the

elastic-plastic stress-strain curve for each element is depicted in Figure 4.5, in the elastic region ($\varepsilon \leq \sigma_Y/E$), the strain increment is expressed as (Hibbett *et al.*, 1998),

$$\dot{\sigma} = E\dot{\varepsilon} \quad (4.5)$$

where $\dot{\sigma}$ is the stress increment. In the plastic region after initial yielding, the total increment for each mesh is given by,

$$\dot{\varepsilon} = \dot{\varepsilon}_e + \dot{\varepsilon}_p \quad (4.6)$$

By integrating, Equation 4.5 and Equation 4.6 become,

$$\sigma = E\varepsilon \quad (4.7)$$

$$\varepsilon = \varepsilon_e + \varepsilon_p \quad (4.8)$$

where σ is the stress, ε is the strain, ε_e is the elastic strain and ε_p is the plastic strain.

For simplicity, a perfectly elastic-plastic material behaviour was assumed, which means the strain hardening exponent was zero, the stress will not increase once the yielding occurs at the yield stress Y . Therefore, the stress-strain relation for each element is given by,

$$\sigma = \begin{cases} E\varepsilon, & \varepsilon \leq \frac{Y}{E} \\ Y, & \varepsilon > \frac{Y}{E} \end{cases} \quad (4.9)$$

In the three-dimensional stress state, the stress-strain relation for each mesh in the elastic region ($\varepsilon \leq \sigma_Y/E$) is then generalized and expressed in tensor notation as (Yu, 2006),

$$\sigma_{ij} = \frac{Ev}{(1+v)(1-2v)} \varepsilon_{kk} \delta_{ij} + \frac{E}{1+v} \varepsilon_{ij} \quad (4.10)$$

$$\gamma_{ij} = 2\varepsilon_{ij} \quad (4.11)$$

where γ is the shear strain and δ_{ij} is the Kronecker delta function. In the plastic region after yielding, stress becomes a constant and independent of strain.

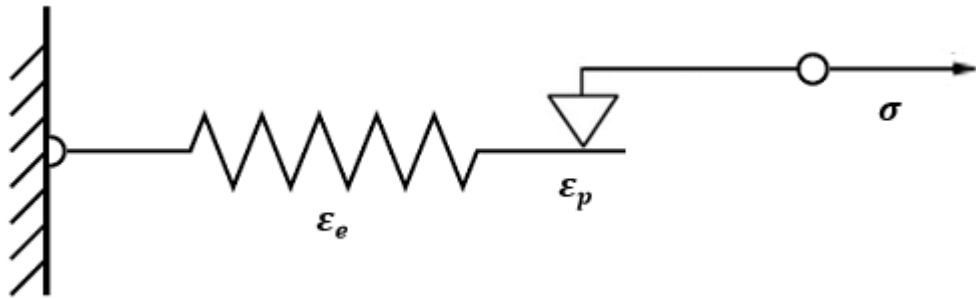


Figure 4.4 Rheological model of an elastic-plastic material by arranging the spring and the friction element in series. The spring represents the elastic behaviour and the friction element represents the plastic behaviour.

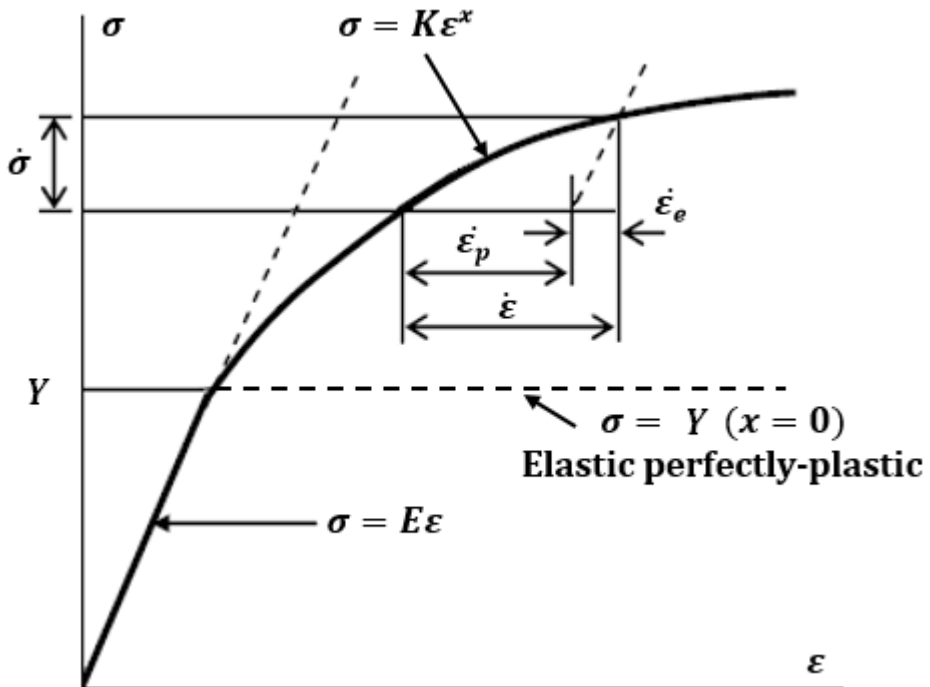


Figure 4.5 Uniaxial elastic-plastic stress-strain curve. x is the strain hardening index, and the proportionality constant $K = Y(E/Y)^x$. For $x = 0$, the material is elastic perfectly-plastic (Yu, 2006).

4.3.4 Curve fitting

Matlab code was written to perform the curve fitting and extract the fitting parameters. In this chapter, the goodness of the fitting was determined by calculating the coefficient of determination (R^2) value, which is given by,

$$R^2 = 1 - \frac{\sum_i (y_i - F(x_i))^2}{\sum_i (y_i - \bar{y})^2} \quad (4.12)$$

where R^2 is a statistical parameter, which varies between 0 and 1. Within this range, a larger value means a better fitting and one represents a perfect fitting. $F(x)$ is the predicted data from the fitting equation, y is the observed data from simulation, and \bar{y} is the mean of the observed data. During the curve fitting, in order to improve the computational efficiency, the fitting parameter b in Clifford model was predefined and manually adjusted until achieving a minimum *resnorm* value. Besides, the influence of fitting parameters with different decimal places (i.e. 1, 2, 3...) on the R^2 value were investigated. Then, as a trade-off between efficiency and accuracy, all the fitting parameters were rounded to 3 decimal places.

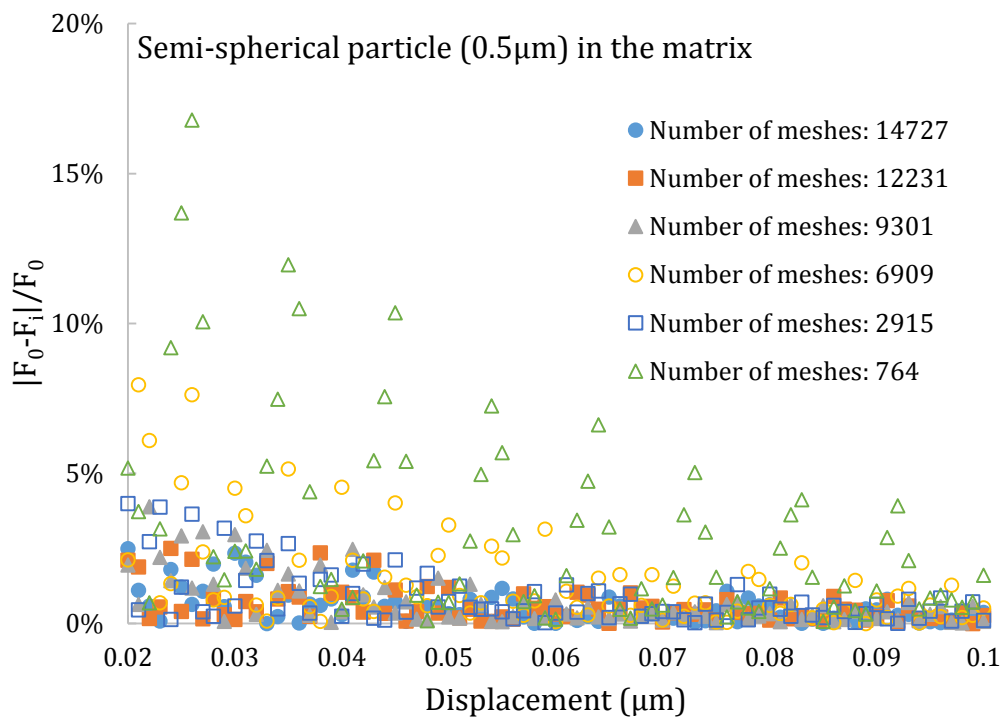
In the previous chapter, the *resnorm* value was used to present the quality of a fitting instead of R^2 , which has the limitation of depending on the magnitudes of the data. Therefore, to avoid the confusion due to the magnitudes of the data, the R^2 value was used to indicate the fitting quality in this chapter.

4.4 Results and discussion

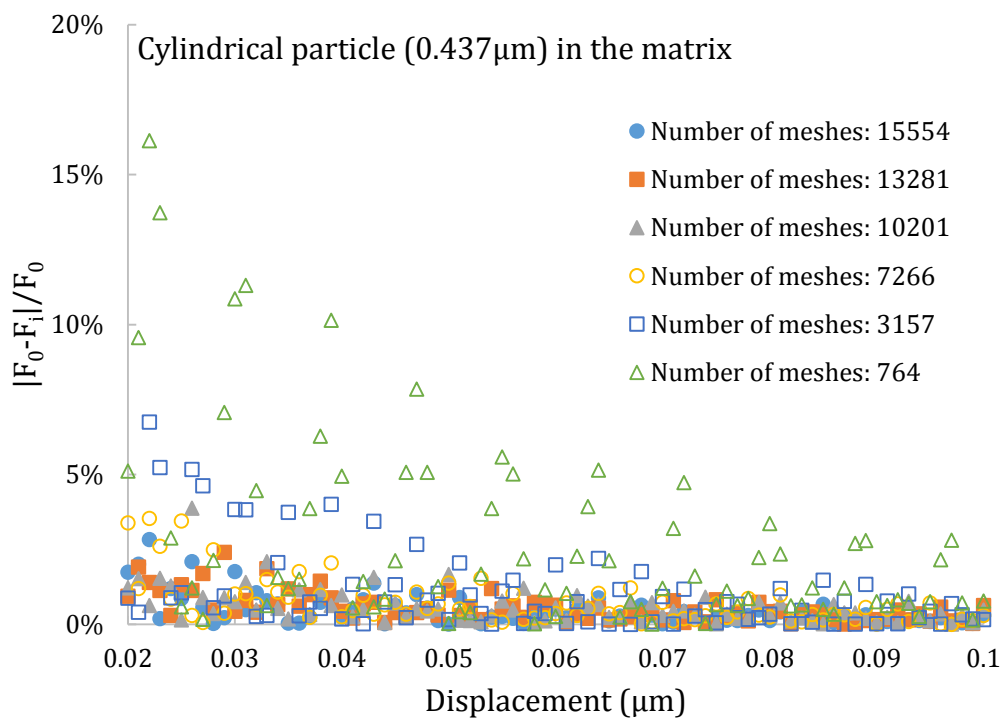
4.4.1 Model validation

Prior to the nanomechanical modelling of the particle/matrix systems, these models should be validated. Since coarse mesh may result in inaccurate simulation results, errors due to the density of mesh should be avoided, and the deviation between the simulated data and the theoretical data should be within an acceptable level.

To investigate the influence from the mesh density, a model with denser or coarser mesh was created by proportionally varying the number of elements in each segment. For each particle/matrix system (namely, different particle geometry), the maximum number of elements was approximately 30000 and the minimum number was approximately 760. According to the literature, these values are reasonable to be set as maximum and minimum values. (After setting the number of elements in each segment, the number of elements is then determined by the finite element software. However, due to different particle geometry in each particle/matrix system, the number of elements for each system with a similar mesh density will be slightly different.) Both particle and matrix were defined as HA material. By performing the nanoindentation modelling with the maximum displacement of 0.1 μm by the defined conical indenter, the F - δ data from loading period for models with different mesh density were compared. By assuming the data from model with densest mesh (number of elements was approximately 30000) as the reference (F_0), the deviation between F_0 and the data from models with other mesh density (F_i) is plotted in Figure 4.6. A big deviation (higher than 20%) was observed in all cases when the displacement was lower than 0.02 μm , which may due to the fact that the indenter was not touching enough elements at shallow penetration depth. Therefore, the data within the displacement range of 0~0.02 μm were discarded. After the indenter touched enough elements, as shown in Figure 4.6, big deviation (higher than 10%) was observed when the number of elements was lower than approximately 9000~10000 in all cases. The deviation was approximately 2~3% when the number of elements was higher than approximately 10000. It indicates that the mesh should be dense enough with the total number of elements higher than 10000 to avoid errors from the mesh density, and the mesh density of models (with a minimum of 12000 elements) used in this study is reasonable.



(a)



(b)

Figure 4.6 Absolute deviation ($\frac{|F_0 - F_i|}{F_0}$) between the force from the models with different mesh density for (a) semi-spherical particle (0.5 μm) embedded in the matrix, (b) cylindrical particle (0.437 μm) embedded in the matrix and (c) cylindrical particle (0.5 μm) embedded in the matrix.

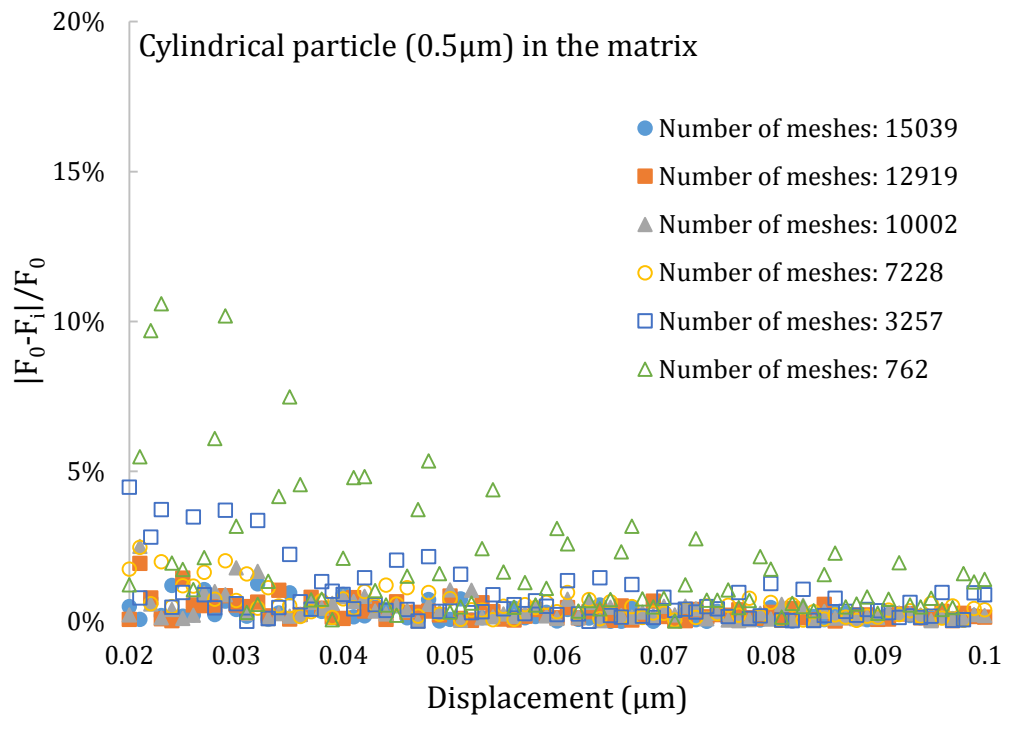


Figure 4.6 (Cont.)

Additional comparison was drawn between the simulated data from FEA and the theoretical data from an empirical equation. Both particle and matrix were set as a linear elastic material with an elastic modulus of 145 GPa and a Poisson's ratio of 0.25. By performing the nanoindentation modelling with the maximum displacement of 0.1 μm by a spherical indenter with a radius of 0.5 μm , the $F-\delta$ data from each particle/matrix system was compared with the theoretical data calculated from the Hertz equation. As shown in Figure 4.7, the deviation is within the range of 2~6% in all cases when the displacement varies from 0.02 μm to 0.1 μm . In general, the Hertz equation is applied to a small strain ($\varepsilon = 0.2a/R$ for a spherical indenter) which is usually lower than 5%. As shown in the graph, the deviation is approximately 2% for a strain of 4.5% (displacement equals 0.02 μm). It will be even lower when the displacement is extrapolated to a smaller displacement. In this case, the deviation is acceptable and less than 2% when the strain is below 5%.

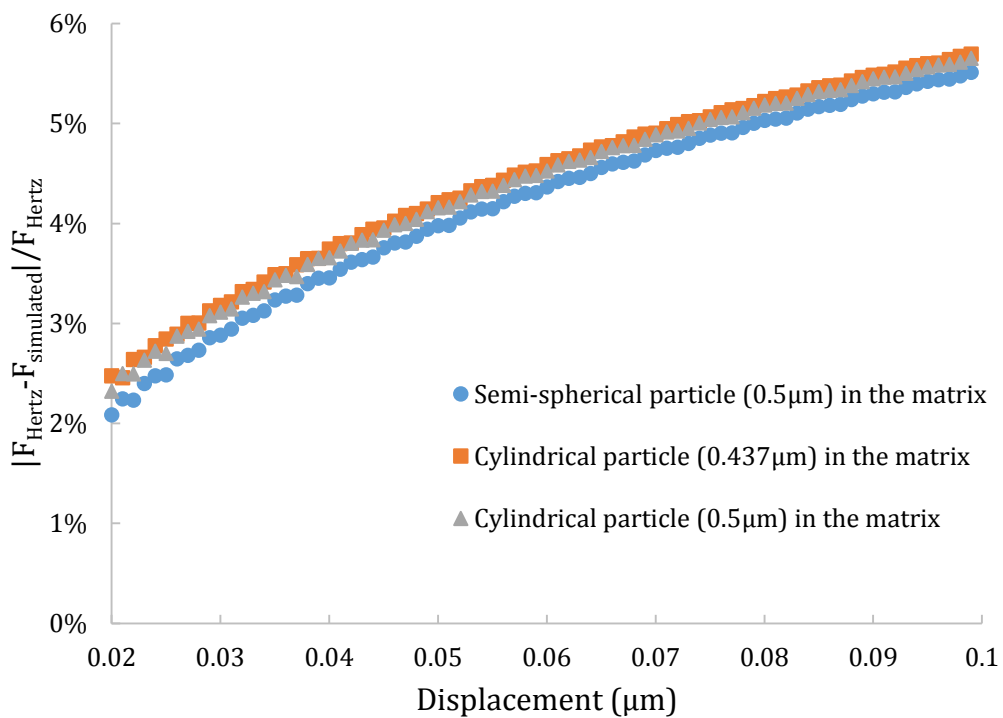
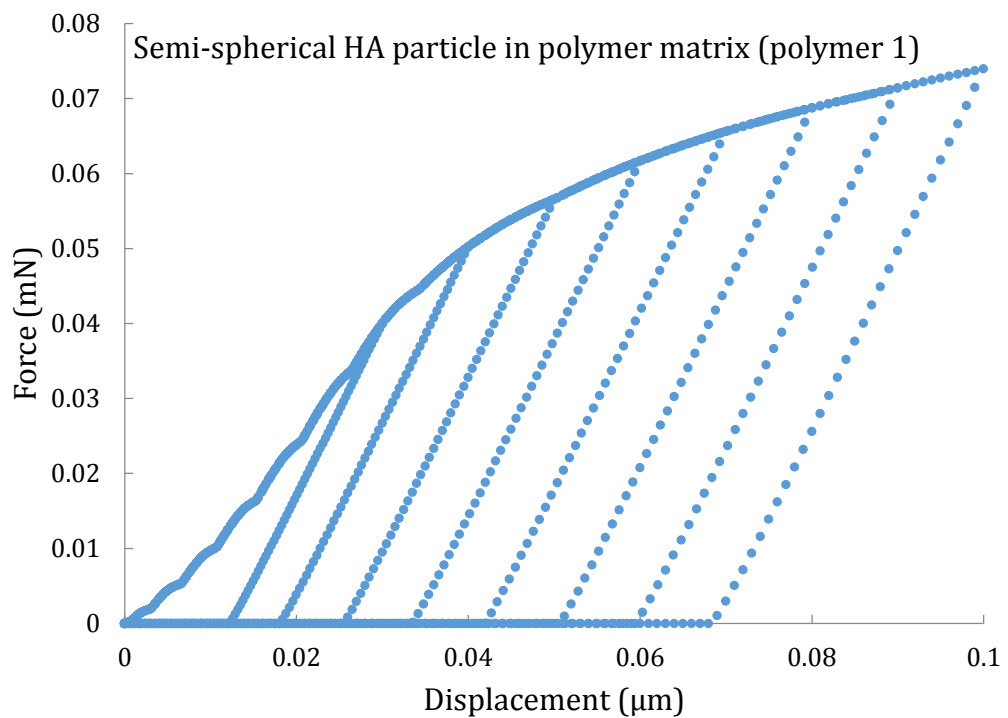


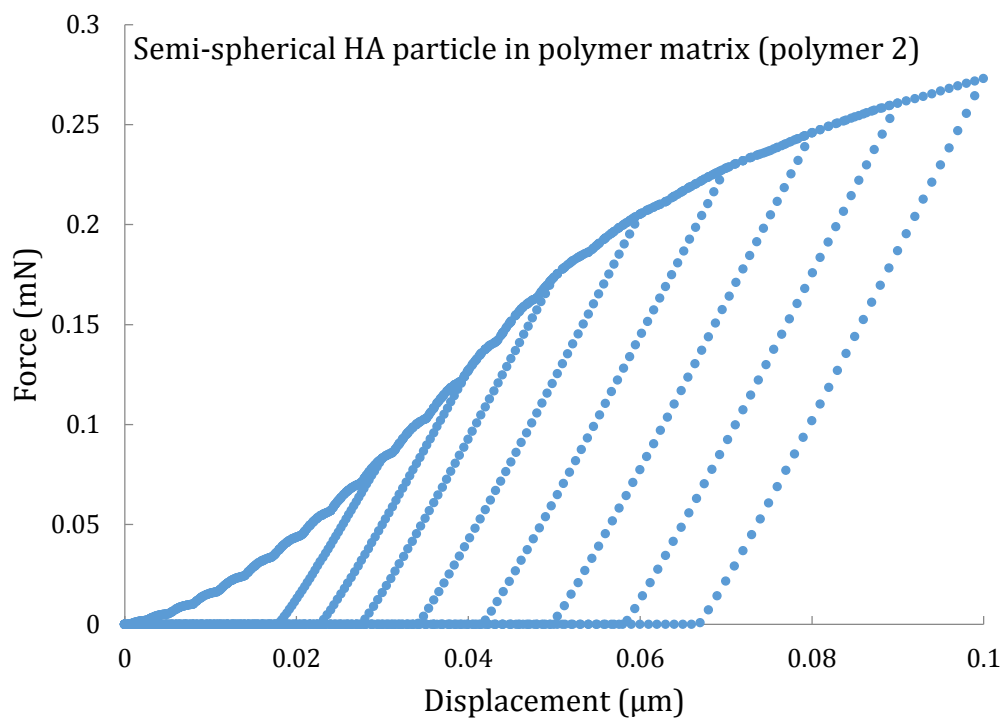
Figure 4.7 Absolute deviation ($\frac{|F_{Hertz} - F_{simulated}|}{F_{Hertz}}$) between the theoretical data and the simulated data for each particle/matrix system when indented by a spherical indenter.

4.4.2 Typical load-displacement curves

Figure 4.8 shows the typical load-displacement curves of the combination of HA and different polymers for a semi-spherical particle embedded in the matrix (namely, HA particle embedded in different biopolymers and polymer particles embedded in the HA matrix). It can be seen that, for very soft matrix (*i.e.* 1.75 GPa and 7 GPa), the clear transition from particle-dominated behaviour to matrix-dominated behaviour was observed. While for soft particles embedded in the hard matrix, such a transition was not evident. Sinusoidal pattern is observed in the initial part of the loading curves, which may due to the artefacts of the finite element software. However, this will not affect the extraction of mechanical properties, as unloading curve method (Oliver and Pharr method) has been used in this study.

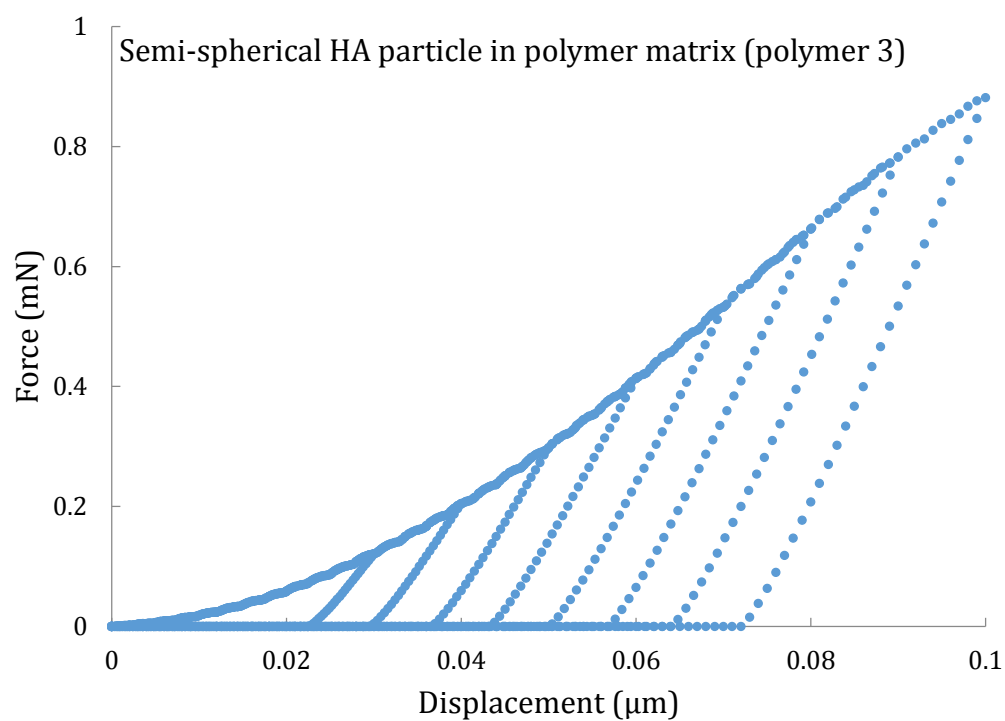


(a)

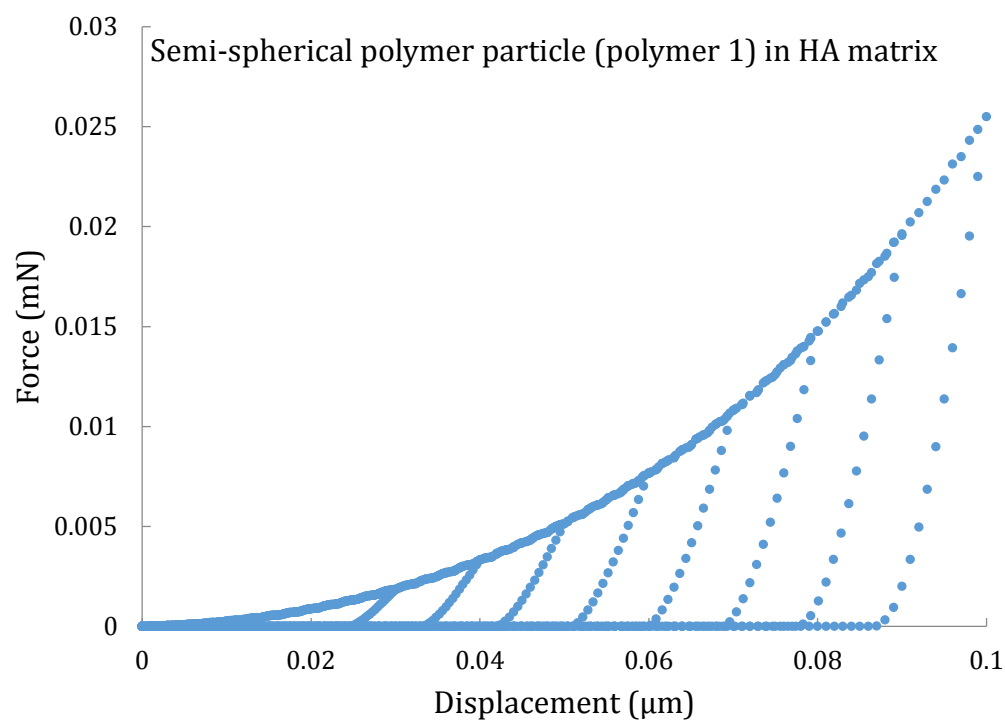


(b)

Figure 4.8 The load-displacement curves for the indentation test upon a semi-spherical particle within the matrix, (a) HA particle embedded in polymer 1, (b) HA particle embedded in polymer 2, (c) HA particle embedded in polymer 3, (d) polymer 1 embedded in the HA matrix, (e) polymer 2 embedded in the HA matrix and (f) polymer 3 embedded in the HA matrix.

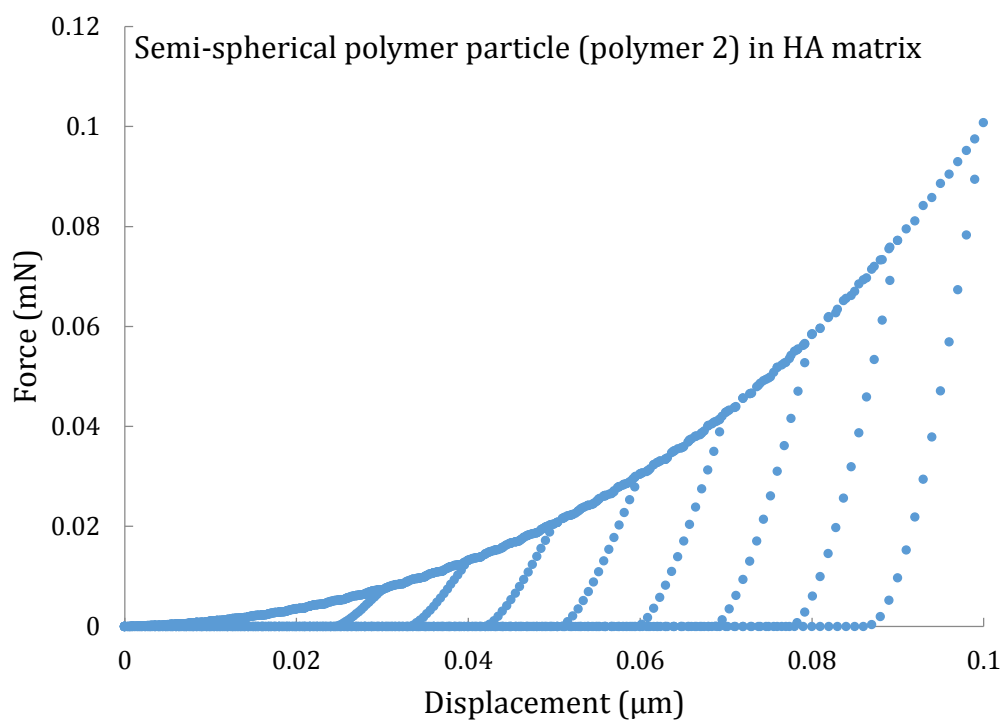


(c)

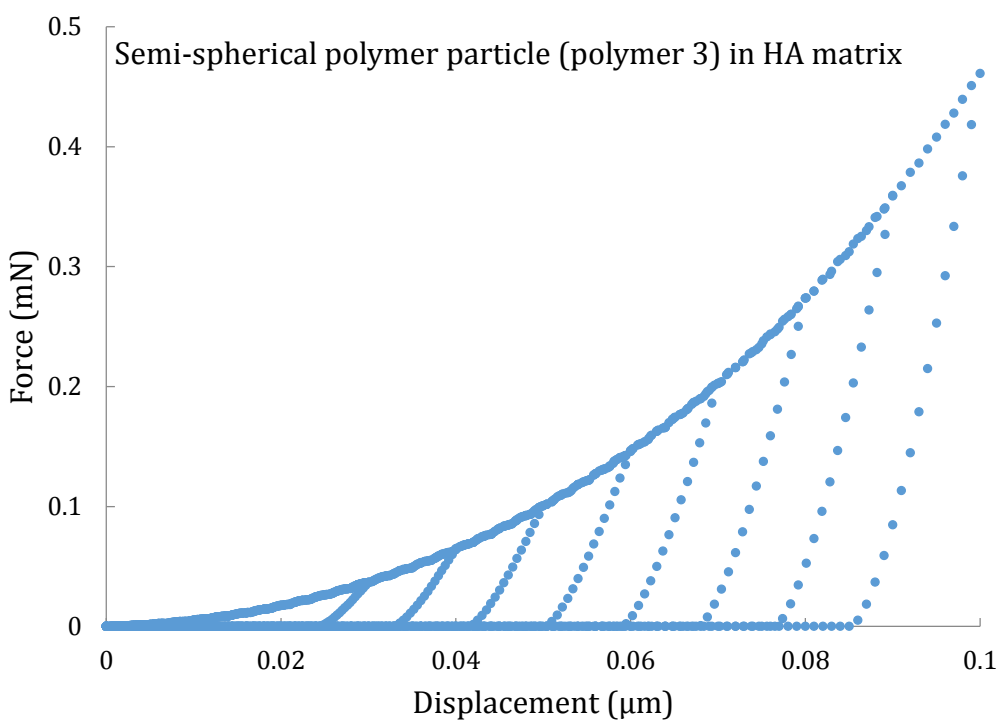


(d)

Figure 4.8 (Cont.)



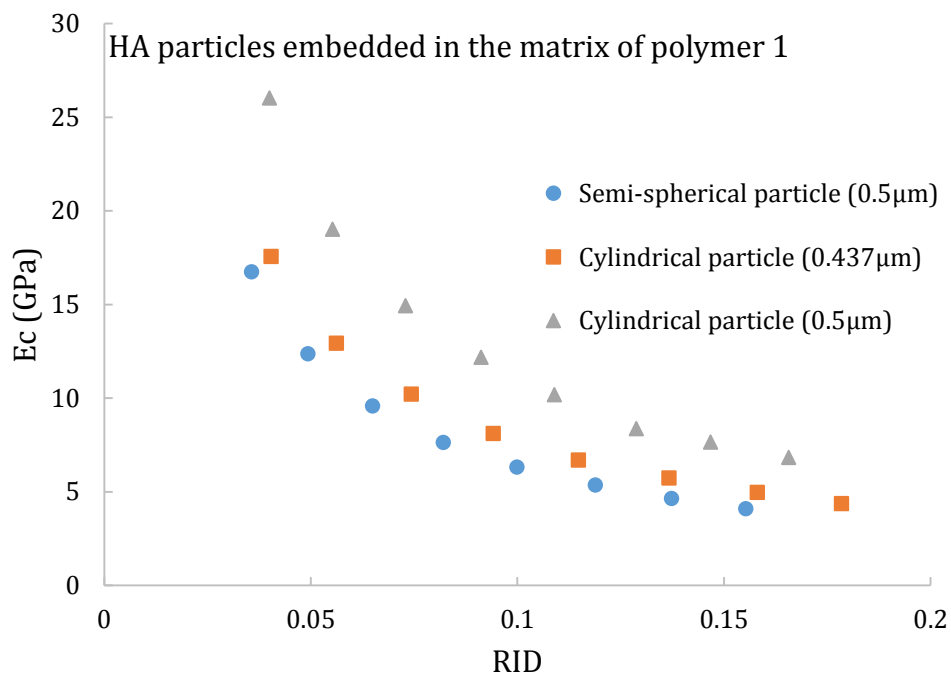
(e)



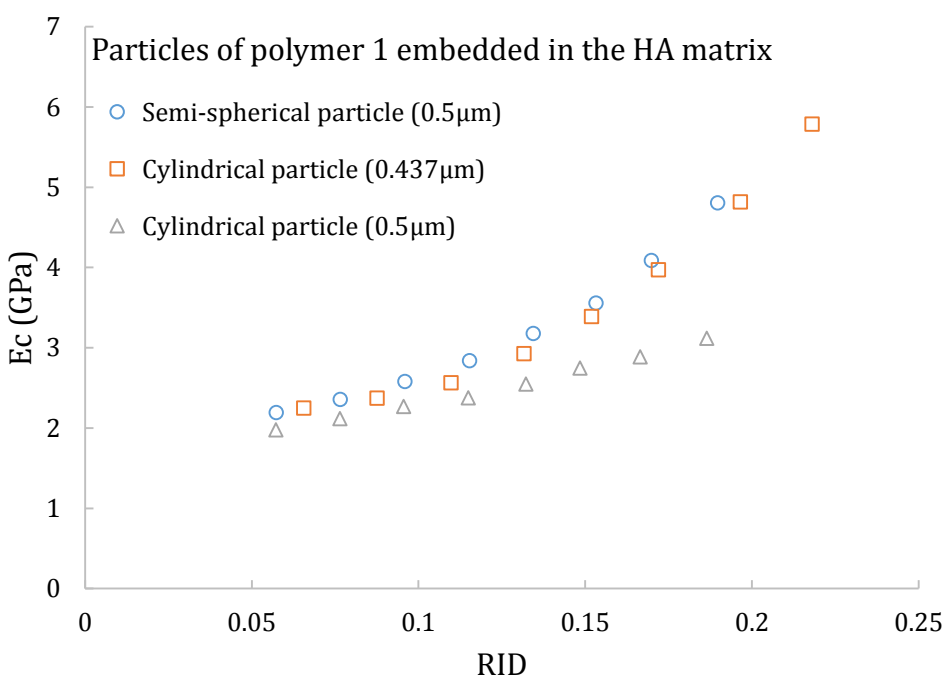
(f)

Figure 4.8 (Cont.)

For simplification, the apparent moduli (E_C) and hardness (H_C) of the composite were plotted against the relative indentation depth (RID, *i.e.* contact depth divided by the particle radius). As a representative example, the plots of E_C and H_C against RID between the combination of HA and polymer 1 (namely, HA particle embedded in polymer 1 and polymer 1 embedded in HA matrix) are shown in Figure 4.9 and Figure 4.10, respectively. For the composite elastic modulus, it was demonstrated that only for the soft particles in hard matrix, one may propose a 5% rule-of-thumb for estimating the particle modulus (Yan *et al.*, 2012). Otherwise, the critical depth to determine the elastic modulus of the particle is strongly dependent on the modulus ratio of particle to matrix (Yan *et al.*, 2012). This statement accurately describes the data shown in Figure 4.9, which shows the results of the composites with large mismatch in mechanical properties. That is, the ratio of E_P/E_M is as high as 83 in Figure 4.9a, and as small as 0.012 in Figure 4.9b. For the composite hardness, it was also reported elsewhere that the hardness of a particle can be measured reliably when the indentation depth is below 13.5% of the particle's radius for the composites with Y_P/Y_M varying from 0.1 to 10 (Low *et al.*, 2015). As shown in Figure 4.10b, such a rule-of-thumb also works well even when the ratio of Y_P/Y_M is as small as 0.013. However, it does not apply to the case of a large ratio of Y_P/Y_M in this study, such as the data shown in Figure 4.10a which shows a large Y_P/Y_M ratio of 77. For example, even at RID as small as 0.05, significant drops of the modulus (drop by 26% for the semi-spherical particle composite) and hardness (drop by 33% for the semi-spherical particle composite) were observed when the RID increased from approximately 0.04 to 0.05. This indicated that the matrix effect is still significant even when the indentation penetration is below 5% of the particle radius.

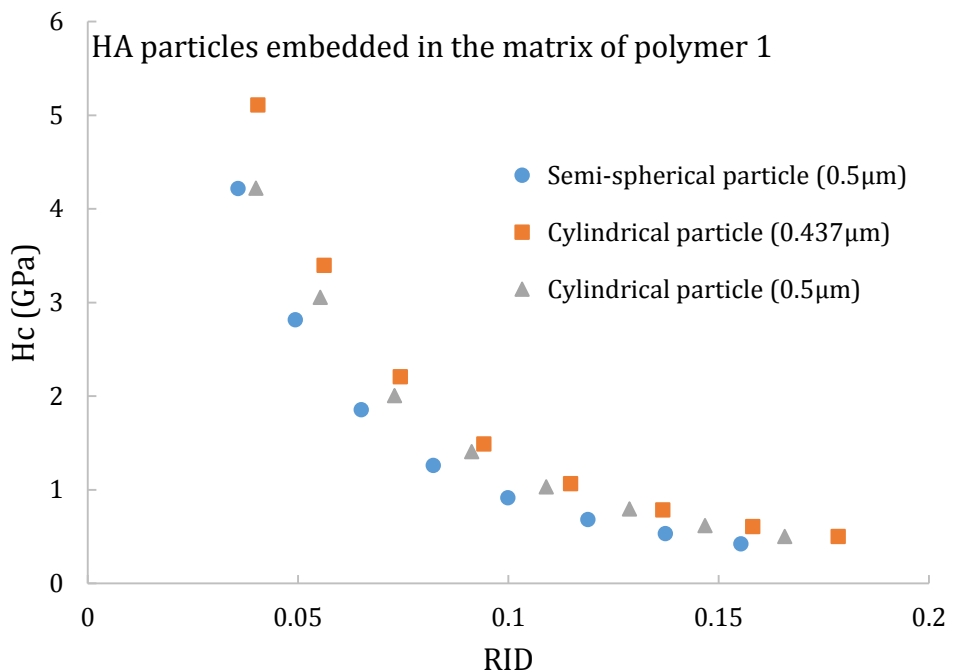


(a)

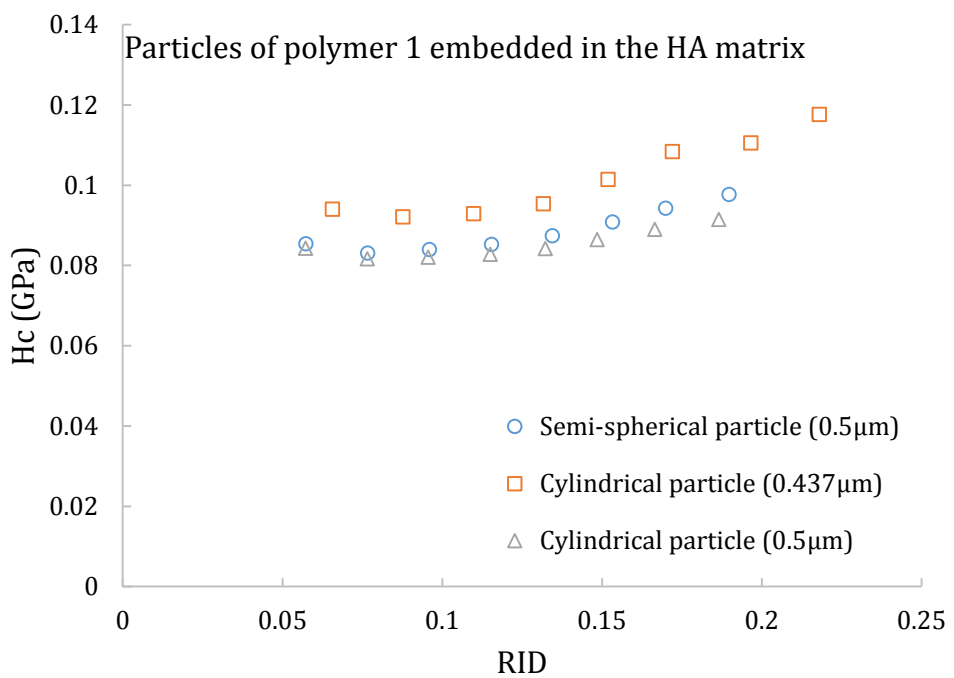


(b)

Figure 4.9 Composite elastic modulus (E_c) against RID for (a) three different HA particles embedded in polymer 1 and (b) three different particles of polymer 1 embedded in the HA matrix.



(a)



(b)

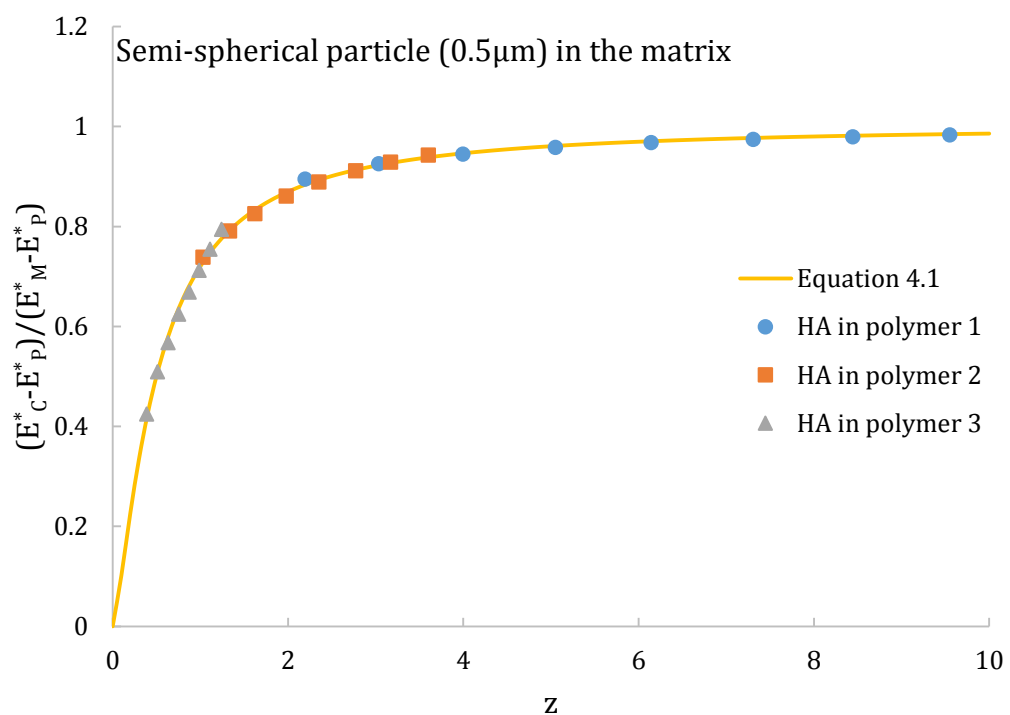
Figure 4.10 Composite hardness (H_c) against RID for (a) three different HA particles embedded in polymer 1 and (b) three different particles of polymer 1 embedded in the HA matrix.

For the particle with the same volume but different geometries (semi-sphere and cylinder), the way how the composite elastic moduli changes with RID is almost indistinguishable. This is because the ratio of radius and vertical dimension equals one for all particles. On the other hand, the volume effect plays

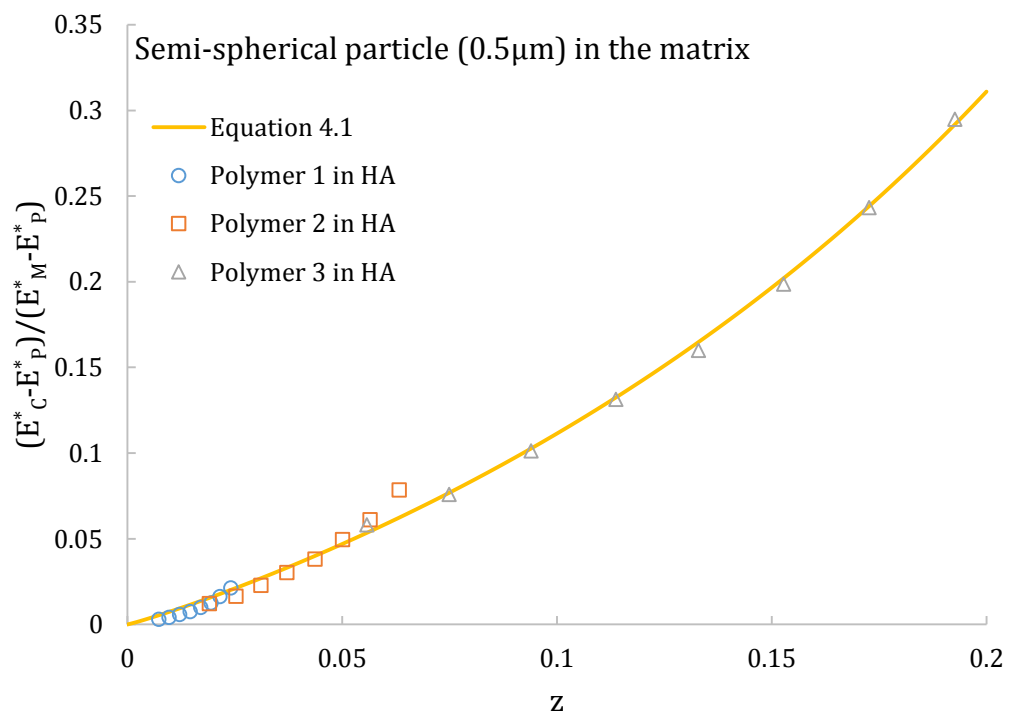
an important role in composite elastic moduli. While, for the given volumes specified in this study, the volume effect of the particle is less significant for the hardness. This is mainly due to the complicated elastic-plastic deformation mechanisms of the composite materials during indentation as suggested in the work conducted by Chen and Bull (Chen and Bull, 2009b). This also suggests that it is more reliable to extrapolate the measured composite hardness to the zero penetration to extract the intrinsic hardness of the particle rather than relying on any thumb rules.

4.4.3 Model elastic-plastic response of the composites during nanoindentation

Applying the Clifford model (*i.e.* Equation 4.1) to the composite modulus in this study, as shown in Figure 4.11, gives good estimations similar to what has been reported for viscoelastic composites (Duan *et al.*, 2015). Similar to the transition observed in Figure 4.8, when the particle was stiffer than the matrix, the transition from particle-dominated to matrix-dominated was also clearly observed in Figure 4.11. When adopting Equation 4.3, as shown in Figure 4.12, we have found that the Clifford model can be extended to determine composite hardness for indentation tests as well. (In Figure 4.12c, a set of relatively constant values is observed in cylindrical HA/polymer 3 model when z is smaller than 1. This may be due to the artefacts of the software, as this phenomenon has not been observed in other models.) However, as listed in Tables 4.3-4.5, the fitting parameters in the Clifford model are very sensitive to the particle shape and volume fraction, which implies that this may not be a generic model. For example, for the soft particle/hard matrix, the power exponent b in Equation 4.1 (*i.e.* elastic modulus) changes from 0.55 to 0.7. The parameter Q in Equation 4.1 (*i.e.* elastic modulus) varies from -2.93 to 0.50. Similar observations ($Q=-0.33\sim1.31$) were found for Equation 4.3 (*i.e.* hardness). Both parameters (b and Q) will determine how the mismatch of particle and matrix elastic modulus (and yield strength) contributes to the composite modulus (and composite hardness). Such significant variations in these two parameters are due to the fact that the mismatch between the particle and matrix elastic modulus (and yield strength) is up to a factor of 80 in this study.

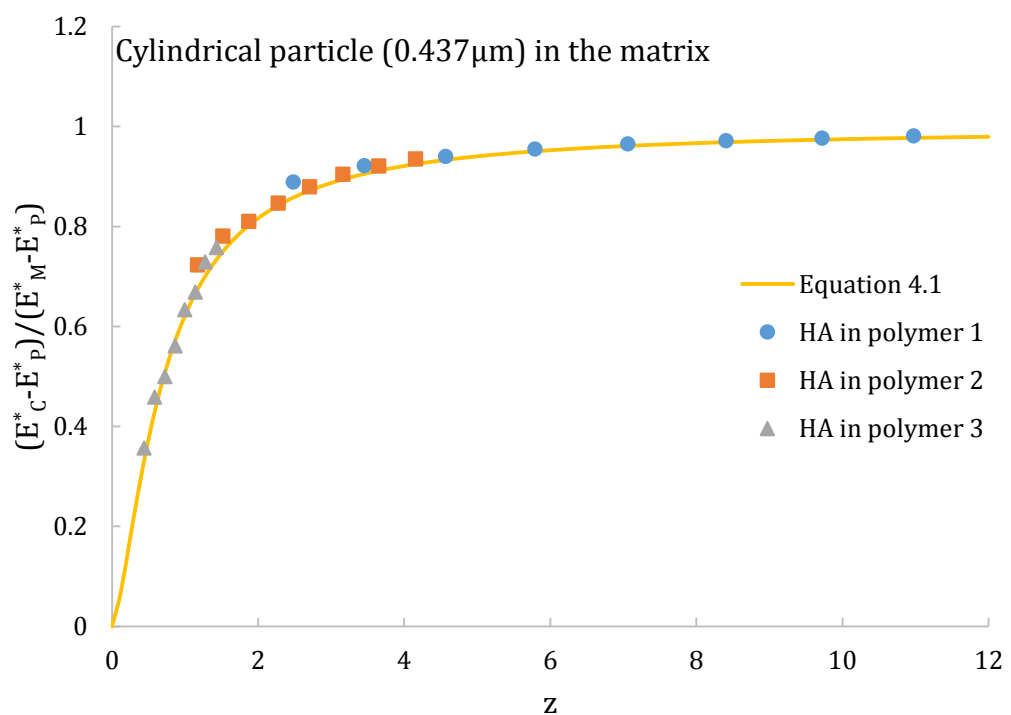


(a)

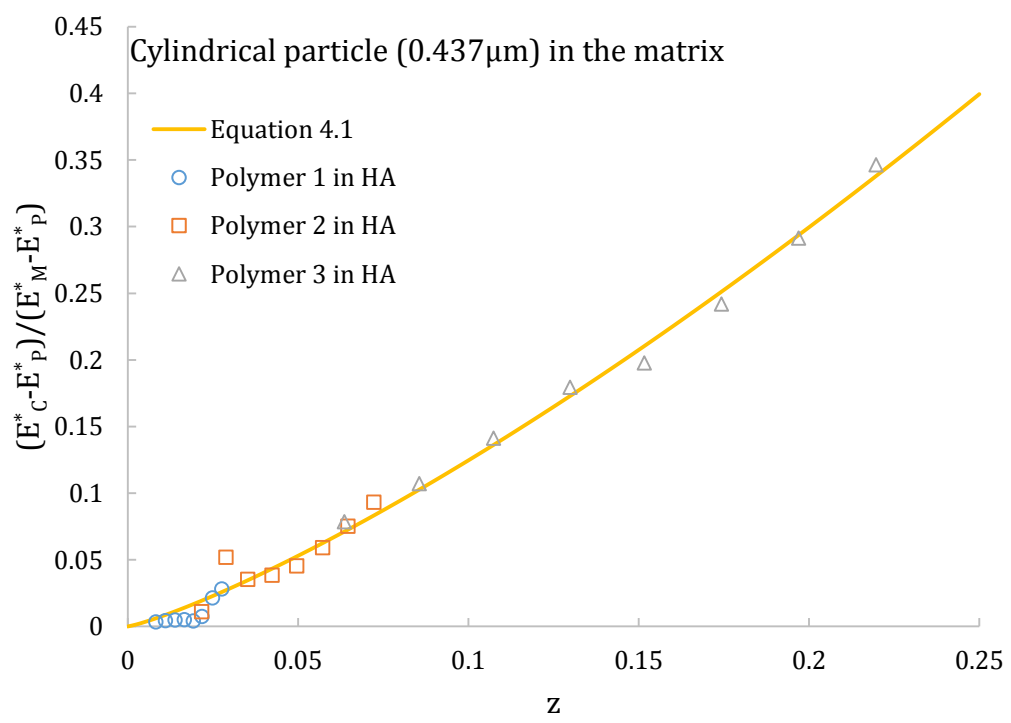


(b)

Figure 4.11 Plots of $\frac{E_C^* - E_P^*}{E_M^* - E_P^*}$ against z using Equation 4.1 for, (a) semi-spherical HA particles (0.5 μm) in polymers, (b) semi-spherical polymers (0.5 μm) in HA matrix, (c) cylindrical HA particles (0.437 μm) in polymers, (d) cylindrical polymers (0.437 μm) in HA matrix, (e) cylindrical HA particles (0.5 μm) in polymers and (f) cylindrical polymers (0.5 μm) in HA matrix.

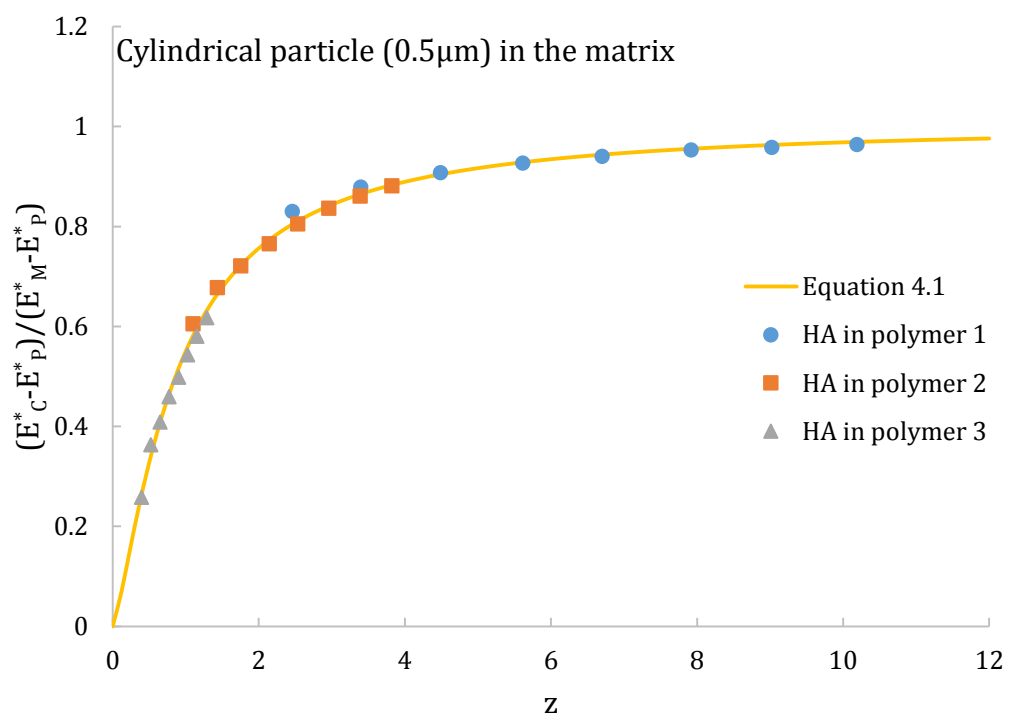


(c)

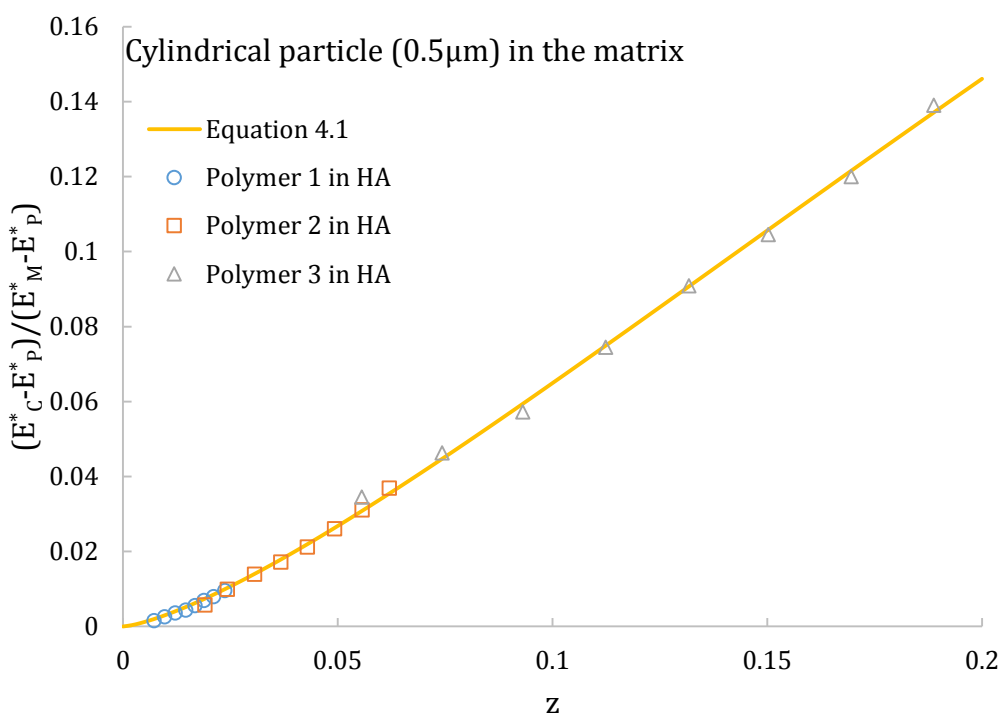


(d)

Figure 4.11 (Cont.)

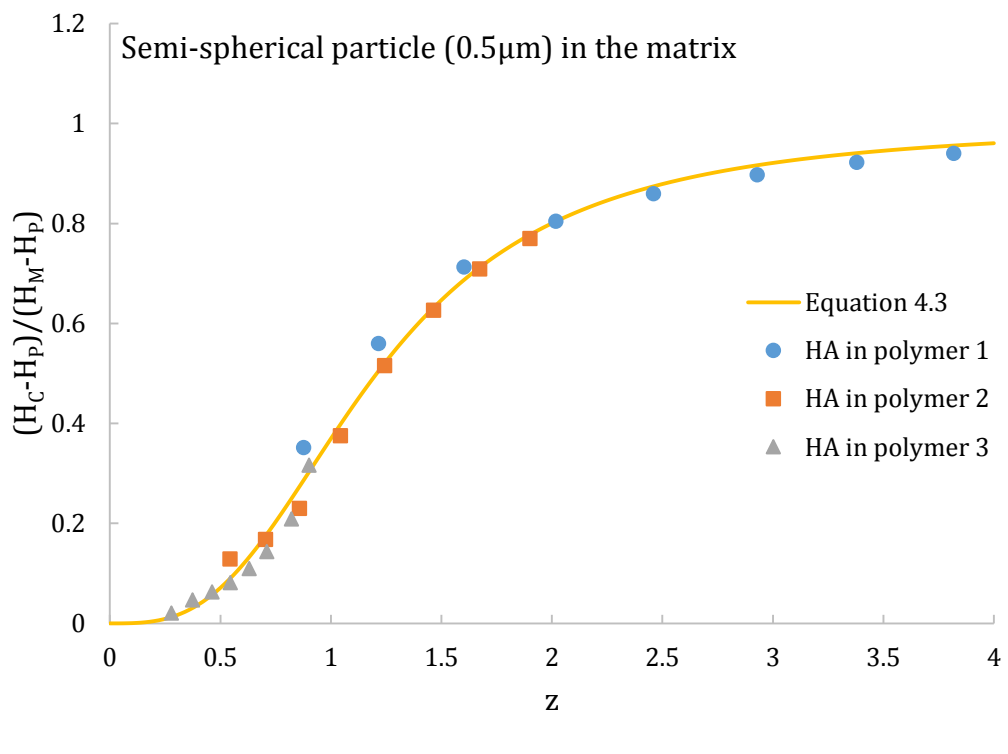


(e)

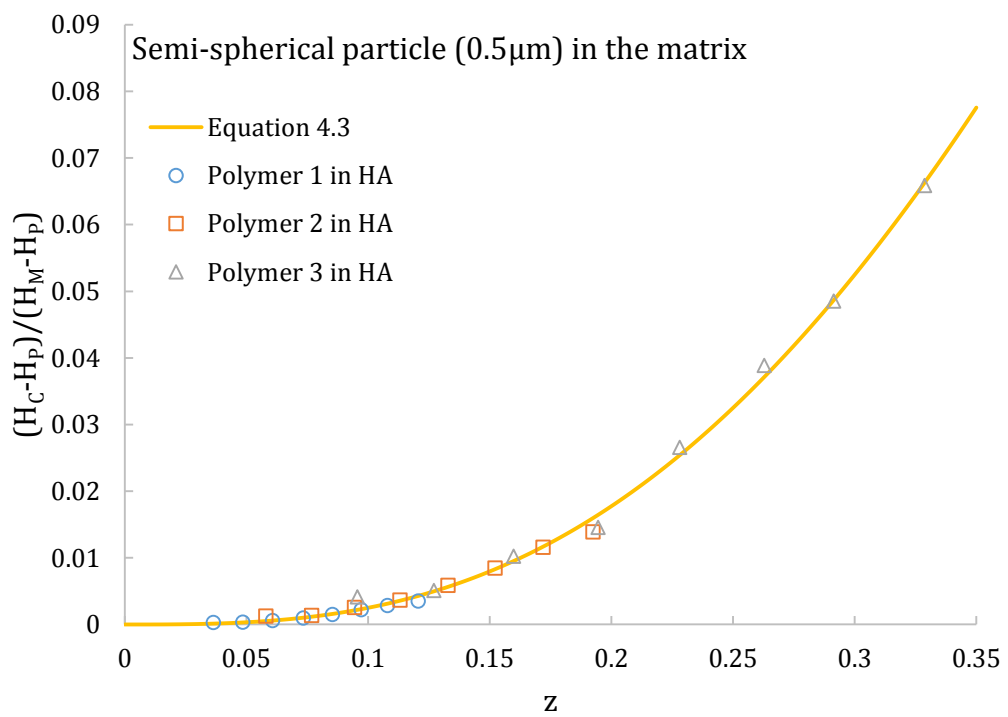


(f)

Figure 4.11 (Cont.)

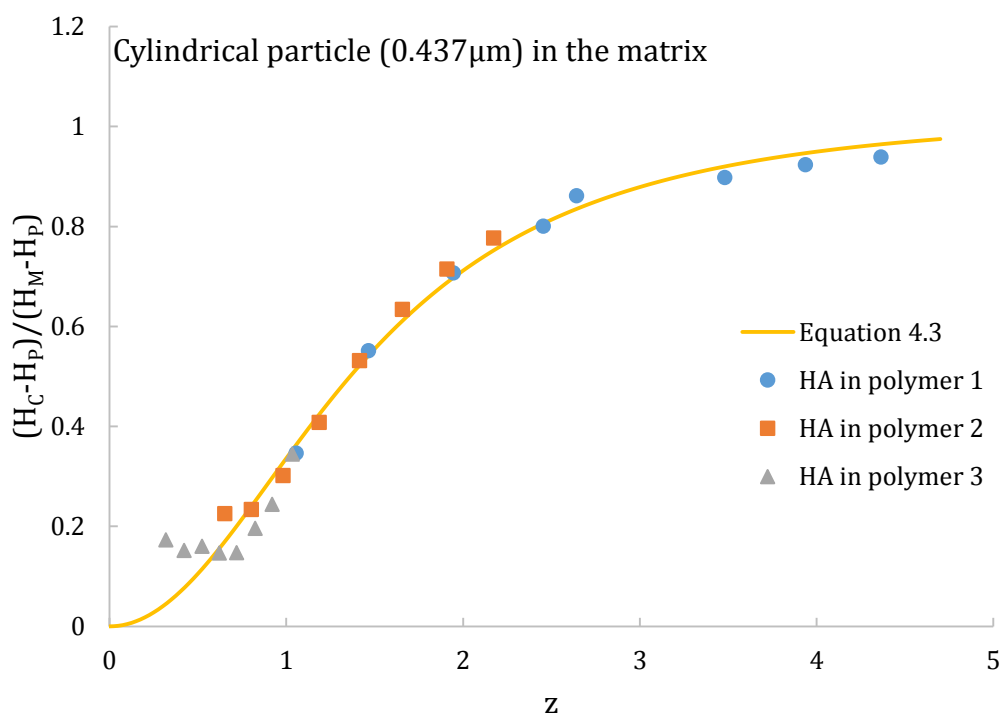


(a)

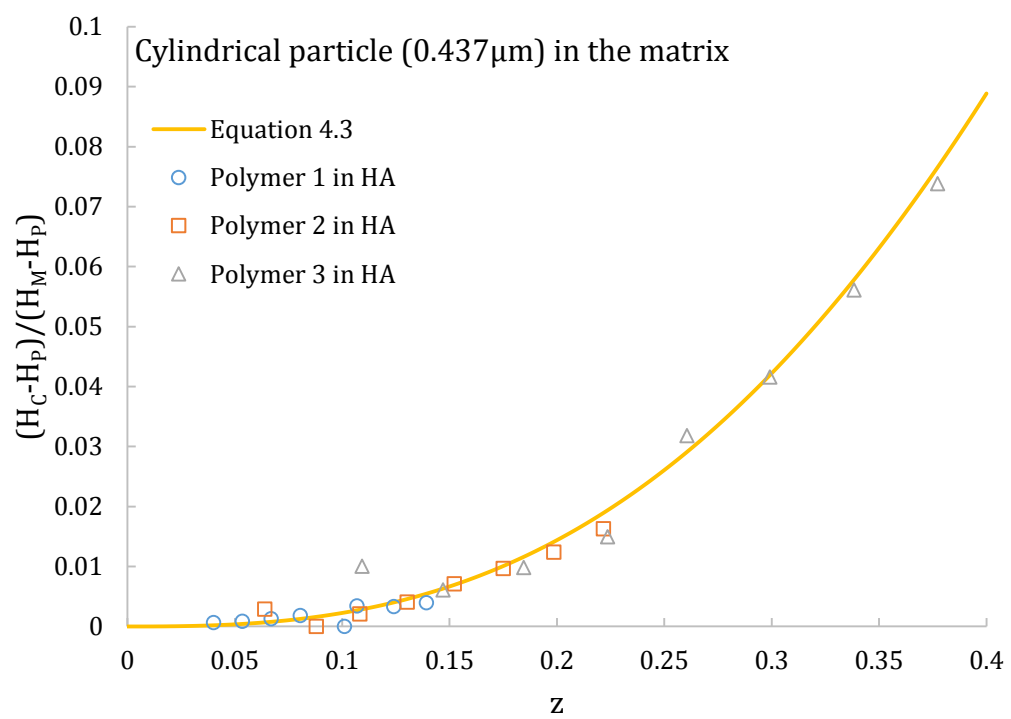


(b)

Figure 4.12 Plots of $\frac{H_c - H_p}{H_m - H_p}$ against z using Equation 4.3 for, (a) semi-spherical HA particles ($0.5 \mu\text{m}$) in polymers, (b) semi-spherical polymers ($0.5 \mu\text{m}$) in HA matrix, (c) cylindrical HA particles ($0.437 \mu\text{m}$) in polymers, (d) cylindrical polymers ($0.437 \mu\text{m}$) in HA matrix, (e) cylindrical HA particles ($0.5 \mu\text{m}$) in polymers and (f) cylindrical polymers ($0.5 \mu\text{m}$) in HA matrix.

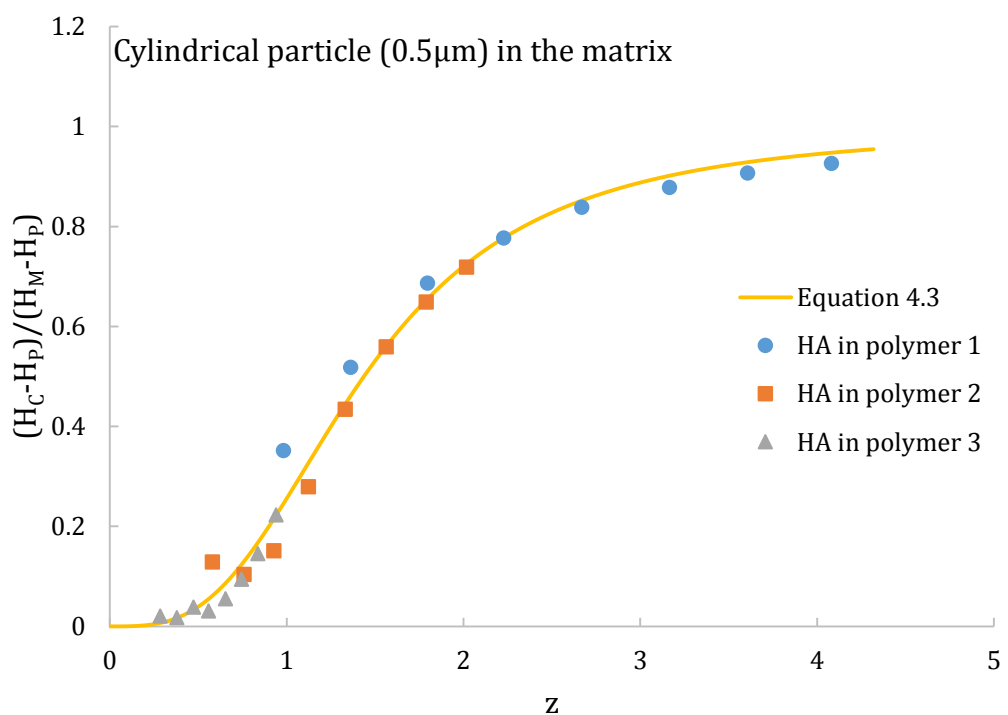


(c)

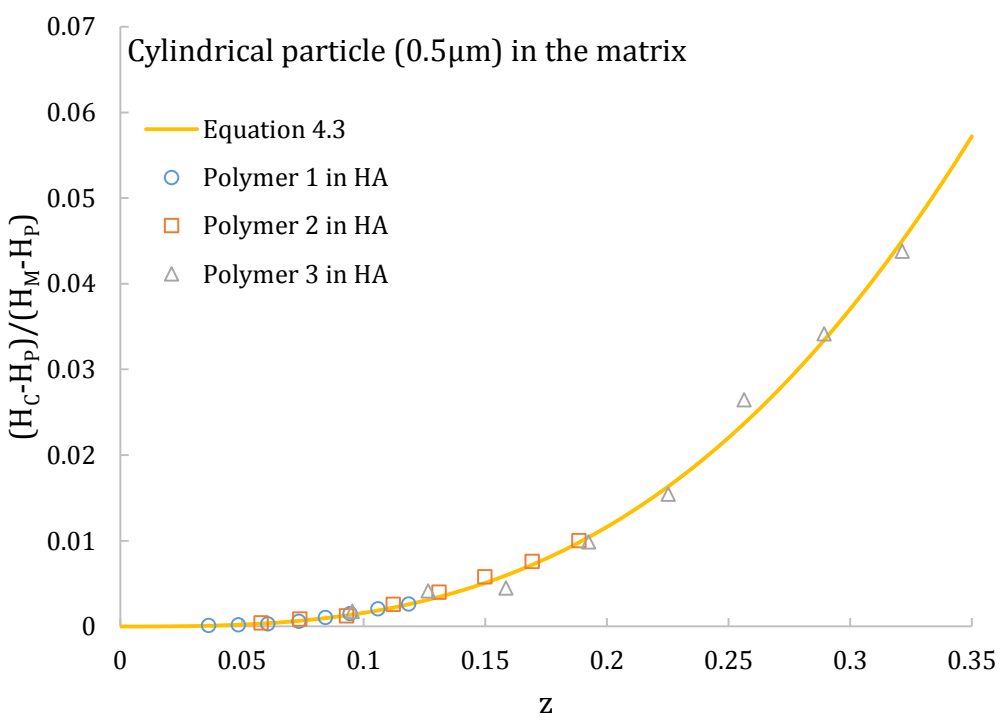


(d)

Figure 4.12 (Cont.)



(e)



(f)

Figure 4.12 (Cont.)

			<i>b</i>	<i>P</i>	<i>Q</i>	<i>n</i>	<i>R</i> ²
Semi-spherical particle (<i>r</i>=0.5 μm)	Hard particle in soft matrix	<i>E</i>	0.75	2.521	-0.020	1.344	0.9963
		<i>H</i>	0.56	0.954	0.627	3.244	0.9815
		<i>E</i>	0.70	1.058	-2.927	1.076	0.9781
	Soft particle in hard matrix	<i>E</i>	0.34	2.884	1.314	3.007	0.9779
		<i>H</i>					

Table 4.3 Best fitting parameters of Clifford model (Equation 4.1 and Equation 4.3) for semi-spherical particle model (*r*=0.5 μ m with volume of 0.131 μm^3) in this study.

			<i>b</i>	<i>P</i>	<i>Q</i>	<i>n</i>	<i>R</i> ²
Cylindrical particle with <i>r</i>=<i>t</i>=0.437 μm	Hard particle in soft matrix	<i>E</i>	0.73	1.702	0.034	1.482	0.9940
		<i>H</i>	0.53	0.423	-0.164	1.970	0.9505
		<i>E</i>	0.55	1.721	-1.979	1.178	0.9540
	Soft particle in hard matrix	<i>E</i>	0.35	0.970	-0.297	2.645	0.9101
		<i>H</i>					

Table 4.4 Best fitting parameters of Clifford model (Equation 4.1 and Equation 4.3) for cylindrical particle model (*r*=*t*=0.437 μ m with volume of 0.131 μm^3) in this study.

			b	P	Q	n	R²
	Hard	E	0.75	1.200	-0.019	1.314	0.9944
	particle in						
Cylindrical	soft matrix	H	0.50	0.552	0.605	3.366	0.9629
particle							
with							
r=t=0.5 μm	Soft	E	0.57	1.704	0.503	1.368	0.9945
	particle in						
	hard matrix	H	0.34	1.055	-0.327	2.836	0.9580

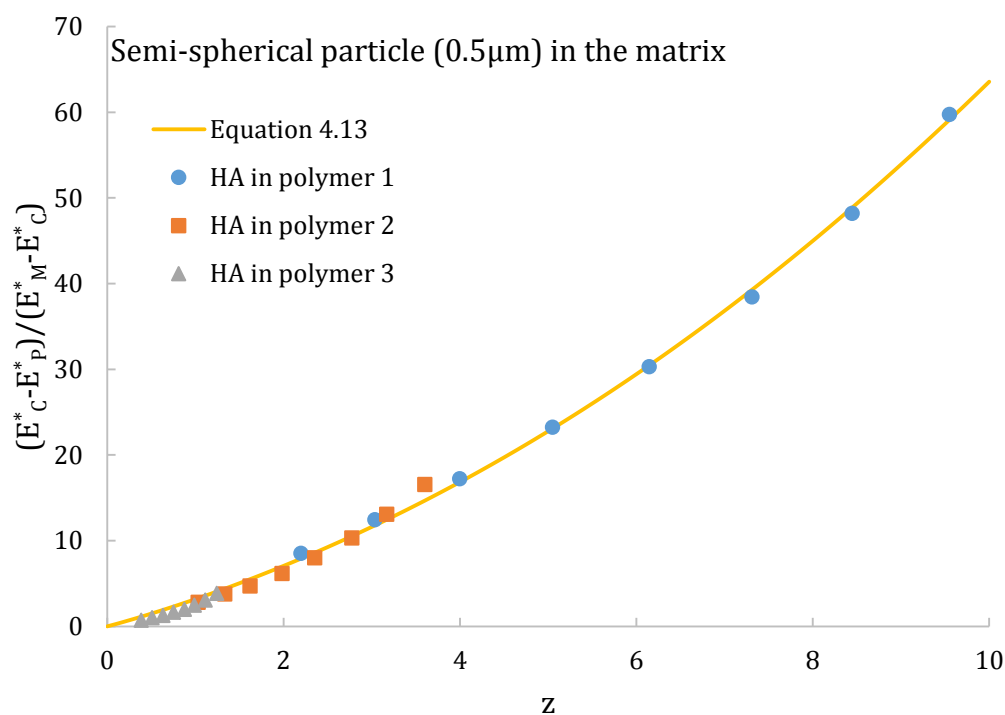
Table 4.5 Best fitting parameters of Clifford model (Equation 4.1 and Equation 4.3) for cylindrical particle model ($r=t=0.5 \mu\text{m}$ with volume of $0.196 \mu\text{m}^3$) in this study.

In order to compare the contributions on the composite modulus and hardness caused by the particle and matrix during an indentation test, we propose the following equations by rewriting the denominator of the left hand side of Equation 4.1 and Equation 4.3,

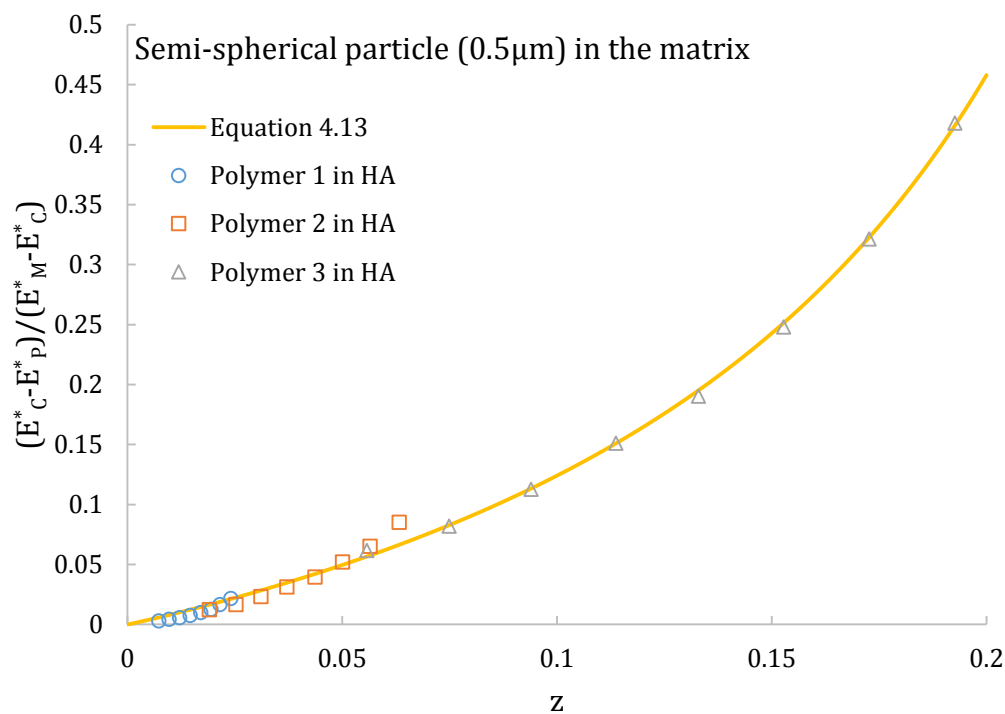
$$\frac{E_C^* - E_P^*}{E_M^* - E_C^*} = \frac{Pz^n}{1 + Pz^n + Qz} \quad (4.13)$$

$$\frac{H_C - H_P}{H_M - H_C} = \frac{Pz^n}{1 + Pz^n + Qz} \quad (4.14)$$

When plotting $\frac{E_C^* - E_P^*}{E_M^* - E_C^*}$ against z , as shown in Figure 4.13, all the data converge on a single curve. A similar observation was also found for the plot of $\frac{H_C - H_P}{H_M - H_C}$ against z , as shown in Figure 4.14. The fitting parameters are summarized in Tables 4.6-4.8.



(a)



(b)

Figure 4.13 Plots of $\frac{E_C^* - E_P^*}{E_M^* - E_C^*}$ against z using Equation 4.13 for, (a) semi-spherical HA particles (0.5 μm) in polymers, (b) semi-spherical polymers (0.5 μm) in HA matrix, (c) cylindrical HA particles (0.437 μm) in polymers, (d) cylindrical polymers (0.437 μm) in HA matrix, (e) cylindrical HA particles (0.5 μm) in polymers and (f) cylindrical polymers (0.5 μm) in HA matrix.

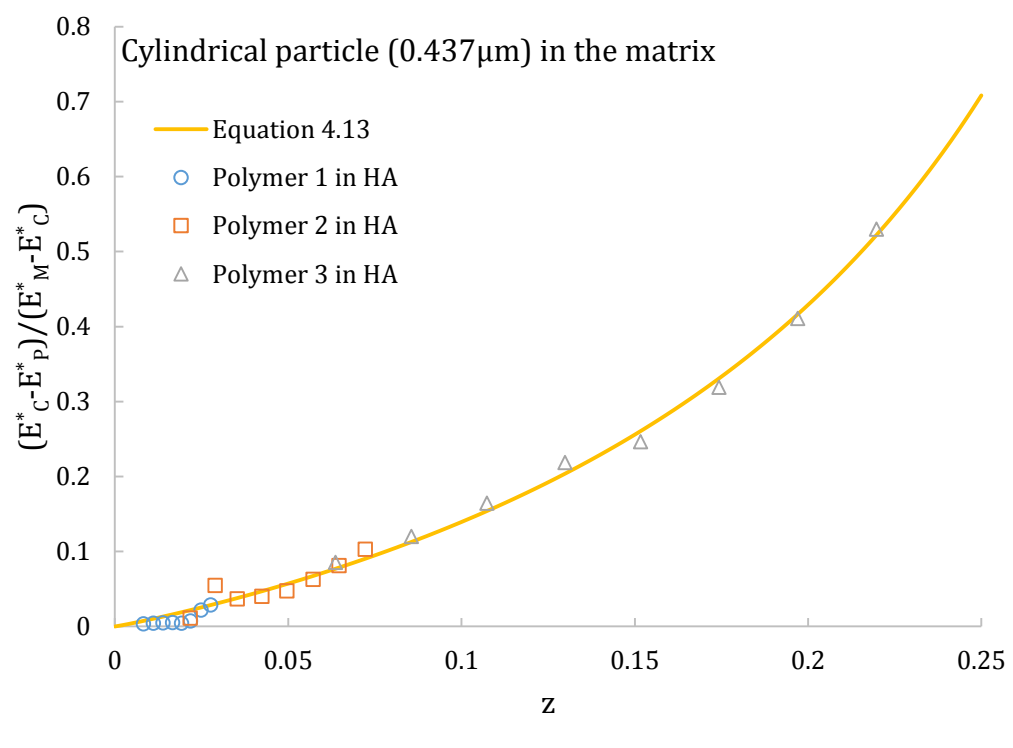
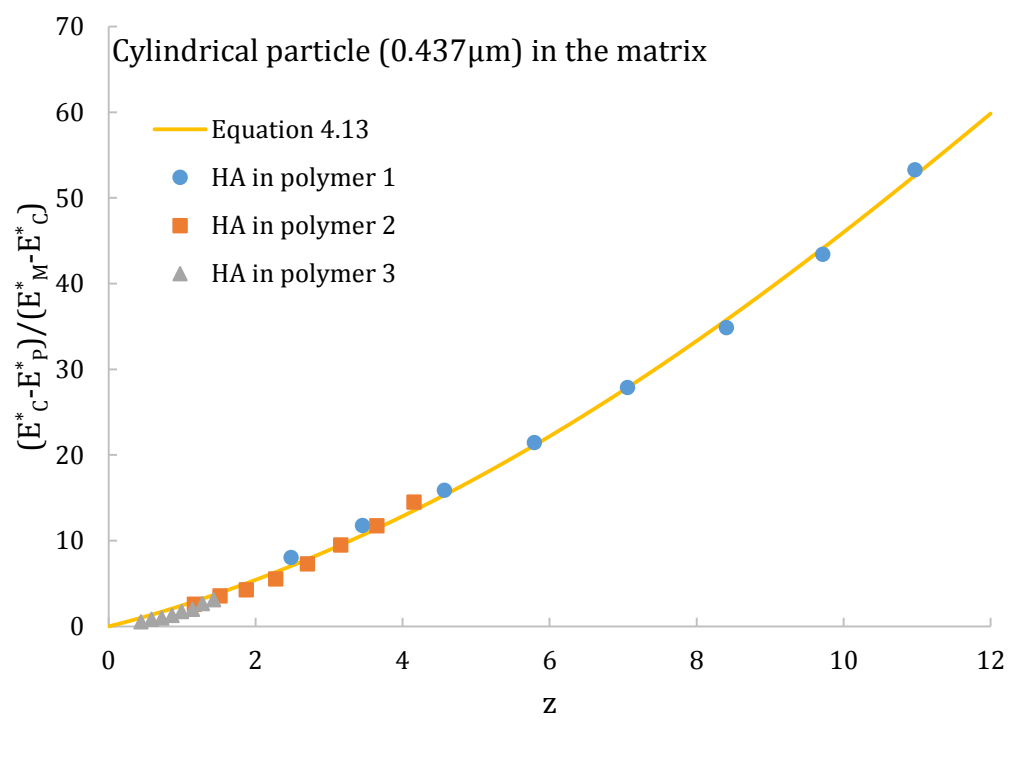
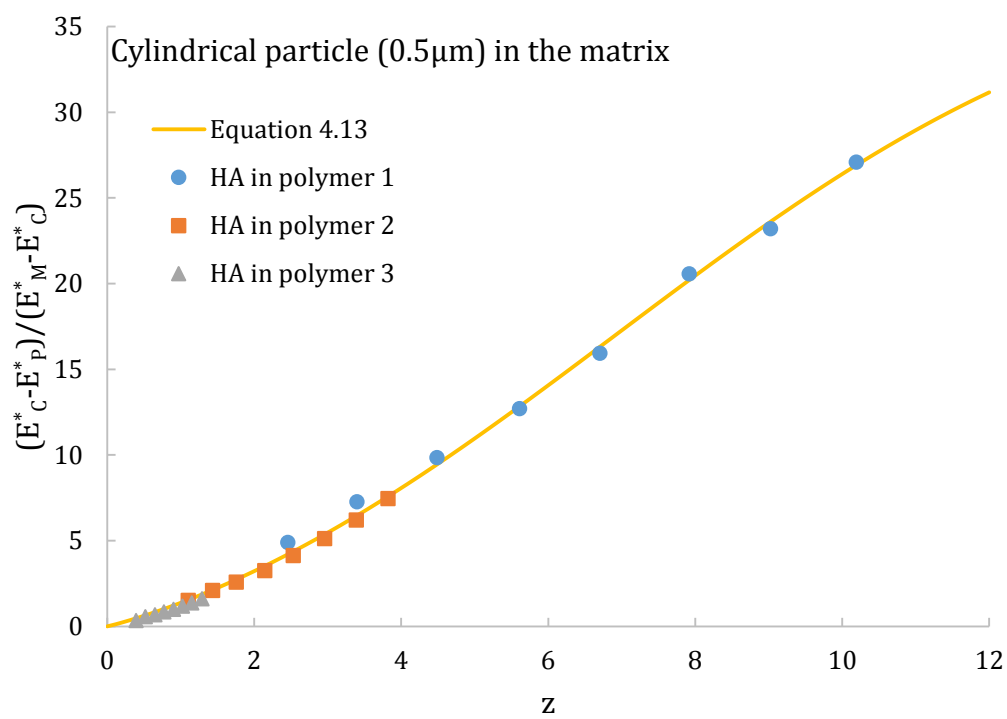
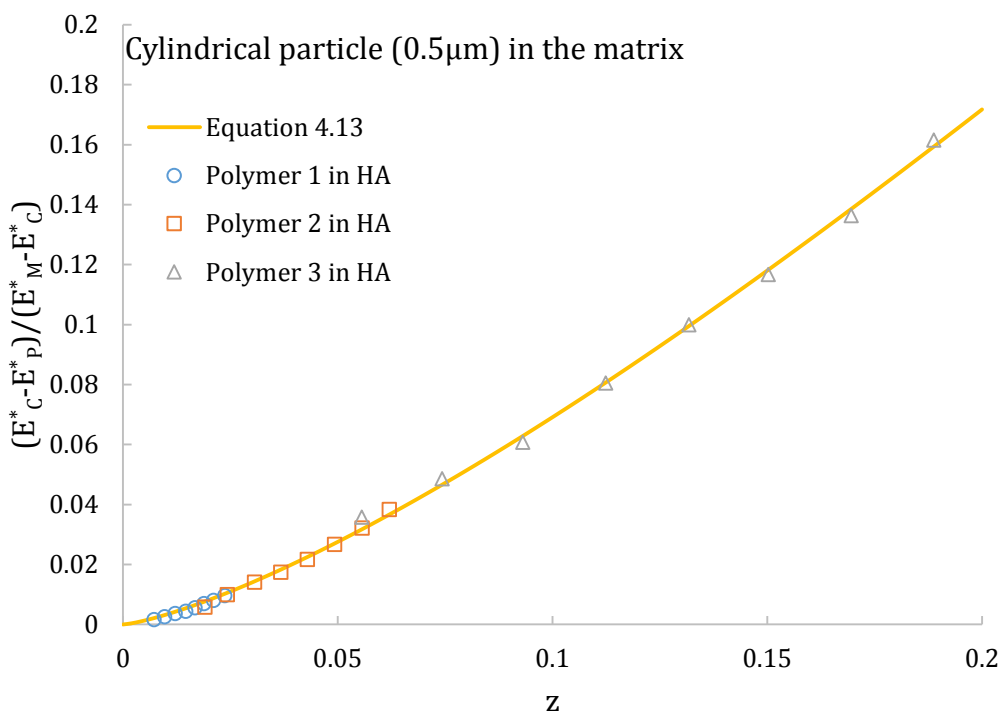


Figure 4.13 (Cont.)



(e)



(f)

Figure 4.13 (Cont.)

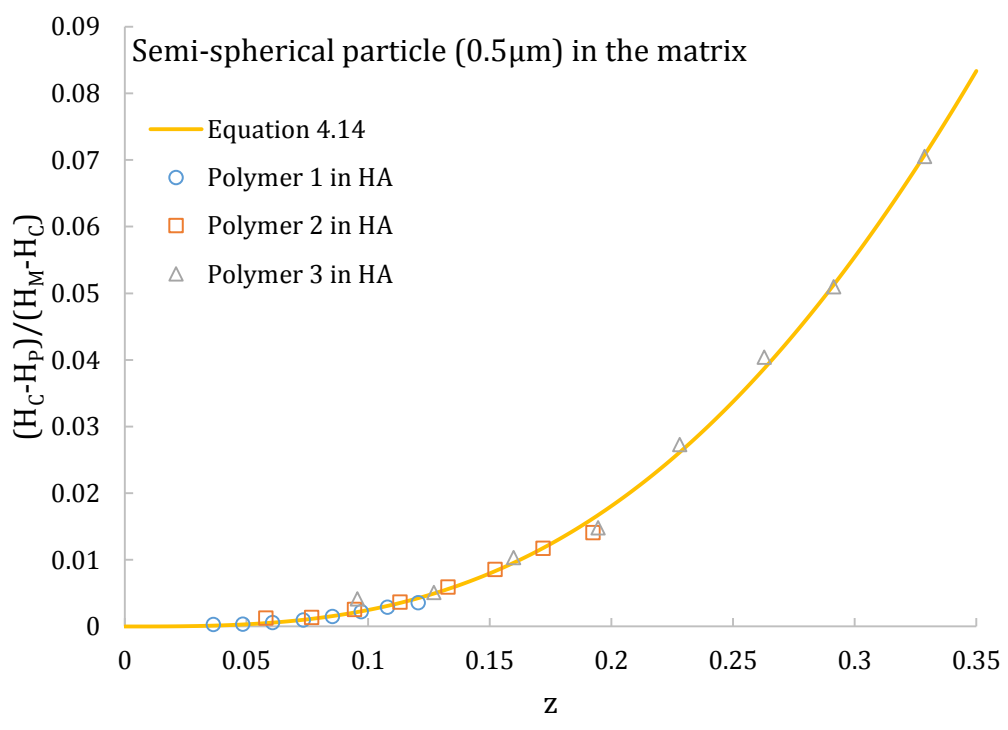
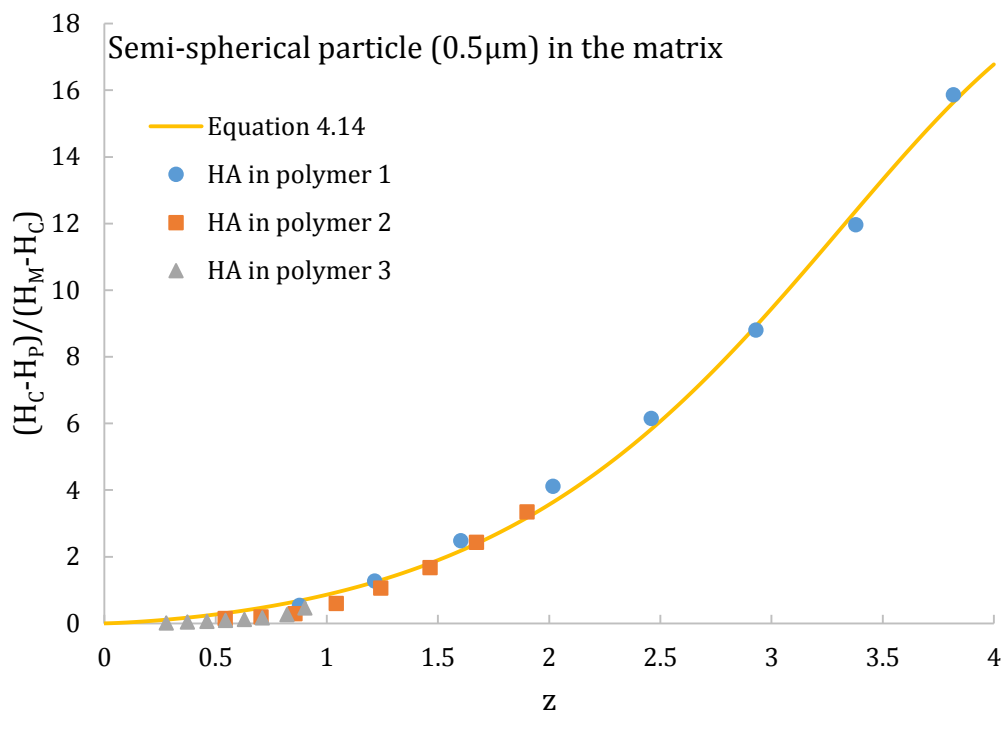
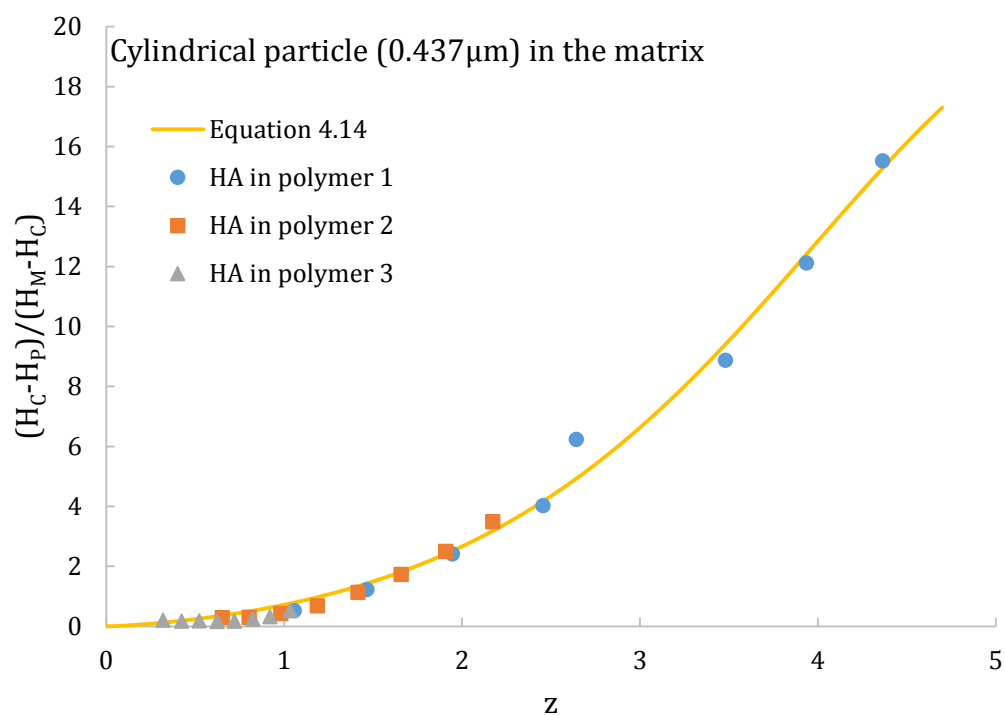
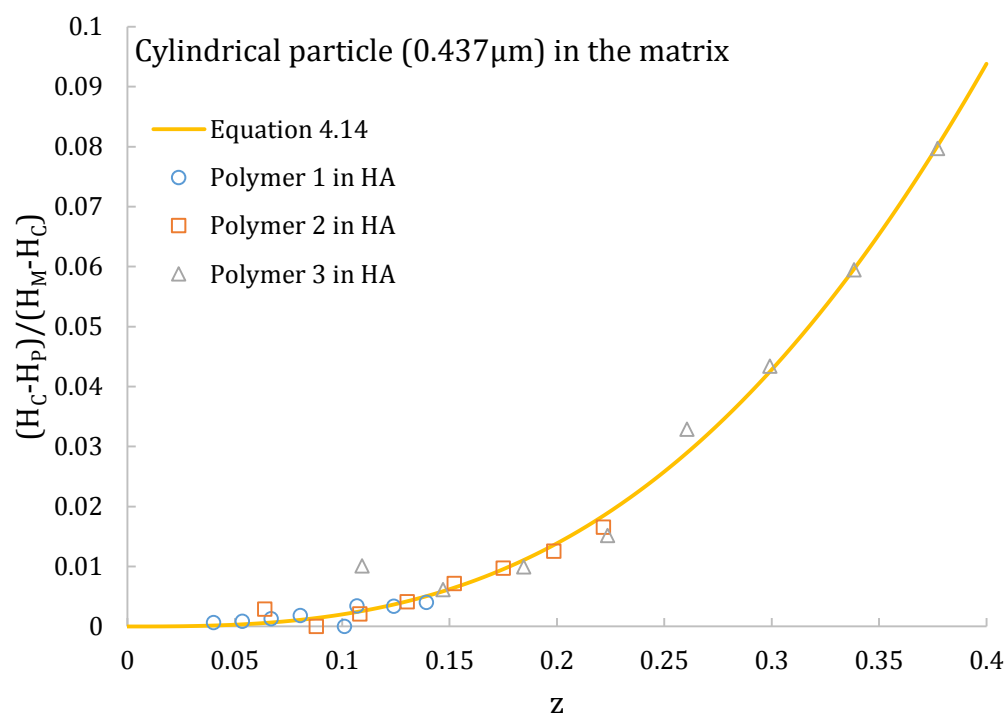


Figure 4.14 Plots of $\frac{H_c - H_p}{H_m - H_c}$ against z using Equation 4.14 for, (a) semi-spherical HA particles ($0.5\mu\text{m}$) in polymers, (b) semi-spherical polymers ($0.5\mu\text{m}$) in HA matrix, (c) cylindrical HA particles ($0.437\mu\text{m}$) in polymers, (d) cylindrical polymers ($0.437\mu\text{m}$) in HA matrix, (e) cylindrical HA particles ($0.5\mu\text{m}$) in polymers and (f) cylindrical polymers ($0.5\mu\text{m}$) in HA matrix.



(c)



(d)

Figure 4.14 (Cont.)

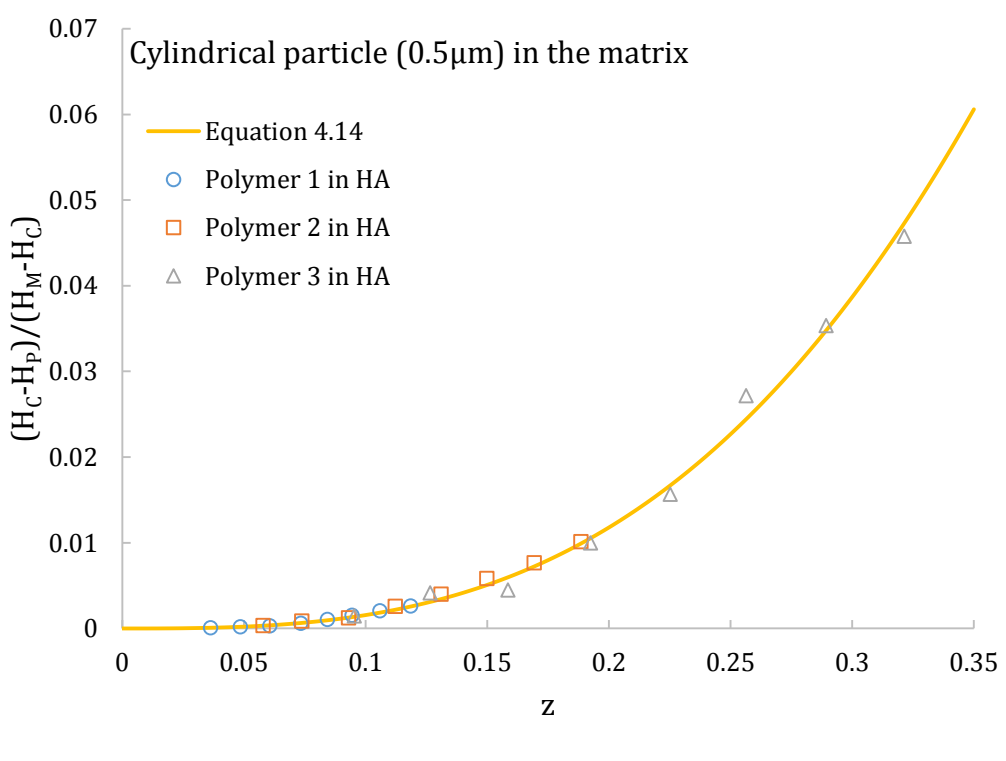
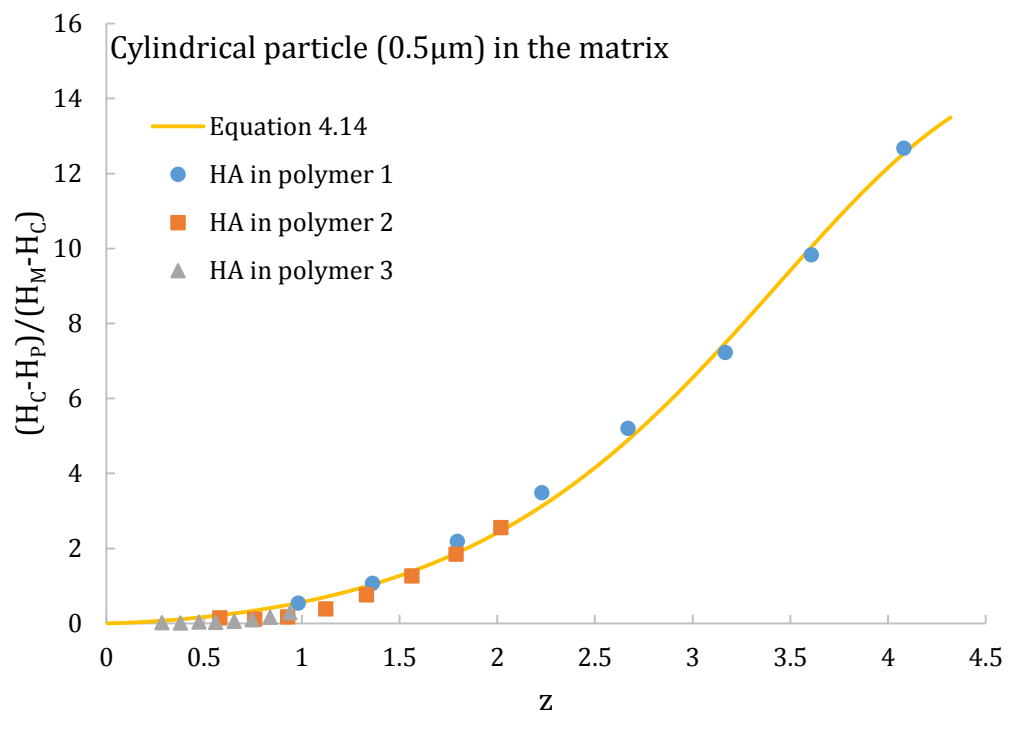


Figure 4.14 (Cont.)

			<i>b</i>	<i>P</i>	<i>Q</i>	<i>n</i>	<i>R</i> ²	
		Hard	<i>E</i>	0.70	2.789	-2.912	1.010	0.9618
		particle in						
Semi-	spherical	soft matrix	<i>H</i>	0.50	0.482	-0.922	1.284	0.9598
particle								
(<i>r</i>=0.5 μm)		Soft	<i>E</i>	0.70	0.918	-3.966	1.031	0.9811
		particle in						
		hard matrix	<i>H</i>	0.34	2.246	0.358	2.942	0.9789

Table 4.6 Best fitting parameters of modified Clifford model (Equation 4.13 and Equation 4.14) for semi-spherical particle model ($r=0.5 \mu\text{m}$ with volume of $0.131 \mu\text{m}^3$) in this study.

			<i>b</i>	<i>P</i>	<i>Q</i>	<i>n</i>	<i>R</i> ²	
		Hard	<i>E</i>	0.70	2.147	-2.268	1.014	0.9803
		particle in						
Cylindrical	particle	soft matrix	<i>H</i>	0.50	0.443	-0.830	1.252	0.9259
with <i>r=t</i>=								
0.437 μm		Soft	<i>E</i>	0.70	1.218	-3.542	1.066	0.9592
		particle in						
		hard matrix	<i>H</i>	0.34	1.032	-0.455	2.728	0.9122

Table 4.7 Best fitting parameters of modified Clifford model (Equation 4.13 and Equation 4.14) for cylindrical particle model ($r=t=0.437 \mu\text{m}$ with volume of $0.131 \mu\text{m}^3$) in this study.

		<i>b</i>	<i>P</i>	<i>Q</i>	<i>n</i>	<i>R</i> ²
	Hard particle in soft matrix	<i>E</i>	0.70	1.144	-1.313	1.042
Cylindrical particle with $r=t=0.5 \mu\text{m}$		<i>H</i>	0.50	0.329	-0.748	1.360
	Soft particle in hard matrix	<i>E</i>	0.70	1.373	-0.996	1.313
		<i>H</i>	0.34	1.020	-0.560	2.838
						0.9941
						0.9581

Table 4.8 Best fitting parameters of modified Clifford model (Equation 4.13 and Equation 4.14) for cylindrical particle model ($r=t=0.5 \mu\text{m}$ with volume of $0.196 \mu\text{m}^3$) in this study.

When the modified model is used, the value of *b* (i.e. $b=0.7$) for elastic modulus (i.e. Equation 4.13) is independent of the material combination, the particle shape and the volume in this study. For the hardness, the value of *b* is independent of the particle shape and the volume but depends on the constraints applied to the particles by the stiff matrix. For hard particle in soft matrix, the value of *b* equals 0.7 and 0.5 for elastic modulus and hardness, respectively, regardless of the particle shape and the volume. While, for soft particle in hard matrix, the value of *b* equals 0.7 and 0.34 for elastic modulus and hardness, respectively. Such consistence in the *b* values cannot be achieved by the Clifford model. The values of *Q* in the modified model are between -3.97 and -1.00 for the elastic modulus. These values are between -0.92 and 0.36 for hardness. The magnitudes of these *Q* values for hardness are consistently greater than their counterparts for elastic modulus. This is due to the fact that the plastic deformation zone is much confined compared to the elastic deformation. However, the values of *Q* in the Clifford model seem random and do not reflect such physical insights.

4.5 Summary

FEM was done to study the spatial-dependent composite modulus and hardness during nanoindentation tests. The reported rule-of-thumb to determine the modulus and hardness of particles at a penetration below 5% and 13.5% are reasonable approximations for composites with relatively small mismatch in elastic modulus and hardness between particle and matrix. But they do not apply to the composites with large mismatch in elastic modulus and hardness between particle and matrix. Therefore, new models have been developed based on the original Clifford model, which enables us to determine elastic modulus and hardness for such composite materials. These models have been successfully applied to various composites regardless of particle geometry, volume and material combination. In principle, such models can also be extended to biological composites such as biofilms which can be treated as hard particles (bacteria) embedded in soft matrix (extracellular polymeric substance).

In the next chapter, finite element modelling for the nanoindentation of inclusion/matrix composite with varying indentation locations and fibre orientations will be presented to assess the elastic response of this inclusion/matrix composite.

Chapter 5

Nanomechanical Modelling of Elastic Fibre with Different Orientations in Elastic Matrix

Chapter 5. Nanomechanical Modelling of Elastic Fibre with Different Orientations in Elastic Matrix

5.1 Introduction

During the past decades, biocomposites (such as bioceramics and biopolymers) have been widely used as artificial scaffold materials in tissue engineering (Venugopal and Ramakrishna, 2005; Rezwan *et al.*, 2006; Soloviev, 2012). As one of the key requirements, implanted scaffolds must be strong enough to avoid the fracture during the patient's normal activities (Hu *et al.*, 2010). Thus, it is of great importance to understand how the surrounding matrix will affect the measured mechanical properties, which will provide a guidance for the optimisation of material processing to achieve the target design properties.

Numerous studies have proved that nanoindentation is a powerful tool to determine the mechanical properties of composite materials (Li and Bhushan, 1998; Lim *et al.*, 1999; Chen *et al.*, 2010a; Chakraborty and Bhowmik, 2014; De Silva *et al.*, 2014; Herruzo *et al.*, 2014). However, when performing nanoindentation on inclusions or the matrix, it is challenging to define the inevitable influence of the surrounding second phase. There is a lack of sophisticated studies on how the indentation location and the inclusion orientation would affect the mechanical behaviours of the composites. Therefore, in this chapter, FEA is adopted to investigate the elastic response of fibre-reinforced composite under nanoindentation test. By varying the indentation location and the fibre orientation, this work reveals the correlation between the elastic properties of fibre-reinforced composite and the elastic properties of each individual constituent. In practice, this work can be used to predict the elastic response of fibre periodically reinforced composites, or extract the properties of the matrix and the fibre.

5.2 Methodology

5.2.1 Analytical method

In the previous chapter, the Clifford model as well as another two proposed linear-based equations have been effectively used to study how the composite elastic modulus changes with the penetration depth for the inclusion/matrix composite. Based on this, these equations were also used in this chapter to study the elastic response of model with different indentation locations and fibre orientations, here repeated for convenience (Clifford and Seah, 2006; Duan *et al.*, 2015),

$$\frac{E^* - E_I^*}{E_M^* - E_I^*} = \frac{Pz^n}{1 + Pz^n + Qz} \quad (5.1)$$

$$\frac{E^* - E_I^*}{E_M^* - E_I^*} = B \cdot z \quad (5.2)$$

$$\frac{1/E^* - 1/E_I^*}{1/E_M^* - 1/E_I^*} = B(e^z - 1) \quad (5.3)$$

where E^* , E_I^* and E_M^* are the reduced modulus of the composite, inclusion and matrix, respectively. P , Q , n and B are the fitting constants. z is the relative contact radius, which is given by,

$$z = \frac{a}{t} \left(\frac{E_I^*}{E_M^*} \right)^b \quad (5.4)$$

where b is a fitting constant, which weights the elastic mismatch between the inclusion and the matrix.

In addition, in order to extract the nanomechanical properties of each individual constituent of the composite, a linear equation and a second order polynomial equation were also proposed in this chapter based on numerical fitting, which is given by (ISO14577, 2007; Clifford and Seah, 2012),

$$E = A \cdot \delta + C \quad (5.5)$$

$$E = A \cdot \delta^2 + B \cdot \delta + C \quad (5.6)$$

where E is the composite elastic modulus, δ is the displacement. A , B and C are the fitting constants. The intercept C gives the elastic modulus of the indented material (inclusion or matrix), because when the displacement is approaching to zero, the apparent elastic modulus should be negligibly influenced by the other component (matrix or inclusion).

5.2.2 Finite element method

In practice, when indenting the inclusion/matrix composite, the indentation may not always take place in the centre of the inclusion and the fibre inclusions may be randomly orientated. During nanoindentation tests, the indentation direction may be parallel, perpendicular or at an arbitrary angle to the inclusion axis. Therefore, in this study, by modelling the nanomechanical response of the inclusion/matrix composite indented by a conical indenter and a Berkovich indenter, FEA was adopted to investigate the effects of the distance between the inclusion and the indenter, the orientation of the fibre inclusion and the geometry of the indenter during the nanoindentation tests. For simplification, the inclusions with vertical orientation and horizontal orientation relative to the indentation direction were modelled. As shown in Figure 5.1, r is the radius of the inclusion, which equals 1 μm . d is the horizontal distance between the centre of the inclusion and the indentation point in the case of a vertical inclusion, or the vertical distance that the centre of inclusion away from the sample free surface in the case of a horizontal inclusion. In this study, the ratio of d/r varied from 0 to 5. For simplification, both the inclusion and the matrix were considered as elastic materials. The Young's modulus of the inclusion and the matrix were fixed at 10 MPa and 2 MPa (similar to the elastic modulus of 50/50 PLLA/PDLA blends and pure PDLA (Chen *et al.*, 2003)), respectively, with their Poisson's ratio set as 0.3. This combination represented one of the combinations studied in Chapter 3. As the nanomechanical response of different material combinations were investigated in previous chapters, only one material combination was considered here. Both a Berkovich indenter and a conical indenter were used, with the tip radius of 0.1 μm . The half-included angle of the conical indenter was set to 70.3°, which was identical to the equivalent angle of the Berkovich indenter.

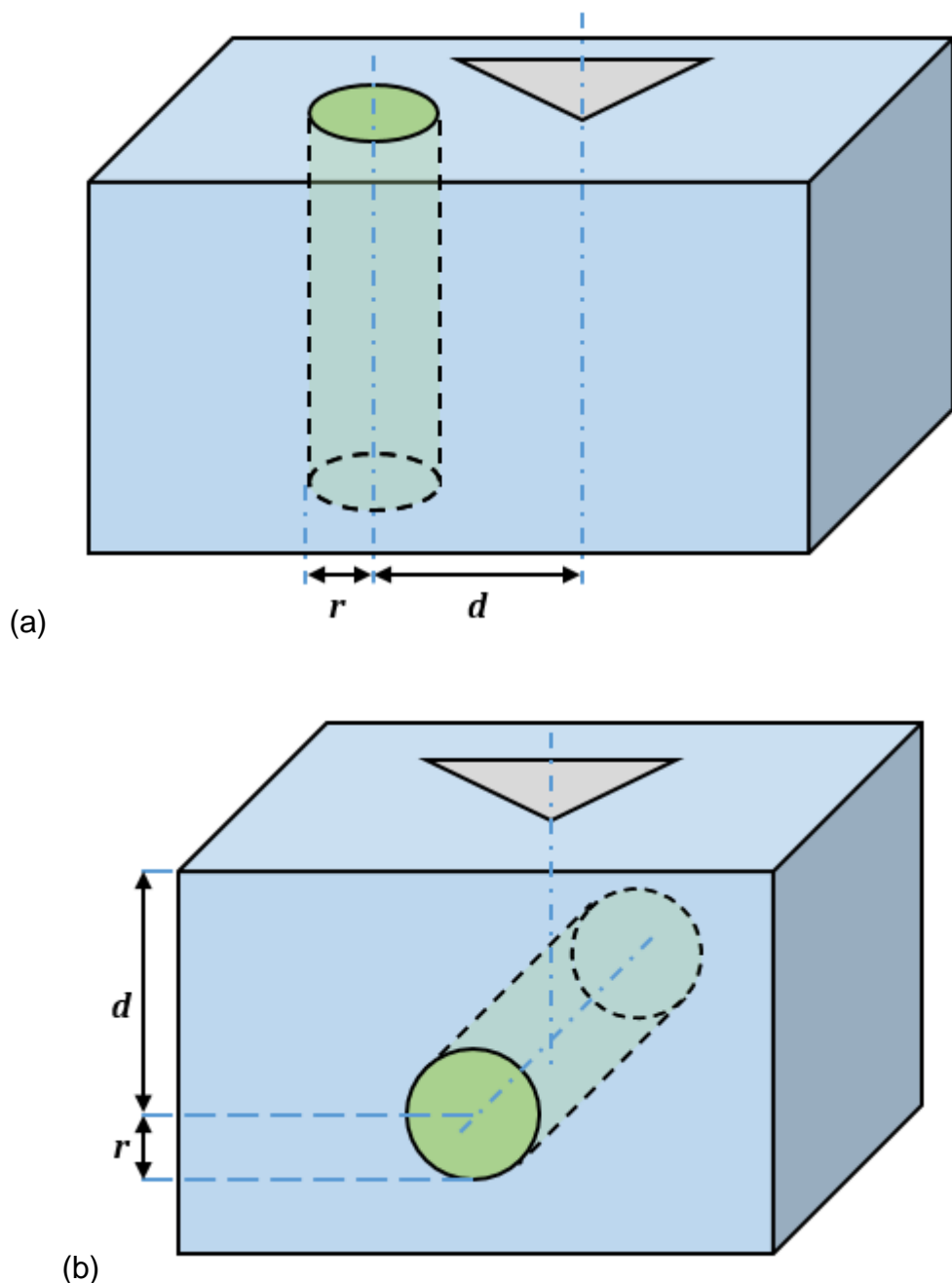
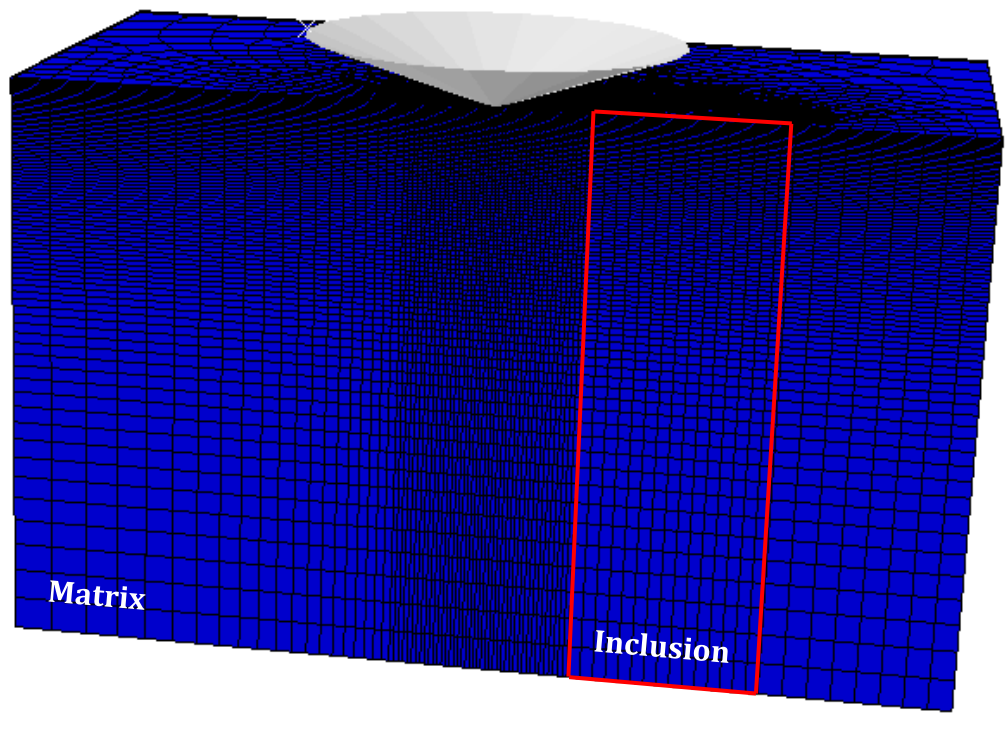


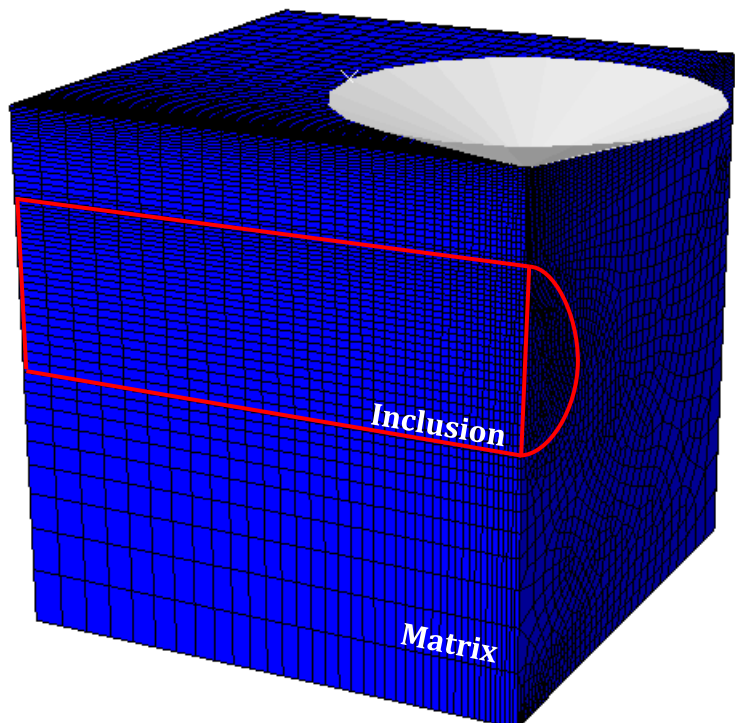
Figure 5.1 Schematic of the indentation of reinforced fibre with different orientations in matrix. (a) A vertical fibre embedded in the matrix and (b) a horizontal fibre embedded in the matrix, with the indenter just above the centre of the inclusion.

Due to the symmetric nature of the indenter and the inclusion/matrix composite, a half three-dimensional model was adopted to improve the computational efficiency. Whenever possible (namely, for the horizontal fibre model and for the vertical fibre model when $d/r = 0$), the model was further simplified to a quarter three-dimensional model or a two-dimensional axisymmetric model to reduce the computing time. The finite element model was

created in the ABAQUS 6.14 software. Figure 5.2 shows the details of the finite element mesh for the representative models: (a) the vertical fibre model when $d/r = 2$, and (b) the horizontal fibre model when $d/r = 2$. The element type is C3D6 (A 6-node linear triangular prism). A minimum number of 200,000 elements were used to create the half model of the inclusion and the matrix (at least 100,000 elements for the quarter model). To improve the simulation accuracy, finer mesh was arranged with proximity to the specimen/indenter contact region. According to the previous experience, the density of mesh set for each model should be fine enough. Thus, the model validation is not repeated in this chapter (Duan *et al.*, 2015). The interface between the indenter and the sample was assumed to be frictionless (Chen and Bull, 2009b; Low *et al.*, 2015). As the indenter was much stiffer than the specimen, the conical indenter was modelled as a rigid body. While the Berkovich indenter (as shown in Figure 5.3) was modelled as a deformable body due to its relatively complicated geometry, with its elastic properties the same as diamond ($E=1141$ GPa, $\nu=0.07$). The inclusion was assumed to be perfectly bonded with the matrix. For the boundary conditions, a completely fixed boundary condition was applied to the bottom of the specimen, and symmetric boundary conditions were applied to the symmetry planes of the specimen. The height and the width of the model are sufficiently large compared to the penetration depth so that the influence from the sample edges will be minimal. To optimize the efficiency, the movement of the indenter was controlled by displacement. A loading-unloading indentation procedure was applied with the maximum displacement varied from 0.2 μm to 0.5 μm . As depicted in Figure 5.4, the indenter reaches the maximum displacement within 1 second, and then gets back to the original place. In all cases, the elastic modulus of the composite was determined from the $F-\delta$ curves by the Oliver and Pharr method.



(a)



(b)

Figure 5.2 Finite element mesh for (a) the vertical fibre model and (b) the horizontal fibre model in the case of $d/r = 2$, indented by the conical indenter.

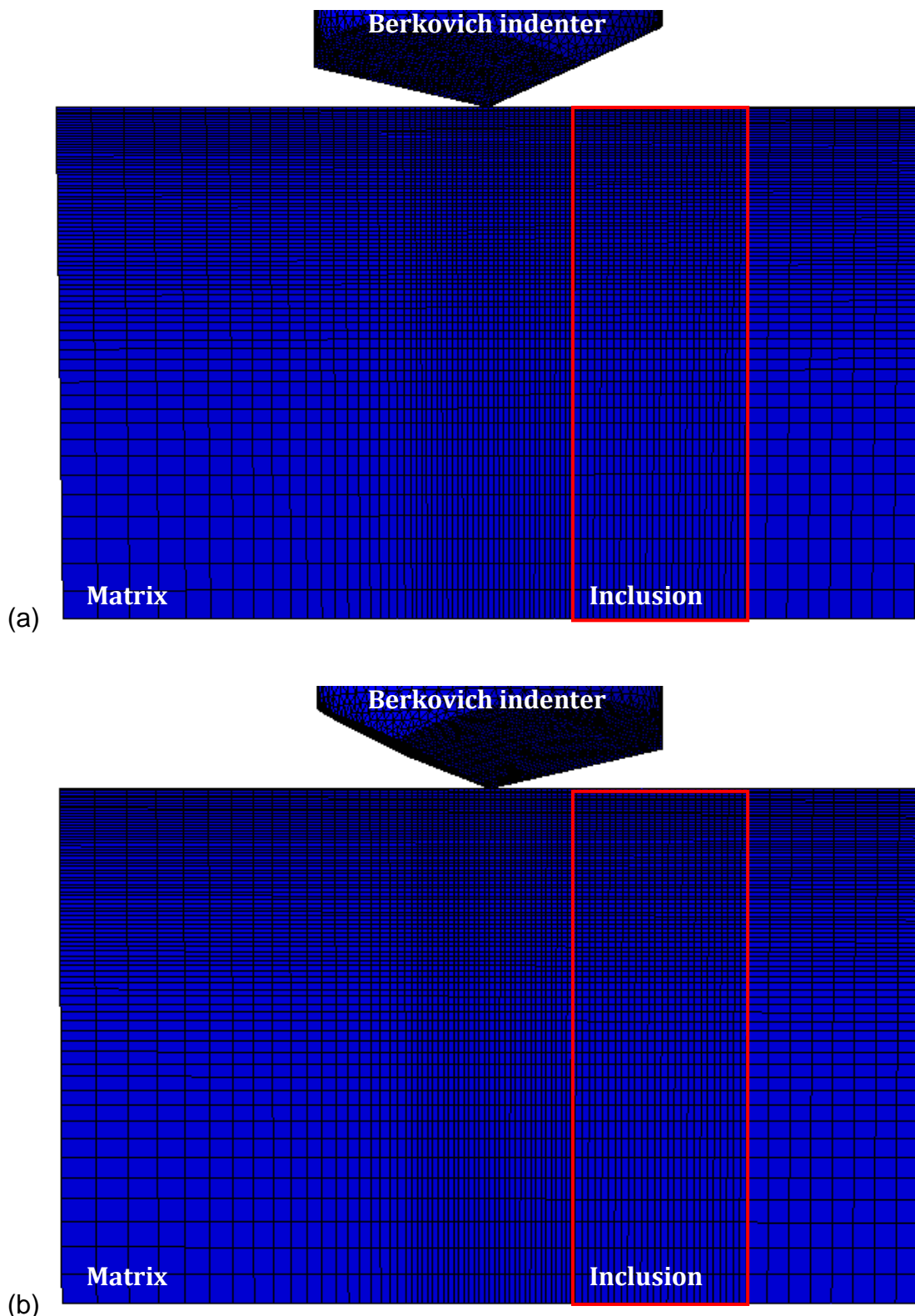


Figure 5.3 Finite element mesh for the vertical fibre model in the case of $d/r = 2$, indented by the Berkovich indenter with two different orientations. That is, (a) the pyramid flat faces toward the fibre and (b) the pyramid edge faces toward the fibre.

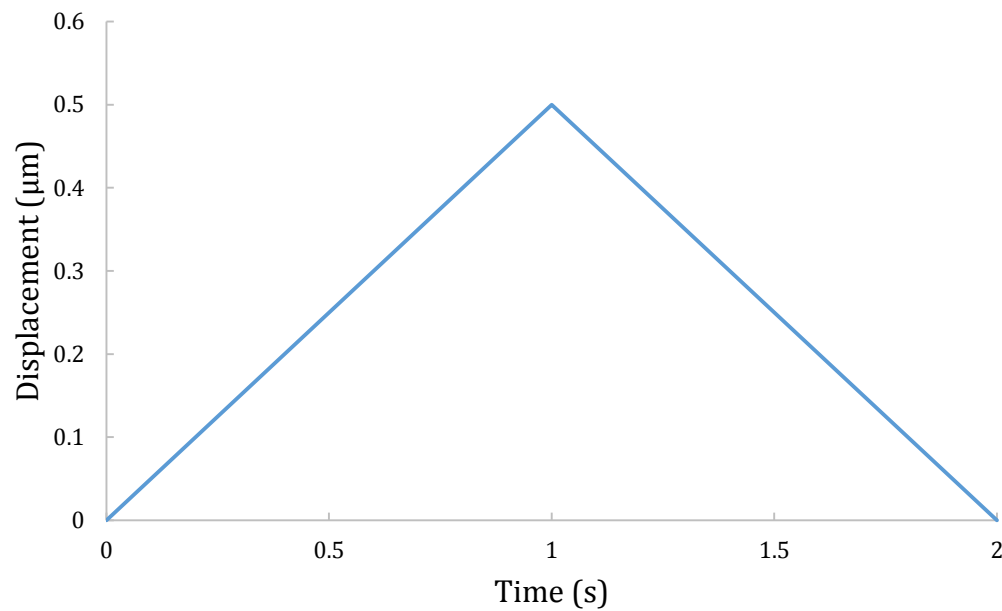


Figure 5.4 Loading-unloading procedure.

5.2.3 Model calibration and curve fitting

The Oliver and Pharr method was used in this study to determine the composite elastic modulus. While, this procedure involves the calculation of contact area, which may be highly affected by the tip radius. To simulate a real indenter, the tip radius was set to $0.1 \mu\text{m}$ in this study, which is comparable to the displacement and will consequently induce errors on the determination of contact area. Similar to the experimental tip area function calibration, this study used numerical simulation as the calibration procedure. The matrix was assigned to share the same elastic properties as the fibre (that is, $E=10 \text{ MPa}$ and $\nu=0.3$). Thereafter, the elastic modulus determined by Oliver and Pharr method was calibrated against the intrinsic elastic modulus. This generates a new area function for data calibration and also eliminates any numerical instability induced errors.

Matlab code was written to perform the curve fitting and extract the composite elastic modulus. Similar to the previous chapter, the coefficient of determination (R^2) value was adopted here to represent the quality of the fitting.

5.3 Results and discussion

5.3.1 The apparent Young's modulus determined by FEA

The data in Figure 5.5 and Figure 5.6 shows the $F-\delta$ curves and the corresponding apparent elastic modulus for the inclusion/matrix systems. For the vertical fibre model, the difference between the forces from d/r equals 0 and 0.5 are negligible. It indicates that the influence from the matrix is not evident when the ratio of d/r is less than 0.5 (namely, the indentation took place in the region of the inclusion). While, when the indentation takes place in the region of the matrix, the response is matrix-dominated. At the same displacement, the influence from the inclusion is decreasing with the increase of the d/r ratio. That is, when the ratio of d/r equals 1.5, the influence of the inclusion is not obvious until the displacement reaches approximately 0.2 μm , which suggests that the effective deformation zone began to be affected by the fibre inclusion. When the ratio of d/r increases up to 2, the influence from the inclusion becomes obvious only after the displacement reaches approximately 0.4 μm . When the ratio of d/r is higher than 3, the influence of the inclusion is undetected even after the displacement reaches 0.5 μm , which implies that the effective deformation zone is within 3 μm radius. For the horizontal fibre model, this statement is observed as well. Namely, when the ratio of d/r equals 2, the influence from the inclusion can be observed only after the displacement reaches approximately 0.2 μm . When the ratio of d/r is higher than 3, the influence from the inclusion is negligible when the displacement is within the range of 0~0.5 μm . It seems that there may exist a critical displacement, which raises with the increase of d/r ratio. Within this critical displacement, the indentation response will be insignificantly affected by the other component. On the other hand, as shown in Figure 5.5b and Figure 5.6b, the force and the apparent elastic modulus from the case of d/r equals 0.5 are always greater than the values from the case of d/r equals 0. It is because that, in the former case (d/r equals 0.5), more volume of the stiffer component (fibre) is involved in the model. Besides, more volume of fibre is within the effective deformation zone in the former case, and consequently there is less influence from the surrounding matrix.

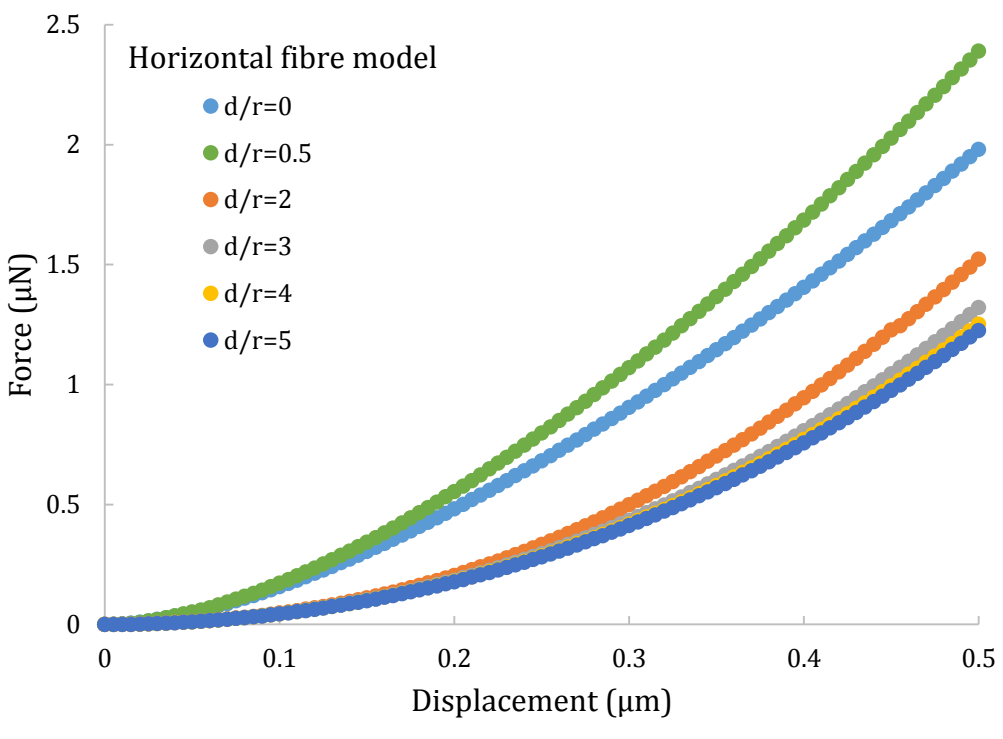
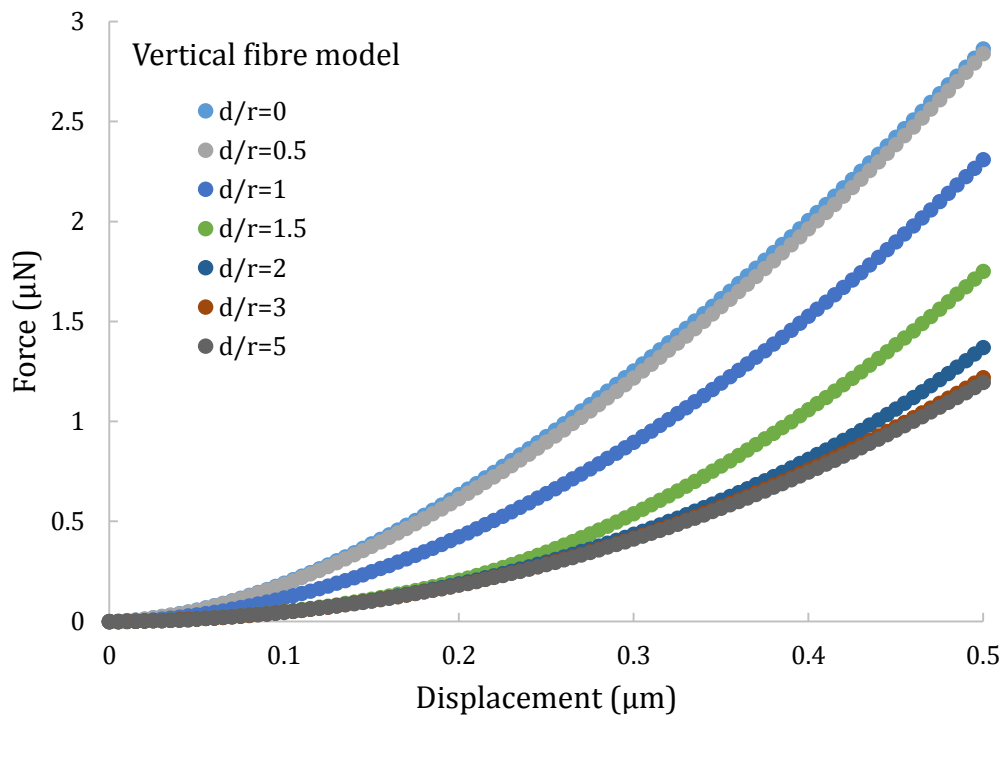
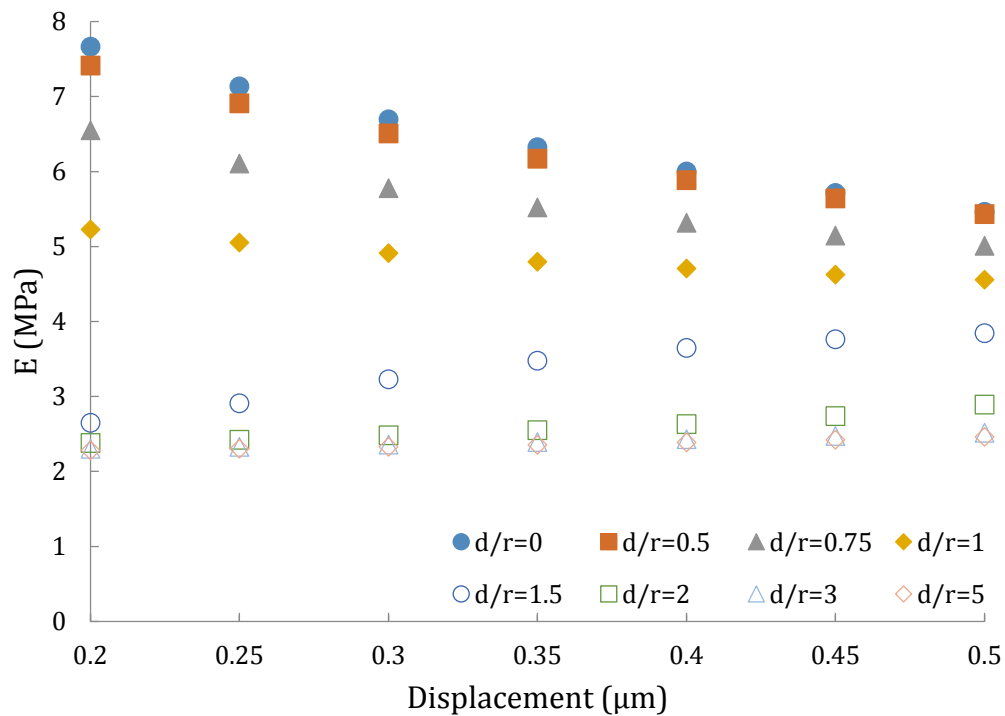
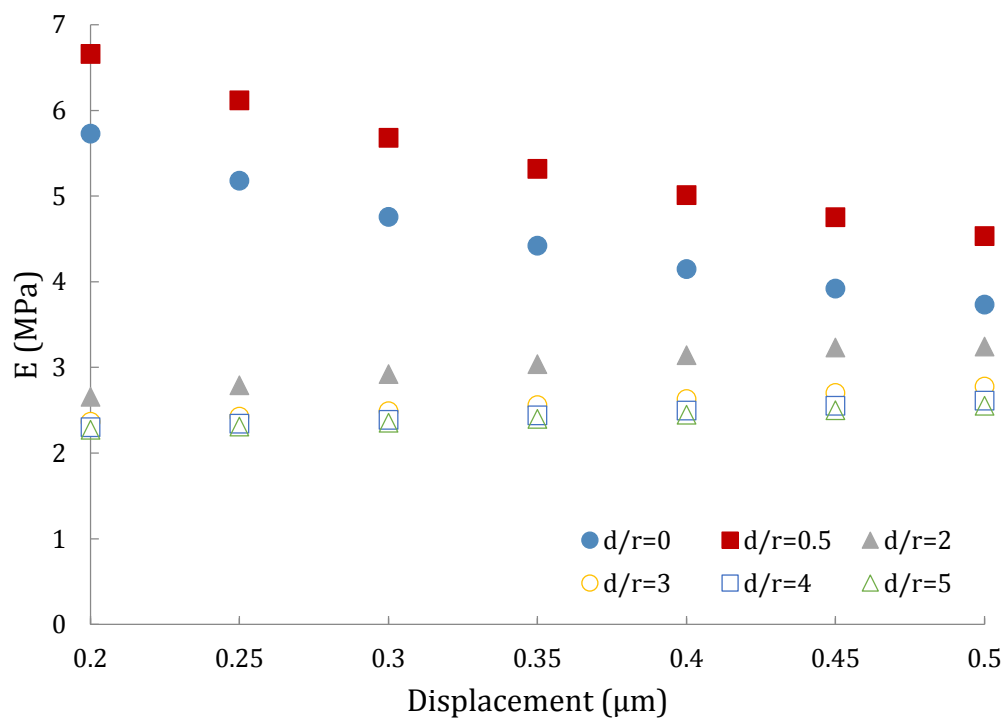


Figure 5.5 The F - δ curves for the indentation test on (a) vertical fibre model and (b) horizontal fibre model, with the conical indenter.



(a)



(b)

Figure 5.6 The composite elastic modulus for (a) the vertical fibre model and (b) the horizontal fibre model, with different distances between the conical indenter and the inclusion.

In order to further analyse the relation between the ratio of d/r and the corresponding nanomechanical response for the inclusion/matrix system, von Mises stress contours are plotted to represent the stress distribution (Guo and Yen, 2004; Walter *et al.*, 2007). As illustrated in Figure 5.7, stress contours for the vertical fibre model indented by the conical indenter are plotted with the displacement equal to 0.5 μm . For standardization, the maximum stress limit was set to 1.2 MPa and the minimum stress limit was set to 0 MPa in all cases. It shows that, for the vertical fibre model, the response is mainly fibre-dominated when the indentation takes place in the region of the fibre ($d/r < 1$, Figure 5.7a). When the interface between the fibre and the matrix is indented ($d/r = 1$, Figure 5.7b), both of them will contribute to the resulting response. Even at a small displacement, it is still difficult to extract the individual properties from the corresponding $F-\delta$ curve. When the indentation occurs in the region of the matrix ($d/r > 1$, Figure 5.7c-e), the response will be matrix-dominated. In this case, the influence from the inclusion can be negligible (Figure 5.7d-e) until the indenter directly touches the inclusion (Figure 5.7c). It indicates that, once the displacement is small enough, the properties for each individual phase can be extracted from the corresponding $F-\delta$ curve.

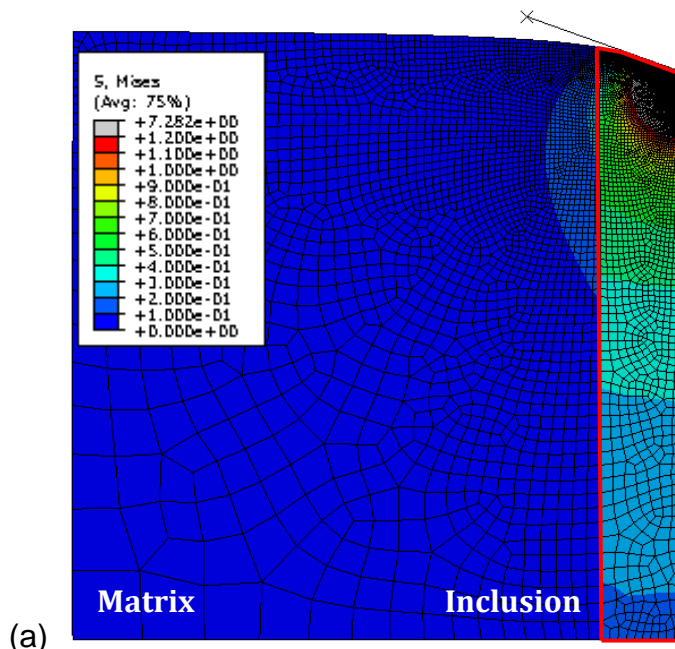


Figure 5.7 Von Mises stress contours for the vertical fibre model with a displacement of 0.5 μm , when (a) $d/r = 0$, (b) $d/r = 1$, (c) $d/r = 2$, (d) $d/r = 3$ and (e) $d/r = 5$. For standardization, all the figures share the same stress scale.

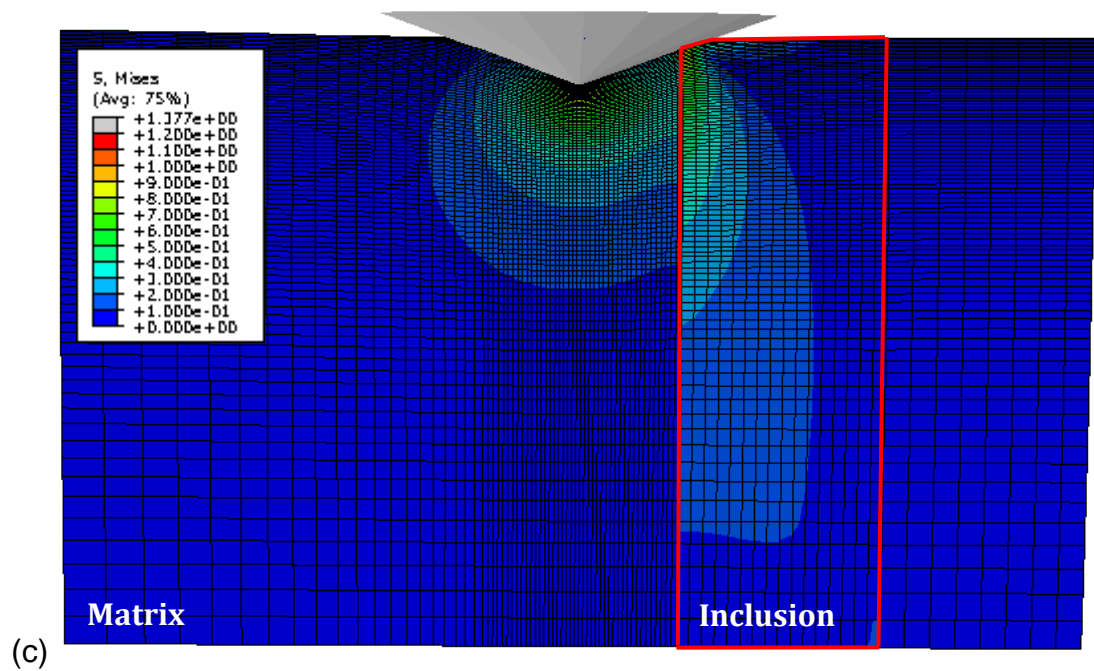
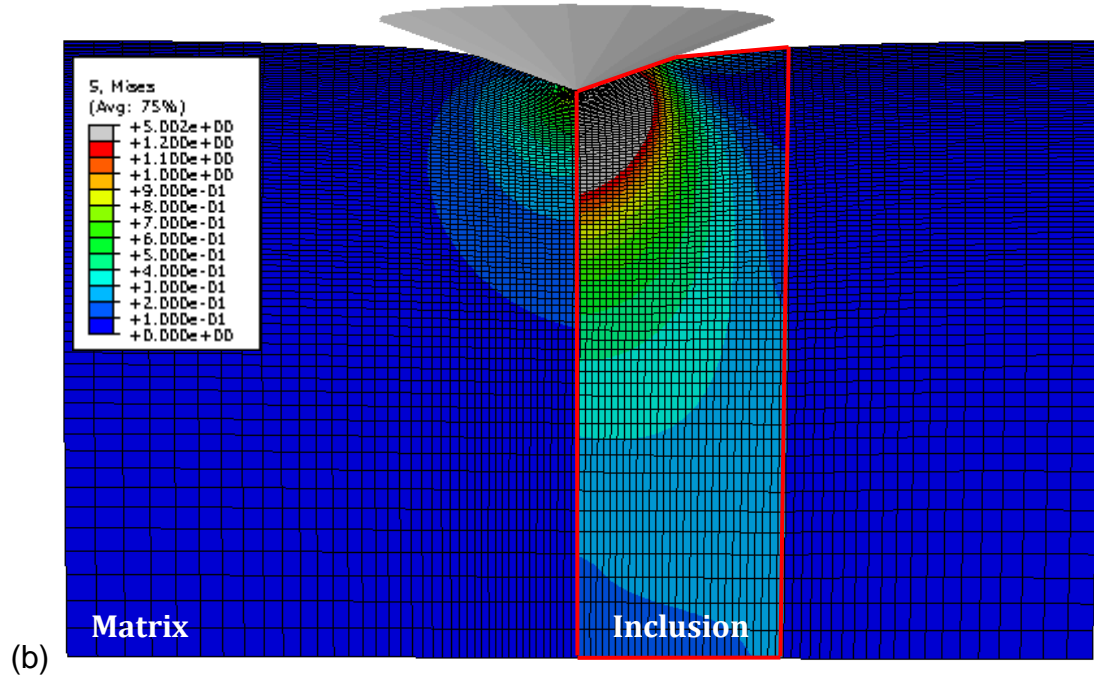


Figure 5.7 (Cont.)

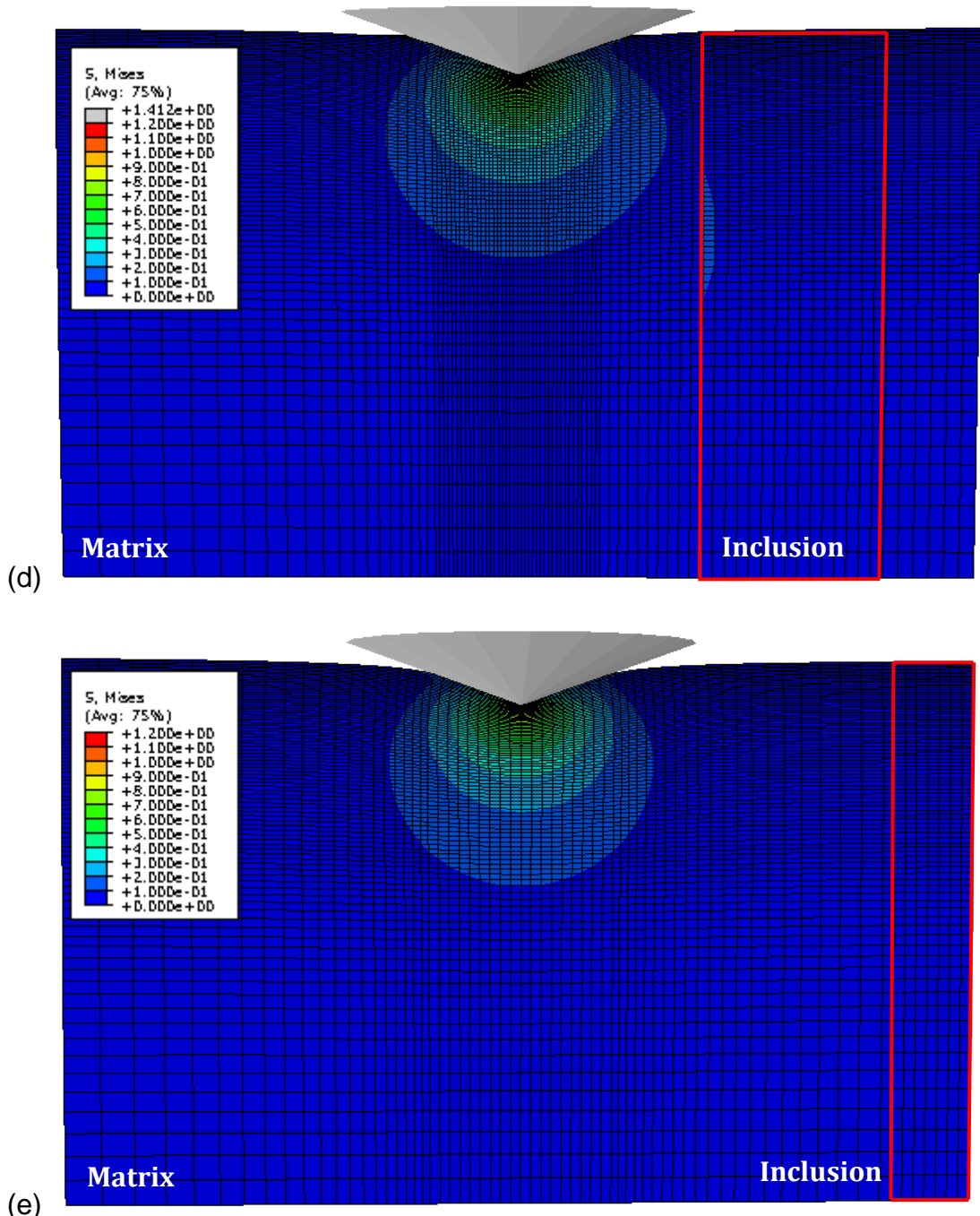


Figure 5.7 (Cont.)

For comparison, stress contours for the horizontal fibre model indented by the conical indenter are plotted in Figure 5.8. The maximum and minimum stress limit was also set to 1.2 MPa and 0 MPa, respectively. Similar to the vertical fibre model, when the indentation is carried out in the region of the inclusion ($d/r < 1$, Figure 5.8a-b), the response is mainly fibre-dominated. Besides, it also indicates that the apparent elastic modulus is highly related to the ratio of $V_{inclusion}/V_{matrix}$ (which is the deforming volume ratio between the inclusion and the matrix involved in the effective stress field (Bull, 2001; G-Berastegui *et al.*, 2004)). For a greater deforming volume ratio of $V_{inclusion}/V_{matrix}$, a higher apparent elastic

modulus will be obtained. When the indentation takes place in the region of the matrix ($d/r > 1$, Figure 5.8c-f), the response is mainly matrix-dominated, especially for a lower displacement or a larger d/r ratio. Compared with the stress contours from the vertical fibre model, for the same ratio of d/r (such as Figure 5.7d and Figure 5.8d for $d/r = 3$), the horizontal inclusion seems to contribute more to the resulting response than the vertical inclusion. It may due to the fact that stress propagates further along the vertical direction (*i.e.* the direction of loading) than along the horizontal direction. On the other hand, similar to the 10% rule-of-thumb for estimating the coating properties (Sawa *et al.*, 1999; Wang *et al.*, 2004; Chen and Bull, 2009b), and also as suggested by Chen and Bull that the size of the deformation zone is related to the maximum displacement (Chen and Bull, 2006b; Chen and Bull, 2009b). Therefore, in this study, there may also exist a critical distance for the inclusion/matrix system, which relates to the ratio of d/r , indenter geometry and maximum displacement. That is, when indenting the matrix within a certain displacement range, the influence from the inclusion will be negligible once beyond this critical distance (or critical d/r ratio). In practical application, when the fibres are periodically distributed in the matrix, the greater volume fraction of the fibre leads to more fibre-dominated response, and the less volume fraction of the fibre stands for more matrix-dominated response.

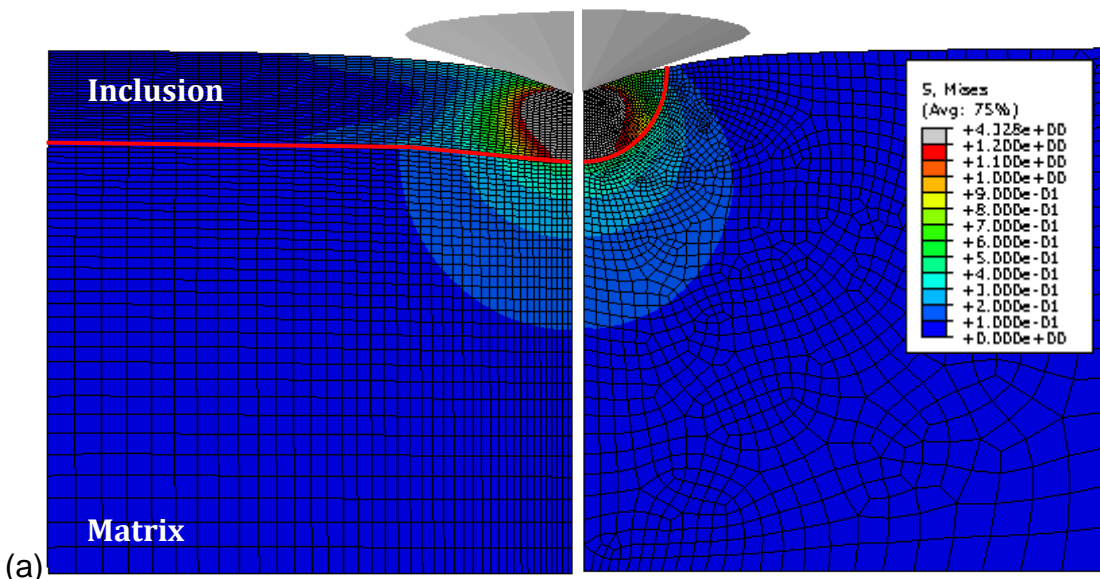


Figure 5.8 Von Mises stress contours for the horizontal fibre model from two orthogonal cross-sections with a displacement of $0.5 \mu\text{m}$, when (a) $d/r = 0$, (b) $d/r = 0.5$, (c) $d/r = 2$, (d) $d/r = 3$, (e) $d/r = 4$ and (f) $d/r = 5$. For standardization, all the figures share the same stress scale.

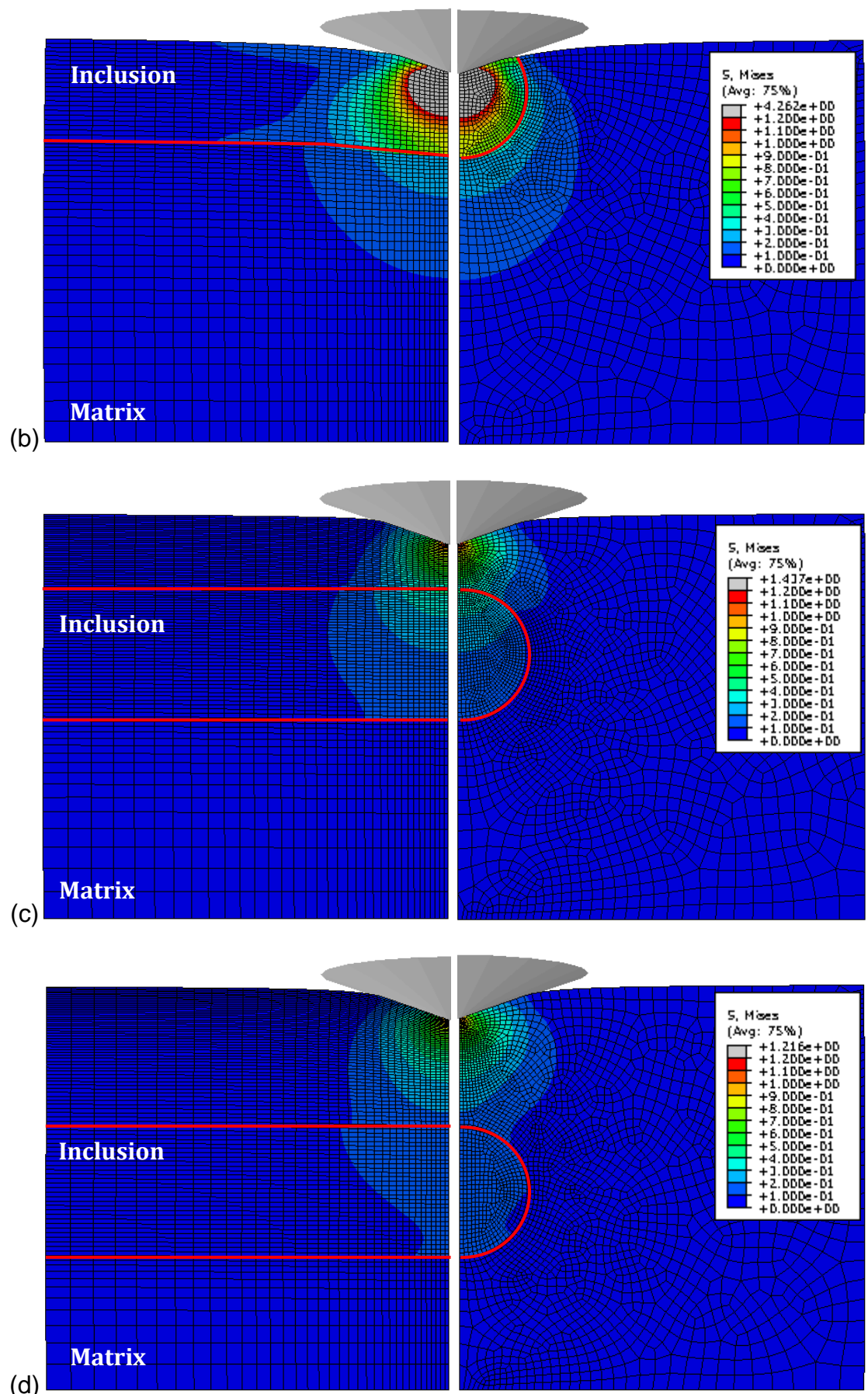


Figure 5.8 (Cont.)

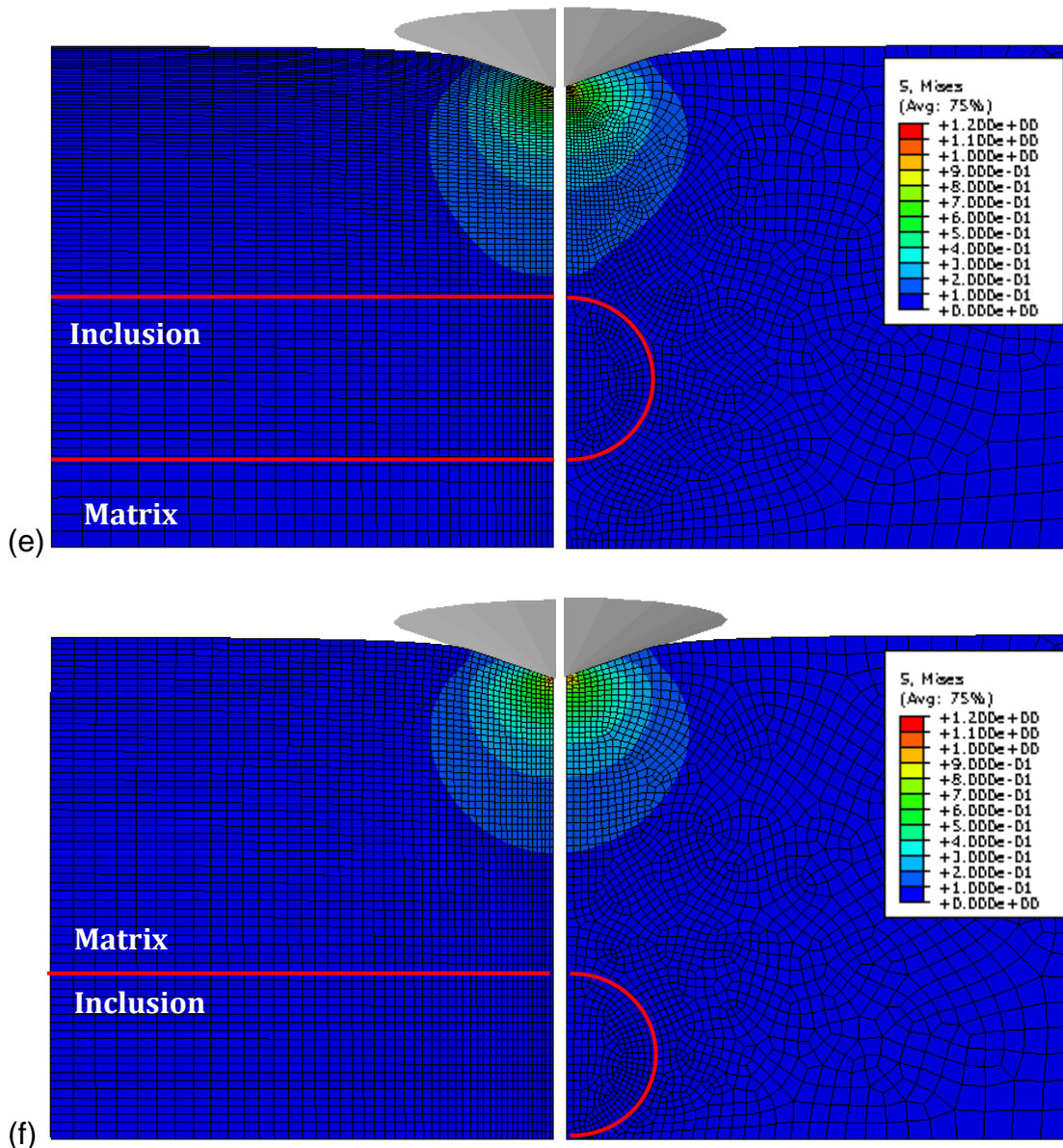


Figure 5.8 (Cont.)

5.3.2 Extraction of the elastic modulus of the inclusion and the matrix

Equations 5.1-5.3 were adopted to describe the apparent elastic modulus plotted in Figure 5.6. Although each curve can be effectively fitted by these empirical equations, they are not able to converge all the data to a master curve. Thus, it does not make much sense to adopt these equations here, as all the fitting parameters depend on the ratio of d/r . Equations 5.1-5.3 work well in the previous chapter as they take consideration of the elastic mismatch between the inclusion and the matrix. While, in this chapter, the variables are the fibre orientation and the indentation location. Hence, as a future work, a more generalized expression should be developed, which considers the variables such

as indentation location, fibre orientation, indenter geometry and even the inclusion geometry.

On the other hand, Equation 5.5 and Equation 5.6 were adopted to extract the elastic modulus of each individual component. By fitting these equations to the curves plotted in Figure 5.6, the relevant fitting parameters are shown in Tables 5.1-5.4. The R^2 value is higher than 0.95 in each case, which shows the good quality of the fitting. For the linear equation, the parameter A reflects the changing trend of the apparent elastic modulus with respect to the displacement. A higher value of A leads to greater increment of the apparent elastic modulus. As listed in Table 5.1 and Table 5.3, when the ratio of d/r is greater than 1, the value of A is decreasing with the increase of d/r . It indicates that, when indenting the matrix, the influence from the fibre will decrease with the increase of d/r ratio. The parameter C represents the modulus of the indented bulk material, which is the intercept of extrapolating the fitting equation to zero contact depth. In both the vertical and horizontal fibre cases, when indenting the matrix, the value of C from the linear equation will be closer to the exact elastic modulus of the matrix (2 MPa) rather than the value from the polynomial equation. In contrast, when indenting the inclusion, the value of C from the polynomial equation will be closer to the exact elastic modulus of the inclusion (10 MPa) rather than the value from the linear equation. While, when indenting the interface between the inclusion and the matrix (as shown in Figure 5.7b), both of these two equations are invalid to extract the elastic modulus of either individual component, because even when extrapolating the displacement to zero, the influence from both the fibre and the matrix still cannot be ignored.

Linear equation (Equation 5.5)								
d/r	0	0.5	0.75	1	1.5	2	3	5
A	-7.2395	-6.5031	-5.0088	-2.1913	4.0865	1.6576	0.7217	0.6005
C	8.9642	8.5582	7.3889	5.6086	1.9314	2.0072	2.1493	2.1542
R^2	0.9835	0.9774	0.9605	0.9730	0.9546	0.9604	0.9893	0.9902

Table 5.1 Fitting parameters of the linear equation (Equation 5.5) for the vertical fibre model.

Polynomial equation (Equation 5.6)								
d/r	0	0.5	0.75	1	1.5	2	3	5
A	10.720	11.322	11.524	4.1705	-10.003	3.7843	0.8581	0.6852
B	-14.744	-14.429	-13.075	-5.1106	11.089	-0.9914	0.1210	0.1208
C	10.170	9.832	8.6853	6.0778	0.8061	2.4329	2.2459	2.2313
R^2	0.9997	0.9996	0.9986	0.9995	0.9975	0.9979	0.9998	0.9999

Table 5.2 Fitting parameters of the polynomial equation (Equation 5.6) for the vertical fibre model.

Linear equation (Equation 5.5)						
d/r	0	0.5	2	3	4	5
A	-6.5054	-6.9854	2.0401	1.3816	1.0472	0.9328
C	6.8331	7.8845	2.2908	2.0819	2.0829	2.0796
R^2	0.9663	0.9761	0.9683	0.9987	0.9963	0.9966

Table 5.3 Fitting parameters of the linear equation (Equation 5.5) for the horizontal fibre model.

Polynomial equation (Equation 5.6)						
d/r	0	0.5	2	3	4	5
A	13.852	12.492	-3.9879	0.5734	0.7300	0.6275
B	-16.202	-15.730	4.8316	0.9802	0.5362	0.4935
C	8.3915	9.2898	1.8422	2.1464	2.1650	2.1501
R^2	0.9991	0.9996	0.9960	0.9999	0.9999	0.9999

Table 5.4 Fitting parameters of the polynomial equation (Equation 5.6) for the horizontal fibre model.

Therefore, it may be suggested that, for an inclusion/matrix composite, a linear equation should be used to extract the elastic modulus of the indented material when the ratio of d/r is higher than 1, and a polynomial equation should be used when the ratio of d/r is lower than 1. This may be due to the fact that, with the development of the stress field, the changing trend of the deforming volume ratio of $V_{inclusion}/V_{matrix}$ that starts from the matrix, is different from the changing trend of the evolved volume ratio that starts from the inclusion. Thus, different equations are applied to each case depending on the ratio of d/r .

5.3.3 Effect of indenter geometry

In practice, the Berkovich indenter is usually equivalent to a conical indenter in the FEM (Bolshakov *et al.*, 1996; Lichinchi *et al.*, 1998). However, its non-axisymmetric geometry actually affects the conclusion drawn from the case of a conical indenter, especially in the case of a non-axisymmetric model (namely, $d/r \neq 0$) (Min *et al.*, 2004; Bei *et al.*, 2005; Swaddiwudhipong *et al.*, 2006). To reveal the effect of the indenter geometry, the vertical fibre model with $d/r = 2$ were indented by (*i*) the Berkovich indenter with the pyramid flat facing toward the fibre, (*ii*) the Berkovich indenter with the pyramid edge facing toward the fibre and (*iii*) the equivalent conical indenter in this study. The stress contours and the composite elastic modulus are shown in Figure 5.9 and Figure 5.10, respectively. To make it clearer, as plotted in Figure 5.11, the stress development with respect to the displacement was quantified with the 0.2 MPa contour line. It can be seen that, in the case of the Berkovich indenter with the edge facing toward the fibre, the indenter will directly press the fibre when the displacement reaches 0.25 μm , which is much earlier than the other two cases. Once the indenter touches the inclusion, the corresponding apparent elastic modulus and the effective deformation zone within the fibre are rapidly increasing. Therefore, it seems that the non-axisymmetric geometry of the indenter will actually affect the effective tip angle relative to the fibre. That is, in the case of the Berkovich indenter with the edge facing toward the fibre, the effective tip angle is 77° which is the angle from the pyramid axis to the edge. While in the case of the Berkovich indenter with the pyramid flat facing toward the fibre, the effective tip angle decreases to 65.3° , which is the angle between the axis and the face. In practice, this random effective tip angle will correspondingly affect the distribution and the development of the effective stress field within the fibre and the matrix. As suggested in the previous discussion, a linear equation was then adopted to extract the elastic modulus of the matrix. While, relatively big deviation (20.14% difference between the extracted value and exact value) was observed in the case of the Berkovich indenter with the edge facing toward the fibre, and acceptable values (with the differences of 0.36% and 8.09%) were obtained in the other two cases. It indicates that, when using Equation 5.5 to extract the elastic modulus of the matrix, it will become invalid once the indenter touches the inclusion. Once the indenter touches the fibre, the effective deformation zone will become irregular

and the corresponding deforming volume ratio of $V_{inclusion}/V_{matrix}$ will increase rapidly.

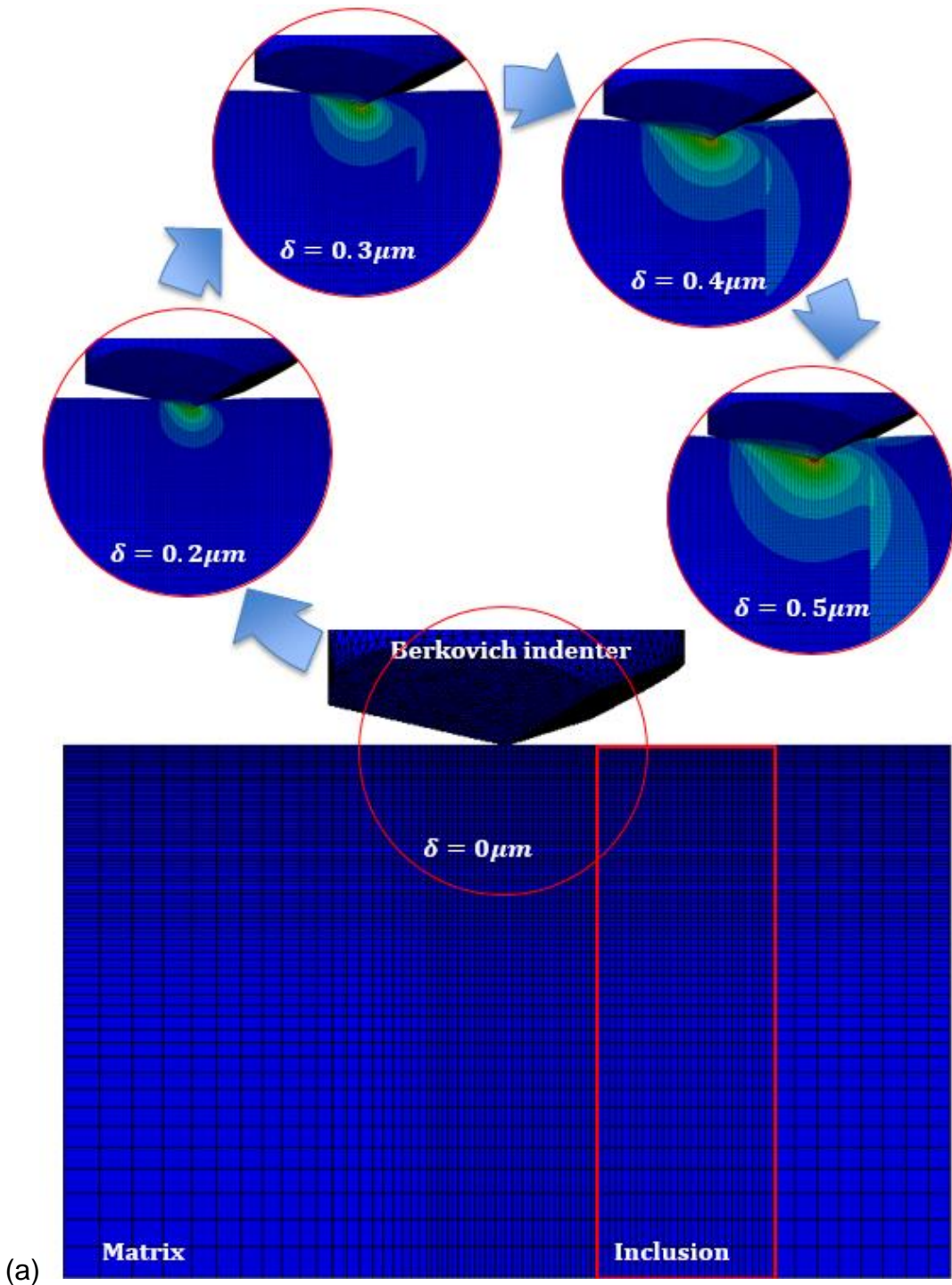


Figure 5.9 Comparison of the von Mises stress contours for the vertical fibre model with $d/r = 2$, indented by (a) the Berkovich indenter with the pyramid flat facing toward the fibre, (b) the Berkovich indenter with the pyramid edge facing toward the fibre and (c) the conical indenter. For standardization, the maximum stress limit was set to 1.2 MPa and the minimum stress limit was set to 0 MPa in all the figures.

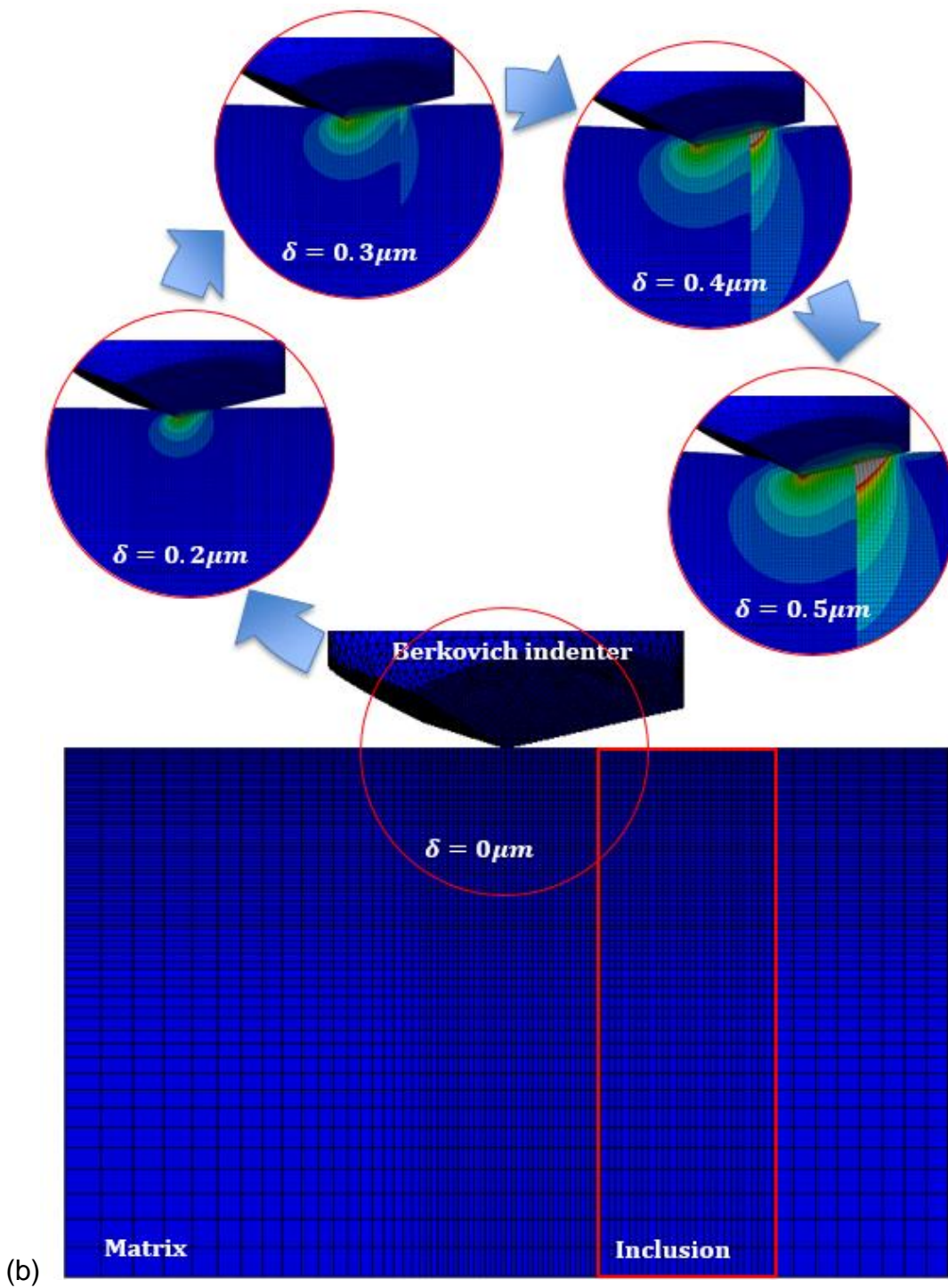


Figure 5.9 (Cont.)

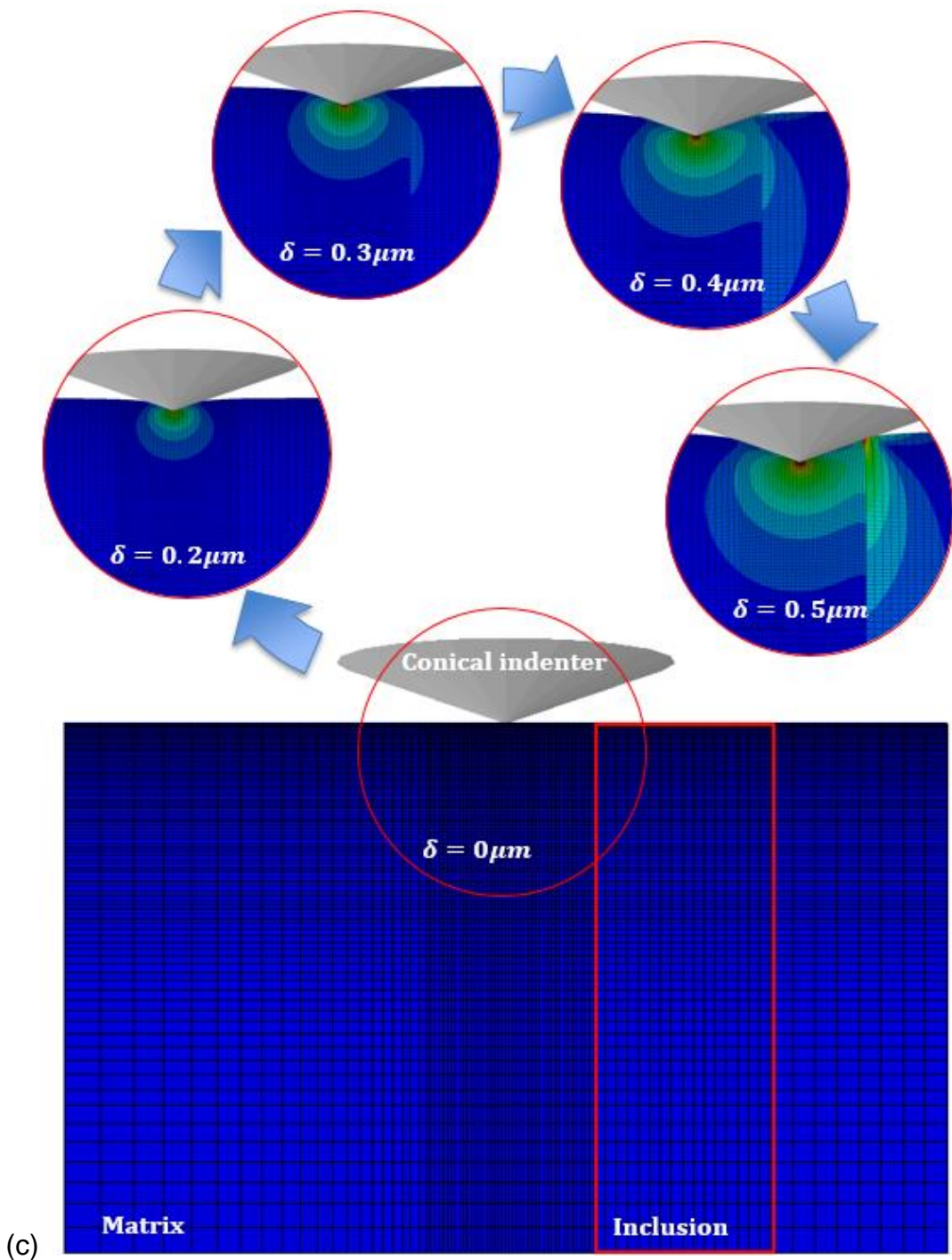


Figure 5.9 (Cont.)

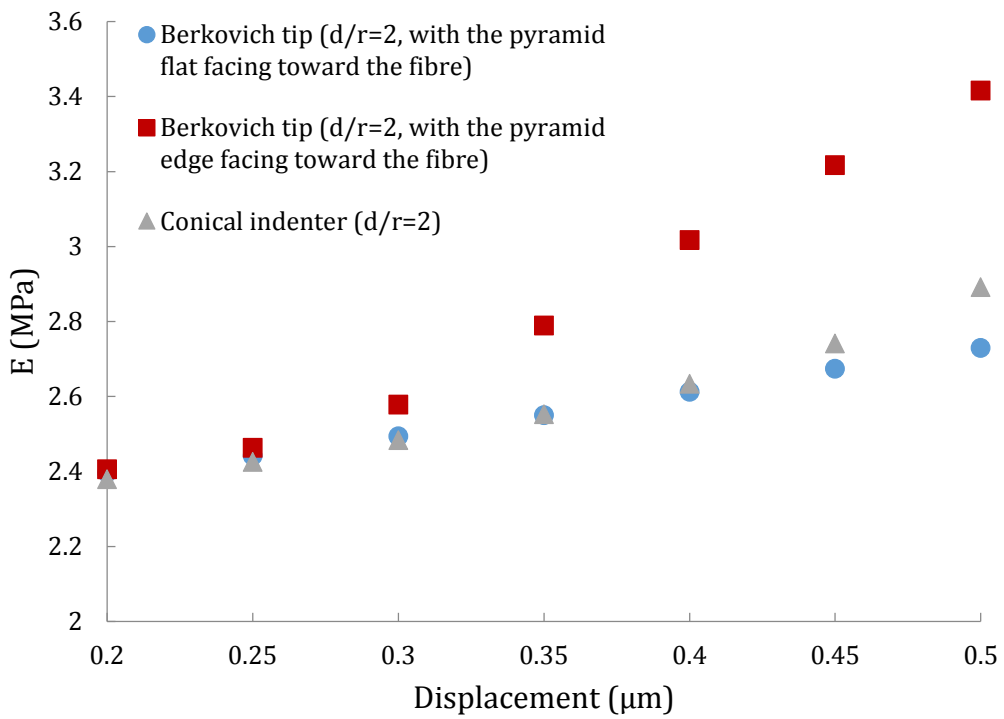


Figure 5.10 The apparent elastic modulus for the vertical fibre model in the case of $d/r = 2$, indented by different indenters and orientations.

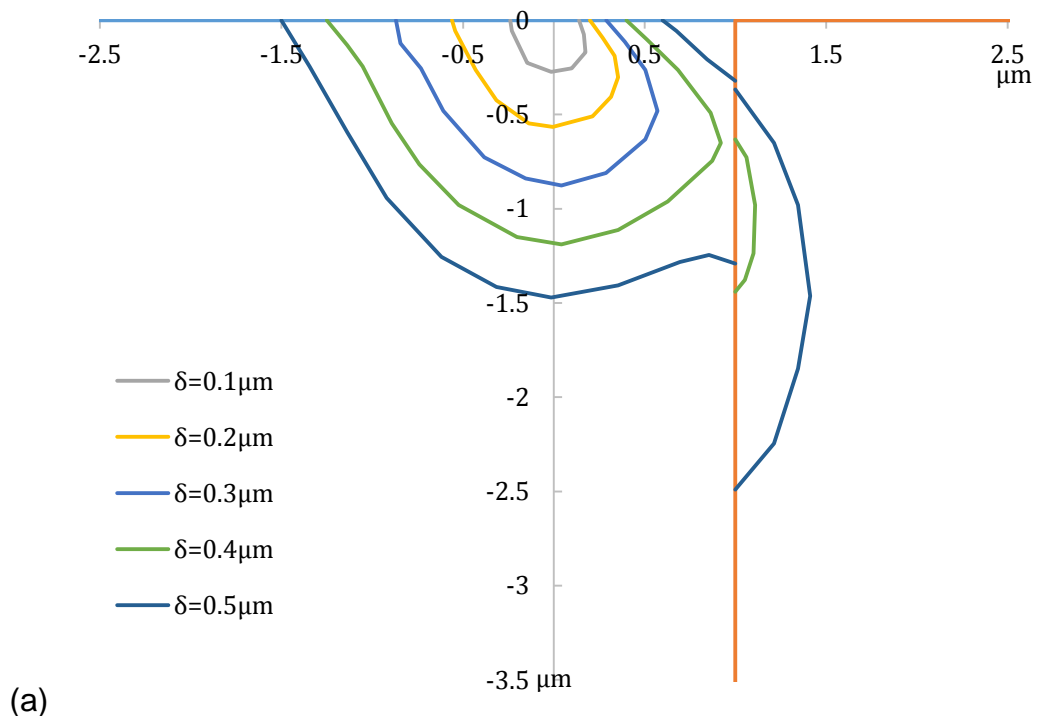


Figure 5.11 The quantification of 0.2 MPa contour line of von Mises stress contours shown in Figure 5.9. That is, the contour lines of the vertical fibre model with $d/r = 2$, when indented by (a) the Berkovich indenter with the pyramid flat facing toward the fibre, (b) the Berkovich indenter with the pyramid edge facing toward the fibre and (c) the conical indenter. The origin of each coordinate system represents the indentation point.

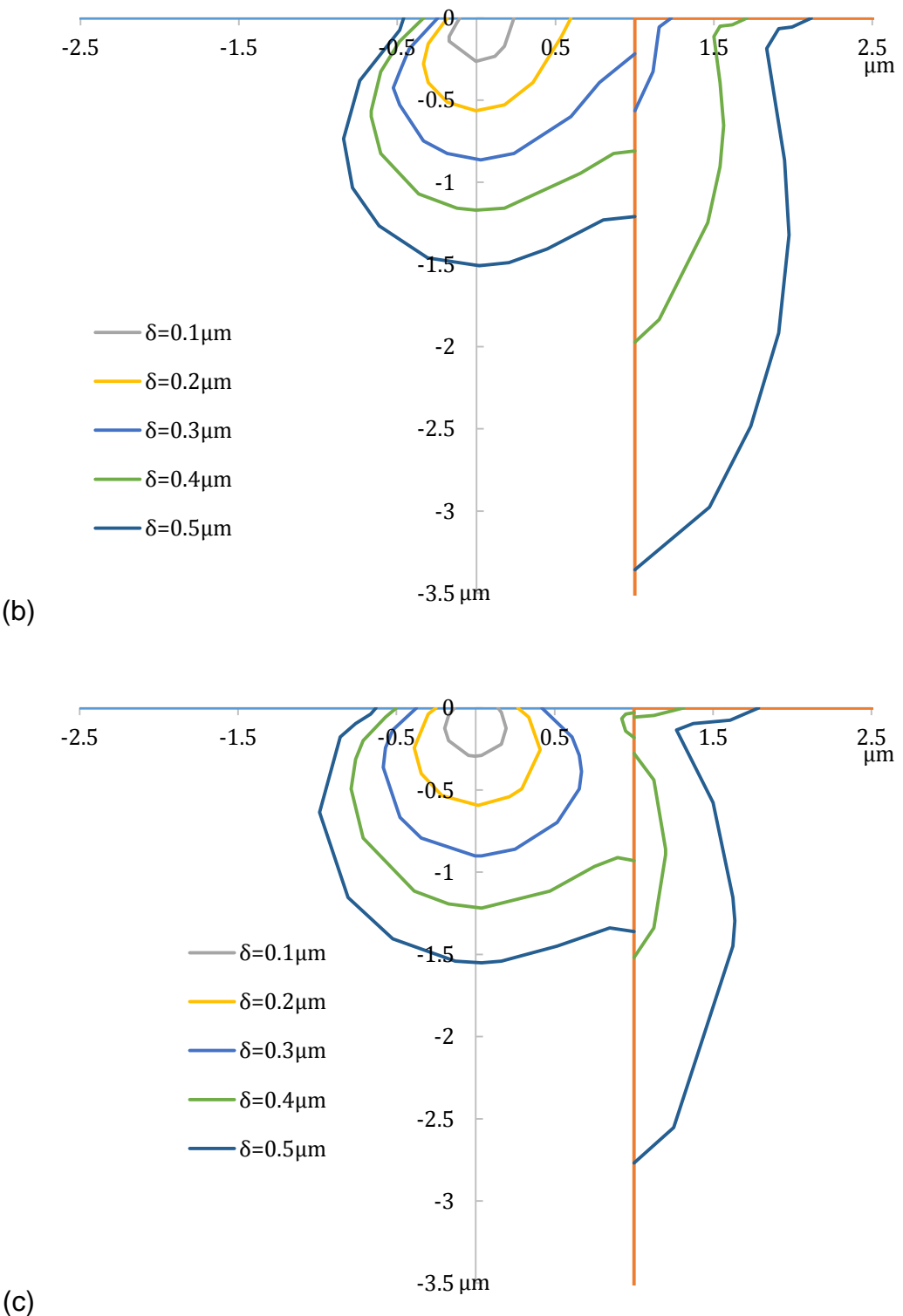


Figure 5.11 (Cont.)

5.4 Summary

FE simulations were performed to investigate the elastic response of the fibre-reinforced composites with different indentation locations and fibre orientations indented by a conical indenter and a Berkovich indenter. FE results have revealed that, there exists a critical ratio of d/r for a given displacement. Beyond this ratio, the indentation response will be negligibly affected by the other component. In other words, for a given ratio of d/r , the maximum displacement should not exceed the corresponding critical displacement to avoid the influence from the other component. It reveals that, for a periodically distributed fibre-reinforced composite, the mechanical response of the composite will transit from matrix-dominated to fibre-dominated with the increase of fibre volume fraction. That is, higher fibre volume fraction indicates more fibre-dominated response, and vice versa.

Empirical equations (Equations 5.1-5.3) which worked well in the previous chapter have been examined. However, these equations are incapable to describe the apparent elastic modulus of inclusion/matrix composites with various d/r ratios. Instead, a linear equation (Equation 5.5) and a second order polynomial equation (Equation 5.6) have been successfully applied to extract the elastic modulus of each individual component. It revealed that, based on the development of the stress field, the polynomial equation (Equation 5.6) will be more effective to extract the elastic modulus of the fibre when the indentation takes place on the fibre. When the indentation occurs on the matrix, before the indenter directly touches the fibre, the linear equation (Equation 5.5) will be more suitable to extract the elastic modulus of the matrix.

In the next chapter, a case study of nanoindentation of mineralized matrix will be presented to characterize its mechanical properties. In addition, surface morphology, microstructure and chemical composition will also be provided with the assistance of microscopy techniques and FEM to understand the deformation processes.

Chapter 6

Nanomechanical Case Study on Mineralized Matrix: Experimental Characterization and Finite Element Modelling

Chapter 6. Nanomechanical Case Study on Mineralized Matrix: Experimental Characterization and Finite Element Modelling

6.1 Introduction

Tissue engineering is the use of a combination of cells, biomaterials and suitable biochemical and physicochemical factors to improve or replace biological tissues. In the last decades, biomaterial scaffolds have been widely used in bone tissue engineering (Stevens, 2008; Zhang *et al.*, 2009; Deb *et al.*, 2010; Baino *et al.*, 2011; Ferreira *et al.*, 2012). Scaffolds with various combinations of constituents are designed to achieve a better biofunctionality and mechanical strength. Of these, cell-based materials have shown promising prospects for future exploitation (Bianco and Robey, 2001; Tuan *et al.*, 2003; Gamie *et al.*, 2012). Very recently, genetic modified cells have been adopted (James *et al.*, 2015). The immortalized cell line Y201 derived from human mesenchymal stem cells (hMSCs) circumvents the issues of limited life-span and high variability of hMSCs (Gong *et al.*, 2011; Liu *et al.*, 2012). However, whether these cells may proliferate in suitable manner and produce appropriate mineralized matrix for given cell culture conditions remains elusive, which is essential for bone regeneration.

To achieve this, it is essential to understand the properties of the mineralized matrix synthesized by these cells (Gough *et al.*, 2004; Jell *et al.*, 2008; Bandyopadhyay-Ghosh *et al.*, 2010; Baino *et al.*, 2011). Due to its inhomogeneity in both chemistry and microstructure, the nanomechanical properties of such inhomogeneous materials are difficult to be reliably measured, especially for a thin layer of mineralized matrix.

Nanoindentation has proven an effective technique to assess the nanomechanical properties of natural tissues such as bone and biological cells (Kavukcuoglu *et al.*, 2007; Pelled *et al.*, 2007a; Tai *et al.*, 2008; Kavukcuoglu *et al.*, 2009; Chen *et al.*, 2010b; Jang *et al.*, 2014; Oyen, 2015). Our previous work has demonstrated that the measured apparent elastic modulus generally has a bimodal distribution and the Gaussian mixture model enabled us to extract properties for two components in the matrix (Duan and Chen, 2015). However,

there is a lack of comprehensive studies on how cell culture conditions would affect the new tissue formation and the mechanical properties of these new tissues. This is important for us to understand the cell-material interactions and the influence of chemical stimuli on biological processes, which will provide an invaluable guideline for the design of scaffold material and the optimisation of cell culture conditions.

Therefore, in this study, we adopted nanoindentation to characterize the mechanical properties of the mineralized matrix synthesized by the immortalized cell line Y201 from hMSCs cultured in basal and osteogenic media for different periods. To reveal more insights into the nanoindentation response of these complex materials, finite element modelling was also employed. From the mechanical point of view, this sample also represents a good example for us to study the nanomechanics of complex composite materials.

Native mature bone always presents an aging effect in its mechanical properties (Burstein *et al.*, 1976; Ziopoulos and Currey, 1998; Ziopoulos *et al.*, 1999). It has been reported that there is a gradual decrease in mechanical properties (stiffness, strength, and toughness) of human femoral bone with age (Ziopoulos *et al.*, 1999). However, the possible aging effect of the mineralized matrix (*i.e.* early stage bone nodule) has never been reported. This is also investigated in this work as it will improve our understanding about biological processes of cells.

6.2 Materials and experimental methods

6.2.1 Sample preparation

An immortalized hMSC line overexpressing human telomerase reverse transcriptase (hTERT) (Y201), which is a highly characterized clonal MSC line that exhibits tri-lineage differentiation capacity (James *et al.*, 2015), was expanded in culture medium containing Dulbecco's modified Eagle's Medium with 10% fetal bovine serum, 20 mM Glutamax and Penicillin/Streptomycin 100 U/ml without further characterisation and passaged when cells reached a confluence of approximate 80%. An osteogenic medium containing culture medium supplemented with 50 µg/ml L-ascorbic acid, 10mM glycerophosphate and 100

nM dexamethasone was used as comparison (Langenbach and Handschel, 2013; Kim *et al.*, 2014; Seo *et al.*, 2014).

Y201 cells were trypsinized and seeded at 15000 cells/cm² onto 13 mm diameter glass slides and were allowed to adhere for 4 hours. They were then cultured in basal medium (BM) and osteogenic medium (OM) for 7, 14 and 21 days. (For samples cultured in the OM, the cells grow so fast that they detached from the substrate at day 21 and thus no samples were harvested from this period.) The medium was replenished every three days. All the samples were dehydrated and firmly stuck onto magnetic discs using double sided tape, prior to the subsequent surface analysis and nanomechanical analysis. For each given cell culture condition, 3 samples were measured for each test.

In order to study the collagen fibre distribution, additional samples were demineralized by immersing the samples in an ethylenediaminetetraacetic acid (EDTA) solution (0.5 M, pH 7.4) for 6 hours to dissolve the mineral phase. After that, each sample was gently rinsed in deionized water several times to remove the EDTA (Ferreira *et al.*, 2009).

6.2.2 Thickness measurement

In order to obtain information about sample thickness, a ball crater tester (Pascall Engineering Co. Ltd., Sussex, UK) was adopted. This instrument is simple and easy to use. The sample is fixed by a holder. A stainless steel sphere with known geometry is rotated by a rotating shaft driven by a motor. This sphere is rotated against the sample surface, with diamond paste applied to the contact area, to wear a crater through the coating layer. With the help of a light microscope, the related sizes of the crater can be measured, as depicted in Figure 6.1.

According to the Pythagorean Theorem, the thickness is then mathematically given by,

$$t = \sqrt{R^2 - \left(\frac{d}{2}\right)^2} - \sqrt{R^2 - \left(\frac{D}{2}\right)^2} \quad (6.1)$$

where t is the thickness of the coating layer, R is the radius of the stainless steel sphere (R equals 12.7 mm in this study), d and D are the diameter of the inner and outer circles, respectively. In this study, the thickness of these matrix layers is $18.5 \pm 8.4 \mu\text{m}$ at the centre of the sample.

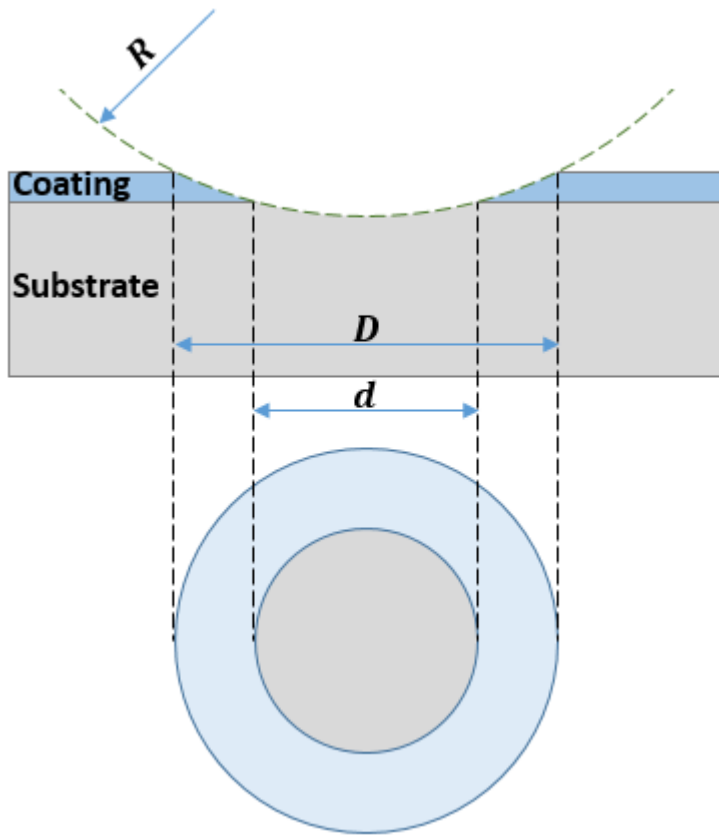


Figure 6.1 Schematic of the crater within the sample produced by a ball crater tester. In practice, the outer circle will be irregular for a coating layer with non-uniform thickness.

6.2.3 Surface analysis

Although nanoindentation techniques are powerful tools, their applications are limited to the mechanical characterization of materials. In order to obtain a further understanding of deformation mechanisms, microstructure, surface morphology or chemical composition of tested materials, the assistance of microscopy techniques is necessary (Pharr, 1998; Goodhew *et al.*, 2000; Wei *et al.*, 2005). In this study, prior to nanomechanical tests, microscopy techniques have been extensively used with the aim of understanding the topography and chemical characterization of the mineralized matrix samples.

6.2.3.1 Optical microscope

The collagen fibre analysis of samples was performed with an Olympus BH2-UMA polarizing microscope (Olympus Europa GmbH, Hamburg, Germany) with a magnification 500X. This instrument adopts a polarized light illumination system with a pair of polarizing plates, which allows the birefringent samples to be observed, such as some crystals, plastics and collagen (Sano, 1988).

6.2.3.2 Profilometer

In this study, the surface roughness measurement was conducted by a ZYGO 5000 profilometer (ZYGO Corporation, Middlefield, CT, USA). This instrument is based on the white light interferometry method, with a fast and non-contact operation, and excellent vertical resolution (up to 0.1 nm). Figure 6.2 shows the representative roughness image of a sample surface, with a view area of 1.58 mm × 1.19 mm.

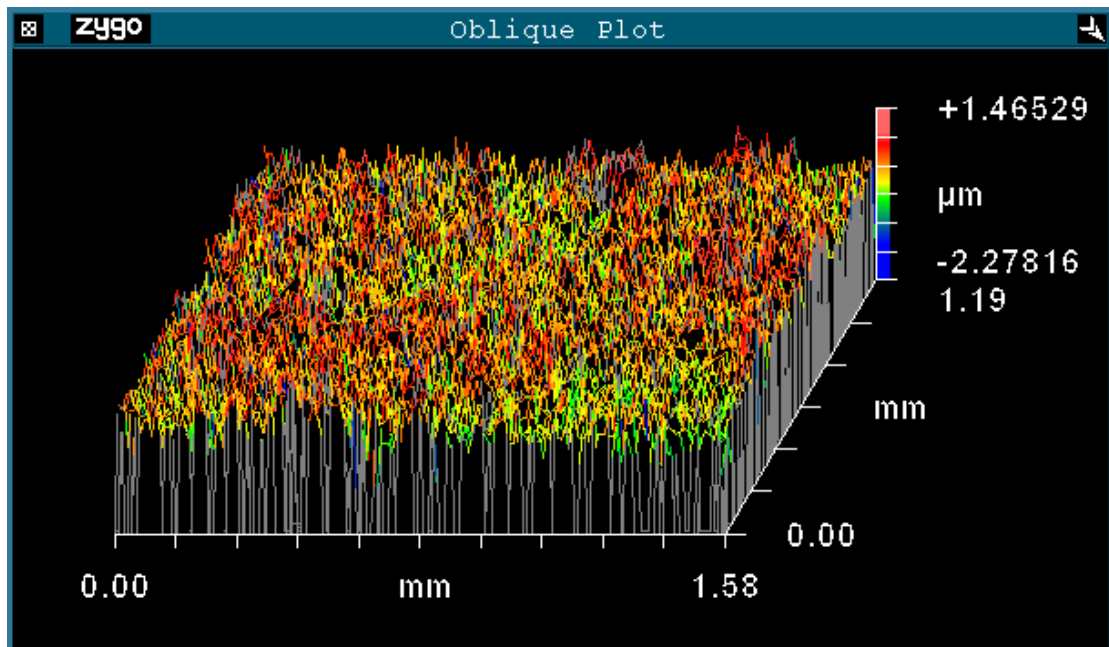


Figure 6.2 Representative surface profile of a mineralized matrix sample.

6.2.3.3 Scanning electron microscope and energy-dispersive X-ray spectroscopy

The scanning electron microscope (SEM) is a type of electron microscope which utilizes a beam of accelerated electrons as the illuminating system. In a typical SEM instrument, as illustrated in Figure 6.3, a beam of electrons is emitted from an electron gun fitted with a filament. Then the electron beam is accelerated and shaped by a system of condenser lenses and an objective lens. This controlled beam can scan the sample surface over a rectangular area in a raster scan pattern. When the electron beam interacts with atoms in the sample, a variety of signals are generated and collected by different detectors. As illustrated in Figure 6.4, the interaction volume within the sample presents a teardrop shape, and the produced signals are secondary electrons (SE), back-scattered electrons (BSE), Auger electrons, characteristic X-rays and transmitted electrons.

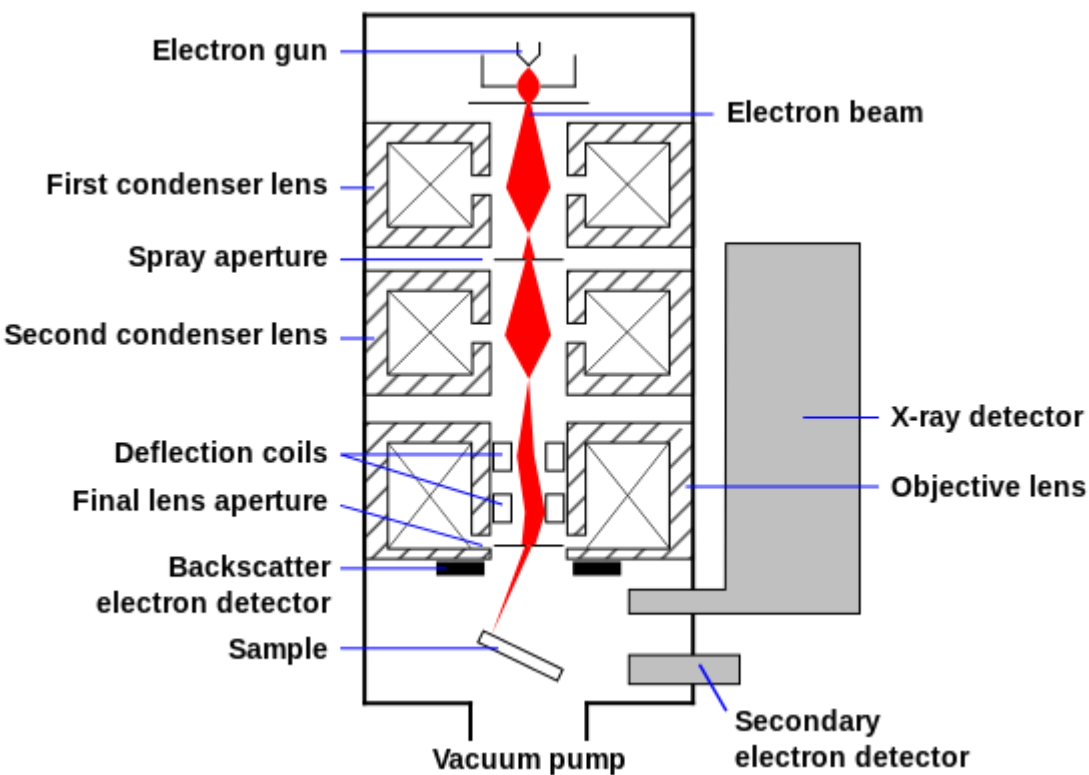


Figure 6.3 Illustration of the main components of a typical SEM (Mintz, 2015).

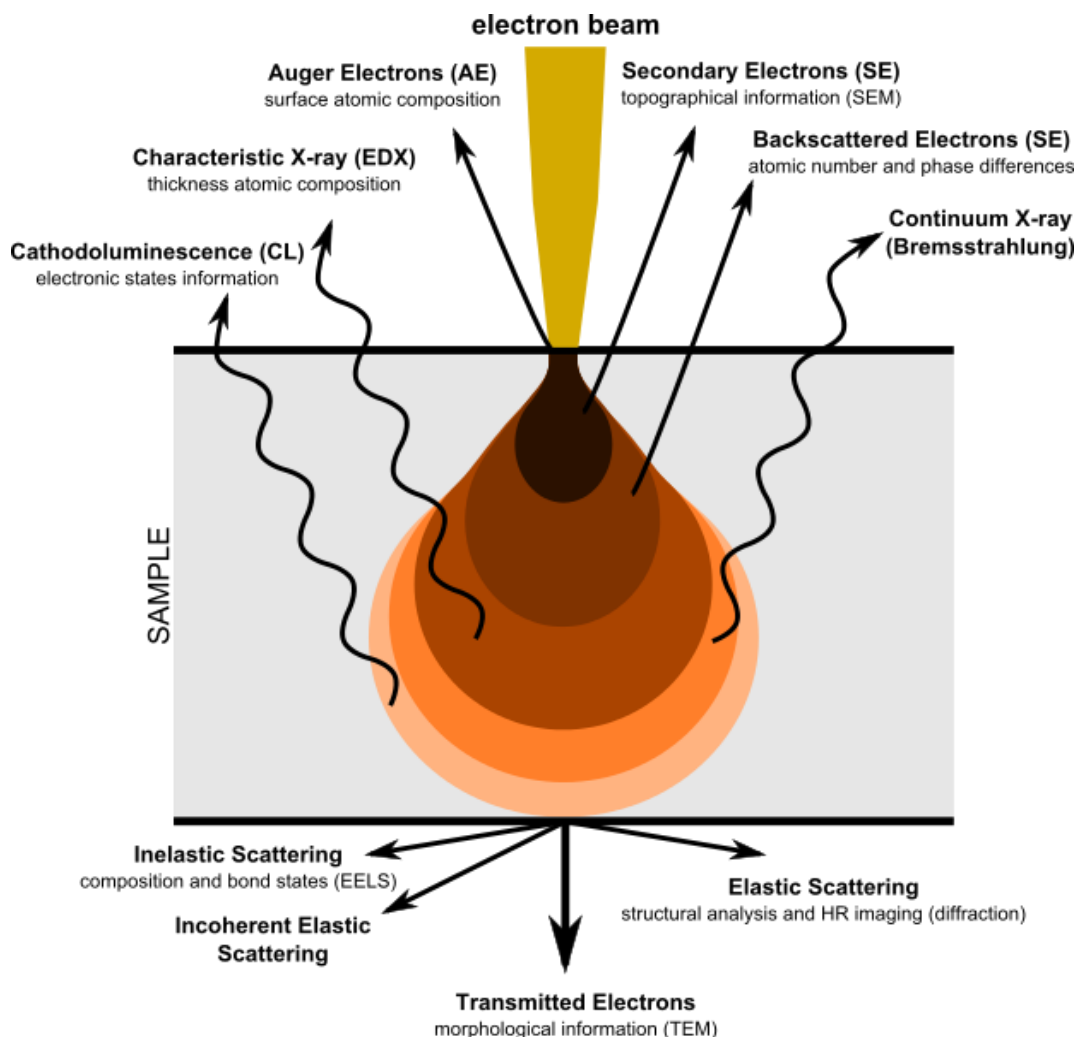


Figure 6.4 Schematic diagram of various signals emitted from the interaction volume when the electron beam hits the sample surface (Claudionico, 2015).

In this study, a HITACHI TM3030 SEM was employed to measure the surface morphology. It was operated in BSE mode with an accelerating voltage of 15 kV, and gives the magnification up to 60,000X. As atomic number of the elements can be obtained by analysing the intensity of BSE signal, the BSE are quite useful in detecting the contrast between regions with different chemical phases. Moreover, this instrument was integrated with an energy-dispersive X-ray spectroscopy (EDS) unit (Quantax 70), which can be used to measure the chemical composition of the samples, as the energy of an X-ray is the feature of the corresponding element. The advantages of this instrument are that it can measure both the morphology and chemical composition at the same detected place due to the integrated EDS unit, and it utilizes a standard low vacuum mode which allows the non-conductive samples to be observed in their natural state without special sample preparation such as coating with conducting material.

6.2.3.4 Atomic-force microscope

The AFM is a high-resolution type of scanning probe microscopy first invented by scientists at IBM in 1982. Until now, the AFM has been widely used in a variety of disciplines, such as solid-state physics, molecular engineering, cell biology and medicine. In this study, detailed features of the mineralized matrix samples were examined by Nanoscope IV AFM (Veeco Instruments, Santa Barbara, CA, USA) in contact mode with a scanning area of 10 µm by 10 µm and image pixels of 512 × 512, equipped with triangular silicon nitride cantilevers (stiffness constant 0.08 N/m, resonant frequency 17 kHz). For this instrument, as illustrated in Figure 6.5, the sharp tip is placed at the end of a cantilever. When the tip contacts with the sample surface, the force between the tip and sample surface will bend the cantilever according to Hooke's law. The deflection of cantilever is measured by the beam deflection method. In this method, the laser light is pointed at the back of the cantilever, and reflected back to a position-sensitive detector. The collected signal is controlled by a feedback loop to keep the cantilever with a constant deflection (a constant contact force). Then, the sample surface topography can be imaged by moving the tip over the surface.

This instrument offers three imaging modes, namely: contact mode, non-contact mode and tapping mode. The basic difference between them is the different working area within the van der Waals interaction force, which determines the contact force associated with the AFM, as shown in Figure 6.6. In the contact mode, the tip-to-sample distance is kept to be small enough (less than a few angstroms) that the overall force is repulsive. Otherwise, the attractive force may be quite strong and cause the tip adhering to the sample surface. This is also the reason why a feedback loop is involved in the system to ensure the contact force remain unchanged.

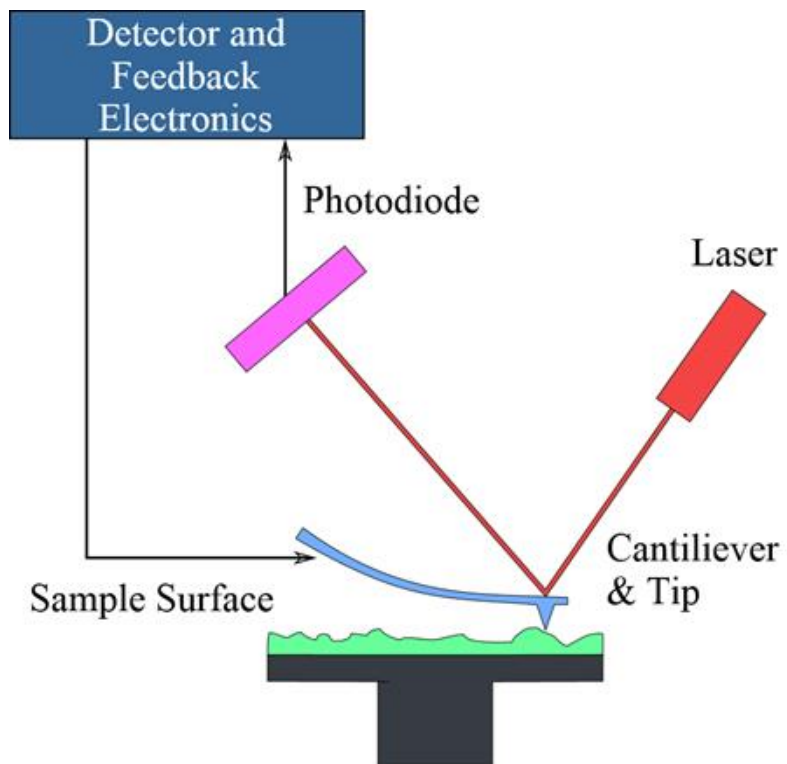


Figure 6.5 Schematic of an AFM using beam deflection detection (Nobelium, 2015).

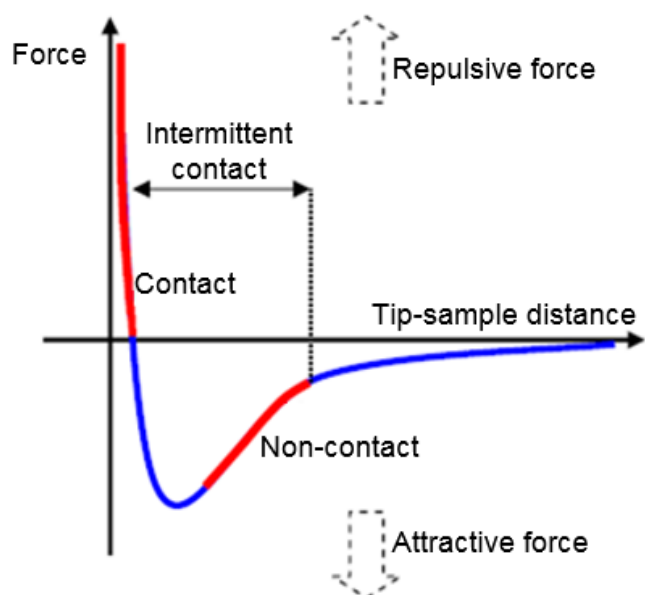


Figure 6.6 Relation between interatomic force and tip-to-sample distance, when the van der Waals force is dominated (Howland and Benatar, 1996; Maver *et al.*, 2013).

Compared with the SEM, the AFM is capable of providing three-dimensional surface profile in ambient air or even a liquid condition with no special surface treatments (such as conducting material coating). However, the AFM also shows

the limitation of image artefacts, which is unavoidable and may result from scanning speed, geometry of the tip or special sample topography (Ricci and Braga, 2004), as shown in Figure 6.7.

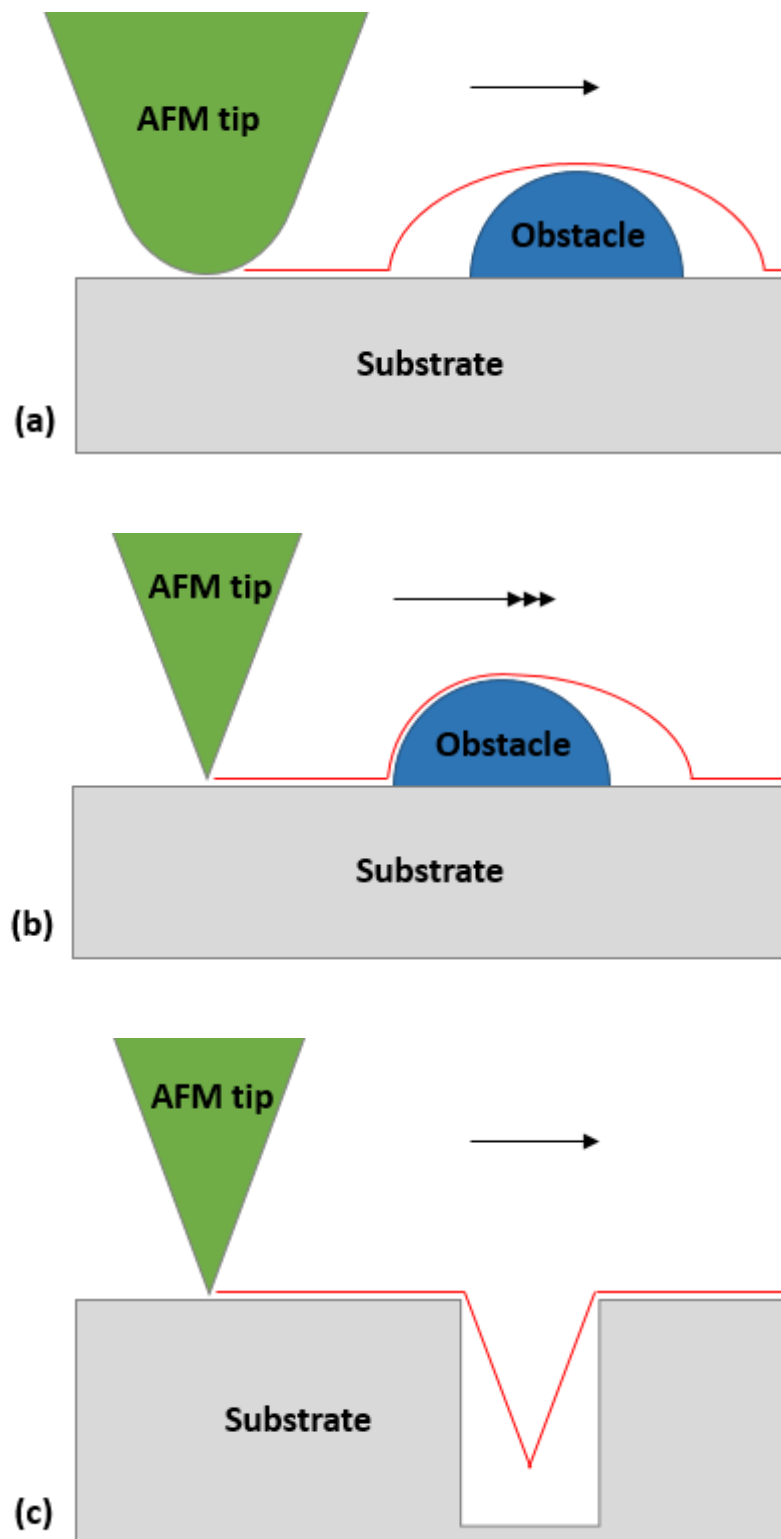


Figure 6.7 Schematic of AFM image artefacts due to (a) the bluntness of the tip, (b) a faster scanning speed, and (c) a steep sample topography.

6.2.4 Nanoindentation

6.2.4.1 Hysitron Triboindenter

A Hysitron TI900 Triboindenter (Hysitron Inc. Nanomechanical Test Instruments, Minneapolis, MN, USA) was used in this study. This machine works with load from a range of appropriately 25 μ N to 10 mN and continuously records the force and displacement data as a function of time. The basic components of the machine, as depicted in Figure 6.8, include: base, X-Y positioning stage, top-down optical microscope, head, vibration isolation platform, acoustic enclosure, control units and a data acquisition computer. To minimize the effect from the environment, the instrument is placed in a clean room with good humidity and temperature control system.

- The head consists of the transducer module and the TriboScanner. The TriboScanner consists of a three axis piezoelectric scanner, which enables the precise positioning of the indenter along with the horizontal direction (with a maximum X and Y range of 60 μ m) and vertical direction (with a maximum Z range of 3 μ m). The minimum positioning resolution is appropriately 20 nm, therefore the TriboScanner is used to do the final approach of the indenter to the surface, surface imaging and scratch tests. The transducer module, which is mounted to the TriboScanner, is the heart of this indenter system. It consists of a three-plate capacitive force/displacement transducer and a drive circuit board. It provides and simultaneously records the applied force and the corresponding movement of the indenter. By controlling the voltage applied to the transducer, the applied load of the indenter can be specified with a force resolution of 1 nN. Associated with a load signal feedback system, the displacement of the indenter can also be precisely controlled with a displacement resolution of 0.04 nm.
- The X-Y positioning stage provides the coarse control of the sample and the tip position with a step resolution of 50 nm.
- The top-down light microscope is incorporated to the Z positioning stage to provide quickly location of the indentation position. The magnification of the system is within the range of 10X to 100X.

- The granite base is primarily used to support the components. Together with vibration isolation platform and acoustic enclosure, the whole system is designed to minimize the vibration, thermal drift and acoustic noise and maximize the stability of the instrument during the testing.

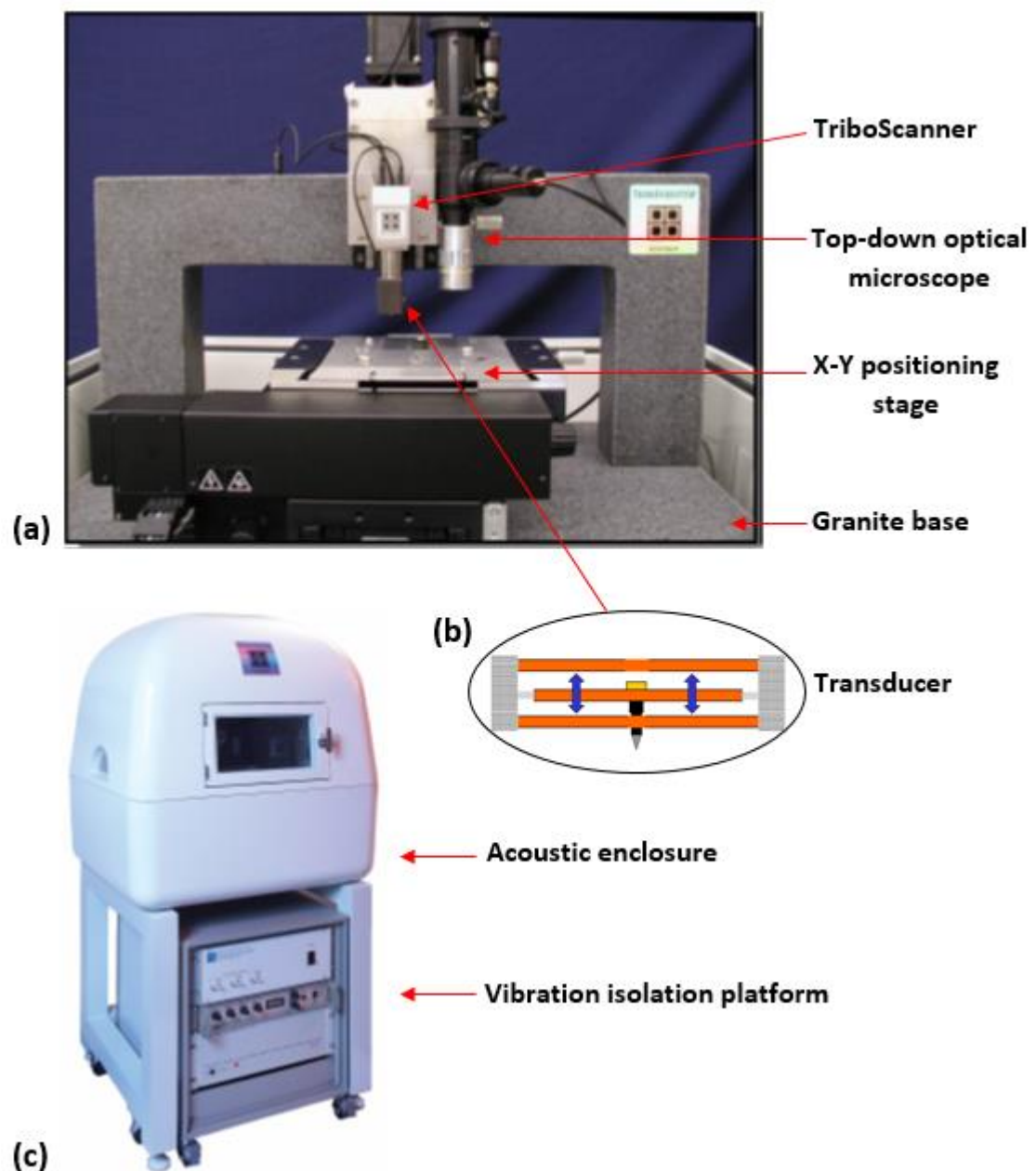


Figure 6.8 Pictures of Hysitron Triboindenter, (a) granite base, X-Y positioning stage, top-down optical microscope, Triboscanner and transducer, (b) schematic of the three-plate capacitive transducer, and (c) vibration isolation platform and acoustic enclosure (Wang et al., 2009).

6.2.4.2 Different test modes

This instrument offers the quasi-static test mode and the dynamic stiffness measurement mode. The quasi-static test mode is typically used to test the purely elastic-plastic materials. While by programming the load functions, this mode also shows the capability of characterization of time-dependent properties. Load functions can be controlled with load or displacement. Many different kinds of load functions can be programmed, as shown in Figure 6.9, varying from a simple loading-unloading function to various multi-cycling functions. A designed function, it can contain up to 50 linear or sinusoidal segments, and the loading and unloading rates can be specified. This instrument automatically calculates the thermal drift before the test is performed. All subsequent displacement data will be corrected for the thermal drift.

The dynamic nanoindentation mode is typically used to measure the materials that present significant time-dependent properties, such as polymers (Chakravartula and Komvopoulos, 2006) and fullerene like CN_x (Palacio and Bull, 2004), by measuring the storage modulus and loss modulus. The basics of this mode is similar to the CSM that has been presented in the previous chapter (Chapter 2, Section 2.2.3).

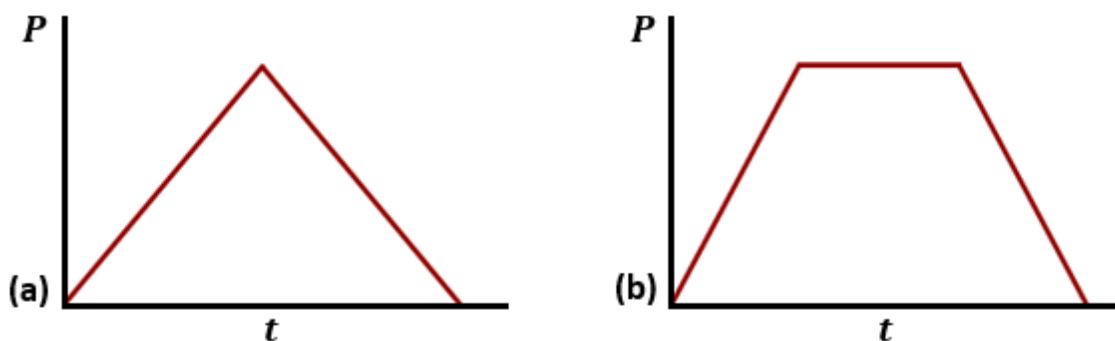


Figure 6.9 Schematic of various load functions, (a) a typical loading-unloading function, (b) a loading-unloading function with holding period at maximum load, (c) multi-cycling load function for constant repetition mode with holding period in each cycle, (d) multi-cycling load function for ramping mode, (e) multi-cycling load function for constant repetition mode, and (f) multi-cycling load function for ramping mode with holding period in each cycle (Nowicki *et al.*, 2003; Chen and Bull, 2008; Bull *et al.*, 2012).

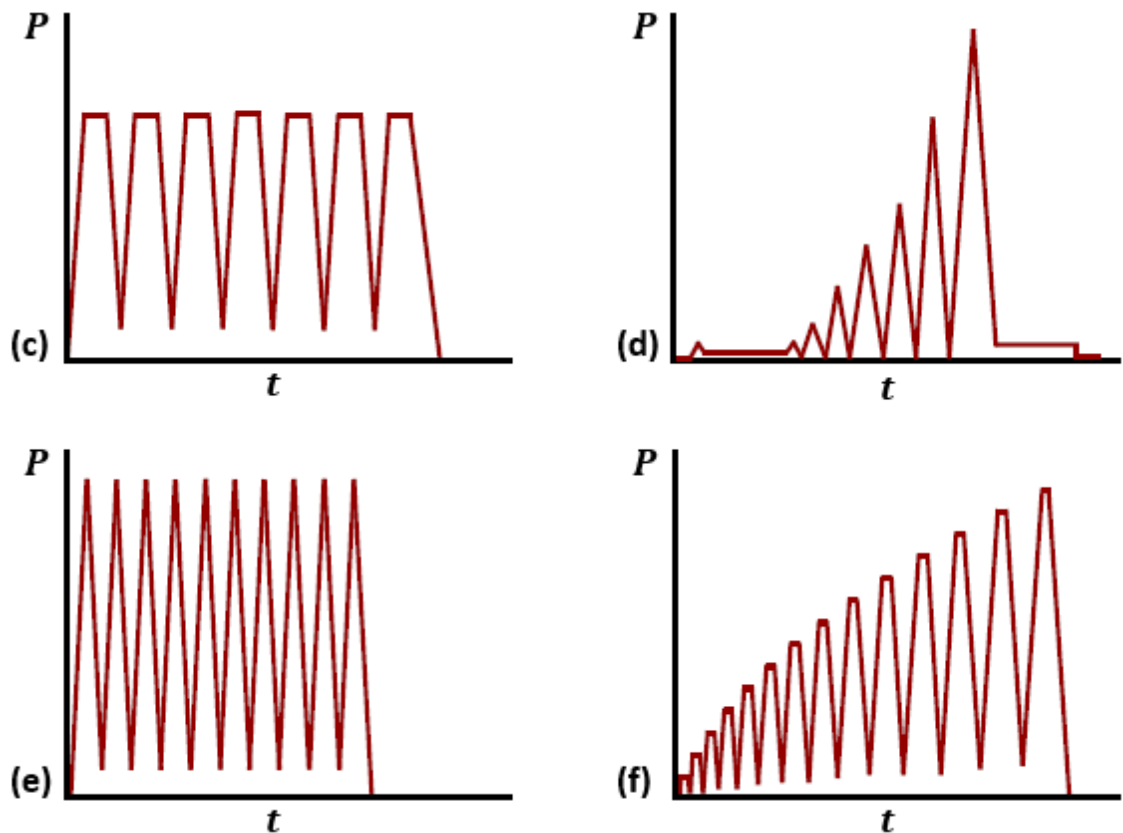


Figure 6.9 (Cont.)

The measurement of the nanomechanical characteristics of mineralized matrix is challenging due to its inhomogeneity at the scale of the deforming volume, and the indentation results will also be affected by the surface. Therefore, in this study, nanoindentation tests of the mineralized matrix were performed by a Berkovich diamond indenter, with a multi-cycling protocol as shown in Figure 6.10. This protocol enables the examination of the depth-dependent response at a specific location without influence from the lateral inhomogeneity (Chen and Bull, 2008). In this protocol, the loading and unloading rates are 400 $\mu\text{N/s}$, in each cycle the sample is partially unloaded to 10% of the peak load to keep the indenter in contact with the surface without lateral sliding. The peak load in each cycle increases from 1000 μN to 9000 μN , followed by a holding period of 5 seconds to allow creep run-out. This minimum and maximum peak loads in the multi-cycling loading function (*i.e.* 1000 μN and 9000 μN) should be carefully selected to minimize the influence from surface roughness and substrate. According to the surface roughness and sample thickness, the displacement within the range of approximately 200 nm to 1 μm is desired. Prior to the multi-cycling tests, samples were preliminarily tested with a displacement-controlled loading-unloading

function, with the maximum displacement of 200 nm and 1 μm . Afterwards, the minimum and maximum peak loads in multi-cycling loading function were accordingly designed as 1000 μN and 9000 μN , respectively.

The indentation tests were made at the centre of the samples. The machine stiffness and tip shape were accurately calibrated using a fused silica standard and the method of Oliver and Pharr. The elastic modulus and hardness were determined by the Oliver and Pharr method (Oliver and Pharr, 1992), and the key equations are given by,

$$S = \frac{dP}{dh} = \frac{2}{\sqrt{\pi}} E_r \sqrt{A} \quad (6.2)$$

$$H = \frac{P_{max}}{A} \quad (6.3)$$

where S is the contact stiffness at peak load calculated from the slope of the upper part of the unloading curve, P is the indentation force, h is the displacement, A is the contact area between the tip and sample, and E_r is the reduced modulus of the material, which is given by,

$$\frac{1}{E_r} = \frac{1 - \nu_s^2}{E_s} + \frac{1 - \nu_t^2}{E_t} \quad (6.4)$$

where E and ν are elastic modulus and Poisson's ratio, respectively. The subscripts s and t stand for the sample and the indenter. For each sample, at least 64 indents were made. Elastic modulus and hardness results were expressed as arithmetic mean values with standard deviation (SD).

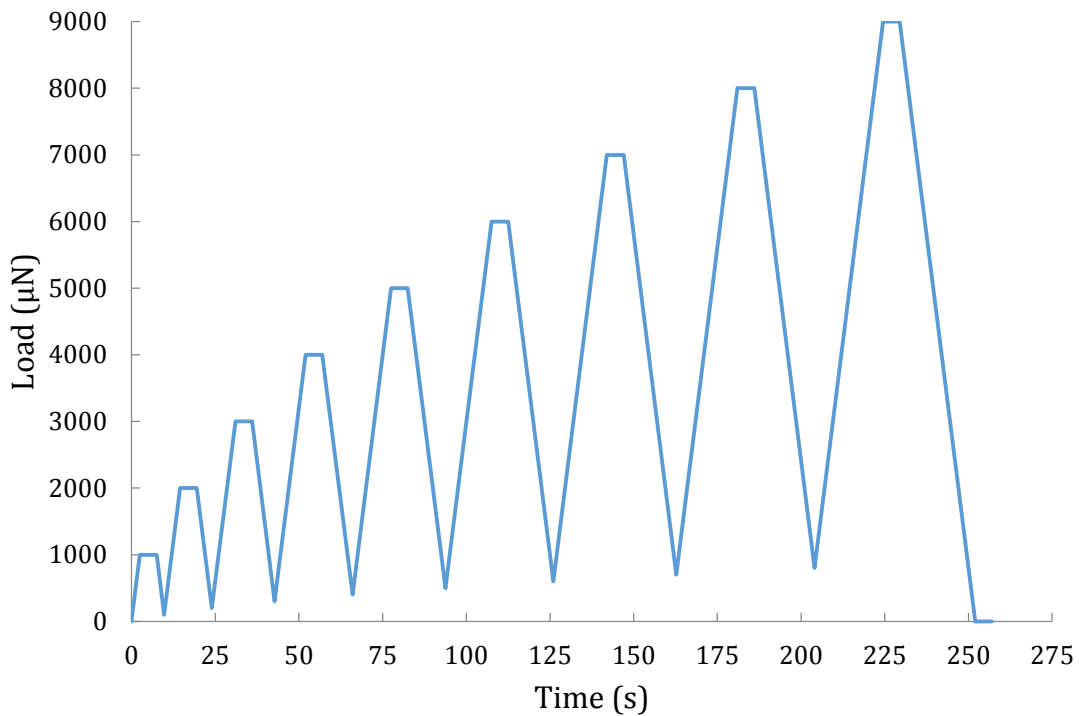


Figure 6.10 Schematic of the multi-cycling loading function

6.2.5 Statistical analysis

To determine the significant differences in the properties between different media and culture periods, two sample t-tests assuming unequal variances ($\alpha = 0.05$) were conducted to assess the p-value between the mechanical properties of samples cultured at different conditions. A Gaussian mixture model was adopted to separate the bimodal mechanical properties of the mineralized matrix from the complex nanoindentation results. In this model, by assuming that the elastic modulus or hardness distribution of each individual component follows a Gaussian distribution, the probability distribution function of elastic modulus or hardness, $f(x)$, is then given by (Nemecek, 2009; Zanjani Zadeh and Bobko, 2013; Zadpoor, 2015),

$$f(x) = \sum_{i=1}^m w_i f_i(x) \quad (6.5)$$

$$\sum_{i=1}^m w_i = 1 \quad (6.6)$$

$$f_i(x) = N(\mu_i, \sigma_i^2) \quad (6.7)$$

where m is the number of the components, w_i and $f_i(x)$ are volume fraction and Gaussian distribution for component i , respectively. Moreover, μ_i and σ_i represent the mean and standard deviation of the mechanical properties for component i , respectively. A Matlab code was written to complete this statistical analysis. Different m values have been assumed (*i.e.* 1, 2, 3...), but only $m=2$ gives the best fitting results. It indicates that there are possibly two major components in the mixture model.

6.2.6 Finite element modelling

To further understand the nanoindentation response of the mineralized matrix, FEM was employed (Fan *et al.*, 2004; Carnelli *et al.*, 2011). As found in our previous study (Duan and Chen, 2015), the distribution of apparent elastic modulus generally appeared to be bimodal (more details will be presented in the following section). This may be attributed to transversely isotropic properties or two components with different mechanical properties. Therefore, in this study we examined these two cases by assuming a transversely isotropic material or the matrix composed of two components in the FE model. A conical tip with equivalent semi-apical angle to a Berkovich indenter was used. This is a reasonable assumption for investigating the elastic response.

As illustrated in Figure 6.11a, part 1 and part 2 present (*i*) the transversely isotropic properties of the matrix in two perpendicular directions, or (*ii*) the isotropic properties of mature and immature matrix, respectively. In the former case, the elastic modulus of the transversely isotropic fibre was set as 15 GPa in the transverse direction, and 28 GPa in the longitudinal direction. In the latter case, the elastic modulus of mature and immature bone nodules was set to be 28 GPa and 15 GPa, respectively. The selected elastic moduli are within the range of our experimental measurements. The Poisson's ratio in both cases was assumed to be 0.3. As illustrated in Figure 6.11b, different locations were indented by a conical tip with tip radius of 0.01 μm : indented on each individual part (point A, I), indented at their interface (point E), and indented at points that are 0.25 μm (point D, F), 0.5 μm (point C, G), and 1 μm (point B, H) away from the interface. For the case of indentation on each individual part, the properties of the two parts were set to be the same and the indentation occurred at the

centre of the model. The model was developed in the ABAQUS 6.14 software. As shown in Figure 6.11c, only half of the whole system was modelled by employing the symmetric boundary condition to the symmetric plane, a flat surface was assumed, a frictionless contact between the indenter and the model was assumed, and the tip was modelled as a rigid body. The interface between part 1 and part 2 was assumed to be perfectly bonded. A completely fixed boundary condition was applied to the bottom of the model. A total number of 48,580 linear C3D8R eight-node elements were used, with denser mesh created underneath the indenter. According to the previous experience, the density of mesh set for each model should be fine enough. Hence, the model validation of these FE models is not repeated here (Duan *et al.*, 2015). The height and the width of the model were sufficiently large compared to the indentation depth so that the simulated response was not significantly affected by the boundaries. Displacement control was applied to a loading-unloading protocol with a maximum indentation depth of 0.1~0.7 μm in each case. The elastic modulus of the model was determined from the force-displacement data generated by using the Oliver and Pharr method.

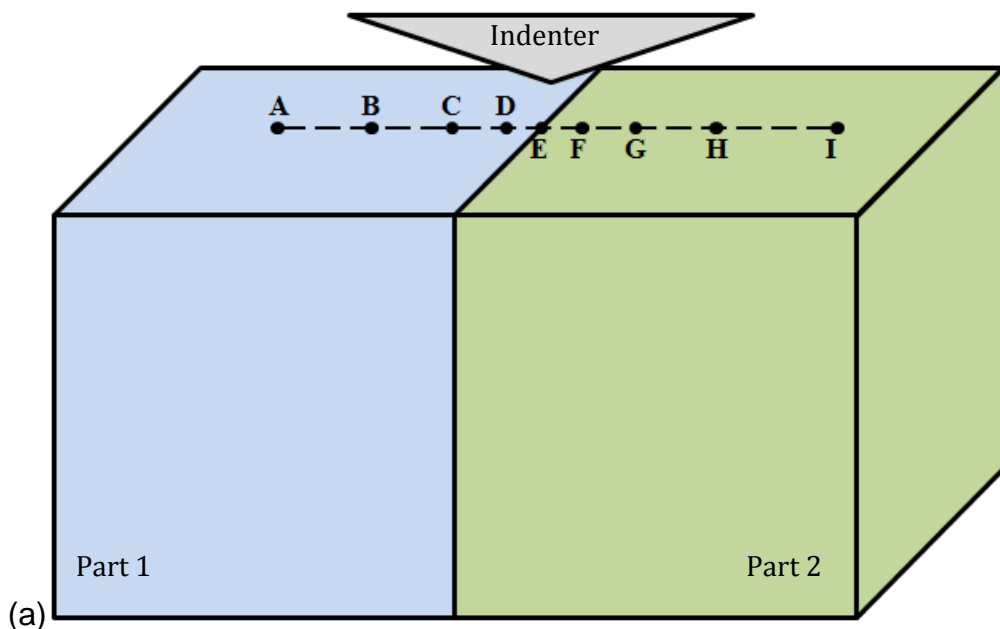


Figure 6.11 Schematic of (a) the model with distribution of different indented locations, (b) vertical distance of each indentation points away from the interface, and (c) the meshes for the model.

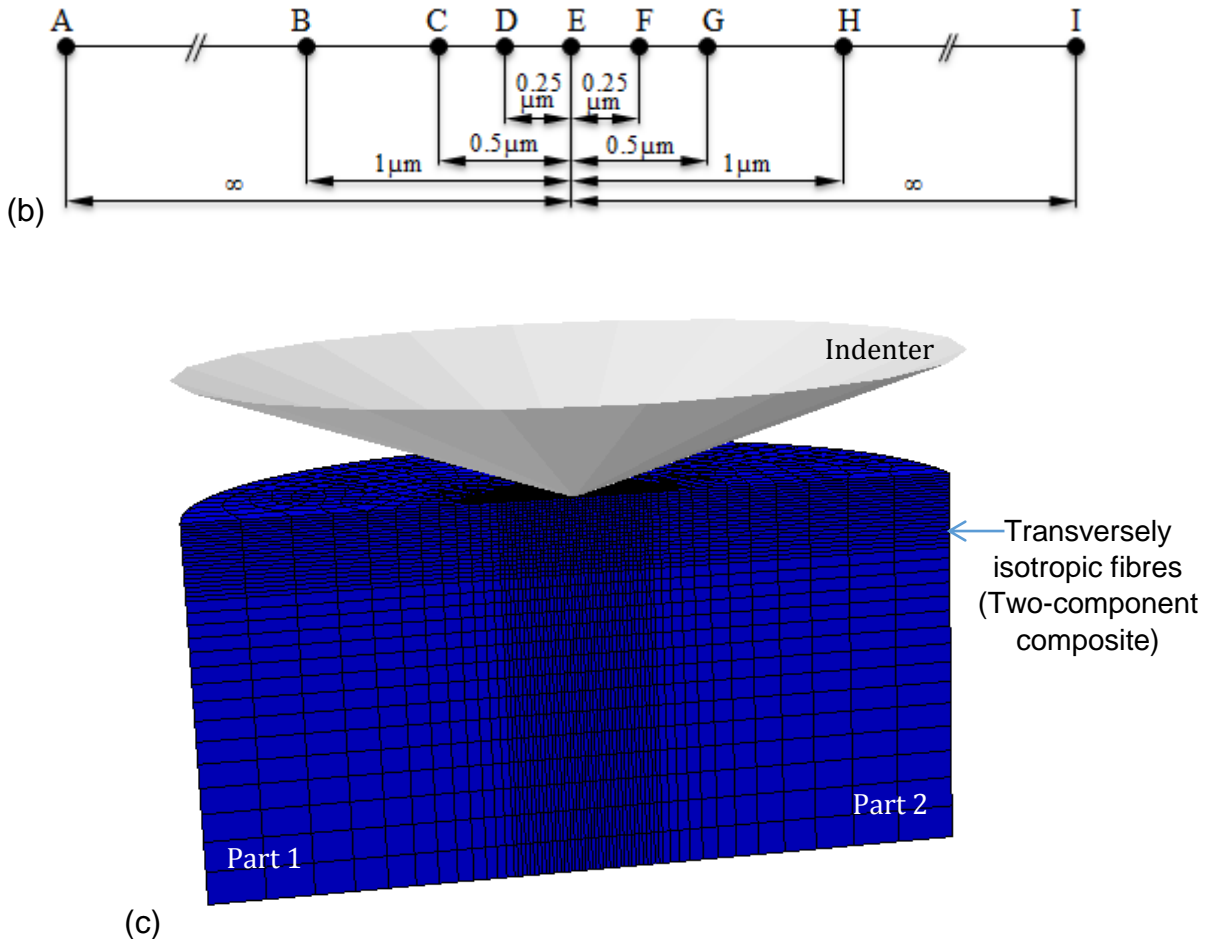


Figure 6.11 (Cont.)

6.3 Results and discussion

6.3.1 Surface analysis

For each sample, surface roughness was measured five times at different locations near the sample centre. The mean roughness (*i.e.* the arithmetic average roughness, R_a) was calculated in this work, which is one of the most commonly adopted surface roughness measures. As shown in Table 6.1, the value of R_a for all the samples demonstrates a positive correlation with the culture period for both culture media. In a fixed cell culture period, there is no significant difference between the roughness of samples cultured in BM and OM. This suggests that the growth of cells contributed to the roughness with a porous structure, especially at day 21. The surface roughness of the matrix is affected by the growth of the cells, rather than by the culture media.

Medium	Sample	$R_a \pm SD (\text{nm})$		
		day 7	day 14	day 21
BM	1	102.2±6.3	174.8±31.4	387.0±57.2
	2	108.6±17.2	204.0±34.7	215.4±23.8
	3	100.0±20.0	198.2±30.6	196.8±18.4
OM	1	115.6±16.5	192.2±21.2	-
	2	147.4±7.9	177.6±21.9	-
	3	107.6±12.7	181.0±14.2	-

Table 6.1 Surface roughness of the samples for different culture periods in BM and OM.

Figure 6.12 shows typical SEM images for cells cultured at different conditions. The cell density at day 7 for the OM is much higher compared to that for the BM. For samples harvested from the BM, the cell number increases rapidly after day 7 and cell segregation has been observed at day 14 and 21. Such cell segregation is less significant for samples harvested from the OM. Mineral particles with the area of $80 \mu\text{m} \times 120 \mu\text{m}$ were clearly observed on the samples cultured in BM for 21 days (Figure 6.12c), and Figure 6.13 shows the enlarged details of these minerals. No minerals were observed for the samples harvested from day 14 and day 7 in SEM micrographs. The chemical composition of the observed minerals was analysed by EDS, with the corresponding analyses shown in Figure 6.14 and Figure 6.15. The important characteristic of these minerals is the Ca/P ratio, as this ratio is normally used to symbolize the quality of bone (Gronthos *et al.*, 1994; Zaichick and Tzaphlidou, 2003; Donzelli *et al.*, 2007). The average Ca/P ratio (by weight) of these minerals is equal to 1.96 ± 0.10 , which agrees well with the reported value (1.74~2.37) of a native femoral trabecular bone (Zaichick and Tzaphlidou, 2003).

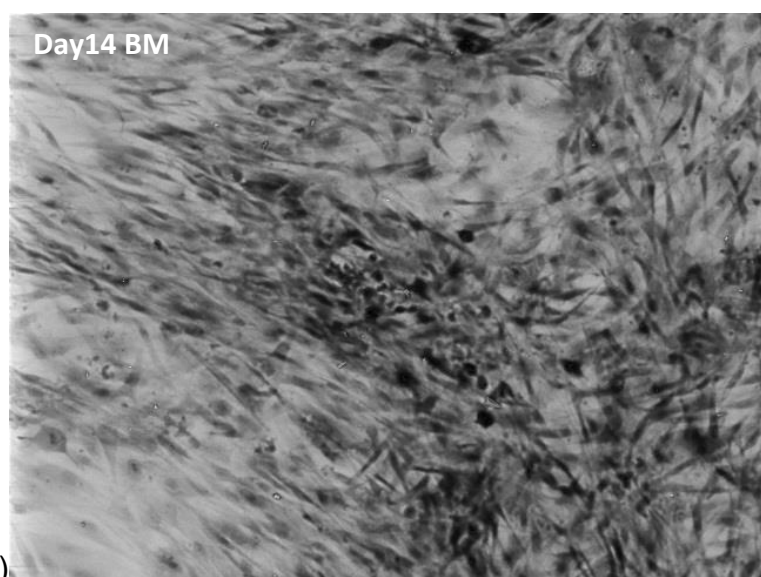
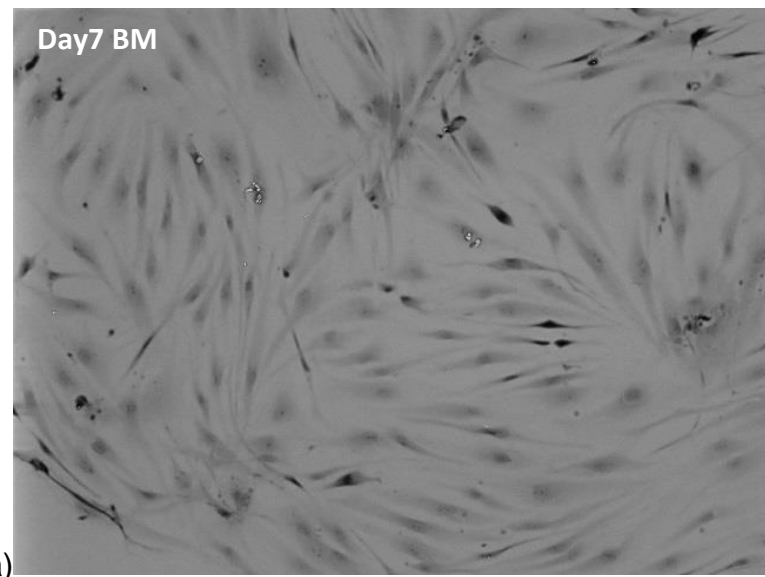


Figure 6.12 Typical SEM images of cells cultured at different conditions (A: day 7, BM; B: day 14, BM; C: day 21, BM; D: day 7, OM; E: day 14, OM), an enlargement of the marked area in figure C is shown in Figure 6.13.

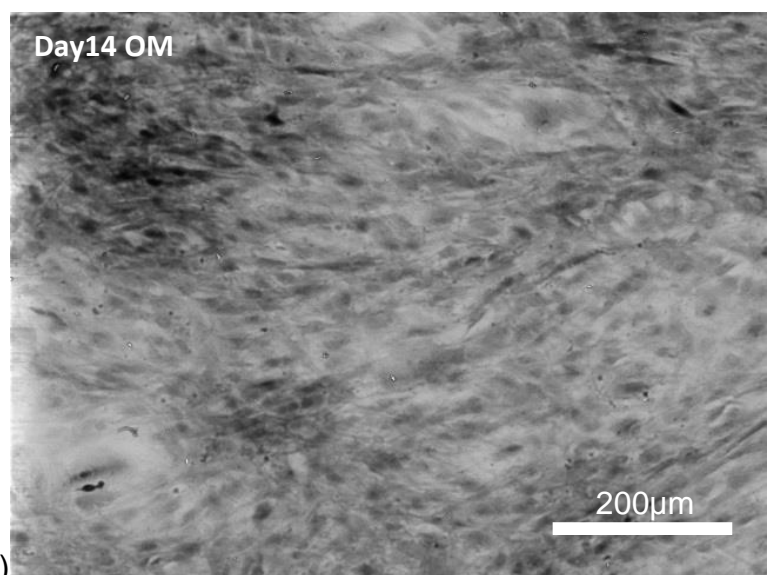
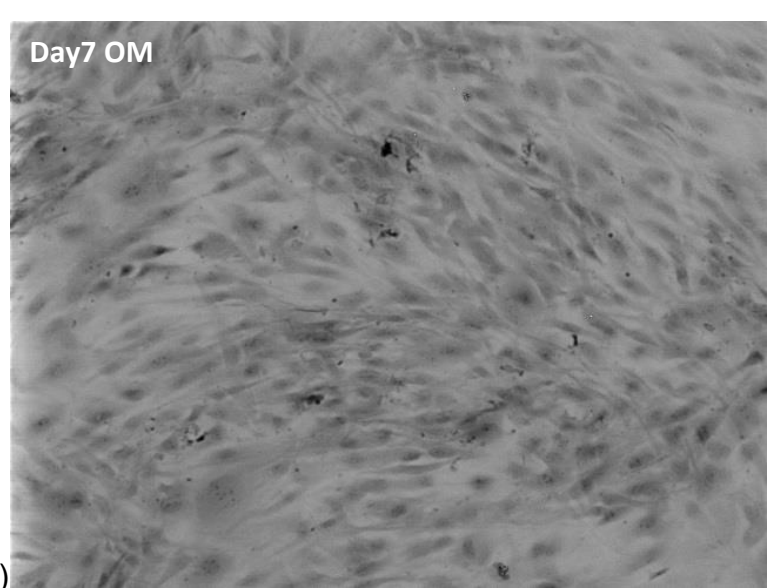
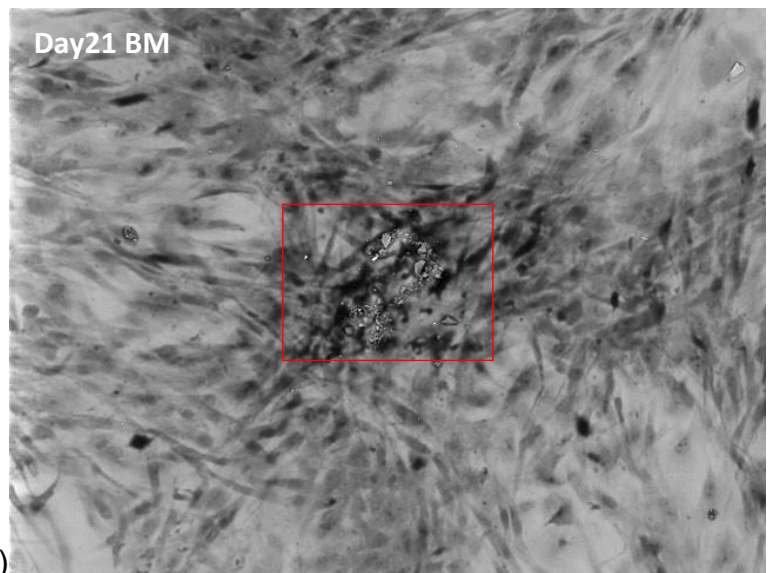


Figure 6.12 (Cont.)

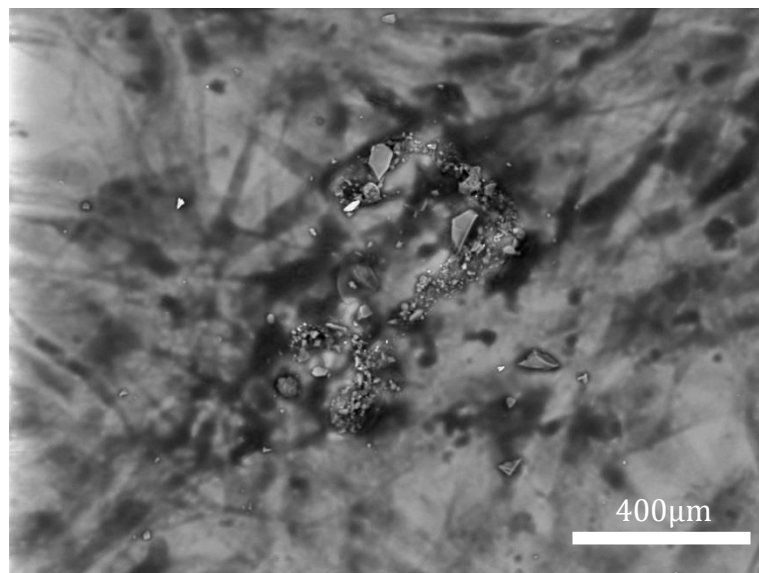


Figure 6.13 Minerals observed on samples cultured in BM for 21 days.

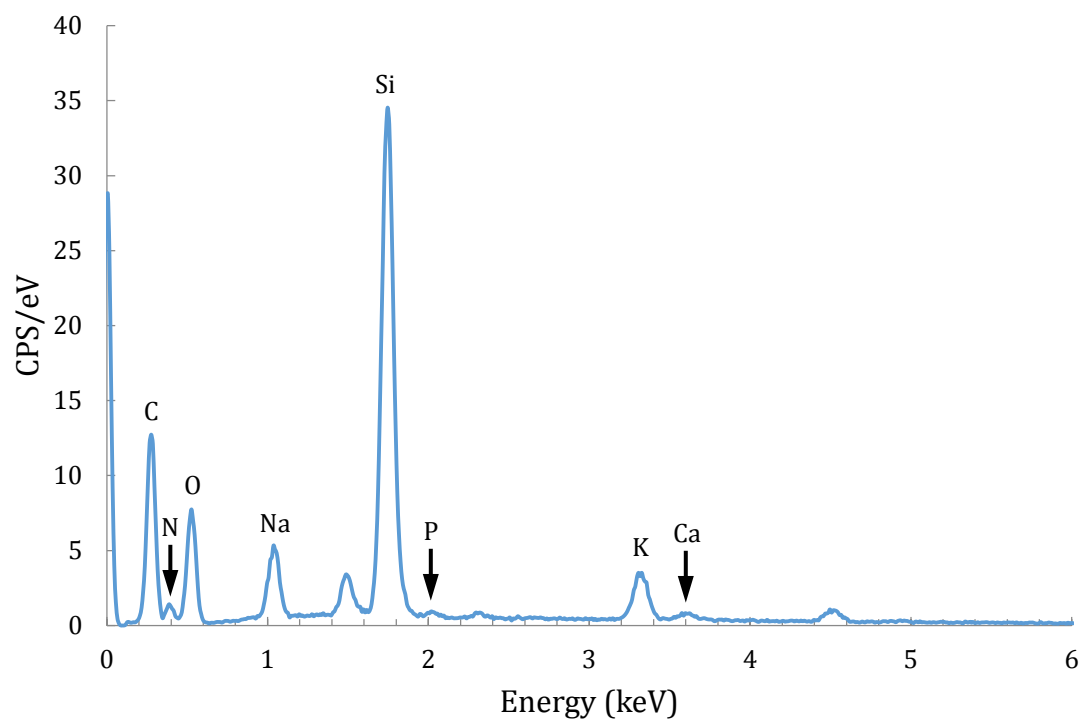


Figure 6.14 EDS spectrum for the minerals observed on the sample cultured in BM for 21 days.

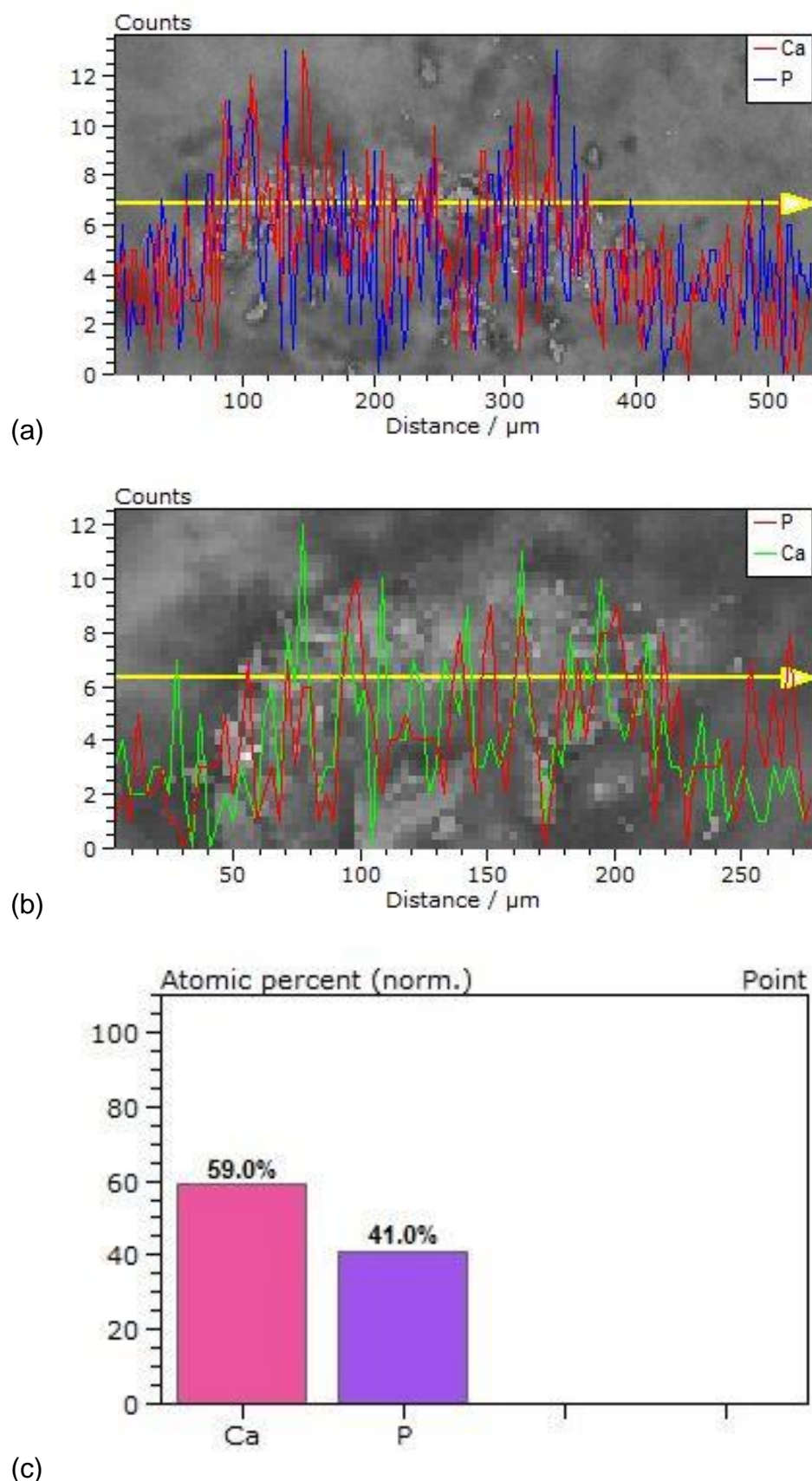


Figure 6.15 Representative intensity profile of calcium and phosphorus for the minerals detected in the line scan mode and the corresponding percentage of calcium and phosphorus.

The AFM images in Figure 6.16 reveal that, for samples harvested from the BM, a porous structure can be seen at an early stage (Figure 6.16a). After that, the structure becomes slightly denser at day 14 (Figure 6.16b), and fully dense at day 21 (Figure 6.16c). For samples harvested from the OM, surfaces are relatively dense (Figure 6.16d-e). Similar structures were also observed on samples cultured by murine osteoblasts (Turner *et al.*, 2007). For BM samples at day 7, it is evident that it has aligned microstructure which is responsible to the highly anisotropic mechanical properties. When the culture period increases to 21 days, some bright dots were observed which are likely due to the precipitation of minerals.

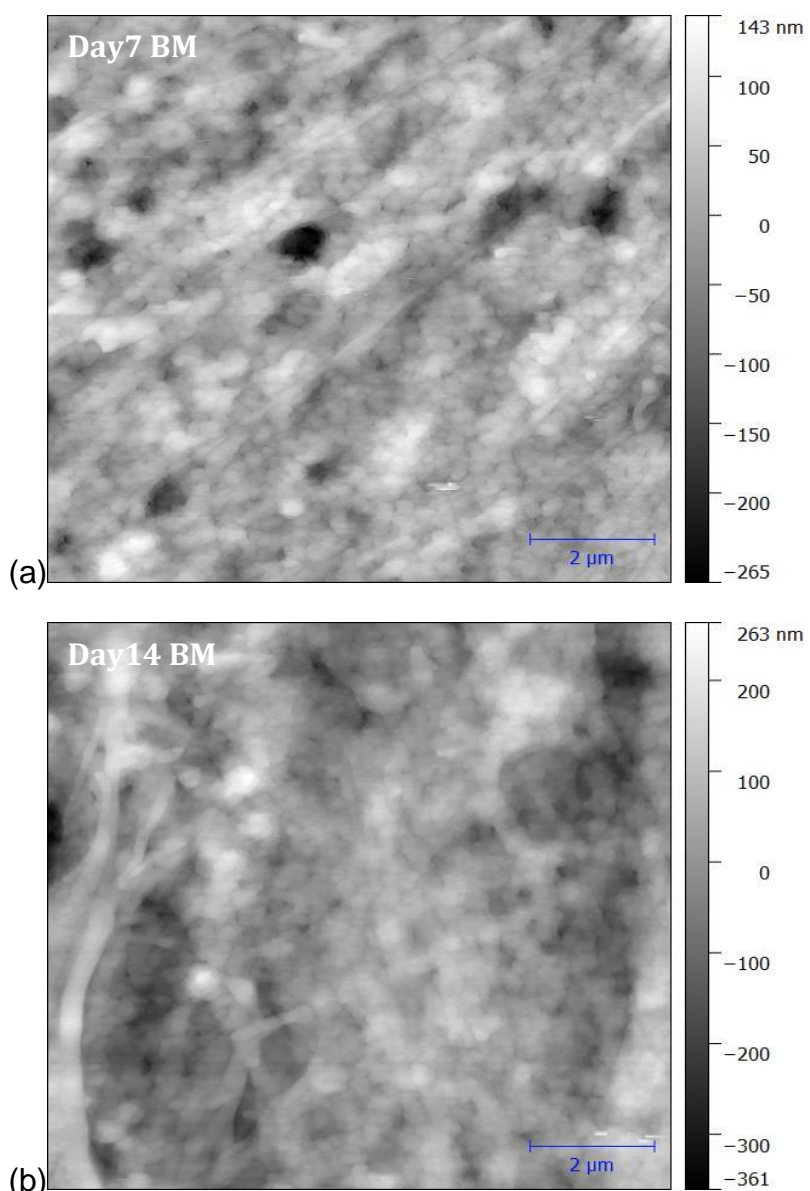


Figure 6.16 Representative AFM images of samples cultured at different conditions (A: day 7, BM; B: day 14, BM; C: day 21, BM; D: day 7, OM; E: day 14, OM).

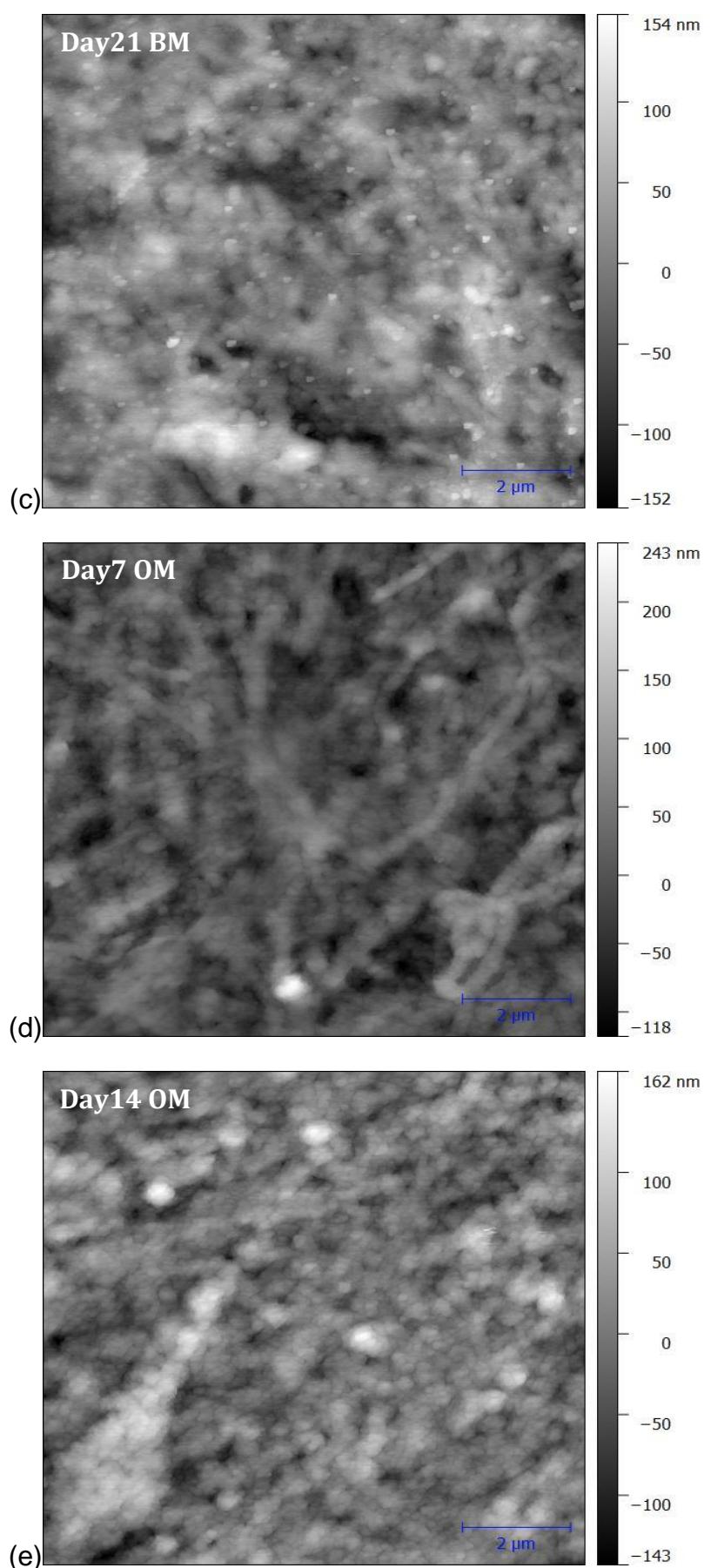


Figure 6.16 (Cont.)

Furthermore, in order to reveal more microstructural details of these extracellular matrix, polarized light images of these samples were also generated. As an example, the polarized light images of samples harvested from day 14 are shown in Figure 6.17; collagen fibre bundles (bright spots) can be identified. They are well-aligned on the samples cultured in BM and randomly distributed on the samples cultured in OM, which suggests that the samples cultured in BM will show anisotropic mechanical properties and the samples cultured in OM will show relatively isotropic mechanical properties (Stylianou *et al.*, 2014). For samples harvested from day 7 and day 21, a similar observation was found.

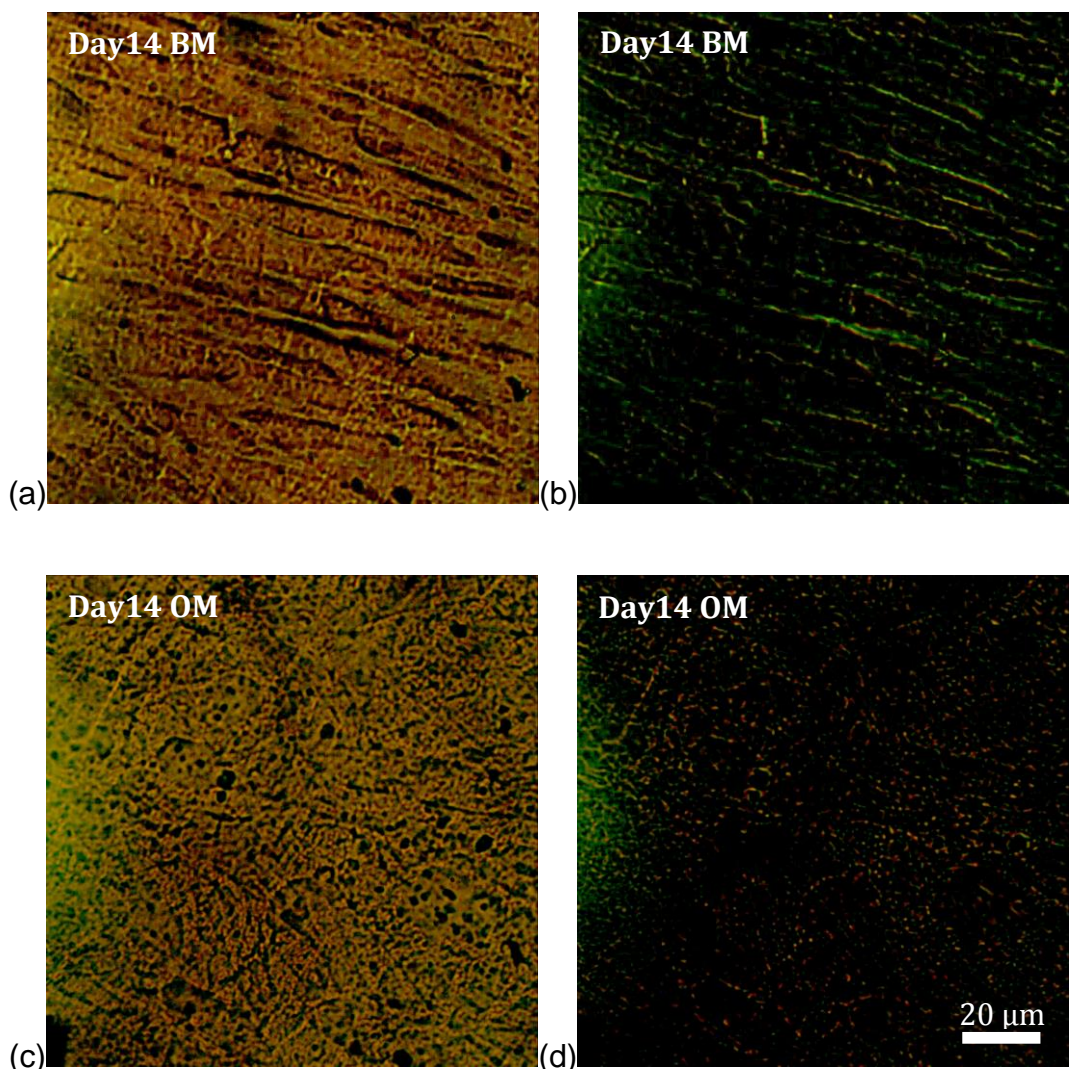


Figure 6.17 Representative polarized light images of samples harvested from (a, b) day 14, BM, (c, d) day 14, OM. Among them, image (a, c) are samples viewed with parallel polars, and image (b, d) are the same field viewed with crossed polars.

6.3.2 Nanoindentation results

6.3.2.1 The apparent elastic modulus and hardness

Figure 6.18 displays a representative force-displacement curve for a multi-cycling nanoindentation test for sample cultured in the BM for 21 days. The hysteresis loop can be caused by fracture, phase transformation or viscosity (Chen *et al.*, 2009). In this study, it is more likely to correlate to viscosity of the matrix. Upon unloading, the recovery of the displacement is more obvious at low force than at high load. This is because the plastic deformation within the material is less likely to occur at low load. With the increase of maximum load in each cycle, the nanomechanical response transits from viscoelastic-dominated to viscoplastic-dominated. Hence, more attention should be paid in the viscoelasticity and viscoplasticity of the sample in the future. Previous work has demonstrated that 5 seconds holding period should be enough to minimize the influence from the viscosity of the matrix (Chen, 2014). By analysing these force-displacement curves, spatial-dependent Young's modulus and hardness values ($P<0.001$) can be determined as a function of contact depth and these are summarized in Table 6.2 and Table 6.3, respectively. To make it more readable, the Young's modulus and hardness against the average contact depth are plotted in Figure 6.19 and Figure 6.20 as well.

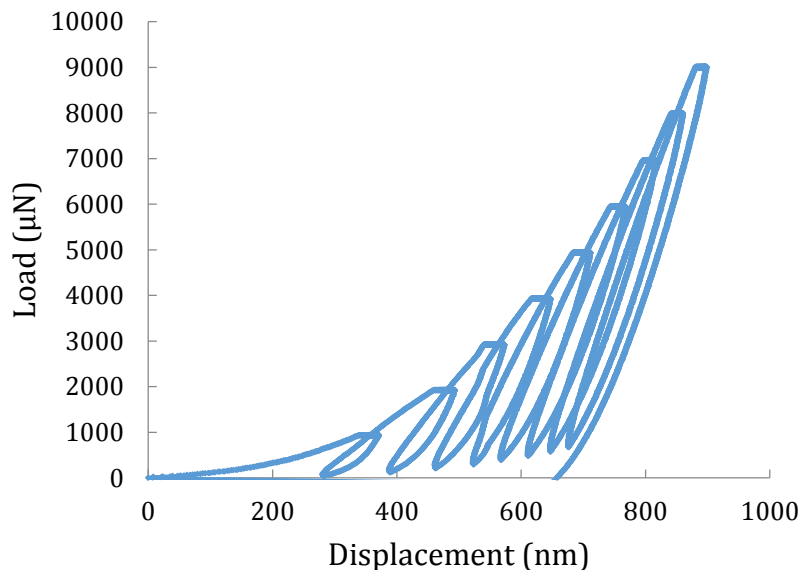


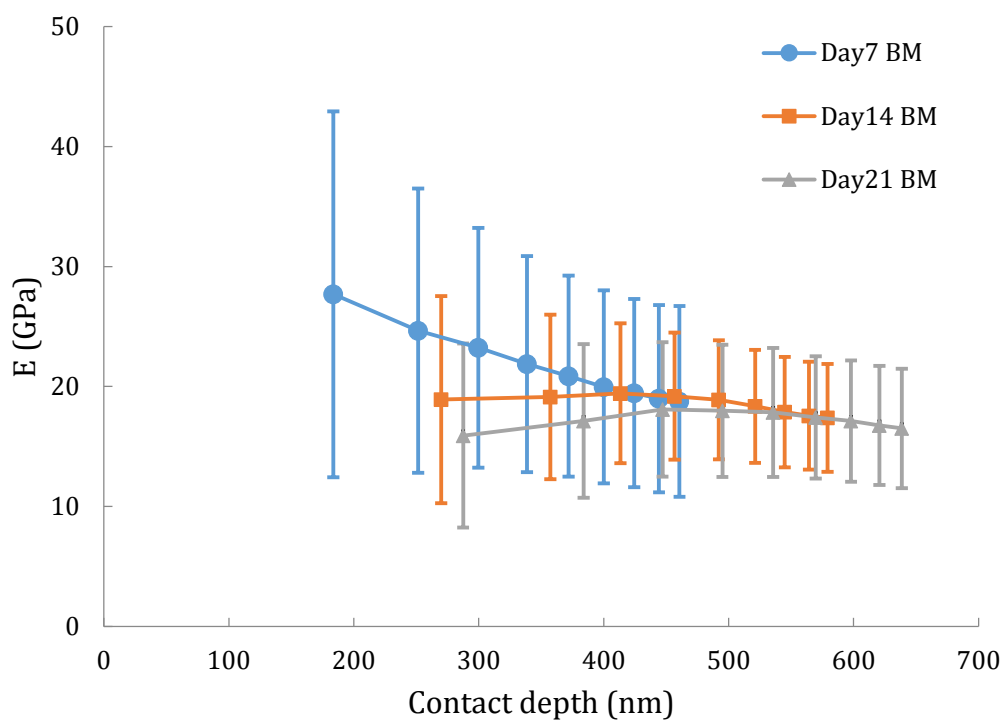
Figure 6.18 Representative force-displacement curve from multi-cycling tests for sample cultured in BM for 21 days.

F(max) in each cycle (μ N)	Elastic modulus			Hardness			Contact depth Mean \pm SD (nm)	
	day 7	day 14	day 21	day 7	day 14	day 21		
1000	27.68 \pm 15.26	18.90 \pm 8.64	15.91 \pm 7.67	1.78 \pm 1.84	0.45 \pm 0.38	0.35 \pm 0.20	183.58 \pm 106.49	269.87 \pm 79.97
2000	24.65 \pm 11.86	19.14 \pm 6.86	17.12 \pm 6.40	1.83 \pm 1.71	0.55 \pm 0.45	0.43 \pm 0.26	251.54 \pm 142.29	357.34 \pm 108.52
3000	23.23 \pm 9.99	19.43 \pm 5.82	18.09 \pm 5.61	1.82 \pm 1.57	0.64 \pm 0.48	0.50 \pm 0.30	299.65 \pm 163.09	413.35 \pm 126.42
4000	21.87 \pm 9.00	19.18 \pm 5.30	17.97 \pm 5.50	1.83 \pm 1.49	0.71 \pm 0.51	0.55 \pm 0.33	338.58 \pm 178.87	456.65 \pm 140.17
5000	20.86 \pm 8.38	18.89 \pm 4.97	17.84 \pm 5.38	1.85 \pm 1.45	0.77 \pm 0.54	0.60 \pm 0.36	371.91 \pm 192.23	492.16 \pm 151.78
6000	19.97 \pm 8.04	18.35 \pm 4.71	17.43 \pm 5.10	1.89 \pm 1.45	0.84 \pm 0.57	0.65 \pm 0.39	400.06 \pm 203.34	521.18 \pm 161.57
7000	19.44 \pm 7.84	17.87 \pm 4.60	17.12 \pm 5.05	1.95 \pm 1.48	0.90 \pm 0.60	0.70 \pm 0.42	424.41 \pm 213.17	544.93 \pm 170.29
8000	18.99 \pm 7.81	17.56 \pm 4.49	16.75 \pm 4.97	2.03 \pm 1.55	0.97 \pm 0.65	0.75 \pm 0.46	444.22 \pm 221.76	564.30 \pm 178.15
9000	18.76 \pm 7.96	17.38 \pm 4.50	16.50 \pm 4.97	2.14 \pm 1.65	1.05 \pm 0.70	0.81 \pm 0.50	460.64 \pm 229.00	579.21 \pm 185.53

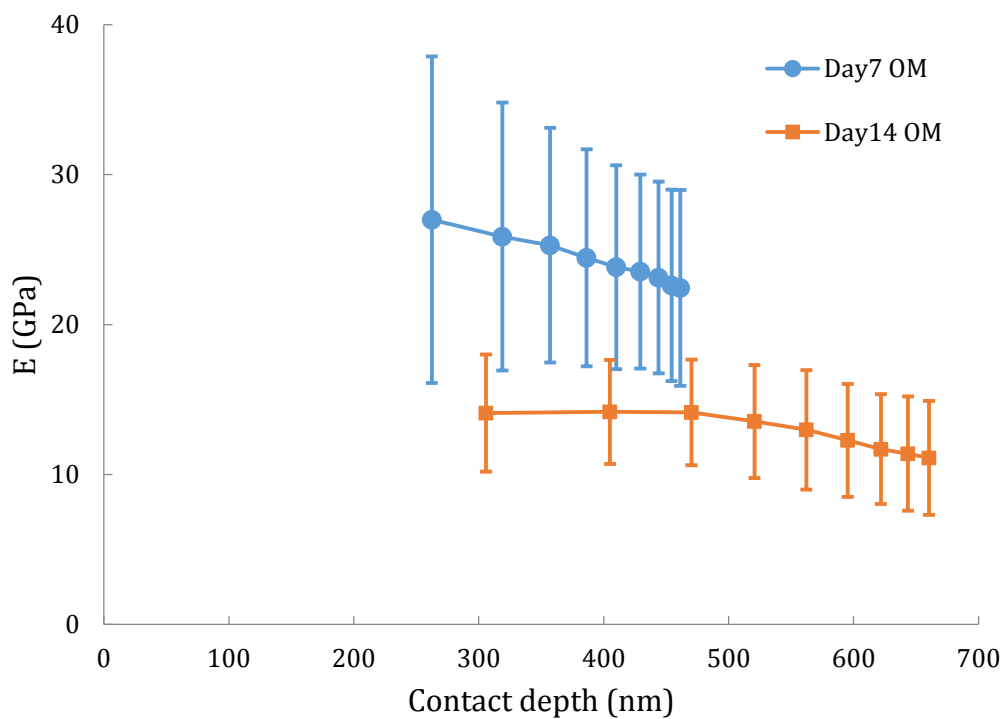
Table 6.2 Elastic modulus, hardness and contact depth of samples cultured in BM detected by multi-cycling tests with different maximum force in each cycle.

F(max) in each cycle (μ N)	Elastic modulus		Hardness		Contact depth Mean \pm SD (nm)
	day 7	day 14	day 7	day 14	
1000	27.00 \pm 10.89	14.10 \pm 3.90	0.85 \pm 1.06	0.29 \pm 0.11	262.43 \pm 212.52
2000	25.87 \pm 8.94	14.18 \pm 3.47	1.03 \pm 1.07	0.36 \pm 0.13	318.85 \pm 221.08
3000	25.30 \pm 7.83	14.15 \pm 3.52	1.14 \pm 1.04	0.42 \pm 0.16	357.11 \pm 226.27
4000	24.46 \pm 7.24	13.54 \pm 3.77	1.25 \pm 1.03	0.47 \pm 0.17	386.35 \pm 229.6
5000	23.83 \pm 6.80	12.98 \pm 3.98	1.34 \pm 1.04	0.51 \pm 0.19	409.96 \pm 232.23
6000	23.54 \pm 6.47	12.28 \pm 3.77	1.44 \pm 1.07	0.55 \pm 0.20	429.26 \pm 234.61
7000	23.14 \pm 6.39	11.70 \pm 3.66	1.55 \pm 1.12	0.60 \pm 0.22	443.96 \pm 236.86
8000	22.63 \pm 6.38	11.40 \pm 3.81	1.69 \pm 1.20	0.65 \pm 0.24	454.26 \pm 239.03
9000	22.45 \pm 6.52	11.11 \pm 3.81	1.85 \pm 1.33	0.70 \pm 0.27	461.32 \pm 241.30

Table 6.3 Elastic modulus, hardness and contact depth of samples cultured in OM detected by multi-cycling tests with different maximum force in each cycle.

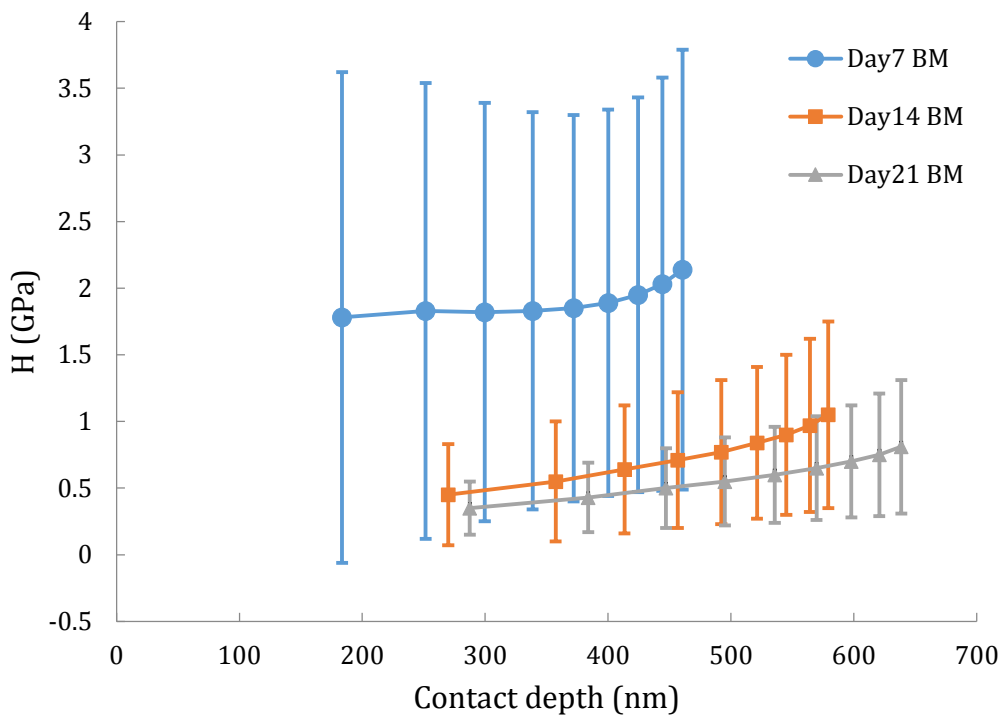


(a)

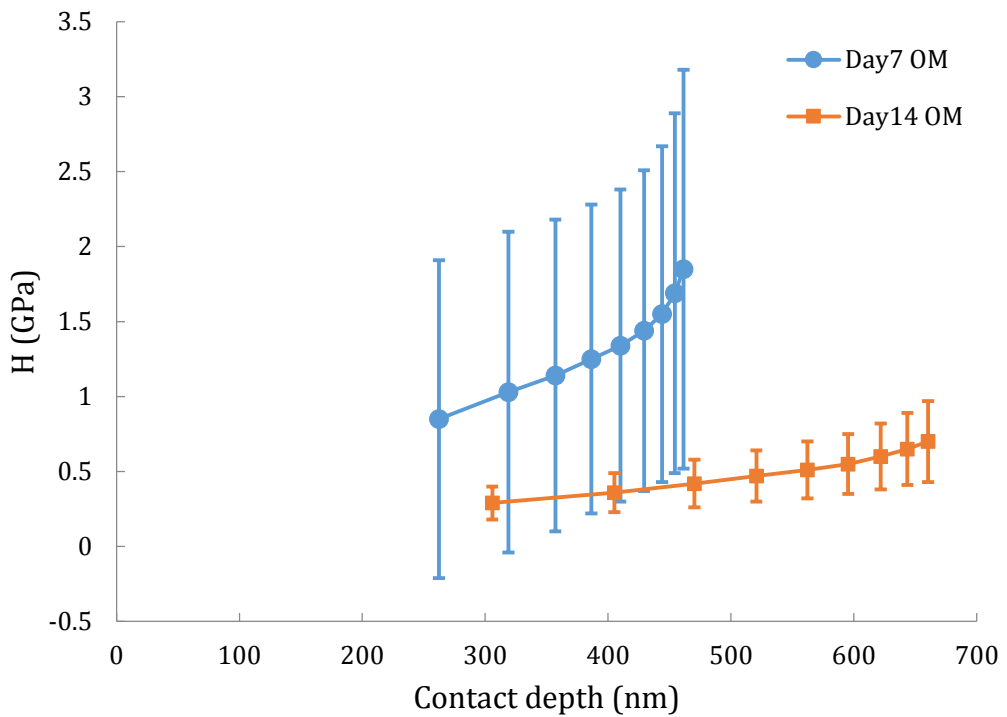


(b)

Figure 6.19 Young's modulus (\pm SD) of samples cultured in (a) BM and (b) OM ($P<0.001$), as a function of average contact depth for nanoindentation tests in the peak load range 1~9 mN.



(a)



(b)

Figure 6.20 Hardness (\pm SD) of samples cultured in (a) BM and (b) OM ($P<0.001$), as a function of average contact depth for nanoindentation tests in the peak load range 1~9 mN.

In the given load range (1~9 mN), the average Young's modulus of samples cultured in the BM changes in the range of 18.8~27.7 GPa at day 7. These values decrease to 17.4~18.9 GPa at day 14 and 15.9~18.1 GPa at day 21. In the same load range, the average Young's modulus of samples cultured in the OM is in the range of 22.5~27.0 GPa at day 7. These values decrease to 11.1~14.2 GPa at day 14. In general, for all the samples, the measured Young's moduli decrease with the contact depth across the entire load range. Similar to the Young's moduli, the measured hardness values also decrease with the cell culture period.

For elastic modulus, it has been reported that the modulus of collagen in nanoindentation ranges from 1.71 GPa to 3.31 GPa (Chaudhry *et al.*, 2009), and modulus of human vertebral trabeculae is from 11.3 GPa to 15.8 GPa (Wolfram *et al.*, 2010). Thus, the elastic modulus of the matrix is similar to native bone after 7 to 14 days, and the relatively high Young's modulus of mineralized matrix in contrast to the collagen fibres indicates that the matrix is highly mineralized (Wenger *et al.*, 2007; Chaudhry *et al.*, 2009). The minerals are likely to be nanocrystals, as a very limited amount of crystals were observed at the micro scale or above by SEM. This may suggest the matrix has a highly inhomogeneous structure near the surface and the effect from the substrate is negligible. When the contact depth is below 450 nm, there is strong depth dependent behaviour for day 7 samples (both BM and OM). It has been reported in the previous AFM results (Figure 6.16) that the sample structure changes from porous to dense with the increasing culture period. Thus, it indicates the elastic modulus will be highly affected by the porous surface structure at shallow contact depth, especially at day 7. With an increase of contact depth, the porous structure underneath the indenter is compressed, pores are closed up and then the corresponding elastic modulus becomes more stable.

It is also interesting to investigate the distribution of the measured apparent elastic modulus. It was reported elsewhere that the engineered bone can have a wide distribution of nanoindentation modulus (Pelled *et al.*, 2007a; Chen *et al.*, 2010b). For example, Figure 6.21 shows the distribution of the nanoindentation modulus for an engineered bone produced by the C3H10T1/2 MSC line grown *in vivo* for 28 days (Pelled *et al.*, 2007a). For comparison, Figure 6.22 displays histograms of the elastic modulus for mineralized matrix samples at the same peak loads (*i.e.* 1000 μ N and 7000 μ N). Similar to the data shown in Figure 6.21,

the distribution of modulus for all the BM samples shown in Figure 6.22 also presents a multimodal distribution at lower peak loads, and a homogenized response at higher peak loads (with comparable peak modulus values). This may suggest that the mineralized matrix produced by Y201 MSCs is similar to mature bone matrix produced by C3H10T1/2 MSCs. For samples cultured in the OM, this multimodal distribution can only be observed at day 7. The measured Young's modulus decreases from day 7 to day 14, but the variation of the Young's modulus is relatively stable with the change of the indentation force. This may suggest that the matrix cultured from the OM is more uniform than the matrix cultured from the BM, just like the topography variation in the previous AFM results (Figure 6.16) and the collagen fibre distribution shown in the previous polarized light images (Figure 6.17).

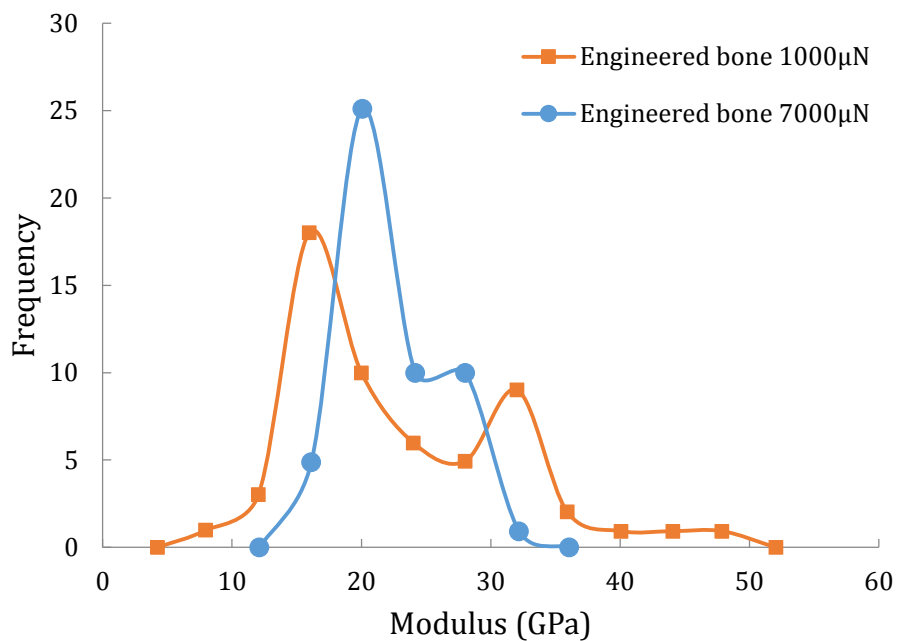
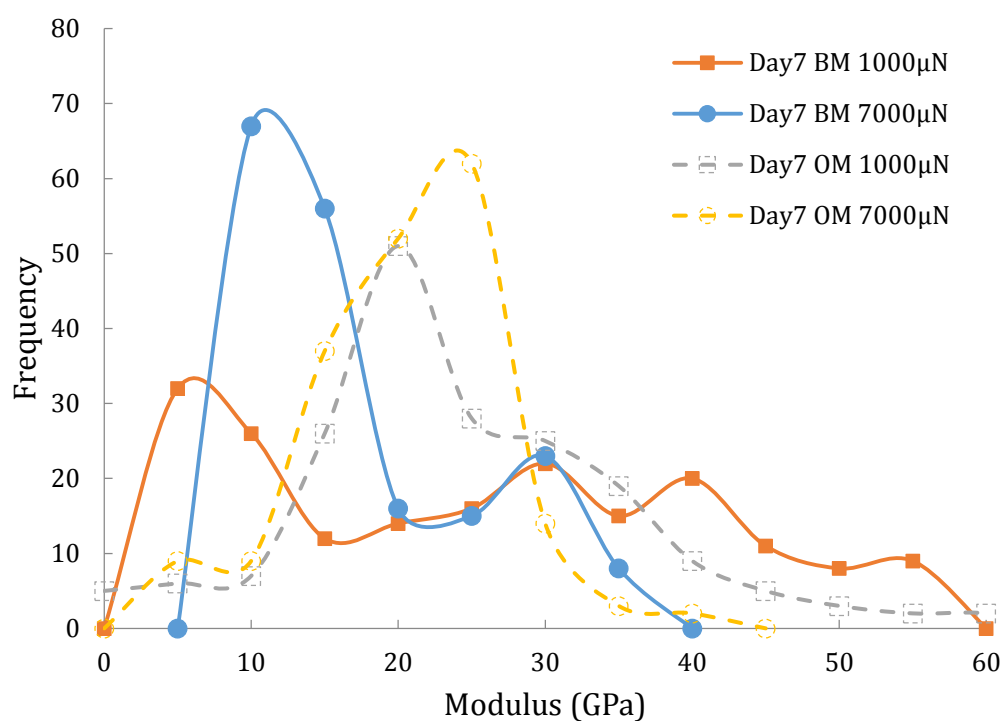
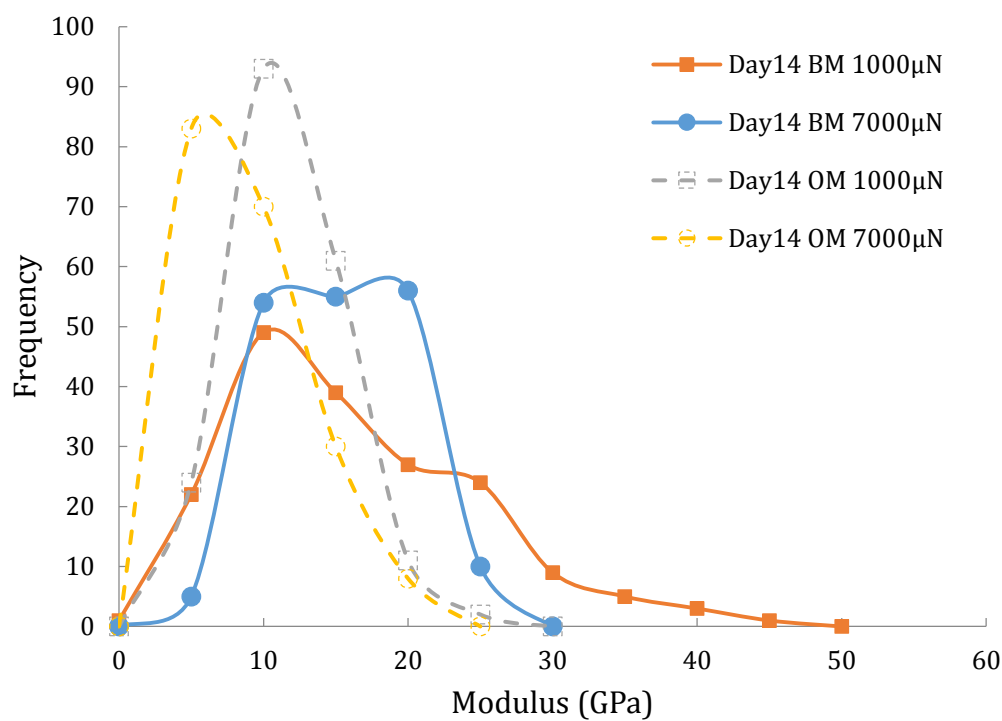


Figure 6.21 Histograms of elastic modulus for reported engineered bone produced by C3H10T1/2 MSC line grown in vivo for 28 days (Pelled *et al.*, 2007a).



(a)



(b)

Figure 6.22 Histograms of elastic modulus for mineralized matrix samples cultured from (a) day 7, (b) day 14 and (c) day 21, tested at two different peak loads (1000 μN and 7000 μN).

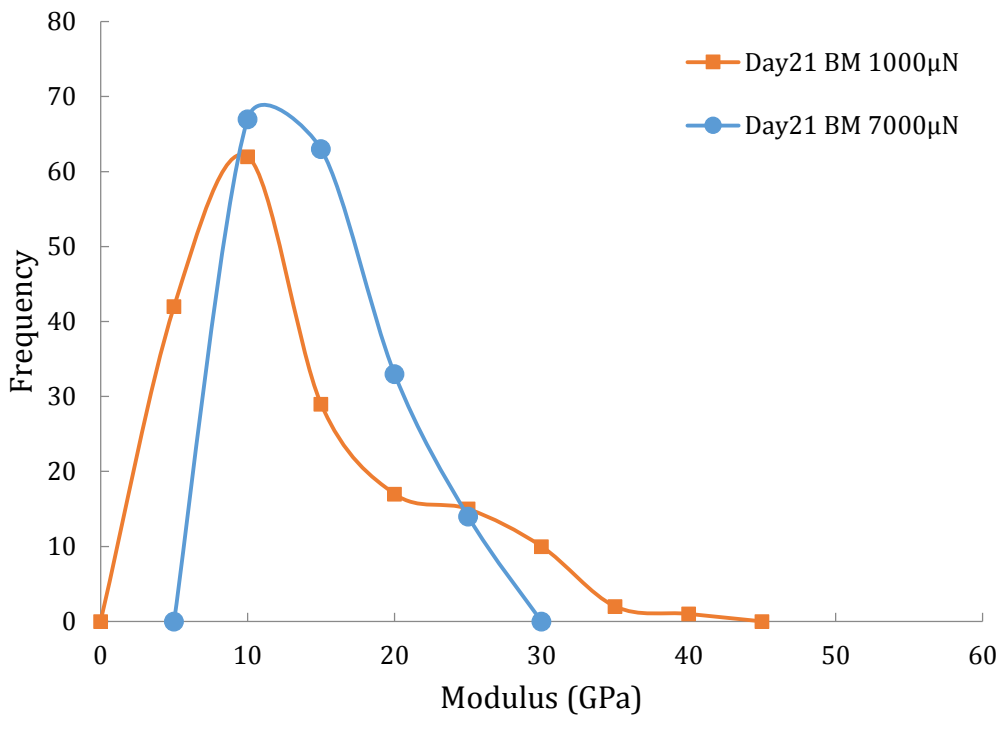


Figure 6.22 (Cont.)

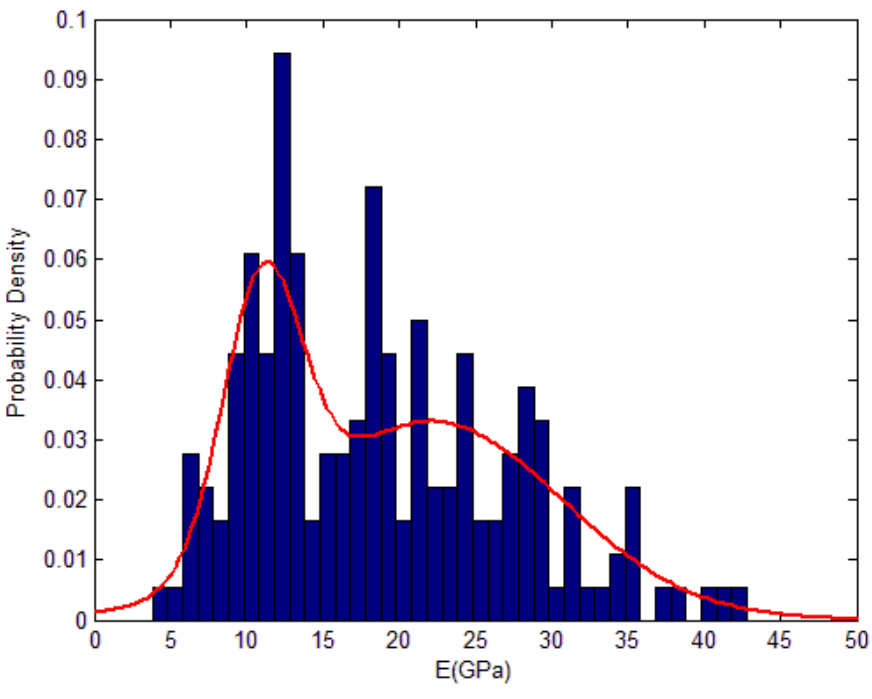
In the given load range (1~9 mN), the average hardness of samples cultured in the BM varies between 1.78~2.14 GPa at day 7. These values decrease to 0.45~1.05 GPa at day 14 and 0.35~0.81 GPa at day 21. The average hardness of samples cultured in the OM varies between 0.85~1.85 GPa at day 7 and then decreases to 0.29~0.70 GPa at day 14. This shows that, in the same period, the hardness of the matrix cultured in BM is greater than that cultured in OM. For both BM and OM, the hardness of the matrix decreases with increasing culture period, and the values (both hardness and SD) from day 7 are much bigger than values from day 14 and day 21. This may suggest that the matrix from day 7 is relatively thin and highly affected by the substrate, and the corresponding collagen fibres are not yet well aligned. The measured hardness values at day 7 (both BM and OM) are much more scattered compared to the rest of the samples. This may suggest that the hardness of the matrix at day 7 is highly affected by its porous heterogeneous structure. It has been reported that the hardness of human cortical bone is 0.85 ± 0.45 GPa measured by a multi-cycling test (Hoffler *et al.*, 2005). This indicates that, compared to the hardness of cortical bone, the matrix cultured in both BM and OM for 7 days is relatively stiff, and the matrix cultured in both BM and OM for 14 and 21 days is more similar to native bone.

6.3.2.2 Data analysis by the Gaussian mixture model

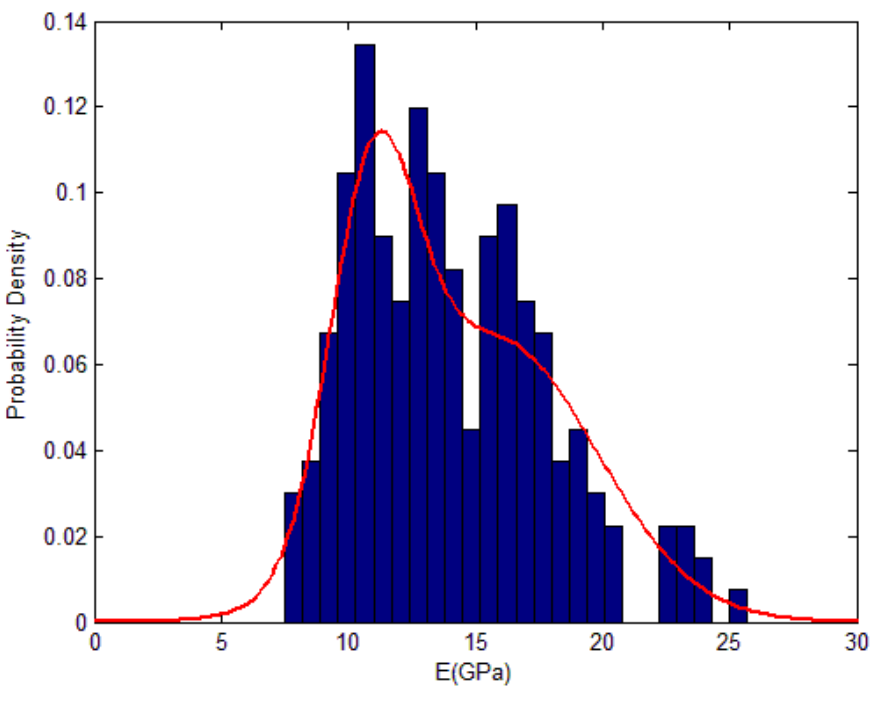
The structure and composition of biological tissues are often complex, which leads to a complicated mechanical response in a nanoindentation test (Gupta *et al.*, 2005; Gupta *et al.*, 2006; Shahar *et al.*, 2007; Zebaze *et al.*, 2011). It has been reported that the Young's modulus of cortical bone is anisotropic (Dong and Guo, 2004; Wenger *et al.*, 2007). For dehydrated human tibial cortical bone, the elastic modulus of osteogenic lamellae measured by nanoindentation is 14~19 GPa in the transverse direction, and 23~27 GPa in the longitudinal direction. The elastic modulus of interstitial lamellae is 17~21 GPa in the transverse direction, and 25~29 GPa in the longitudinal direction (Fan *et al.*, 2002). Thus, the mineralized matrix may also be anisotropic like the bone tissue.

Figure 6.23 depicts the representative distributions of Young's modulus for the matrix harvested from BM and OM after 14 days, tested at a peak load of 1000 μN . Therefore, it is essential to do statistical analysis by the Gaussian mixture model (Equations 6.5-6.7). In this model, it assumes that the measured probability distribution of elastic modulus or hardness of each sample is a weighted combination of a finite number of components. For each individual component, its elastic modulus or hardness distribution follows Gaussian distribution. The deconvolution is performed by fitting Equations 6.5-6.7 (the weighted combination of a finite number of components) to the measured probability distribution curve. A Matlab code was written to complete this curve fitting procedure. Different number of components have been assumed (*i.e.* 1, 2, 3...), from the mathematical point of view, only when there are 2 components it gives the best fitting results. It indicates that there are possibly two major components in the mixture model. (There may exist more than 2 components, but some of them may share the similar properties or have a negligible volume friction. Hence, the number of components is mathematically chosen as 2.) The extracted elastic modulus and hardness of each component are shown in Figure 6.24 and Figure 6.25. For samples cultured in BM, the Young's modulus of component 1 is approximately 10~17 GPa, which seems almost independent of cell culture period. The Young's modulus of component 2 is approximately 28~34 GPa at day 7. After day 7, this value decreases to 20~25 GPa. The hardness of component 1 is about 0.3~0.7 GPa, and is almost independent of culture period as well. The hardness of component 2 is 2.52~2.84 GPa at day 7, this value decreases to

0.97~1.75 GPa at day 14, and further decreases to 0.6~1.27 GPa at day 21. For samples cultured in the OM, it seems that the elastic modulus and hardness are dependant on the cell culture period. From day 7 to day 14, the elastic modulus of component 1 decreases from 21.6~23.7 GPa to 7.8~11.4 GPa, and the elastic modulus of component 2 decreases from 22.8~28.4 GPa to 13.4~19.6 GPa. The hardness of component 1 decreases from 0.42~1.15 GPa to 0.24~0.57 GPa, and the hardness of component 2 decreases from 2.04~2.96 GPa to 0.39~0.90 GPa in the same period. To further investigate the aging and culture medium effects on the mechanical properties, the mean values of Young's modulus and hardness of each component are taken across the entire contact depth range, which is shown in Figure 6.26. For samples cultured in the BM, both the Young's modulus and hardness values of component 1 are almost independent of culture period, but those of component 2 decrease with increasing culture period. For samples cultured in OM, both the Young's modulus and hardness of each component decrease from day 7 to day 14. It has been reported that a high seeding density (higher than 5000 cells/cm²) will lead to the detachment of the cell layers between day 12 and day 16 (Jaiswal *et al.*, 1997). Thus, according to the seeding density in this study (15000 cells/cm²), the decrease of the stiffness and hardness is probably due to the fact that the early stage of cell detachment occurs before day 14.

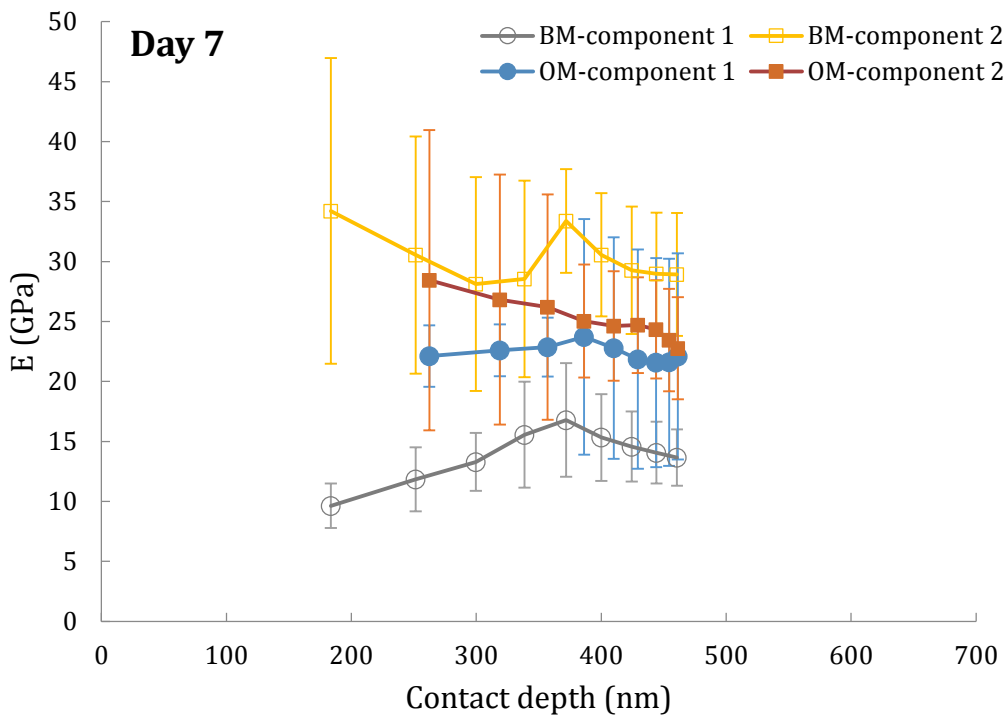


(a)

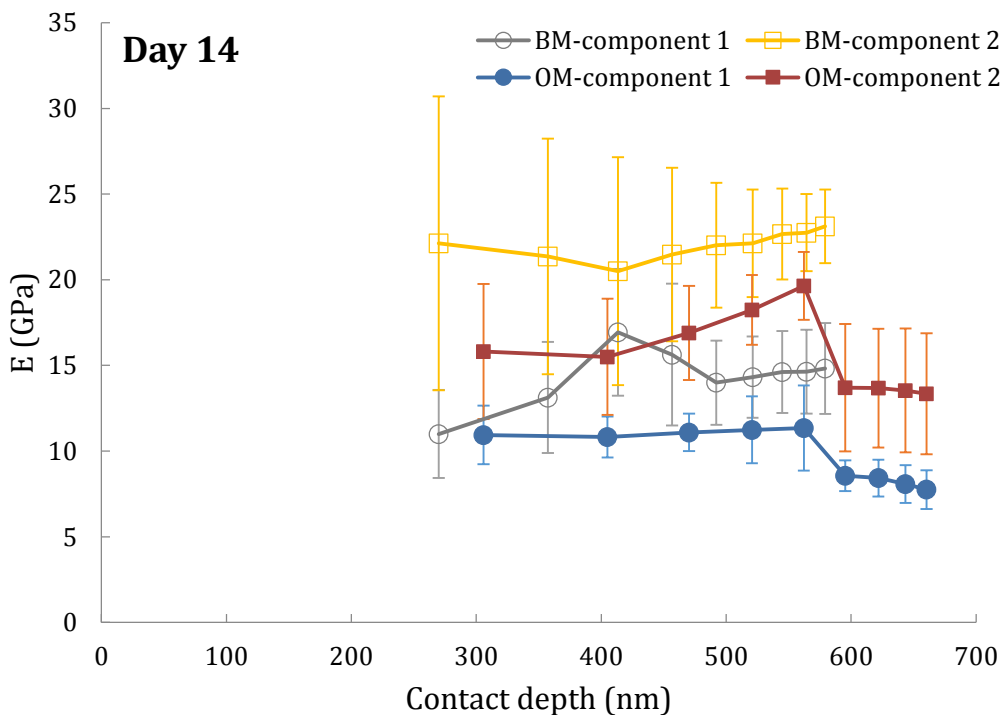


(b)

Figure 6.23 Representative distributions of Young's modulus for the matrix harvested from (a) day 14, BM, (b) day 14, OM, tested at a peak load of 1000 μN .

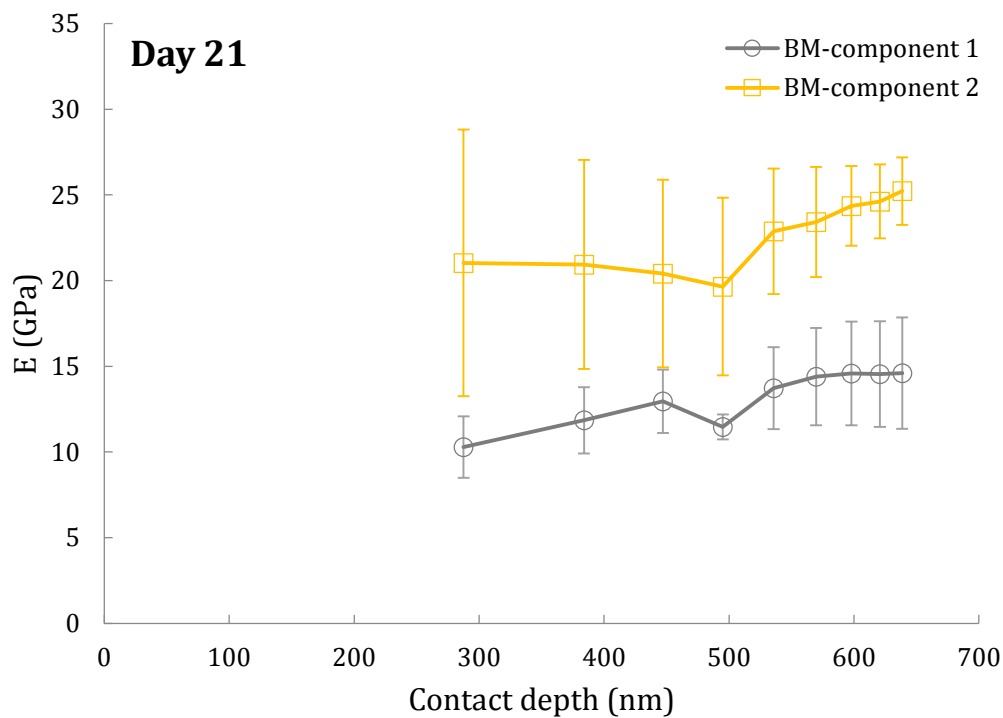


(a)



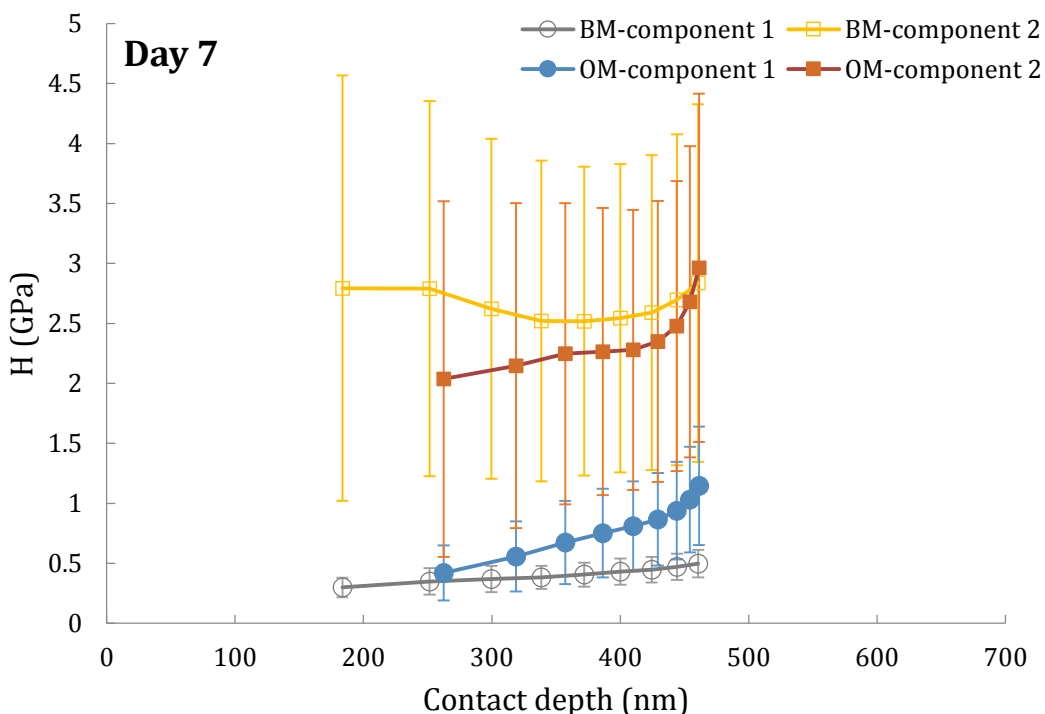
(b)

Figure 6.24 Young's modulus of two different components in the matrix cultured in different media for (a) 7 days, (b) 14 days and (c) 21 days, determined by the Gaussian mixture model for nanoindentation tests in the peak load range 1~9 mN.



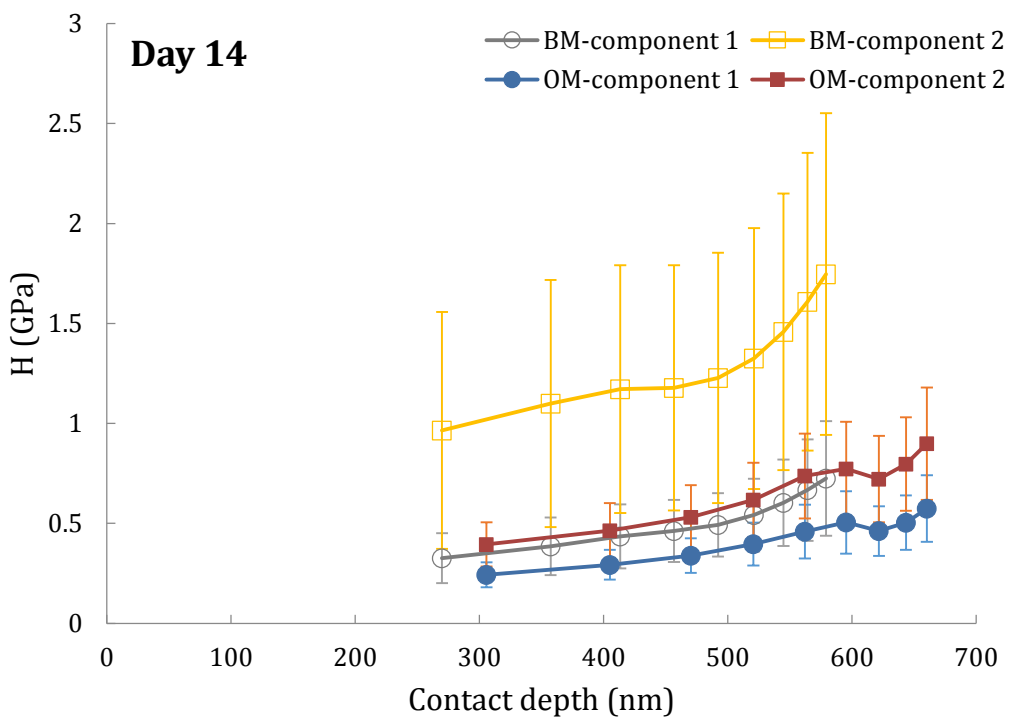
(c)

Figure 6.24 (Cont.)

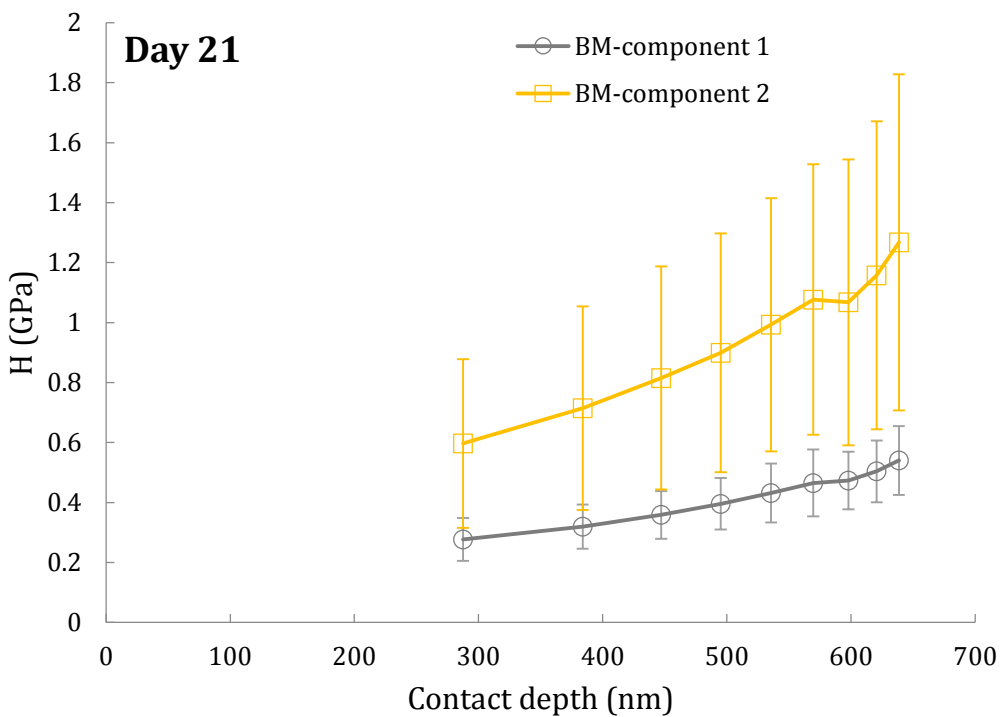


(a)

Figure 6.25 Hardness of two different components in the matrix cultured in different media for (a) 7 days, (b) 14 days and (c) 21 days, determined by the Gaussian mixture model for nanoindentation tests in the peak load range 1~9 mN.



(b)



(c)

Figure 6.25 (Cont.)

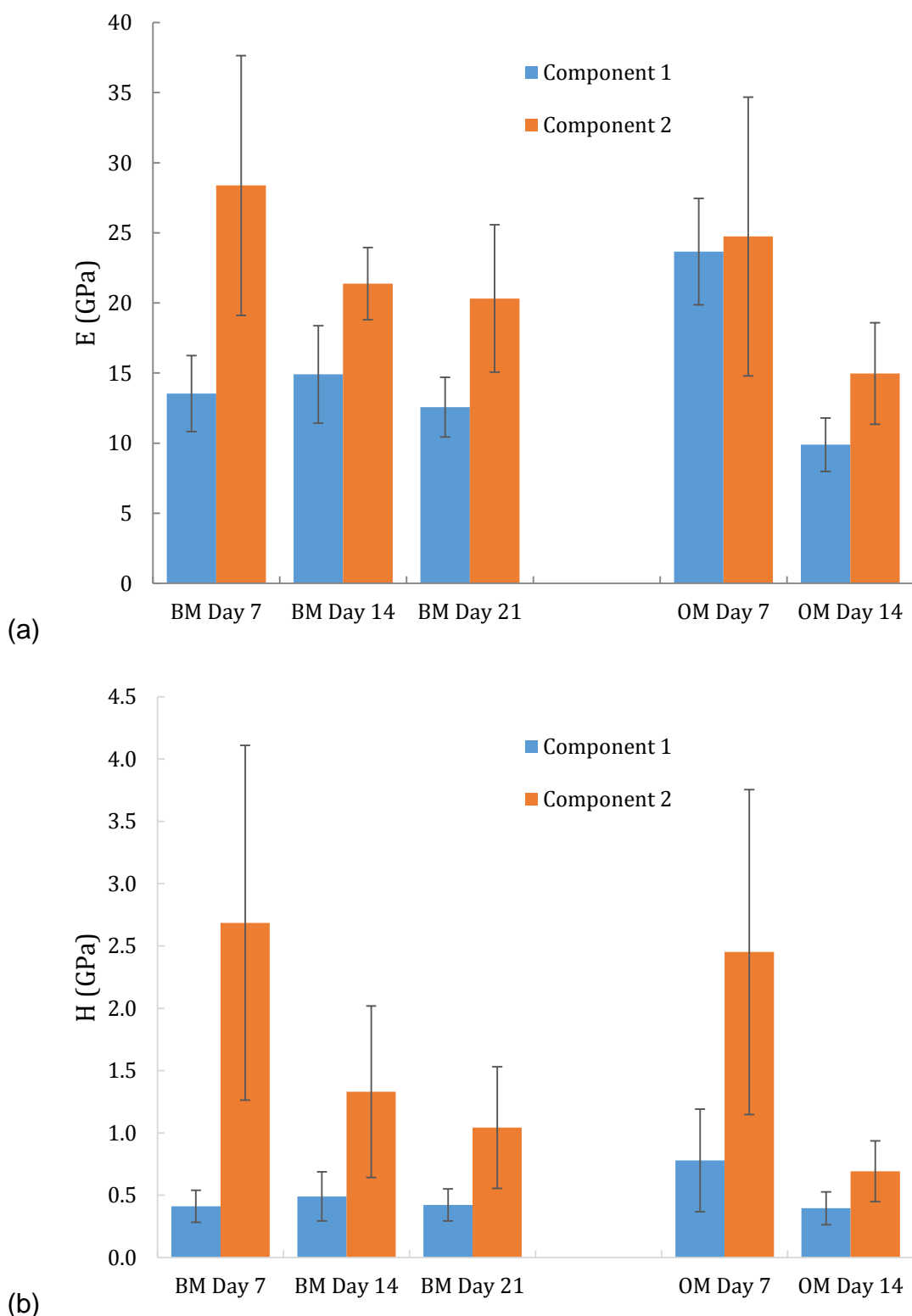
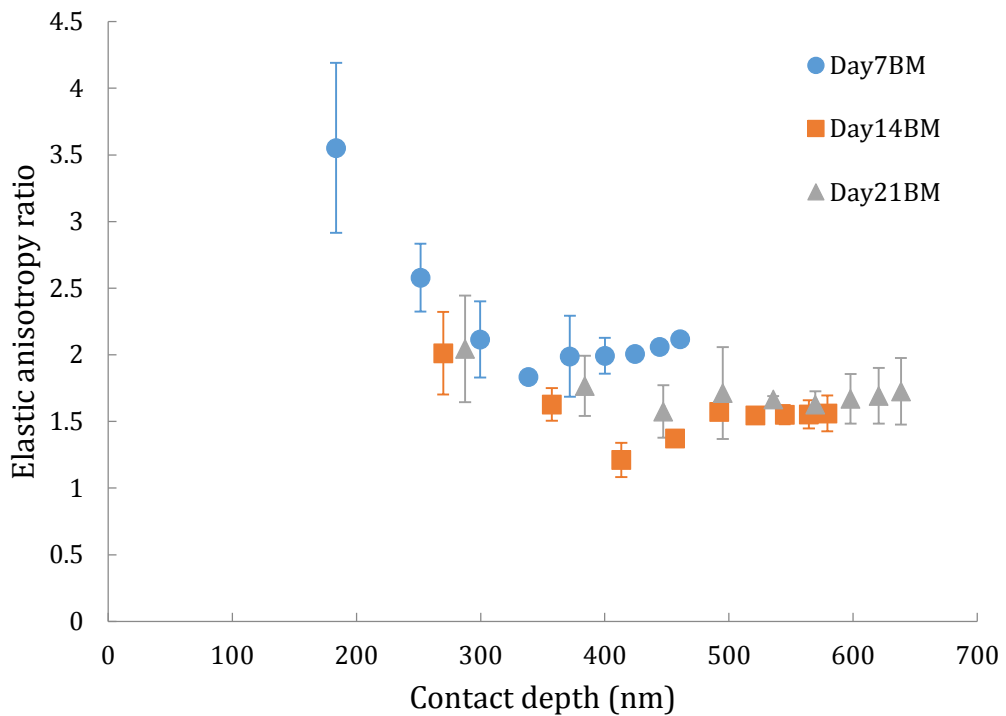


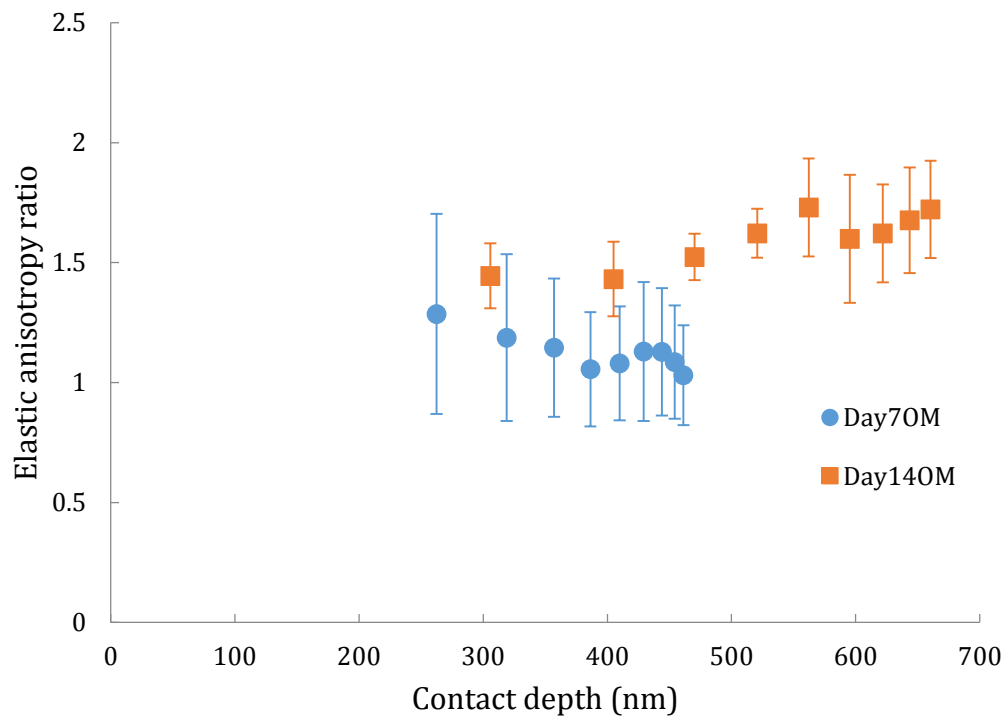
Figure 6.26 The (a) Young's modulus and (b) hardness of each component in the matrix cultured in different media as a function of culture period.

From the mathematical point of view, the two components can be due to the elastic modulus mismatch at longitudinal and transverse directions (*i.e.* transverse isotropy). It may also be attributed to the two components with different mechanical properties. For native bone, the transversely isotropic

properties can be evident in various native strain regions (such as compressive strain region, tensile strain region and the neutral axis of bending) (Takano *et al.*, 1999). If we assume that the similar transverse characteristic will also be presented in the mineralized matrix, we could then investigate its anisotropy ratio. Figure 6.27 illustrates the anisotropy ratio of elastic modulus and hardness between component 1 and component 2 for different samples, as a function of average contact depth. In Figure 6.27a, a higher elastic anisotropy ratio can be observed at day 7 for samples cultured in BM (especially when contact depth is smaller than 200 nm), and in Figure 6.27b, the ratio is much lower at day 7 for samples cultured in OM. As shown in Figure 6.27c and Figure 6.27d, the anisotropy ratio of hardness and its variation at day 7, which seem depend on the average contact depth, is much greater than values at day 14 and day 21. After day 14, the anisotropy ratio of hardness becomes independent of the average contact depth, with the value changing between 2.2~3.0 for samples cultured in BM and 1.5~1.6 for samples cultured in OM. These observations seem coherent with the previous polarized light results (Figure 6.17). Namely, the matrix cultured from the OM is more uniform than the matrix cultured from the BM. Besides, it has been reported that the elastic anisotropy ratio of human vertebral trabeculae is 1.18~1.27 (Wolfram *et al.*, 2010), and the ratio of bone tissue from the canine radius of the adult foxhound is 1.334 ± 0.007 , and this value reduces to 1.141 ± 0.029 after demineralization or increases to 1.658 ± 0.107 after deproteinization (Takano *et al.*, 1999). It indicates that, after 7 to 14 days, the elastic anisotropy ratios of samples (cultured in both BM and OM) are similar to the native bone. The relatively high elastic anisotropy ratio of samples cultured in BM for 7 days may result from both the porous structure as small contact depth and the less protein content in the sample. In contrast, the anisotropy of properties of mineralized matrix cultured in OM is not clear until day 14. The two components are relatively compliant, indicating that OM promotes cell proliferation rather than mineralization.

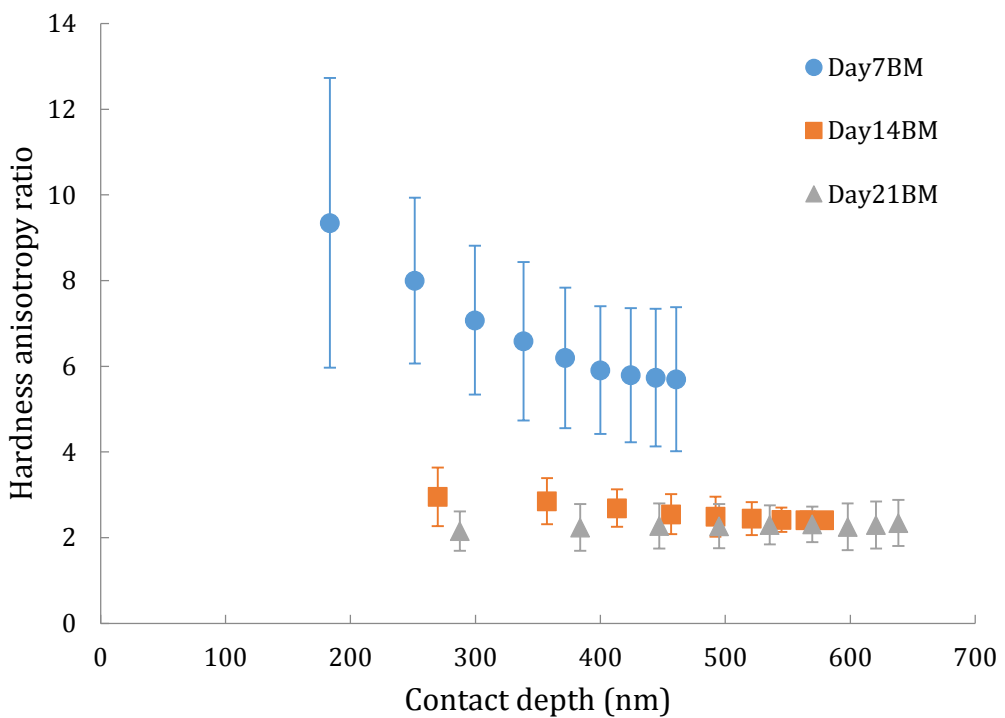


(a)

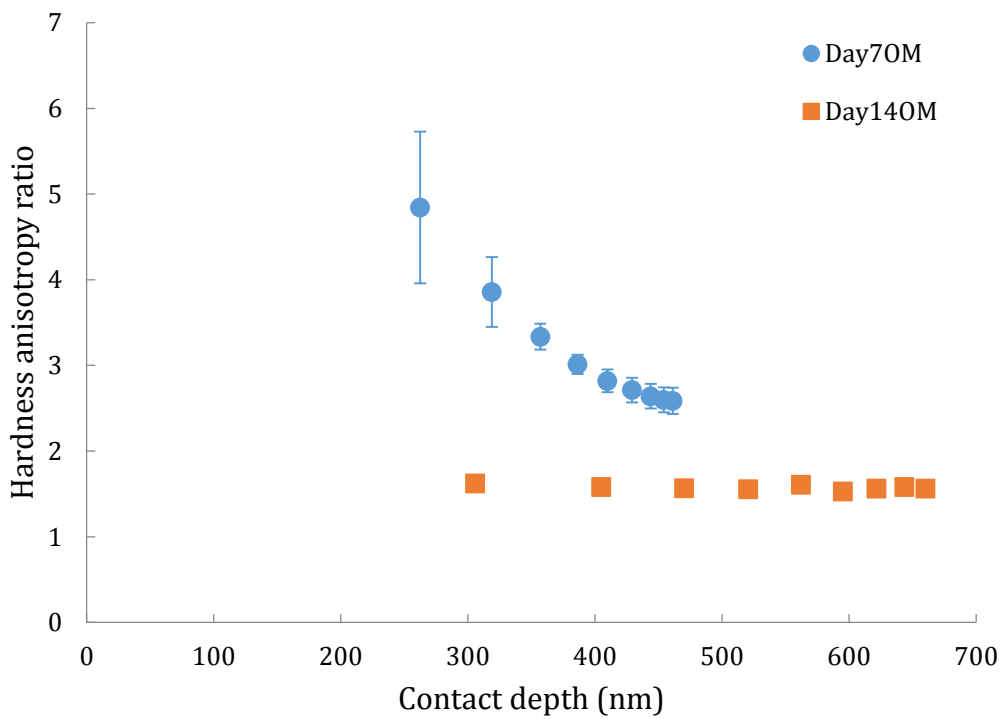


(b)

Figure 6.27 The depth dependent elastic anisotropy ratio for samples cultured in (a) BM and (b) OM, and hardness anisotropic ratio for samples cultured in (c) BM and (d) OM, as a function of contact depth for nanoindentation tests in the peak load range 1~9 mN.



(c)



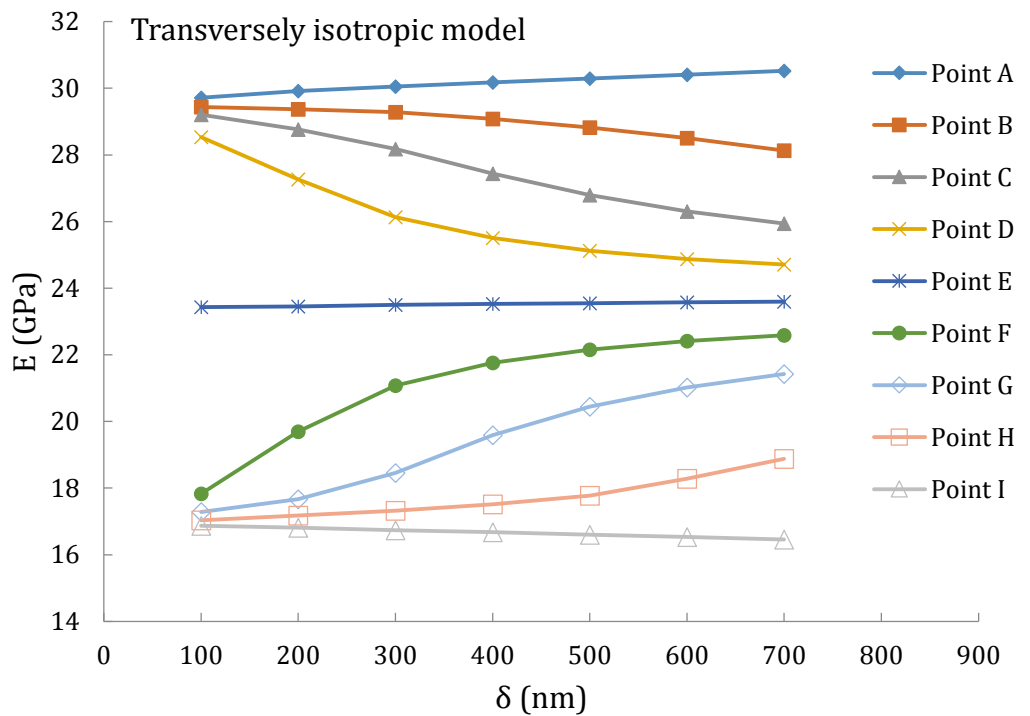
(d)

Figure 6.27 (Cont.)

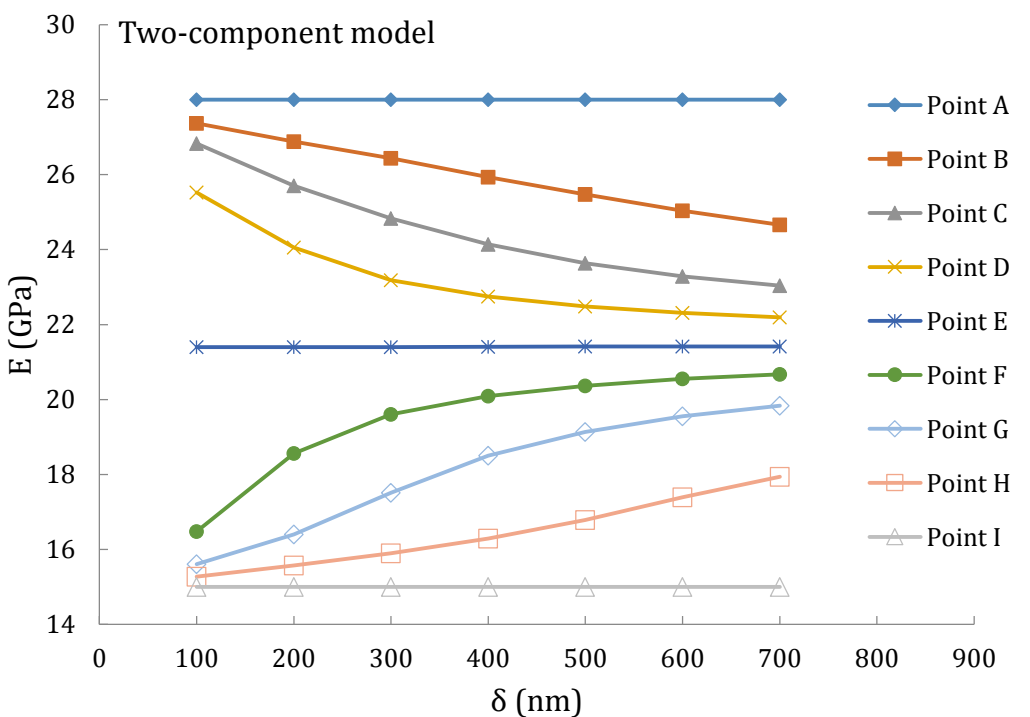
6.3.3 Finite element simulations

In addition to being transversely isotropic as the native bone is, the mineralized matrix may also be composed of two components with different properties, which represent the mature and immature bone nodules. In order to identify which of these two situations is most likely using a theoretical approach, FE simulations were performed to simulate the nanoindentation in these two cases. The elastic moduli of the numerical model indented at different locations (as illustrated in Figure 6.11) around the interface are shown in Figure 6.28, as a function of indentation depth. The Oliver and Pharr method to extract mechanical properties from load-displacement data slightly overestimates the modulus obtained from the FEA results for anisotropic materials (Fan *et al.*, 2004; Carnelli *et al.*, 2011). From a qualitative perspective, it can be seen that transversely isotropic and two-component assumptions lead to similar pattern of the nanoindentation modulus variation with indentation penetration. With reducing the distance between the indentation point and the interface (point E), the effect from the other part is increasing. A multimodal distribution of elastic modulus for mineralized matrix can be observed at lower indentation depth. By contrast, this elastic modulus is scattered and reaches the equilibrium value at larger indentation depth. The values obtained at the same penetrations and locations for both cases are very similar with a deviation between 5~12%. For both cases, the distribution of the apparent nanoindentation modulus is not as wide as that observed in the experimental measurements.

The effect of porous structure (with a given porosity) on sample mechanical properties was also investigated by FEM, which is shown in Appendix B.



(a)



(b)

Figure 6.28 The elastic modulus of the numerical model indented at different locations (as illustrated in Figure 6.11) around the interface between (a) two orthogonal fibres, and (b) mature and immature bone nodules.

6.4 Summary

In this study, the nanoindentation with multi-cycling protocol proved to be effective to study how the nanomechanical properties of the matrix synthesized by the cell would be affected by cell culture media and culture duration. Together with surface analysis and FEA, the correlation between the sample microstructure and nanomechanics has been studied.

Nanoindentation tests have revealed that the stiffness and hardness of bone nodules (*i.e.* mineralized matrix) produced by Y201 cell line are comparable to native bone, and present a multimodal distribution. As an explanation, these bone nodules may present both mature (stiff phase) and immature (compliant phase) state. However, there is no direct evidence to support this assumption. As another explanation, similar to native bone, the multimodal distribution is more likely due to the anisotropic behaviour of these bone nodules, which has been revealed in the polarized light images. The ratio of elastic modulus and hardness at these two orthogonal directions (or between stiffer and softer phases) can be up to 2 and 5, respectively. The bone nodules produced by cells in basal medium appear to be stiffer and more anisotropic compared to that in osteogenic medium, as confirmed in both nanoindentation tests and polarized light images. In the polarized light images, an anisotropic collagen fibre distribution has been observed on BM samples and a relatively uniform collagen fibre distribution has been observed on their counterparts from OM. This anisotropic collagen fibre distribution explains the multimodal distribution of the mechanical properties, as confirmed in the FE simulations.

From the point of culture period, it has also been shown that the cell culture duration does not affect the elastic modulus and hardness in the transverse direction but it significantly affects the elastic modulus and hardness at longitudinal direction after day 7. When cell culture period reaches 14 days, the matrix becomes stabilized in the longitudinal direction and there is no further change with the cell culture period. In addition, mineralized matrix has revealed a more porous structure at day 7, compared to that at day 14 and 21, which explains the wider span of the distribution of measured mechanical properties at day 7. For both basal and osteogenic media, the bone nodules have exhibited reverse aging behaviour compared to native bone despite the fact that their

microstructure becomes denser with the increase of cell culture period. This is possibly due to the fact that cell proliferation outcompetes the mineralization processes.

Chapter 7

Conclusions and Further Work

Chapter 7. Conclusions and Further Work

7.1 Conclusions

Firstly, some empirical equations have been modified and two new equations have been proposed to describe the nanoindentation response of inclusion/matrix composite materials. For an indentation test, many empirical or semi-analytical models have been proposed to study how the elastic modulus of the coated systems changes with the penetration. However, little work has been done for the inclusion/matrix composite materials. In this work, those indentation-based empirical or semi-analytical models have been examined. The analysis has shown that those semi-analytical models need to be modified before they can be extended to the inclusion/matrix systems, by considering the elastic mismatch between the fibre and the matrix. In addition, two simpler models have been proposed, which show good performance but with less fitting parameters compared to other empirical models.

In practice, according to different applications, the reinforcement of composite materials may have different geometries. Therefore, it is necessary to investigate the effect of inclusion geometry on the nanomechanical behaviour of composite materials, which has not been well studied. On the other hand, many particle/matrix systems may also exhibit elastic-plastic behaviour. Some empirical models have been developed to describe the spatial-dependent composite modulus during nanoindentation tests for linear elastic particles embedded in a linear elastic matrix. No such models have been developed for elastic-plastic composites. Based on the original Clifford model, extended Clifford models have been proposed in this study, which enable us to determine the elastic modulus and the hardness of composites with large mismatch in elastic modulus and hardness. These models have been successfully applied to various composites regardless of particle shape, volume and material combination.

During nanoindentation tests of composite materials, the relative indentation location will also affect their nanomechanical response. Analysis has shown that, the empirical equations, which work well in the previous chapters, failed to describe the composite elastic modulus of an inclusion/matrix system with various

d/r ratios. Hence, as a future work, those existing models should be further developed to specify the effects of indentation location and indenter geometry. On the other hand, a linear equation and a polynomial equation have been adopted to extract the elastic modulus of each individual component by extrapolating the equation to zero displacement. It has revealed that the second order polynomial equation can effectively extract the elastic modulus of the fibre in the case of indenting the fibre. In the case of indenting the matrix, before the indenter touches the fibre, a linear equation can effectively extract the elastic modulus of the matrix.

Finally, in addition to the theoretical analyses, a nanomechanical case study of a typical biocomposite materials (namely extracellular mineralized matrix) was performed. For these complex composites, the existing analytical models may not be directly applied. However, with the assistance of microscopy techniques, a statistical model and FEA, the anisotropic behaviour of the mineralized matrix has been revealed and the corresponding mechanical properties of each individual component have been determined. Moreover, the effects of both cell culture medium and culture duration on the nanomechanical properties and microstructure of the mineralized matrix have also been successfully demonstrated.

7.2 Further follow up

In the nanomechanical modelling part, some analytical models have been proposed and successfully applied to the system with different composite material combinations, and the system with different inclusion geometries. However, these equations have not been expanded to the case of different inclusion alignments and indentation locations. Thus, to further complete the description of the nanomechanical response of the inclusion/matrix composite, a more generalized equation should be developed in a future study, which considers the change of the material properties, inclusion geometries, inclusion alignments and indentation locations.

In the nanomechanical case study part, the viscosity of the sample has been avoided by adding a holding period in each loading cycle. Hence, as a future work,

a comprehensive study of the visco-elastic-plastic behaviour of the sample should be undertaken.

Appendix A. Experimental Tests of a Viscoelastic Fibre in a Viscoelastic Matrix

A.1 Introduction

Due to the fact that all the parameters involved in the ABAQUS software are dimensionless, it is necessary to specify the system of units and make sure all the units are coherent during the analysis. Therefore, the simulation results shown in Chapter 3 should be also suitable for a sample in wide scale range. In order to simplify the sample preparation, the experiment was performed with fibre/matrix samples prepared in the millimetre range. The purpose of this experiment is not to provide a validation of the values of the parameters, but to give a reference of the changing trend of those parameters when the sample is indented with a sharper indenter.

A.2 Description of the samples and the instrument

In this study, three types of 20 mm thickness polymer plates (namely: polypropylene (PP), polyethylene (PE) and polyamide 6 (Nylon 6)) were adopted as the matrix material. As depicted in Figure A.1, for each material, the plate was cut into four 50 mm × 50 mm × 20 mm cubes. Three of them had a drilled through-hole of 8 mm diameter in the centre of the cube to act as the mould of the fibre. The additional one was used to measure the mechanical properties of the material. The fibre was made from the polydimethylsiloxane (PDMS) (SYLGARD 184 Silicone Elastomer Kit, Dow Corning, Midland, MI, USA). The PDMS was prepared by thoroughly mixing the pre-polymer and cross-linker in a weight ratio of 10:1. The mixture was placed in a low vacuum desiccator to remove the air bubbles in the liquid. Thereafter, the mixture was poured into each matrix mould and cured for 48 hours at ambient temperature. In addition, the mixture was also poured into a petri dish, which will be used to measure the properties of the PDMS.

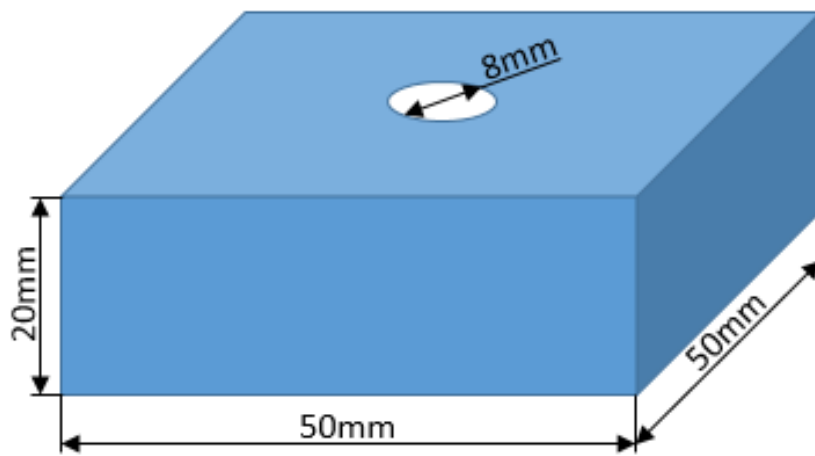


Figure A.1 Schematic of a fibre/matrix cube, with an 8mm diameter through-hole in the centre.

Indentation tests were performed by a Shimadzu EZ-SX universal tester (Shimadzu UK Ltd., UK). The indentation of each block material was performed with a stainless steel spherical indenter with a diameter of 10 mm. The maximum displacement was 0.05 mm. The loading rate was set as 0.025 mm/min to make the resultant response elastic-dominated. The indentation of the fibre/matrix samples was performed with an acrylic conical indenter, which has a half-included angle of 45°. The elastic modulus and Poisson's ratio of these indenters were well known and listed in Table A.1. In order to obtain similar a/t ratio, the maximum displacement was set as 1mm. The loading rate was set as 0.025 mm/min. As shown in Figure A.2, the tip radius of the conical indenter was 43 μm .

Indenter material	E (GPa)	ν
Acrylic	3.2	0.37
Stainless steel	195	0.27

Table A.1 Elastic modulus and Poisson's ratio of acrylic and stainless steel indenters.

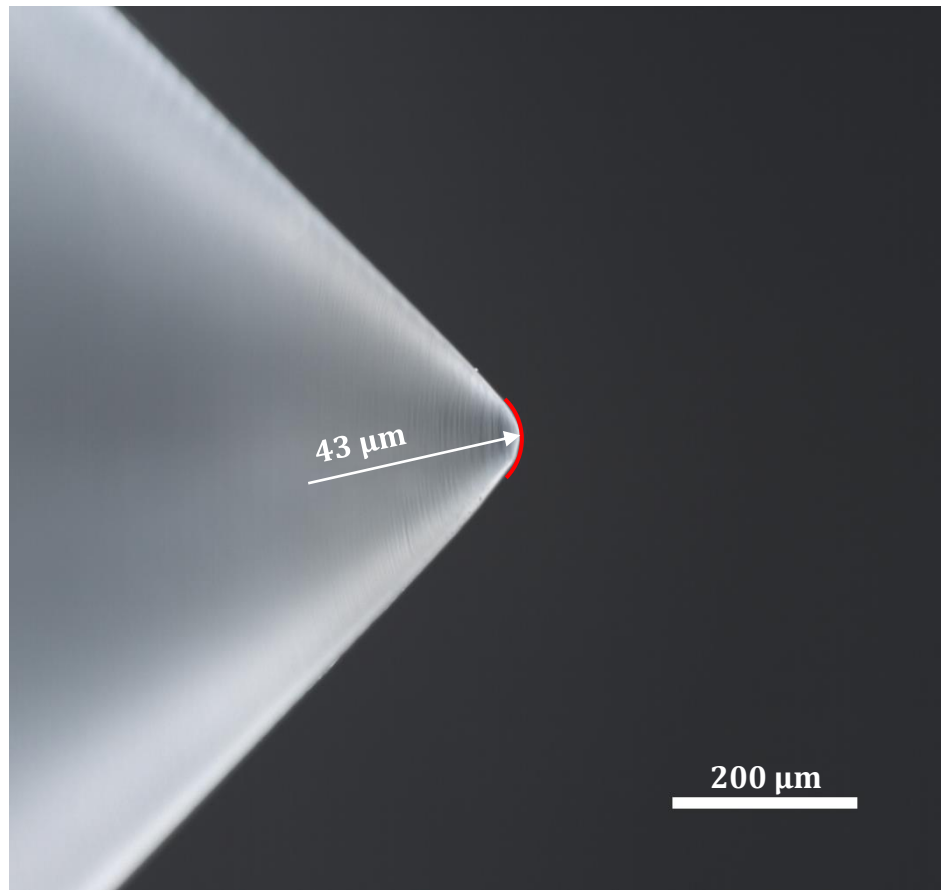
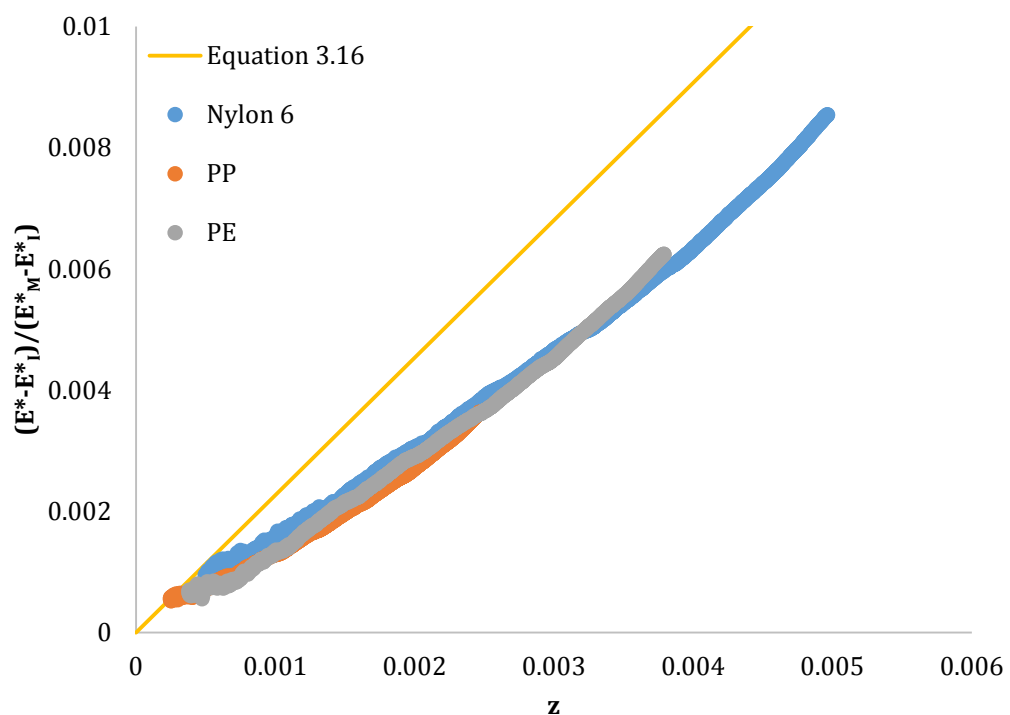


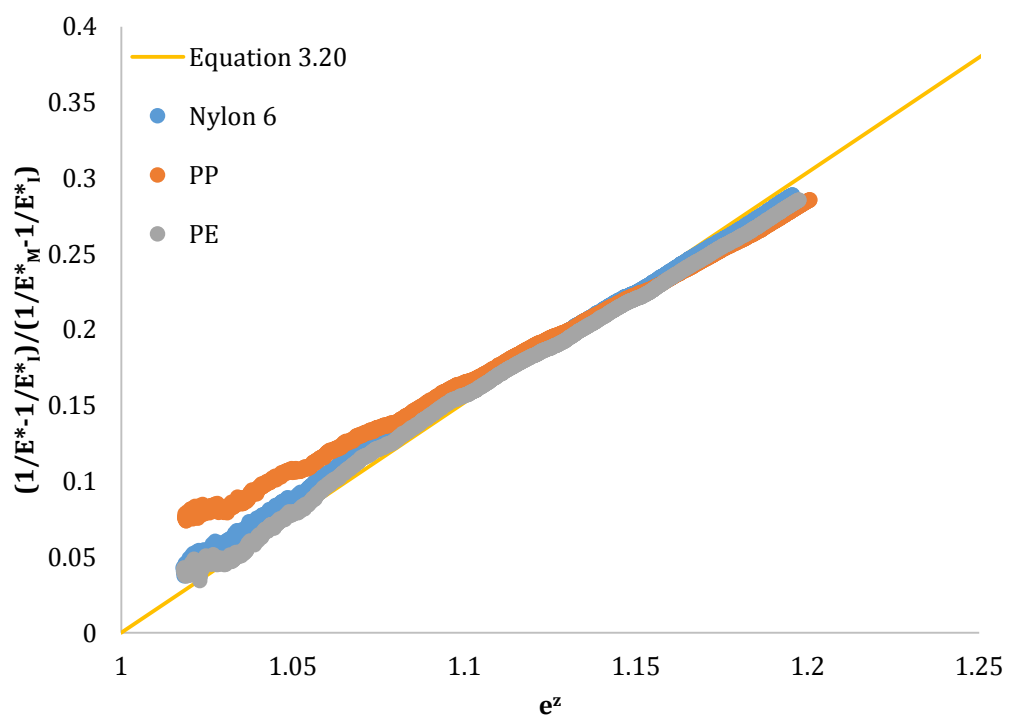
Figure A.2 Microscope image for the conical tip, which has the tip radius of 43 μm .

A.3 Experiment results

Based on Hertz equations, the elastic modulus of each individual material was extracted from the initial elastic contact region with the values listed in Table A.2. The composite elastic modulus of the fibre/matrix samples was measured with Equation 3.15. As shown in Figure A.3, all the composite elastic modulus curves converged to a master curve, and both Equation 3.16 and Equation 3.20 showed good accuracy to fit these data. The fitting parameters are provided in Table A.3. Compared to the values shown in Table 3.4 and Table 3.5, it seems that the selection of the values of weighting factor b is reasonable here. Namely, the value of b is dependent on the indenter geometry and is increasing with the increase of indenter half-included angle.



(a)



(b)

Figure A.3 Fit the experiment results with (a) Equation 3.16 and (b) Equation 3.20.

Material	E_r (MPa)	E (MPa)	ν
Nylon 6	264.39	222.36	0.4
PP	574.70	484.07	0.4
PE	356.87	300.28	0.4
PDMS	5.61	4.32	0.48

Table A.2 Elastic modulus of the tested materials extracted by the stainless steel spherical indenter.

	b	B	resnorm
Equation 3.16	0.9	1.5443	0.0004
Equation 3.20	-0.03	1.5189	0.3360

Table A.3 Fitting parameters for Equation 3.16 and Equation 3.20 when fitted with the experiment results.

A.4 Finite element modelling results

Additional FEM was performed in the software ABAQUS to verify the parameters shown in Table A.3. This model shared the same material properties, sample diameter, indenter geometry and indentation protocols as the experimental tests. In the model, as shown in Figure A.4, the inclusion/matrix composite was represented as a 2D axisymmetric model with a total number of 22500 CAX4R type elements (among which 15000 elements were assigned to the inclusion). The indenter was modelled as a rigid body, with a half-included angle of 45° and tip radius of 0.25 mm. The indenter was controlled by displacement with the maximum displacement set as 1mm. Other settings (namely, contact conditions and boundary conditions) were the same as that used in Chapter 3.

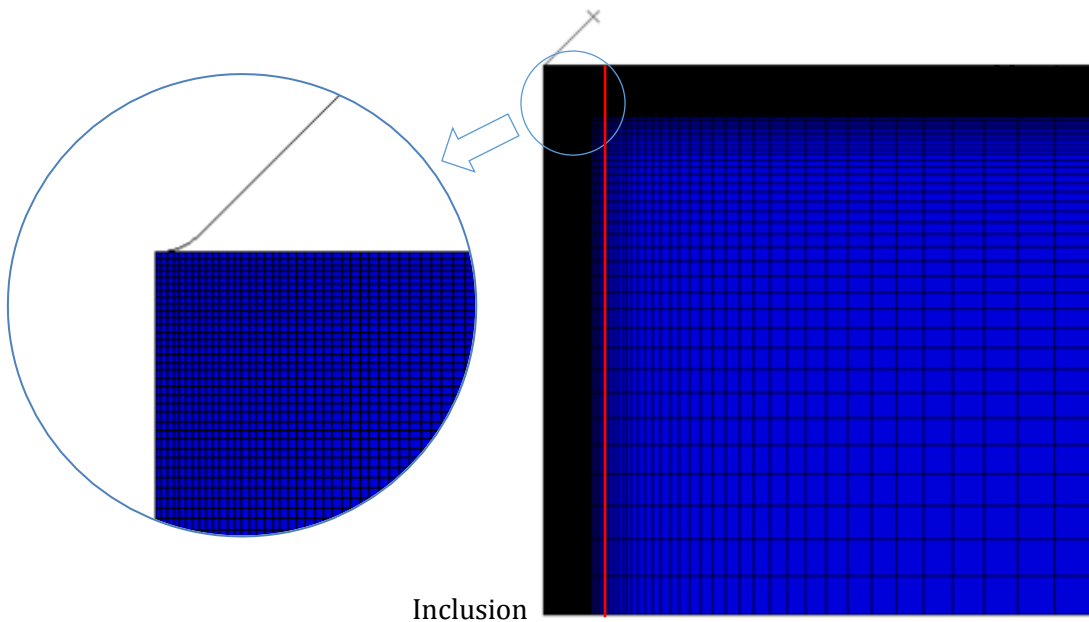
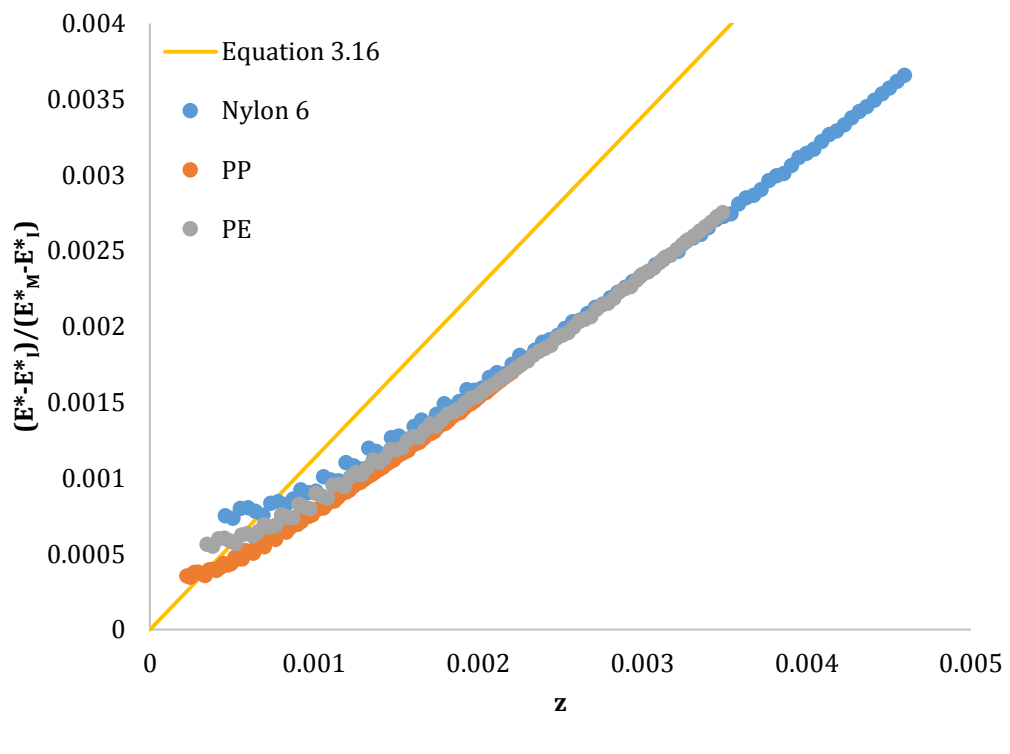
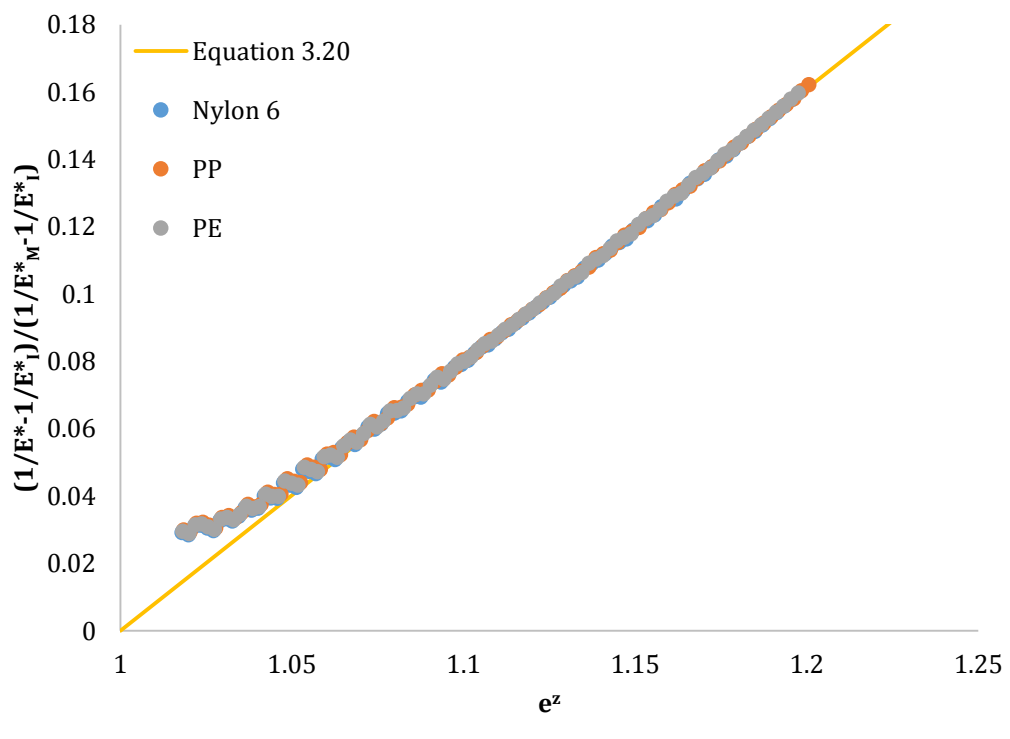


Figure A.4 Overview of the finite element mesh for the inclusion/matrix composite, and the enlarged details of elements underneath the tip.

The composite elastic modulus that was extracted from the simulated results was also fitted by Equation 3.16 and Equation 3.20. As shown in Figure A.5, both of these equations showed good accuracy to fit these data, which agrees well with the previous observation. The fitting parameters are listed in Table A.4. The value of b was almost identical (namely, approximately 0.9 for Equation 3.16 and -0.03 for Equation 3.20) with the values shown in Table A.3, which demonstrates the accuracy of Equation 3.16 and Equation 3.20. However, the difference between the value of fitting parameter B shown in Table A.3 and Table A.4 is not negligible (namely, approximately 1.52~1.54 for the experimental results and approximately 0.79~0.81 for the FEM results). It could be argued that the experimental indents may not ideally take place at the centre of the inclusion or the displacement data may be affected by the initial penetration depth. In either case, the composite elastic modulus will be overestimated and correspondingly lead to a higher value of B .



(a)



(b)

Figure A.5 Fit the FEM results with (a) Equation 3.16 and (b) Equation 3.20.

	<i>b</i>	<i>B</i>	<i>resnorm</i>
Equation 3.16	0.92	0.7874	1.97E-6
Equation 3.20	-0.03	0.8050	0.0046

Table A.4 Fitting parameters for Equation 3.16 and Equation 3.20 when fitted with the FEM results.

Appendix B. Nanomechanical Modelling of a Porous Structure

B.1 Modelling of a porous structure

As the native bone and engineered bone appeared to be porous, additional simulations were done by assuming a porous structure of the matrix, where the elastic modulus was set as 28 GPa and the Poisson's ratio was set as 0.3. For simplicity, as shown in Figure B.1, the pores were assumed to be spherical and underneath the point of indentation. The porosity was assumed to be 7.2% similar to that of cortical bone (Martin and Boardman, 1993; Roschger *et al.*, 2001; Wang and Ni, 2003), with the distance between the centre of the hole and indented surface varied between 4 μm and 6 μm . In each case, approximately 60,000 linear C3D8R eight-node elements were used, with denser mesh created underneath the indenter. Similar to the previous model, a symmetric boundary condition and a completely fixed boundary condition were applied to the symmetric plane and the bottom, respectively. In addition, to achieve the 7.2% porosity, symmetric boundary conditions were also applied to the sides of this representative volume to simulate a periodically porous structure. The surface was assumed to be flat, and has a frictionless contact with the rigid indenter. The same lateral dimensions were adopted to minimize edge effects on the simulated response. Displacement control with the same loading protocol was applied.

B.2 Finite element modelling results

As a porous structure was observed on mineralized matrix at early stage (*i.e.* day 7) by AFM, additional simulations of porous model were done by FEM. The corresponding simulation results are plotted in Figure B.2. It can be seen that the indenter position relative to the pore would lead to a significantly large span of peak values of nanoindentation modulus. This is particularly significant for the low indentation penetration. Such an observation agrees with experimental observations (see Figure 6.19 and Figure 6.20). For relatively short cell culture period, the mineralized matrix is usually very porous which will result in large span of peak values of nanoindentation modulus. With the increase of cell culture

period, the matrix becomes denser and thus the span decreases. All these agree with the experimental observations.

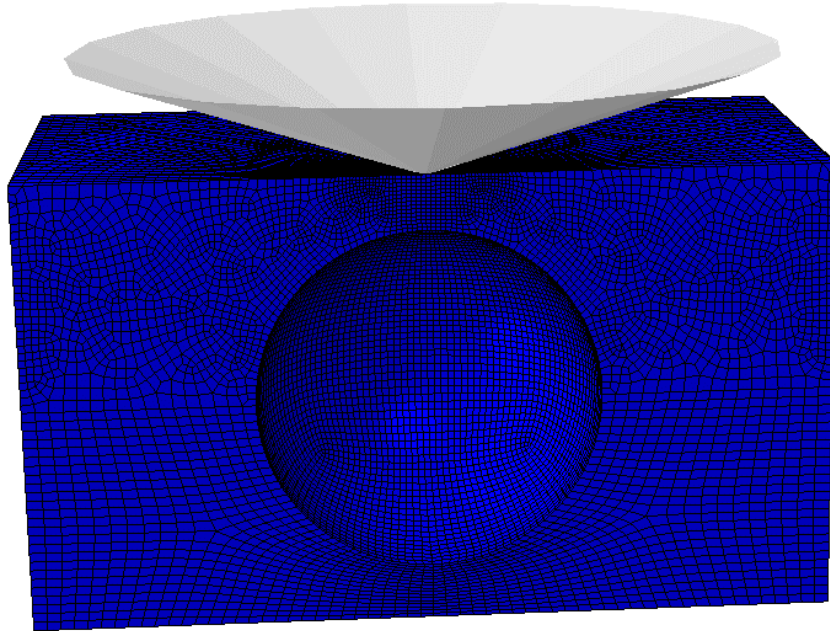


Figure B.1 Finite element meshes for the porous model. The diameter of the hole was set as $3.78 \mu\text{m}$, symmetric boundary conditions were applied to the sides to simulate a periodically porous structure, and the distance between the centre of the hole and indented surface varied between $4 \mu\text{m}$ and $6 \mu\text{m}$.

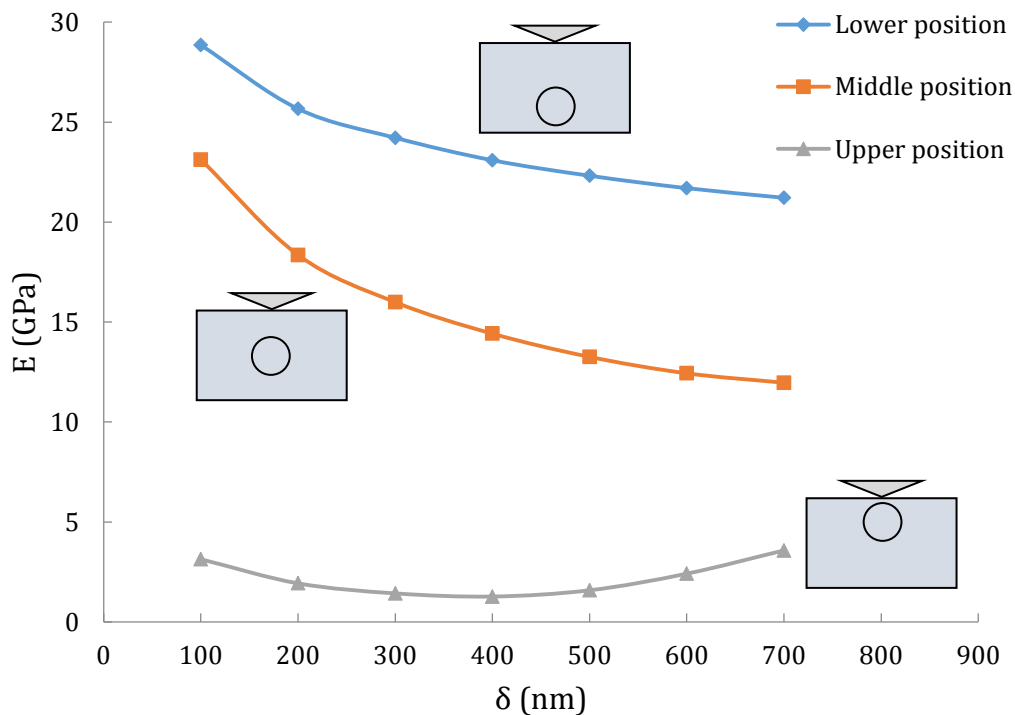


Figure B.2 The elastic modulus of the porous model with hole arranged to a lower, middle or upper position.

References

- Ahn, J.-H. and Kwon, D. (2001) 'Derivation of plastic stress–strain relationship from ball indentations: examination of strain definition and pileup effect', *Journal of Materials Research*, 16(11), pp. 3170-3178.
- Akhter, M.P., Fan, Z. and Rho, J.Y. (2004) 'Bone intrinsic material properties in three inbred mouse strains', *Calcified Tissue International*, 75(5), pp. 416-420.
- Akil, H., Omar, M.F., Mazuki, A.A.M., Safiee, S., Ishak, Z.A.M. and Bakar, A.A. (2011) 'Kenaf fiber reinforced composites: A review', *Materials & Design*, 32(8), pp. 4107-4121.
- Angker, L., Swain, M.V. and Kilpatrick, N. (2005) 'Characterising the micro-mechanical behaviour of the carious dentine of primary teeth using nano-indentation', *Journal of Biomechanics*, 38(7), pp. 1535-1542.
- Aryaei, A. and Jayasuriya, A.C. (2013) 'Mechanical properties of human amniotic fluid stem cells using nanoindentation', *Journal of Biomechanics*, 46(9), pp. 1524-1530.
- Baino, F., Ferraris, M., Bretcanu, O., Verné, E. and Vitale-Brovarone, C. (2011) 'Optimization of composition, structure and mechanical strength of bioactive 3-D glass-ceramic scaffolds for bone substitution', *Journal of Biomaterials Applications*, p. 0885328211429193.
- Bakis, C.E., Bank, L.C., Brown, V., Cosenza, E., Davalos, J.F., Lesko, J.J., Machida, A., Rizkalla, S.H. and Triantafillou, T.C. (2002) 'Fiber-reinforced polymer composites for construction—state-of-the-art review', *Journal of Composites for Construction*, 6(2), pp. 73-87.
- Balakrishnan, B. and Banerjee, R. (2011) 'Biopolymer-based hydrogels for cartilage tissue engineering', *Chemical reviews*, 111(8), pp. 4453-4474.

Balooch, M., Wu-Magidi, I.C., Balazs, A., Lundkvist, A.S., Marshall, S.J., Marshall, G.W., Siekhaus, W.J. and Kinney, J.H. (1998) 'Viscoelastic properties of demineralized human dentin measured in water with atomic force microscope (AFM)-based indentation', *Journal of Biomedical Materials Research*, 40(4), pp. 539-544.

Bandyopadhyay-Ghosh, S., Faria, P.E.P., Johnson, A., Felipucci, D.N.B., Reaney, I.M., Salata, L.A., Brook, I.M. and Hatton, P.V. (2010) 'Osteoconductivity of modified fluorcanasite glass-ceramics for bone tissue augmentation and repair', *Journal of Biomedical Materials Research Part A*, 94(3), pp. 760-768.

Barbero, E.J. (2010) *Introduction to composite materials design*. CRC press.

Beake, B.D. and Smith, J.F. (2002) 'High-temperature nanoindentation testing of fused silica and other materials', *Philosophical Magazine A*, 82(10), pp. 2179-2186.

Bei, H., George, E.P., Hay, J.L. and Pharr, G.M. (2005) 'Influence of indenter tip geometry on elastic deformation during nanoindentation', *Physical Review Letters*, 95(4), p. 045501.

Bell, T.J., Field, J.S. and Swain, M.V. (1992) 'Elastic-plastic characterization of thin films with spherical indentation', *Thin Solid Films*, 220(1-2), pp. 289-294.

Berasategui, E.G. and Page, T.F. (2003) 'The contact response of thin SiC-coated silicon systems—Characterisation by nanoindentation', *Surface and Coatings Technology*, 163, pp. 491-498.

Bhattacharya, A.K. and Nix, W.D. (1988) 'Finite element simulation of indentation experiments', *International Journal of Solids and Structures*, 24(9), pp. 881-891.

Bhushan, B. and Li, X. (2003) 'Nanomechanical characterisation of solid surfaces and thin films', *International Materials Reviews*, 48(3), pp. 125-164.

Bianco, P. and Robey, P.G. (2001) 'Stem cells in tissue engineering', *Nature*, 414(6859), pp. 118-121.

- Bobji, M.S. and Biswas, S.K. (1999) 'Deconvolution of hardness from data obtained from nanoindentation of rough surfaces', *Journal of Materials Research*, 14(6), pp. 2259-2268.
- Bobji, M.S., Fahim, M. and Biswas, S.K. (1996) 'Hardness estimated from the indentation of a spherical body. Some implications for nanoindentation test results', *Tribology Letters*, 2(4), pp. 381-391.
- Bolshakov, A., Oliver, W.C. and Pharr, G.M. (1996) 'Influences of stress on the measurement of mechanical properties using nanoindentation: Part II. Finite element simulations', *Journal of Materials Research*, 11(03), pp. 760-768.
- Bolshakov, A. and Pharr, G.M. (1998) 'Influences of pileup on the measurement of mechanical properties by load and depth sensing indentation techniques', *Journal of Materials Research*, 13(04), pp. 1049-1058.
- Bruet, B.J.F., Qi, H.J., Boyce, M.C., Panas, R., Tai, K., Frick, L. and Ortiz, C. (2005) 'Nanoscale morphology and indentation of individual nacre tablets from the gastropod mollusc *Trochus niloticus*', *Journal of Materials Research*, 20(09), pp. 2400-2419.
- Bull, S.J. (2001) 'Modelling the hardness response of bulk materials, single and multilayer coatings', *Thin Solid Films*, 398, pp. 291-298.
- Bull, S.J. (2002) 'Extracting hardness and Young's modulus from load-displacement curves', *Zeitschrift für Metallkunde*, 93(9), pp. 870-874.
- Bull, S.J. (2003) 'On the origins and mechanisms of the indentation size effect', *Zeitschrift für Metallkunde*, 94(7), pp. 787-792.
- Bull, S.J., Page, T.F. and Yoffe, E.H. (1989) 'An explanation of the indentation size effect in ceramics', *Philosophical Magazine Letters*, 59(6), pp. 281-288.
- Bull, S.J., Sanderson, L., Moharrami, N. and Oila, A. (2012) 'Effect of microstructure on hardness of submicrometre thin films and nanostructured devices', *Materials Science and Technology*, 28(9-10), pp. 1177-1185.

Bulychev, S.I., Alekhin, V.P., Shorshorov, M.H., Ternovskii, A.P. and Shnyrev, G.D. (1975) 'Determining Young's modulus from the indentor penetration diagram', *Ind. Lab.*, 41(9), pp. 1409-1412.

Burnett, P.J. and Rickerby, D.S. (1987a) 'The mechanical properties of wear-resistant coatings: I: Modelling of hardness behaviour', *Thin Solid Films*, 148(1), pp. 41-50.

Burnett, P.J. and Rickerby, D.S. (1987b) 'The mechanical properties of wear-resistant coatings: II: Experimental studies and interpretation of hardness', *Thin Solid Films*, 148(1), pp. 51-65.

Burstein, A.H., Reilly, D.T. and Martens, M. (1976) 'Aging of bone tissue: mechanical properties', *J Bone Joint Surg Am*, 58(1), pp. 82-86.

Calvert, P. (1992) 'Biomimetic ceramics and composites', *Mrs Bulletin*, 17(10), pp. 37-40.

Cao, Y.-P. and Chen, K.-L. (2012) 'Theoretical and computational modelling of instrumented indentation of viscoelastic composites', *Mechanics of Time-Dependent Materials*, 16(1), pp. 1-18.

Cao, Y.-P., Ji, X.-Y. and Feng, X.-Q. (2010) 'Geometry independence of the normalized relaxation functions of viscoelastic materials in indentation', *Philosophical Magazine*, 90(12), pp. 1639-1655.

Cao, Y., Ma, D. and Raabe, D. (2009) 'The use of flat punch indentation to determine the viscoelastic properties in the time and frequency domains of a soft layer bonded to a rigid substrate', *Acta Biomaterialia*, 5(1), pp. 240-248.

Carnelli, D., Lucchini, R., Ponzoni, M., Contro, R. and Vena, P. (2011) 'Nanoindentation testing and finite element simulations of cortical bone allowing for anisotropic elastic and inelastic mechanical response', *Journal of Biomechanics*, 44(10), pp. 1852-1858.

Chakraborty, H. and Bhowmik, N. (2014) 'Quasi-static and dynamic nanoindentation and scratch behavior of multifunctional titania/poly (methyl methacrylate) composite', *Polymer Composites*, 35(7), pp. 1372-1376.

- Chakravartula, A. and Komvopoulos, K. (2006) 'Viscoelastic properties of polymer surfaces investigated by nanoscale dynamic mechanical analysis', *Applied Physics Letters*, 88(13), p. 131901.
- Chaudhry, B., Ashton, H., Muhamed, A., Yost, M., Bull, S. and Frankel, D. (2009) 'Nanoscale viscoelastic properties of an aligned collagen scaffold', *Journal of Materials Science: Materials in Medicine*, 20(1), pp. 257-263.
- Chen, C.-C., Chueh, J.-Y., Tseng, H., Huang, H.-M. and Lee, S.-Y. (2003) 'Preparation and characterization of biodegradable PLA polymeric blends', *Biomaterials*, 24(7), pp. 1167-1173.
- Chen, J. (2012) 'Indentation-based methods to assess fracture toughness for thin coatings', *Journal of Physics D: Applied Physics*, 45(20), p. 203001.
- Chen, J. (2014) 'Nanobiomechanics of living cells: a review', *Interface Focus*, 4(2), p. 20130055.
- Chen, J., Birch, M.A. and Bull, S.J. (2010a) 'Nanomechanical characterization of tissue engineered bone grown on titanium alloy in vitro', *Journal of Materials Science: Materials in Medicine*, 21(1), pp. 277-282.
- Chen, J., Birch, M.A. and Bull, S.J. (2010b) 'Nanomechanical characterization of tissue engineered bone grown on titanium alloy in vitro', *J Mater Sci Mater Med*, 21(1), pp. 277-82.
- Chen, J. and Bull, S.J. (2006a) 'Assessment of the toughness of thin coatings using nanoindentation under displacement control', *Thin Solid Films*, 494(1), pp. 1-7.
- Chen, J. and Bull, S.J. (2006b) 'A critical examination of the relationship between plastic deformation zone size and Young's modulus to hardness ratio in indentation testing', *Journal of Materials Research*, 21(10), pp. 2617-2627.
- Chen, J. and Bull, S.J. (2006c) 'On the relationship between plastic zone radius and maximum depth during nanoindentation', *Surface and Coatings Technology*, 201(7), pp. 4289-4293.

Chen, J. and Bull, S.J. (2007) 'Indentation fracture and toughness assessment for thin optical coatings on glass', *Journal of Physics D: Applied Physics*, 40(18), p. 5401.

Chen, J. and Bull, S.J. (2008) 'Multi-cycling nanoindentation study on thin optical coatings on glass', *Journal of Physics D: Applied Physics*, 41(7), p. 074009.

Chen, J. and Bull, S.J. (2009a) 'Modelling the limits of coating toughness in brittle coated systems', *Thin Solid Films*, 517(9), pp. 2945-2952.

Chen, J. and Bull, S.J. (2009b) 'On the factors affecting the critical indenter penetration for measurement of coating hardness', *Vacuum*, 83(6), pp. 911-920.

Chen, J. and Bull, S.J. (2009c) 'Relation between the ratio of elastic work to the total work of indentation and the ratio of hardness to Young's modulus for a perfect conical tip', *Journal of Materials Research*, 24(03), pp. 590-598.

Chen, J. and Bull, S.J. (2010) 'Approaches to investigate delamination and interfacial toughness in coated systems: an overview', *Journal of Physics D: Applied Physics*, 44(3), p. 034001.

Chen, J., Bull, S.J., Roy, S., Kapoor, A., Mukaibo, H., Nara, H., Momma, T., Osaka, T. and Shacham-Diamand, Y. (2009) 'Nanoindentation and nanowear study of Sn and Ni–Sn coatings', *Tribology international*, 42(6), pp. 779-791.

Chen, J. and Lu, G. (2012) 'Finite element modelling of nanoindentation based methods for mechanical properties of cells', *Journal of Biomechanics*, 45(16), pp. 2810-2816.

Chen, J., Wright, K.E. and Birch, M.A. (2014) 'Nanoscale viscoelastic properties and adhesion of polydimethylsiloxane for tissue engineering', *Acta Mechanica Sinica*, 30(1), pp. 2-6.

Chen, P.-Y., Lin, A.Y.-M., McKittrick, J. and Meyers, M.A. (2008) 'Structure and mechanical properties of crab exoskeletons', *Acta Biomaterialia*, 4(3), pp. 587-596.

- Cheng, L., Xia, X., Yu, W., Scriven, L.E. and Gerberich, W.W. (2000) 'Flat-punch indentation of viscoelastic material', *Journal of Polymer Science Part B: Polymer Physics*, 38(1), pp. 10-22.
- Cheng, Y.-T. and Cheng, C.-M. (2004) 'Scaling, dimensional analysis, and indentation measurements', *Materials Science and Engineering: R: Reports*, 44(4-5), pp. 91-149.
- Cheng, Y.-T., Li, Z. and Cheng, C.-M. (2002) 'Scaling relationships for indentation measurements', *Philosophical Magazine A*, 82(10), pp. 1821-1829.
- Claudionico (2015) *File:Electron Interaction with Matter.svg*. Available at: https://commons.wikimedia.org/wiki/File:Electron_Interaction_with_Matter.svg#metadata (Accessed: 05 April 2017).
- Clifford, C.A. and Seah, M.P. (2006) 'Modelling of nanomechanical nanoindentation measurements using an AFM or nanoindenter for compliant layers on stiffer substrates', *Nanotechnology*, 17(21), p. 5283.
- Clifford, C.A. and Seah, M.P. (2012) 'Modelling of surface nanoparticle inclusions for nanomechanical measurements by an AFM or nanoindenter: spatial issues', *Nanotechnology*, 23(16), p. 165704.
- Constantinides, G., Chandran, K.S.R., Ulm, F.J. and Van Vliet, K.J. (2006) 'Grid indentation analysis of composite microstructure and mechanics: Principles and validation', *Materials Science and Engineering: A*, 430(1-2), pp. 189-202.
- Cuy, J.L., Mann, A.B., Livi, K.J., Teaford, M.F. and Weihs, T.P. (2002) 'Nanoindentation mapping of the mechanical properties of human molar tooth enamel', *Archives of Oral Biology*, 47(4), pp. 281-291.
- Cyganik, Ł., Binkowski, M., Kokot, G., Rusin, T., Popik, P., Bolechała, F., Nowak, R., Wrobel, Z. and John, A. (2014) 'Prediction of Young's modulus of trabeculae in microscale using macro-scale's relationships between bone density and mechanical properties', *Journal of the Mechanical Behavior of Biomedical Materials*, 36, pp. 120-134.

Dadbin, S. and Naimian, F. (2014) 'Gamma radiation induced property modification of poly (lactic acid)/hydroxyapatite bio-nanocomposites', *Polymer International*, 63(6), pp. 1063-1069.

De Jong, W.H. and Borm, P.J.A. (2008) 'Drug delivery and nanoparticles: applications and hazards', *International Journal of Nanomedicine*, 3(2), p. 133.

De Silva, R.T., Pasbakhsh, P., Goh, K.L., Chai, S.P. and Chen, J. (2014) 'Synthesis and characterisation of poly (lactic acid)/halloysite bionanocomposite films', *Journal of Composite Materials*, 48(30), pp. 3705-3717.

Deb, S., Mandegaran, R. and Di Silvio, L. (2010) 'A porous scaffold for bone tissue engineering/45S5 Bioglass® derived porous scaffolds for co-culturing osteoblasts and endothelial cells', *Journal of Materials Science: Materials in Medicine*, 21(3), pp. 893-905.

Den Toonder, J., Malzbender, J. and Balkenende, R. (2002) 'Fracture toughness and adhesion energy of sol-gel coatings on glass', *Journal of Materials Research*, 17(1), pp. 224-233.

Doerner, M.F. and Nix, W.D. (1986) 'A method for interpreting the data from depth-sensing indentation instruments', *Journal of Materials Research*, 1(04), pp. 601-609.

Dong, X.N. and Guo, X.E. (2004) 'The dependence of transversely isotropic elasticity of human femoral cortical bone on porosity', *Journal of biomechanics*, 37(8), pp. 1281-1287.

Donnelly, E., Baker, S.P., Boskey, A.L. and van der Meulen, M.C.H. (2006) 'Effects of surface roughness and maximum load on the mechanical properties of cancellous bone measured by nanoindentation', *Journal of Biomedical Materials Research Part A*, 77(2), pp. 426-435.

- Donzelli, E., Salvadè, A., Mimo, P., Viganò, M., Morrone, M., Papagna, R., Carini, F., Zaopo, A., Miloso, M., Baldoni, M. and Tredici, G. (2007) 'Mesenchymal stem cells cultured on a collagen scaffold: In vitro osteogenic differentiation', *Archives of Oral Biology*, 52(1), pp. 64-73.
- Duan, P., Bull, S. and Chen, J. (2015) 'Modeling the nanomechanical responses of biopolymer composites during the nanoindentation', *Thin Solid Films*, 596, pp. 277-281.
- Duan, P. and Chen, J. (2015) 'Nanomechanical and microstructure analysis of extracellular matrix layer of immortalized cell line Y201 from human mesenchymal stem cells', *Surface and Coatings Technology*, 284, pp. 417-421.
- Ebenstein, D.M., Kuo, A., Rodrigo, J.J., Reddi, A.H., Ries, M. and Pruitt, L. (2004) 'A nanoindentation technique for functional evaluation of cartilage repair tissue', *Journal of Materials Research*, 19(01), pp. 273-281.
- Ebenstein, D.M. and Pruitt, L.A. (2004) 'Nanoindentation of soft hydrated materials for application to vascular tissues', *Journal of Biomedical Materials Research Part A*, 69(2), pp. 222-232.
- Ebenstein, D.M. and Pruitt, L.A. (2006) 'Nanoindentation of biological materials', *Nano Today*, 1(3), pp. 26-33.
- Ebenstein, D.M. and Wahl, K.J. (2006) 'Anisotropic nanomechanical properties of Nephila clavipes dragline silk', *Journal of Materials Research*, 21(08), pp. 2035-2044.
- Eggedi, O., Valiyaneerilakkal, U., Darla, M.R. and Varghese, S. (2014) 'Nanoindentation and thermal characterization of poly(vinylidenefluoride)/MWCNT nanocomposites', *AIP Advances*, 4(4), p. 047102.
- Emri, I. and Tschoegl, N.W. (1993) 'Generating line spectra from experimental responses. Part I: Relaxation modulus and creep compliance', *Rheologica Acta*, 32(3), pp. 311-322.

Fan, Z., Rho, J.Y. and Swadener, J.G. (2004) 'Three-dimensional finite element analysis of the effects of anisotropy on bone mechanical properties measured by nanoindentation', *Journal of materials research*, 19(01), pp. 114-123.

Fan, Z., Swadener, J.G., Rho, J.Y., Roy, M.E. and Pharr, G.M. (2002) 'Anisotropic properties of human tibial cortical bone as measured by nanoindentation', *Journal of orthopaedic research*, 20(4), pp. 806-810.

Feng, G. and Ngan, A.H.W. (2002) 'Effects of creep and thermal drift on modulus measurement using depth-sensing indentation', *Journal of Materials Research*, 17(03), pp. 660-668.

Ferreira, A.M., Gentile, P., Chiono, V. and Ciardelli, G. (2012) 'Collagen for bone tissue regeneration', *Acta biomaterialia*, 8(9), pp. 3191-3200.

Ferreira, A.M., González, G., González-Paz, R.J., Feijoo, J.L., Lira-Olivares, J. and Noris-Suárez, K. (2009) 'Bone Collagen Role in Piezoelectric Mediated Remineralization', *Acta Microscopica*, 18(3).

Field, J.S. and Swain, M.V. (1995) 'Determining the mechanical properties of small volumes of material from submicrometer spherical indentations', *Journal of Materials Research*, 10(01), pp. 101-112.

Field, J.S., Swain, M.V. and Dukino, R.D. (2003) 'Determination of fracture toughness from the extra penetration produced by indentation-induced pop-in', *Journal of Materials Research*, 18(06), pp. 1412-1419.

Fischer-Cripps, A.C. (2007) 'Elastic-plastic indentation stress fields', *Introduction to Contact Mechanics*, pp. 137-150.

Fischer-Cripps, A.C. (2011a) 'Analysis of nanoindentation test data', in *Nanoindentation*. Springer, pp. 39-75.

Fischer-Cripps, A.C. (2011b) 'Factors affecting nanoindentation test data', in *Nanoindentation*. Springer, pp. 77-104.

Fischer-Cripps, A.C. (2011c) 'Nanoindentation testing', in *Nanoindentation*. Springer, pp. 21-37.

- Fischer-Cripps, A.C. (2011d) 'Simulation of Nanoindentation Test Data', in *Nanoindentation*. Springer, pp. 105-117.
- Fischer-Cripps, A.C. (2011e) 'Time-dependent Nanoindentation', in *Nanoindentation*. Springer, pp. 125-145.
- Fong, H., Sarikaya, M., White, S.N. and Snead, M.L. (1999) 'Nano-mechanical properties profiles across dentin–enamel junction of human incisor teeth', *Materials Science and Engineering: C*, 7(2), pp. 119-128.
- G-Berasategui, E., Bull, S.J. and Page, T.F. (2004) 'Mechanical modelling of multilayer optical coatings', *Thin Solid Films*, 447, pp. 26-32.
- Gamie, Z., Tran, G.T., Vyzas, G., Korres, N., Heliotis, M., Mantalaris, A. and Tsiridis, E. (2012) 'Stem cells combined with bone graft substitutes in skeletal tissue engineering', *Expert opinion on biological therapy*, 12(6), pp. 713-729.
- Gao, H. (2006) 'Application of fracture mechanics concepts to hierarchical biomechanics of bone and bone-like materials', *Advances in Fracture Research*, pp. 101-137.
- Gao, H., Chiu, C.-H. and Lee, J. (1992) 'Elastic contact versus indentation modeling of multi-layered materials', *International Journal of Solids and Structures*, 29(20), pp. 2471-2492.
- Gao, S.-L. and Mäder, E. (2002) 'Characterisation of interphase nanoscale property variations in glass fibre reinforced polypropylene and epoxy resin composites', *Composites Part A: Applied Science and Manufacturing*, 33(4), pp. 559-576.
- Ge, J., Cui, F.Z., Wang, X.M. and Feng, H.L. (2005) 'Property variations in the prism and the organic sheath within enamel by nanoindentation', *Biomaterials*, 26(16), pp. 3333-3339.
- Georges, J.M. and Meille, G. (1984) 'Vickers indentation curves of magnesium oxide (MgO)', *Journal of Tribology* 106(1), pp. 43-48.

Gong, M., Bi, Y., Jiang, W., Zhang, Y., Chen, L., Hou, N., Liu, Y., Wei, X., Chen, J. and Li, T. (2011) 'Immortalized mesenchymal stem cells: an alternative to primary mesenchymal stem cells in neuronal differentiation and neuroregeneration associated studies', *Journal of biomedical science*, 18(1), p. 1.

Goodhew, P.J., Humphreys, J. and Beanland, R. (2000) *Electron microscopy and analysis*. CRC Press.

Gough, J.E., Jones, J.R. and Hench, L.L. (2004) 'Nodule formation and mineralisation of human primary osteoblasts cultured on a porous bioactive glass scaffold', *Biomaterials*, 25(11), pp. 2039-2046.

Gronthos, S., Graves, S.E., Ohta, S. and Simmons, P.J. (1994) 'The STRO-1+ fraction of adult human bone marrow contains the', *Blood*, 84(12), pp. 4164-4173.

Guo, Y.B. and Yen, D.W. (2004) 'A FEM study on mechanisms of discontinuous chip formation in hard machining', *Journal of Materials Processing Technology*, 155, pp. 1350-1356.

Gupta, H.S., Seto, J., Wagermaier, W., Zaslansky, P., Boesecke, P. and Fratzl, P. (2006) 'Cooperative deformation of mineral and collagen in bone at the nanoscale', *Proceedings of the National Academy of Sciences*, 103(47), pp. 17741-17746.

Gupta, H.S., Wagermaier, W., Zickler, G.A., Raz-Ben Aroush, D., Funari, S.S., Roschger, P., Wagner, H.D. and Fratzl, P. (2005) 'Nanoscale deformation mechanisms in bone', *Nano Letters*, 5(10), pp. 2108-2111.

Hainsworth, S.V., Chandler, H.W. and Page, T.F. (1996) 'Analysis of nanoindentation load-displacement loading curves', *Journal of Materials Research*, 11(08), pp. 1987-1995.

Hainsworth, S.V. and Page, T.F. (1994) 'Nanoindentation studies of chemomechanical effects in thin film coated systems', *Surface and Coatings Technology*, 68, pp. 571-575.

- Hajiali, H., Shahgasempour, S., Naimi-Jamal, M.R. and Peirovi, H. (2011) 'Electrospun PGA/gelatin nanofibrous scaffolds and their potential application in vascular tissue engineering', *International Journal of Nanomedicine*, 6, p. 2133.
- Haque, F. (2003) 'Application of nanoindentation development of biomedical to materials', *Surface Engineering*, 19(4), pp. 255-268.
- Hasan, M.S., Ahmed, I., Parsons, A.J., Walker, G.S. and Scotchford, C.A. (2013) 'The influence of coupling agents on mechanical property retention and long-term cytocompatibility of phosphate glass fibre reinforced PLA composites', *Journal of the Mechanical Behavior of Biomedical Materials*, 28, pp. 1-14.
- Hashin, Z. (1966) 'Viscoelastic fiber reinforced materials', *AIAA Journal*, 4(8), pp. 1411-1417.
- Hasler, E.M., Herzog, W., Wu, J.Z., Müller, W. and Wyss, U. (1998) 'Articular cartilage biomechanics: theoretical models, material properties, and biosynthetic response', *Critical Reviews in Biomedical Engineering*, 27(6), pp. 415-488.
- Hay, J.C., Bolshakov, A. and Pharr, G.M. (1999) 'A critical examination of the fundamental relations used in the analysis of nanoindentation data', *Journal of Materials Research*, 14(06), pp. 2296-2305.
- Hay, J.L. and Wolff, P.J. (2001) 'Small correction required when applying the Hertzian contact model to instrumented indentation data', *Journal of Materials Research*, 16(05), pp. 1280-1286.
- Herruzo, E.T., Perrino, A.P. and Garcia, R. (2014) 'Fast nanomechanical spectroscopy of soft matter', *Nature Communications*, 5.
- Hibbett, Karlsson and Sorensen (1998) *ABAQUS/standard: User's Manual*. Hibbett, Karlsson & Sorensen.

Ho, S.P., Balooch, M., Goodis, H.E., Marshall, G.W. and Marshall, S.J. (2004) 'Ultrastructure and nanomechanical properties of cementum dentin junction', *Journal of Biomedical Materials Research Part A*, 68(2), pp. 343-351.

Ho, S.P., Sulyanto, R.M., Marshall, S.J. and Marshall, G.W. (2005) 'The cementum–dentin junction also contains glycosaminoglycans and collagen fibrils', *Journal of Structural Biology*, 151(1), pp. 69-78.

Hoffler, C.E., Guo, X.E., Zysset, P.K. and Goldstein, S.A. (2005) 'An application of nanoindentation technique to measure bone tissue lamellae properties', *Journal of Biomechanical Engineering*, 127(7), pp. 1046-1053.

Hoffler, C.E., Moore, K.E., Kozloff, K., Zysset, P.K., Brown, M.B. and Goldstein, S.A. (2000) 'Heterogeneity of bone lamellar-level elastic moduli', *Bone*, 26(6), pp. 603-609.

Howland, R. and Benatar, L. (1996) *A Practical Guide: To Scanning Probe Microscopy*. Park scientific instruments.

Hu, H., Onyebueke, L. and Abatan, A. (2010) 'Characterizing and modeling mechanical properties of nanocomposites-review and evaluation', *Journal of Minerals and Materials Characterization and Engineering*, 9(04), p. 275.

Hull, D. and Clyne, T.W. (1996) *An introduction to composite materials*. Cambridge university press.

Hutmacher, D.W. (2000) 'Scaffolds in tissue engineering bone and cartilage', *Biomaterials*, 21(24), pp. 2529-2543.

ISO14577 (2007) 'Metallic materials—Instrumented indentation test for hardness and materials parameters—Part 4. Test method for metallic and non-metallic coatings', *International Standards Organisation, Geneva, Switzerland*.

Jaiswal, N., Haynesworth, S.E., Caplan, A.I. and Bruder, S.P. (1997) 'Osteogenic differentiation of purified, culture-expanded human mesenchymal stem cells in vitro', *Journal of Cellular Biochemistry*, 64(2), pp. 295-312.

- James, S., Fox, J., Afsari, F., Lee, J., Clough, S., Knight, C., Ashmore, J., Ashton, P., Preham, O. and Hoogduijn, M. (2015) 'Multiparameter analysis of human bone marrow stromal cells identifies distinct immunomodulatory and differentiation-competent subtypes', *Stem cell reports*, 4(6), pp. 1004-1015.
- Jämsä, T., Rho, J.-Y., Fan, Z., MacKay, C.A., Marks, S.C. and Tuukkanen, J. (2002) 'Mechanical properties in long bones of rat osteopetrotic mutations', *Journal of Biomechanics*, 35(2), pp. 161-165.
- Jang, I.K., Tanaka, R., Wurihan, Suzuki, D., Shibata, Y., Fujisawa, N., Tanimoto, Y., Ogura, K., Kamijo, R. and Miyazaki, T. (2014) 'Nanomechanical properties and molecular structures of in vitro mineralized tissues on anodically-oxidized titanium surfaces', *Nanomedicine*, 10(3), pp. 629-37.
- Jaramillo-Isaza, S., Mazeran, P.E., El-Kirat, K. and Ho Ba Tho, M.C. (2014) 'Effects of bone density in the time-dependent mechanical properties of human cortical bone by nanoindentation', *Computer Methods in Biomechanics and Biomedical Engineering*, 17(sup1), pp. 34-35.
- Jell, G., Notingher, I., Tsigkou, O., Notingher, P., Polak, J.M., Hench, L.L. and Stevens, M.M. (2008) 'Bioactive glass-induced osteoblast differentiation: A noninvasive spectroscopic study', *Journal of Biomedical Materials Research Part A*, 86(1), pp. 31-40.
- Jiang, L., Xiong, C., Jiang, L. and Xu, L. (2014) 'Effect of hydroxyapatite with different morphology on the crystallization behavior, mechanical property and in vitro degradation of hydroxyapatite/poly (lactic-co-glycolic) composite', *Composites Science and Technology*, 93, pp. 61-67.
- Jiang, W.-G., Su, J.-J. and Feng, X.-Q. (2008) 'Effect of surface roughness on nanoindentation test of thin films', *Engineering Fracture Mechanics*, 75(17), pp. 4965-4972.
- Johnson, K.L. (1987) *Contact mechanics*. Cambridge university press.

Johnson, K.L., Kendall, K. and Roberts, A.D. (1971) 'Surface energy and the contact of elastic solids', *Proceedings of the Royal Society of London A: Mathematical, Physical and Engineering Sciences*, 324, pp. 301-313.

Jönsson, B. and Hogmark, S. (1984) 'Hardness measurements of thin films', *Thin Solid Films*, 114(3), pp. 257-269.

Joslin, D.L. and Oliver, W.C. (1990) 'A new method for analyzing data from continuous depth-sensing microindentation tests', *Journal of Materials Research*, 5(01), pp. 123-126.

Jung, Y.-G., Lawn, B.R., Martyniuk, M., Huang, H. and Hu, X.Z. (2004) 'Evaluation of elastic modulus and hardness of thin films by nanoindentation', *Journal of Materials Research*, 19(10), pp. 3076-3080.

Kalia, S., Kaith, B.S. and Kaur, I. (2009) 'Pretreatments of natural fibers and their application as reinforcing material in polymer composites—a review', *Polymer Engineering & Science*, 49(7), pp. 1253-1272.

Katti, D.R., Katti, K.S., Sopp, J.M. and Sarikaya, M. (2001) '3D finite element modeling of mechanical response in nacre-based hybrid nanocomposites', *Computational and Theoretical Polymer Science*, 11(5), pp. 397-404.

Kavukcuoglu, N.B., Denhardt, D.T., Guzelsu, N. and Mann, A.B. (2007) 'Osteopontin deficiency and aging on nanomechanics of mouse bone', *J Biomed Mater Res A*, 83(1), pp. 136-44.

Kavukcuoglu, N.B., Patterson-Buckendahl, P. and Mann, A.B. (2009) 'Effect of osteocalcin deficiency on the nanomechanics and chemistry of mouse bones', *J Mech Behav Biomed Mater*, 2(4), pp. 348-54.

Kim, K.-I., Park, S. and Im, G.-I. (2014) 'Osteogenic differentiation and angiogenesis with cocultured adipose-derived stromal cells and bone marrow stromal cells', *Biomaterials*, 35(17), pp. 4792-4804.

King, R.B. (1987) 'Elastic analysis of some punch problems for a layered medium', *International Journal of Solids and Structures*, 23(12), pp. 1657-1664.

- Kinney, J.H., Balooch, M., Marshall, S.J., Marshall, G.W. and Weihs, T.P. (1996a) 'Atomic force microscope measurements of the hardness and elasticity of peritubular and intertubular human dentin', *Journal of Biomechanical Engineering*, 118, pp. 133-135.
- Kinney, J.H., Balooch, M., Marshall, S.J., Marshall, G.W. and Weihs, T.P. (1996b) 'Hardness and Young's modulus of human peritubular and intertubular dentine', *Archives of Oral Biology*, 41(1), pp. 9-13.
- Kinney, J.H., Marshall, S.J. and Marshall, G.W. (2003) 'The mechanical properties of human dentin: a critical review and re-evaluation of the dental literature', *Critical Reviews in Oral Biology & Medicine*, 14(1), pp. 13-29.
- Knoop, F., Peters, C.G. and Emerson, W.B. (1939) 'A sensitive pyramidal-diamond tool for indentation measurements', *Journal of Research of the National Bureau of Standards*, 23(1), pp. 39-61.
- Kubozono, K., Takechi, M., Ohta, K., Ono, S., Nakagawa, T., Fujimoto, S. and Kamata, N. (2014) 'Aesthetic recovery of alveolar atrophy following autogenous onlay bone grafting using interconnected porous hydroxyapatite ceramics (IP-CHA) and resorbable poly-L-lactic/polyglycolic acid screws: case report', *BMC Oral Health*, 14(1), p. 60.
- Langenbach, F. and Handschel, J. (2013) 'Effects of dexamethasone, ascorbic acid and β -glycerophosphate on the osteogenic differentiation of stem cells in vitro', *Stem Cell Res Ther*, 4(5), p. 117.
- Lee, S.-H., Wang, S., Pharr, G.M. and Xu, H. (2007) 'Evaluation of interphase properties in a cellulose fiber-reinforced polypropylene composite by nanoindentation and finite element analysis', *Composites Part A: Applied Science and Manufacturing*, 38(6), pp. 1517-1524.
- Leipner, H.S., Lorenz, D., Zeckzer, A., Lei, H. and Grau, P. (2001) 'Nanoindentation pop-in effect in semiconductors', *Physica B: Condensed Matter*, 308, pp. 446-449.

Lewis, G. and Nyman, J.S. (2008) 'The use of nanoindentation for characterizing the properties of mineralized hard tissues: State-of-the art review', *Journal of Biomedical Materials Research Part B: Applied Biomaterials*, 87(1), pp. 286-301.

Li, H., Ghosh, A., Han, Y.H. and Bradt, R.C. (1993) 'The frictional component of the indentation size effect in low load microhardness testing', *Journal of Materials Research*, 8(5), pp. 1028-1032.

Li, X. and Bhushan, B. (1998) 'Measurement of fracture toughness of ultra-thin amorphous carbon films', *Thin Solid Films*, 315(1), pp. 214-221.

Li, X., Chang, W.-C., Chao, Y.J., Wang, R. and Chang, M. (2004) 'Nanoscale structural and mechanical characterization of a natural nanocomposite material: the shell of red abalone', *Nano Letters*, 4(4), pp. 613-617.

Lichinchi, M., Lenardi, C., Haupt, J. and Vitali, R. (1998) 'Simulation of Berkovich nanoindentation experiments on thin films using finite element method', *Thin Solid Films*, 312(1-2), pp. 240-248.

Lim, Y.Y., Chaudhri, M.M. and Enomoto, Y. (1999) 'Accurate determination of the mechanical properties of thin aluminum films deposited on sapphire flats using nanoindentations', *Journal of Materials Research*, 14(06), pp. 2314-2327.

Liu, H. and Brinson, L.C. (2008) 'Reinforcing efficiency of nanoparticles: A simple comparison for polymer nanocomposites', *Composites Science and Technology*, 68(6), pp. 1502-1512.

Liu, T.M., Ng, W.M., Tan, H.S., Vinitha, D., Yang, Z., Fan, J.B., Zou, Y., Hui, J.H., Lee, E.H. and Lim, B. (2012) 'Molecular basis of immortalization of human mesenchymal stem cells by combination of p53 knockdown and human telomerase reverse transcriptase overexpression', *Stem cells and development*, 22(2), pp. 268-278.

Lou, Y.C. and Schapery, R.A. (1971) 'Viscoelastic characterization of a nonlinear fiber-reinforced plastic', *Journal of Composite Materials*, 5(2), pp. 208-234.

- Loubet, J.L., Georges, J.M. and Meille, G. (1986) 'Vickers indentation curves of elastoplastic materials', in *Microindentation Techniques in Materials Science and Engineering*. ASTM International.
- Low, T.F., Pun, C.L. and Yan, W. (2015) 'Theoretical study on nanoindentation hardness measurement of a particle embedded in a matrix', *Philosophical Magazine*, 95(14), pp. 1573-1586.
- Lucas, B.N., Oliver, W.C. and Swindeman, J.E. (1998) 'The dynamics of frequency-specific, depth-sensing indentation testing', *MRS Online Proceedings Library Archive*, 522.
- Lundkvist, A., Lilleodden, E., Siekhaus, W., Kinney, J., Pruitt, L. and Balooch, M. (1996) 'Viscoelastic properties of healthy human artery measured in saline solution by AFM-based indentation technique', *MRS Proceedings*, 436, p. 353.
- Luo, J., Zhao, Z., Shen, J. and Zhang, C. (2014) 'Elastic–plastic analysis of ultrafine-grained $\text{Si}_2\text{N}_2\text{O}$ – Si_3N_4 composites by nanoindentation and finite element simulation', *Ceramics International*, 40(5), pp. 7073-7080.
- Malzbender, J. (2002) 'Indentation load–displacement curve, plastic deformation, and energy', *Journal of Materials Research*, 17(02), pp. 502-511.
- Malzbender, J. and de With, G. (2000) 'Energy dissipation, fracture toughness and the indentation load–displacement curve of coated materials', *Surface and Coatings Technology*, 135(1), pp. 60-68.
- Malzbender, J. and de With, G. (2002) 'A model to determine the interfacial fracture toughness for chipped coatings', *Surface and Coatings Technology*, 154(1), pp. 21-26.
- Malzbender, J., de With, G. and Den Toonder, J.M.J. (2000) 'Elastic modulus, indentation pressure and fracture toughness of hybrid coatings on glass', *Thin Solid Films*, 366(1), pp. 139-149.
- Malzbender, J. and den Toonder, J. (2000) 'The $P-h^2$ relationship in indentation', *Journal of Materials Research*, 15(05), pp. 1209-1212.

Marshall, D.B., Noma, T. and Evans, A.G. (1982) 'A Simple Method for Determining Elastic-Modulus-to-Hardness Ratios using Knoop Indentation Measurements', *Journal of the American Ceramic Society*, 65(10).

Marshall, G.W., Balooch, M., Gallagher, R.R., Gansky, S.A. and Marshall, S.J. (2001a) 'Mechanical properties of the dentinoenamel junction: AFM studies of nanohardness, elastic modulus, and fracture', *Journal of Biomedical Materials Research*, 54(1), pp. 87-95.

Marshall, G.W., Habelitz, S., Gallagher, R., Balooch, M., Balooch, G. and Marshall, S.J. (2001b) 'Nanomechanical properties of hydrated carious human dentin', *Journal of Dental Research*, 80(8), pp. 1768-1771.

Martin, R.B. and Boardman, D.L. (1993) 'The effects of collagen fiber orientation, porosity, density, and mineralization on bovine cortical bone bending properties', *Journal of biomechanics*, 26(9), pp. 1047-1054.

Matthews, F.L. and Rawlings, R.D. (1999) *Composite materials: engineering and science*. Elsevier.

Maver, U., Maver, T., Peršin, Z., Mozetic, M., Vesel, A., Gaberšček, M. and Stana-Kleinschek, K. (2013) 'Polymer characterization with the atomic force microscope', in *Polymer Science*. InTech.

Menčík, J., Munz, D., Quandt, E., Weppelmann, E.R. and Swain, M.V. (1997) 'Determination of elastic modulus of thin layers using nanoindentation', *Journal of Materials Research*, 12(09), pp. 2475-2484.

Min, L., Wei-Min, C., Nai-Gang, L. and Ling-Dong, W. (2004) 'A numerical study of indentation using indenters of different geometry', *Journal of Materials Research*, 19(01), pp. 73-78.

Mintz (2015) *File:Schema MEB (en).svg*. Available at:
[https://commons.wikimedia.org/wiki/File:Schema_MEB_\(en\).svg](https://commons.wikimedia.org/wiki/File:Schema_MEB_(en).svg) (Accessed: 06 April 2017).

Mukherjee, T. and Kao, N. (2011) 'PLA based biopolymer reinforced with natural fibre: a review', *Journal of Polymers and the Environment*, 19(3), pp. 714-725.

Nemecek, I.J. (2009) *Nanoindentation of heterogeneous structural materials*. PhD thesis, Czech Technical University, Prague, Czech Republic.

Newey, D., Wilkins, M.A. and Pollock, H.M. (1982) 'An ultra-low-load penetration hardness tester', *Journal of Physics E: Scientific Instruments*, 15(1), p. 119.

Ni, W., Cheng, Y.-T., Cheng, C.-M. and Grummon, D.S. (2004) 'An energy-based method for analyzing instrumented spherical indentation experiments', *Journal of Materials Research*, 19(01), pp. 149-157.

Nikolov, S., Petrov, M., Lymperakis, L., Friák, M., Sachs, C., Fabritius, H.O., Raabe, D. and Neugebauer, J. (2010) 'Revealing the Design Principles of High-Performance Biological Composites Using Ab Initio and Multiscale Simulations: The Example of Lobster Cuticle', *Advanced Materials*, 22(4), pp. 519-526.

Nix, W.D. and Gao, H. (1998) 'Indentation size effects in crystalline materials: a law for strain gradient plasticity', *Journal of the Mechanics and Physics of Solids*, 46(3), pp. 411-425.

Nobelium (2015) *File:Atomic force microscope block diagram.svg*. Available at: https://commons.wikimedia.org/wiki/File:Atomic_force_microscope_block_diagram.svg (Accessed: 06 April 2017).

Nowicki, M., Richter, A., Wolf, B. and Kaczmarek, H. (2003) 'Nanoscale mechanical properties of polymers irradiated by UV', *Polymer*, 44(21), pp. 6599-6606.

Oliver, W.C. (2001) 'Alternative technique for analyzing instrumented indentation data', *Journal of Materials Research*, 16(11), pp. 3202-3206.

Oliver, W.C. and Pharr, G.M. (1992) 'An improved technique for determining hardness and elastic modulus using load and displacement sensing indentation experiments', *Journal of Materials Research*, 7(06), pp. 1564-1583.

- Oliver, W.C. and Pharr, G.M. (2004) 'Measurement of hardness and elastic modulus by instrumented indentation: Advances in understanding and refinements to methodology', *Journal of Materials Research*, 19(01), pp. 3-20.
- Oyen, M.L. (2005) 'Spherical indentation creep following ramp loading', *Journal of Materials Research*, 20(08), pp. 2094-2100.
- Oyen, M.L. (2013) 'Nanoindentation of biological and biomimetic materials', *Experimental Techniques*, 37(1), pp. 73-87.
- Oyen, M.L. (2014) 'Mechanical characterisation of hydrogel materials', *International Materials Reviews*, 59(1), pp. 44-59.
- Oyen, M.L. (2015) 'Nanoindentation of hydrated materials and tissues', *Current Opinion in Solid State and Materials Science*, 19(6), pp. 317-323.
- Ozbakkaloglu, T., Chen, J.-F., Smith, S.T. and Dai, J.-G. (2016) 'Applications of Fiber Reinforced Polymer Composites', *International Journal of Polymer Science*, 2016, p. 1.
- Page, T.F. and Hainsworth, S.V. (1993) 'Using nanoindentation techniques for the characterization of coated systems: a critique', *Surface and Coatings Technology*, 61(1-3), pp. 201-208.
- Palacio, J.F. and Bull, S.J. (2004) 'Dynamic indentation measurements on amorphous materials', *Zeitschrift für Metallkunde*, 95(5), pp. 335-339.
- Pelled, G., Tai, K., Sheyn, D., Zilberman, Y., Kumbar, S., Nair, L.S., Laurencin, C.T., Gazit, D. and Ortiz, C. (2007a) 'Structural and nanoindentation studies of stem cell-based tissue-engineered bone', *J Biomech*, 40(2), pp. 399-411.
- Pelled, G., Tai, K., Sheyn, D., Zilberman, Y., Kumbar, S., Nair, L.S., Laurencin, C.T., Gazit, D. and Ortiz, C. (2007b) 'Structural and nanoindentation studies of stem cell-based tissue-engineered bone', *Journal of Biomechanics*, 40(2), pp. 399-411.
- Pelletier, H. (2006) 'Predictive model to estimate the stress-strain curves of bulk metals using nanoindentation', *Tribology International*, 39(7), pp. 593-606.

- Pethica, J.B., Hutchings, R. and Oliver, W.C. (1983) 'Hardness measurement at penetration depths as small as 20 nm', *Philosophical Magazine A*, 48(4), pp. 593-606.
- Pethica, J.B. and Oliver, W.C. (1988) 'Mechanical properties of nanometre volumes of material: use of the elastic response of small area indentations', *MRS Proceedings*, 130, p. 13.
- Pharr, G.M. (1998) 'Measurement of mechanical properties by ultra-low load indentation', *Materials Science and Engineering: A*, 253(1), pp. 151-159.
- Pradid, J., Keawwattana, W. and Tangbunsuk, S. (2014) 'Study the effect of HAp content in PLA/HAp microsphere on the efficiency of drug (Clindamycin) loading process', *Advanced Materials Research*, 834, pp. 559-562.
- Ramakrishna, S., Huang, Z.-M., Kumar, G.V., Batchelor, A.W. and Mayer, J. (2004) *An introduction to biocomposites*. World Scientific.
- Randall, N.X., Vandamme, M. and Ulm, F.-J. (2009) 'Nanoindentation analysis as a two-dimensional tool for mapping the mechanical properties of complex surfaces', *Journal of Materials Research*, 24(03), pp. 679-690.
- Rezwan, K., Chen, Q.Z., Blaker, J.J. and Boccaccini, A.R. (2006) 'Biodegradable and bioactive porous polymer/inorganic composite scaffolds for bone tissue engineering', *Biomaterials*, 27(18), pp. 3413-3431.
- Rho, J.Y., Ziopoulos, P., Currey, J.D. and Pharr, G.M. (1999) 'Variations in the individual thick lamellar properties within osteons by nanoindentation', *Bone*, 25(3), pp. 295-300.
- Rho, J.Y., Ziopoulos, P., Currey, J.D. and Pharr, G.M. (2002) 'Microstructural elasticity and regional heterogeneity in human femoral bone of various ages examined by nano-indentation', *Journal of Biomechanics*, 35(2), pp. 189-198.
- Ricci, D. and Braga, P.C. (2004) 'Recognizing and avoiding artifacts in AFM imaging', *Atomic Force Microscopy: Biomedical Methods and Applications*, pp. 25-37.

Riester, L., Bell, T.J. and Fischer-Cripps, A.C. (2001) 'Analysis of depth-sensing indentation tests with a Knoop indenter', *Journal of Materials Research*, 16(06), pp. 1660-1667.

Roberts, S.G., Lawrence, C.W., Bisrat, Y., Warren, P.D. and Hills, D.A. (1999) 'Determination of surface residual stresses in brittle materials by Hertzian indentation: Theory and experiment', *Journal of the American Ceramic Society*, 82(7), pp. 1809-1816.

Roschger, P., Rinnerthaler, S., Yates, J., Rodan, G.A., Fratzl, P. and Klaushofer, K. (2001) 'Alendronate increases degree and uniformity of mineralization in cancellous bone and decreases the porosity in cortical bone of osteoporotic women', *Bone*, 29(2), pp. 185-191.

Sano, Y. (1988) 'Optical anisotropy of bovine serum albumin', *Journal of Colloid and Interface Science*, 124(2), pp. 403-406.

Sarikaya, M., Fong, H., Sunderland, N., Flinn, B.D., Mayer, G., Mescher, A. and Gaino, E. (2001) 'Biomimetic model of a sponge-spicular optical fiber—mechanical properties and structure', *Journal of Materials Research*, 16(05), pp. 1420-1428.

Sato, K., Hotta, Y., Nagaoka, T., Yasuoka, M. and Watari, K. (2006) 'Agglomeration control of hydroxyapatite nano-crystals grown in phase-separated microenvironments', *Journal of Materials Science*, 41(17), pp. 5424-5428.

Sawa, T., Akiyama, Y., Shimamoto, A. and Tanaka, K. (1999) 'Nanoindentation of a 10 nm thick thin film', *Journal of Materials Research*, 14(06), pp. 2228-2232.

Schuh, C.A., Mason, J.K. and Lund, A.C. (2005) 'Quantitative insight into dislocation nucleation from high-temperature nanoindentation experiments', *Nature Materials*, 4(8), pp. 617-621.

- Seo, C.H., Jeong, H., Feng, Y., Montagne, K., Ushida, T., Suzuki, Y. and Furukawa, K.S. (2014) 'Micropit surfaces designed for accelerating osteogenic differentiation of murine mesenchymal stem cells via enhancing focal adhesion and actin polymerization', *Biomaterials*, 35(7), pp. 2245-2252.
- Shahar, R., Zaslansky, P., Barak, M., Friesem, A.A., Currey, J.D. and Weiner, S. (2007) 'Anisotropic Poisson's ratio and compression modulus of cortical bone determined by speckle interferometry', *Journal of Biomechanics*, 40(2), pp. 252-264.
- Shinohara, K., Yasuda, K., Yamada, M. and Kinoshita, C. (1994) 'Universal method for evaluating work-hardening exponent of metals using ultra-microhardness tests', *Acta Metallurgica et Materialia*, 42(11), pp. 3909-3915.
- Simha, N.K., Carlson, C.S. and Lewis, J.L. (2004) 'Evaluation of fracture toughness of cartilage by micropenetration', *Journal of Materials Science: Materials in Medicine*, 15(5), pp. 631-639.
- Sneddon, I.N. (1965) 'The relation between load and penetration in the axisymmetric Boussinesq problem for a punch of arbitrary profile', *International Journal of Engineering Science*, 3(1), pp. 47-57.
- Soare, S., Bull, S.J., O'Neil, A.G., Wright, N., Horsfall, A. and dos Santos, J.M.M. (2004) 'Nanoindentation assessment of aluminium metallisation; the effect of creep and pile-up', *Surface and Coatings Technology*, 177, pp. 497-503.
- Soloviev, M. (2012) *Nanoparticles in Biology and Medicine: Methods and Protocols*. Humana Press.
- Stevens, M.M. (2008) 'Biomaterials for bone tissue engineering', *Materials today*, 11(5), pp. 18-25.

Stylianou, A., Kontomaris, S.V., Yova, D. and Balogiannis, G. (2014) 'AFM multimode imaging and nanoindentation method for assessing collagen nanoscale thin films heterogeneity', *XIII Mediterranean Conference on Medical and Biological Engineering and Computing 2013*, pp. 407-410.

Sun, J., Ling, M., Wang, Y., Chen, D., Zhang, S., Tong, J. and Wang, S. (2014) 'Quasi-static and dynamic nanoindentation of some selected biomaterials', *Journal of Bionic Engineering*, 11(1), pp. 144-150.

Sun, Y., Zheng, S., Bell, T. and Smith, J. (1999) 'Indenter tip radius and load frame compliance calibration using nanoindentation loading curves', *Philosophical Magazine Letters*, 79(9), pp. 649-658.

Swaddiwudhipong, S., Hua, J., Tho, K.K. and Liu, Z.S. (2006) 'Equivalency of Berkovich and conical load-indentation curves', *Modelling and Simulation in Materials Science and Engineering*, 14(1), p. 71.

Tabor, D. (1954) 'Mohs's hardness scale-a physical interpretation', *Proceedings of the Physical Society. Section B*, 67(3), p. 249.

Tai, K., Pelled, G., Sheyn, D., Bershteyn, A., Han, L., Kallai, I., Zilberman, Y., Ortiz, C. and Gazit, D. (2008) 'Nanobiomechanics of repair bone regenerated by genetically modified mesenchymal stem cells', *Tissue Eng Part A*, 14(10), pp. 1709-20.

Takano, Y., Turner, C.H., Owan, I., Martin, R.B., Lau, S.T., Forwood, M.R. and Burr, D.B. (1999) 'Elastic anisotropy and collagen orientation of osteonal bone are dependent on the mechanical strain distribution', *Journal of orthopaedic research*, 17(1), pp. 59-66.

Taljat, B. and Pharr, G.M. (1999) 'Measurement of residual stresses by load and depth sensing spherical indentation', *MRS Proceedings*, 594, p. 519.

- Tayton, E., Purcell, M., Aarvold, A., Smith, J.O., Briscoe, A., Kanczler, J.M., Shakesheff, K.M., Howdle, S.M., Dunlop, D.G. and Oreffo, R.O.C. (2014) 'A comparison of polymer and polymer–hydroxyapatite composite tissue engineered scaffolds for use in bone regeneration. An in vitro and in vivo study', *Journal of Biomedical Materials Research Part A*, 102(8), pp. 2613-2624.
- Tesch, W., Eidelman, N., Roschger, P., Goldenberg, F., Klaushofer, K. and Fratzl, P. (2001) 'Graded microstructure and mechanical properties of human crown dentin', *Calcified Tissue International*, 69(3), pp. 147-157.
- Thomas, V., Dean, D.R., Jose, M.V., Mathew, B., Chowdhury, S. and Vohra, Y.K. (2007) 'Nanostructured biocomposite scaffolds based on collagen coelectrospun with nanohydroxyapatite', *Biomacromolecules*, 8(2), pp. 631-637.
- Thurner, P.J., Oroudjev, E., Jungmann, R., Kreutz, C., Kindt, J.H., Schitter, G., Okouneva, T.O., Lauer, M.E., Fantner, G.E. and Hansma, H.G. (2007) 'Imaging of bone ultrastructure using atomic force microscopy', *Modern Research and Educational Topics in Microscopy*, pp. 37-48.
- Tsui, T.Y., Oliver, W.C. and Pharr, G.M. (1996) 'Indenter geometry effects on the measurement of mechanical properties by nanoindentation with sharp indenters', *MRS Proceedings*, 436, p. 147.
- Tuan, R.S., Boland, G. and Tuli, R. (2003) 'Adult mesenchymal stem cells and cell-based tissue engineering', *Arthritis Research and Therapy*, 5(1), pp. 32-45.
- Tuck, J.R., Korsunsky, A.M., Bull, S.J. and Davidson, R.I. (2001) 'On the application of the work-of-indentation approach to depth-sensing indentation experiments in coated systems', *Surface and Coatings Technology*, 137(2), pp. 217-224.
- Turner, C.H., Rho, J., Takano, Y., Tsui, T.Y. and Pharr, G.M. (1999) 'The elastic properties of trabecular and cortical bone tissues are similar: results from two microscopic measurement techniques', *Journal of Biomechanics*, 32(4), pp. 437-441.

Underwood, J.H. (1973) 'Residual-stress measurement using surface displacements around an indentation', *Experimental Mechanics*, 13(9), pp. 373-380.

Urabe, I., Nakajima, S., Sano, H. and Tagami, J. (2000) 'Physical properties of the dentin-enamel junction region', *American Journal of Dentistry*, 13(3), pp. 129-135.

Uskokovic, P.S., Tang, C.Y., Tsui, C.P., Ignjatovic, N. and Uskokovic, D.P. (2007) 'Micromechanical properties of a hydroxyapatite/poly-L-lactide biocomposite using nanoindentation and modulus mapping', *Journal of the European Ceramic Society*, 27(2), pp. 1559-1564.

Van de Velde, K. and Kiekens, P. (2002) 'Biopolymers: overview of several properties and consequences on their applications', *Polymer Testing*, 21(4), pp. 433-442.

Venugopal, J. and Ramakrishna, S. (2005) 'Applications of polymer nanofibers in biomedicine and biotechnology', *Applied Biochemistry and Biotechnology*, 125(3), pp. 147-157.

Waite, J.H., Lichtenegger, H.C., Stucky, G.D. and Hansma, P. (2004) 'Exploring molecular and mechanical gradients in structural bioscaffolds', *Biochemistry*, 43(24), p. 7653.

Walter, C., Antretter, T., Daniel, R. and Mitterer, C. (2007) 'Finite element simulation of the effect of surface roughness on nanoindentation of thin films with spherical indenters', *Surface and Coatings Technology*, 202(4), pp. 1103-1107.

Wang, M., Liechti, K.M., White, J.M. and Winter, R.M. (2004) 'Nanoindentation of polymeric thin films with an interfacial force microscope', *Journal of the Mechanics and Physics of Solids*, 52(10), pp. 2329-2354.

Wang, X. and Ni, Q. (2003) 'Determination of cortical bone porosity and pore size distribution using a low field pulsed NMR approach', *Journal of Orthopaedic Research*, 21(2), pp. 312-319.

- Wang, X.H., Jacobsen, S., He, J.Y., Zhang, Z.L., Lee, S.F. and Lein, H.L. (2009) 'Application of nanoindentation testing to study of the interfacial transition zone in steel fiber reinforced mortar', *Cement and Concrete Research*, 39(8), pp. 701-715.
- Wei, G., Bhushan, B. and Torgerson, P.M. (2005) 'Nanomechanical characterization of human hair using nanoindentation and SEM', *Ultramicroscopy*, 105(1), pp. 248-266.
- Wenger, M.P.E., Bozec, L., Horton, M.A. and Mesquida, P. (2007) 'Mechanical properties of collagen fibrils', *Biophysical journal*, 93(4), pp. 1255-1263.
- Westbrook, J.H. (1973) 'The science of hardness testing and its research applications'.
- Wierenga, P.E. and Franken, A.J.J. (1984) 'Ultramicroindentation apparatus for the mechanical characterization of thin films', *Journal of Applied Physics*, 55(12), pp. 4244-4247.
- Willam, K. (2002) 'Constitutive models for engineering materials', *Encyclopedia of Physical Science and Technology*, 3, pp. 603-633.
- Wolfram, U., Wilke, H.-J. and Zysset, P.K. (2010) 'Transverse isotropic elastic properties of vertebral trabecular bone matrix measured using microindentation under dry conditions (effects of age, gender, and vertebral level)', *Journal of Mechanics in Medicine and Biology*, 10(01), pp. 139-150.
- Yan, W., Pun, C.L. and Simon, G.P. (2012) 'Conditions of applying Oliver–Pharr method to the nanoindentation of particles in composites', *Composites Science and Technology*, 72(10), pp. 1147-1152.
- Yan, W., Pun, C.L., Wu, Z. and Simon, G.P. (2011) 'Some issues on nanoindentation method to measure the elastic modulus of particles in composites', *Composites Part B: Engineering*, 42(8), pp. 2093-2097.
- Yang, B., Riester, L. and Nieh, T.G. (2006) 'Strain hardening and recovery in a bulk metallic glass under nanoindentation', *Scripta Materialia*, 54(7), pp. 1277-1280.

Yang, H.S., Park, J., La, W.G., Jang, H.-k., Lee, M. and Kim, B.-S. (2011) '3, 4-Dihydroxyphenylalanine-assisted hydroxyapatite nanoparticle coating on polymer scaffolds for efficient osteoconduction', *Tissue Engineering Part C: Methods*, 18(4), pp. 245-251.

Yang, W., Liu, Q., Yue, Z., Li, X. and Xu, B. (2017) 'Rotation of hard particles in a soft matrix', *Journal of the Mechanics and Physics of Solids*, 101, pp. 285-310.

Yu, M.-H. (2006) *Generalized plasticity*. Springer Science & Business Media.

Yuan, Y. and Verma, R. (2006) 'Measuring microelastic properties of stratum corneum', *Colloids and Surfaces B: Biointerfaces*, 48(1), pp. 6-12.

Zadpoor, A.A. (2015) 'Nanomechanical characterization of heterogeneous and hierarchical biomaterials and tissues using nanoindentation: The role of finite mixture models', *Materials Science and Engineering: C*, 48(0), pp. 150-157.

Zaichick, V. and Tzaphlidou, M. (2003) 'Calcium and phosphorus concentrations and the calcium/phosphorus ratio in trabecular bone from the femoral neck of healthy humans as determined by neutron activation analysis', *Applied radiation and isotopes*, 58(6), pp. 623-627.

Zamiri, A. and De, S. (2011) 'Mechanical properties of hydroxyapatite single crystals from nanoindentation data', *Journal of the Mechanical Behavior of Biomedical Materials*, 4(2), pp. 146-152.

Zanjani Zadeh, V. and Bobko, C.P. (2013) 'Nanoscale mechanical properties of concrete containing blast furnace slag and fly ash before and after thermal damage', *Cement and Concrete Composites*, 37(0), pp. 215-221.

Zebaze, R.M.D., Jones, A.C., Pandy, M.G., Knackstedt, M.A. and Seeman, E. (2011) 'Differences in the degree of bone tissue mineralization account for little of the differences in tissue elastic properties', *Bone*, 48(6), pp. 1246-1251.

- Zhang, C.Y., Zhang, Y.W., Zeng, K.Y. and Shen, L. (2005) 'Nanoindentation of polymers with a sharp indenter', *Journal of Materials Research*, 20(06), pp. 1597-1605.
- Zhang, H., Ye, X.-J. and Li, J.-S. (2009) 'Preparation and biocompatibility evaluation of apatite/wollastonite-derived porous bioactive glass ceramic scaffolds', *Biomedical Materials*, 4(4), p. 045007.
- Zhang, S. (2010) *Nanostructured thin films and coatings: mechanical properties*. CRC Press.
- Zheng, L., Schmid, A.W. and Lambropoulos, J.C. (2007) 'Surface effects on Young's modulus and hardness of fused silica by nanoindentation study', *Journal of Materials Science*, 42(1), pp. 191-198.
- Zioupos, P. and Currey, J.D. (1998) 'Changes in the stiffness, strength, and toughness of human cortical bone with age', *Bone*, 22(1), pp. 57-66.
- Zioupos, P., Currey, J.D. and Hamer, A.J. (1999) 'The role of collagen in the declining mechanical properties of aging human cortical bone', *Journal of biomedical materials research*, 45(2), pp. 108-116.
- Zong, C., Qian, X., Tang, Z., Hu, Q., Chen, J., Gao, C., Tang, R., Tong, X. and Wang, J. (2014) 'Biocompatibility and bone-repairing effects: comparison between porous poly-lactic-co-glycolic acid and nano-hydroxyapatite/poly (lactic acid) scaffolds', *Journal of Biomedical Nanotechnology*, 10(6), pp. 1091-1104.
- Zysset, P.K., Guo, X.E., Hoffler, C.E., Moore, K.E. and Goldstein, S.A. (1999) 'Elastic modulus and hardness of cortical and trabecular bone lamellae measured by nanoindentation in the human femur', *Journal of Biomechanics*, 32(10), pp. 1005-1012.

